Multi-dimensional Teager-Kaiser signal processing for improved characterization using white light interferometry

Gianto Gianto

UNIVERSITÉ DE STRASBOURG

ÉCOLE DOCTORALE MATHEMATIQUES, SCIENCES DE L'INFORMATION ET DE L'INGENIEUR (MSII) – ED 269

LABORATOIRE DES SCIENCES DE L'INGENIEUR, DE L'INFORMATIQUE ET DE L'IMAGERIE (ICUBE UMR 7357)

THÈSE présentée par :

Gianto GIANTO

soutenue le : 14 **Septembre 2018**

pour obtenir le grade de : **Docteur de l'université de Strasbourg**

Discipline/ Spécialité : SIAR-Traitement du signal et des images

Multi-dimensional Teager-Kaiser signal processing for improved characterization using white light interferometry

THÈSE dirigée par :
Dr. MONTGOMERY Paul Directeur de recherche, CNRS, ICube (Strasbourg)
Encadrant :
Dr. SALZENSTEIN Fabien Maître de conférences, ICube (Strasbourg)

RAPPORTEURS :
Pr. CHONAVEL Thierry Professeur des Universités, IMT Atlantique (Brest)
Dr. SANDOZ Patrick Chargé de Recherche, CNRS, FEMTO-ST (Besançon)

AUTRES MEMBRES DU JURY :
Dr. BOUDRAA Abdel Maître de conférences, Ecole Naval IRENAV (Brest)
Pr. HAEBERLE Olivier Professeur des Universités, IRIMAS (Mulhouse)

CONTENTS

To my families…

ACKNOWLEDGEMENTS

This PhD research would not have been possible without the help, the support, and the contribution of many people and institutions.

Firstly, I am very grateful to my supervisor (Directeur de thèse), Paul Montgomery, whom I greatly respect, for supervising my research work over the years. Many thanks for all the advice, the encouragement, the availability and the hours he spent for reading and correcting the manuscript. I am also very grateful to my co-supervisor (Encadrant), Fabien Salzenstein, for his great availability for discussion whenever I had a problem or a question about my PhD research. Many thanks also for the help, the encouragement, and the contribution for the improvement of the manuscript.

Thanks are given to Audrey Leong-Hoï and Husneni Mukhtar for providing the measurements on real samples and to Stéphane Perrin for useful discussions, all from the IPP team. Finally, I will always remember all of the kindness of my colleagues in the IPP team and to all parties that cannot be mentioned one by one for their support during my study.

My appreciation is also extended to the institution where I work, the Metrological Resources Development Centre, which gave me permission to study in France. I am also grateful to the Indonesian Government (Ministry of Trade), which provided the scholarship for my studies.

TABLE OF FIGURES

LIST OF TABLES

RÉSUMÉ

L'utilisation de franges d'interférence en lumière blanche comme une sonde optique en microscopie interférométrique est d'une importance croissante dans la caractérisation des matériaux, la métrologie de surfaces et l'imagerie médicale. La technique, basée sur la microscopie interférométrique, a l'avantage d'y parvenir en ne faisant qu'un balayage vertical de l'échantillon, alors que les techniques de mesure ponctuelle nécessitent un grand nombre de balayages dans le plan horizontal pour imager un échantillon. L'Interférométrie en lumière blanche (Coherence Scanning Interferometry, CSI, également connu comme White Light Scanning Interferometry, WLSI) est une technique basée sur la détection de l'enveloppe de franges d'interférence. Cette technique (CSI) utilise généralement un échantillonnage des franges selon l'axe optique par moyen d'une acquisition d'une pile d'images XYZ. Le traitement d'image est ensuite utilisé pour identifier les enveloppes des franges, le long de l'axe Z à chaque pixel afin de mesurer les positions d'une surface unique ou des structures enterrées dans une couche. La mesure de la forme de la surface en CSI, nécessite généralement la détection d'un pic ou l'extraction de la phase du signal de franges mono-dimensionnel.

La plupart des méthodes sont basées sur un modèle de signal AM-FM, qui représente la variation de l'intensité lumineuse mesurée le long de l'axe optique d'un microscope interférométrique. Il a été démontré antérieurement, la capacité des approches 2D à rivaliser avec certaines méthodes classiques utilisées dans le domaine de l'interférométrie, en termes de robustesse et de temps de calcul. En outre, alors que la plupart des méthodes tiennent compte seulement des données 1D, il semblerait avantageux de prendre en compte le voisinage spatial utilisant des approches multidimensionnelles (2D, 3D), y compris le paramètre de temps afin d'améliorer les mesures.

Dans ce projet de recherche, nous sommes intéressés à développer de nouvelles approches n-D en utilisant Multi dimensionel Teager Kaiser qui sont appropriées pour une meilleure caractérisation des surfaces plus complexes et des couches transparentes. Dans ce travail, nous effectuons trois étapes pour le traitement des signaux de frange, à savoir le pré-traitement afin de supprimer le bruit et supprimer la composante de

décalage, la détection d'enveloppe et le post-traitement afin de déterminer plus précisément la mesure.

Nous commençons notre étude en évaluant la détection d'enveloppe en utilisant 1D Teager kaiser Energy Operator dans le traitement des signaux de frange, qui est comparé à d'autres techniques. Nous avons développé un programme de simulation de franges blanches (sur MATLAB) qui permet de comparer les résultats de mesures synthétiques (une couche transparente) effectués par différentes techniques de traitement de signal. Ces méthodes consistent en la Transformée de Fourier (TF), ondelettes, la FSA (Five-Sample-Adaptive), Opérateur d'énergie de Teager Kaiser (TKEO). Sur la base des résultats de simulation utilisant les images de franges synthétiques, il a été démontré que TKEO fournit les résultats les plus précis pour l'extraction de la surface supérieure et plus proche de la performance de CWT pour l'extraction de l'interface enterrée (surface arrière), mais présente l'avantage d'être plus compact et donc plus rapide. Les algorithmes TKEO et CWT fournissent également une meilleure extraction de surface que les algorithmes HT et FSA. Enfin, nous avons étudié la réalisation des algorithmes en utilisant des données réelles, c'est-à-dire l'image de frange de la couche de résine sur Silicium. Le résultat montre que CWT et TKEO ont des capacités différentes pour identifier deux positions de pic adjacentes. Sur la zone où se trouvent deux signaux de franges qui se chevauchent, le TKEO est capable d'obtenir l'enveloppe de frange qui distingue deux couches, tandis que CWT échoue dans le cas.

Après avoir commencé sur des signaux 1D, nous avons implémenté des traitements sur des signaux 2D. Dans ce projet de recherche, l'étude de la robustesse du traitement des franges 2D en CSI a également été réalisée pour la caractérisation d'un film de polymère Mylar transparent. Nous avons démontré la capacité des approches 2D Teager Kaiser à concurrencer certaines méthodes classiques (approches 1D) utilisées dans le domaine de l'interférométrie, en termes de robustesse. Ces résultats démontrent que l'enveloppe de frange XZ extraite par les approches 2D Teager Kaiser donne des résultats plus satisfaisants que l'approche 1D en révélant les structures internes et la surface arrière. La technique permet également une amélioration des détails dans les images XZ ainsi que des mesures plus précises de l'épaisseur du film polymère.

À la fin de ce travail, nous présentons l'étude de l'application de 3D Teager Kaiser Energy Operator (3DTKEO), qui est développé sur la base de l'opérateur d'énergie TK multi-dimensionnel. Grâce à une simulation utilisant un signal de frange synthétique,

nous avons évalué la robustesse des performances de 3DTKEO dans le traitement des signaux de franges, qui est comparé à l'approche 1D et 2D. De plus, nous avons également effectué l'algorithme sur des données réelles, c'est-à-dire une norme de hauteur de pas (VLSI Standard Inc.) afin d'évaluer la précision de la mesure. De plus, nous avons enrichi le domaine d'étude en testant l'algorithme sur différents échantillons, tels que le graphène, les DOE (Diffractive Optical Elements), la résine sur silicium, le câble et la roche.

NOMENCLATURE

$s(x,y,z)$	Intensity signal at a given point of the sample surface (x,y)
z	Vertical scanning position along the optical axis in relation to the surface
$a(x,y,z)$	Offset intensity related to the reference and object beam intensities
$b(x,y)$	Fringe contrast
$g(z)$	Fringe envelope function
λ_0	Mean wavelength of the light source
$\alpha(x,y)$	Phase offset
$A_n(x,y)$	Amplitude - value of the envelope for a single sampling position
$\phi(x,y)$	Phase shift due to the scanning step
$I_n(x,y)$	Intensities of sampling positions
$\dot{s}(z)$	First derivative of signal $s(z)$
$\ddot{s}(z)$	Second derivative of signal $s(z)$
$\psi[s(z)]$	Teager Kaiser Energy Operator
$\lvert a(t)\rvert$	Instantaneous envelope
$\lvert\dot{\phi}(t)\rvert$	Instantaneous phase
$W(a,b)$	CWT coefficient function, where a is the scale factor and b is the shift factor
$\psi(z)$	Continuous function in time and frequency domain called the mother wavelet
R_t	Total (or peak-valley) roughness
$z_{\max}$	Highest peak of the surface profile
$z_{\min}$	Lowest peak of the surface profile
R_a	Arithmetic roughness
$\bar{z}$	mean line of the roughness profile height z_j

ABBREVIATIONS

1D	One dimensional
2D	Two dimensional
2DHT	Two dimensional analytic signal-Hilbert Transform
2DTKEO	Two dimensional Teager-Kaiser energy operator
3D	Three dimensional
AM-FM	Amplitude Modulation - Frequency Modulation
CSI	Coherence Scanning Interferometry
CWT	Continuous Wavelet Transform
DEOs	Differential energy operators
EMD	Empirical Mode Decomposition
ESA	Energy Separation Algorithm
FF-OCT	Full Field Optical Coherence Tomography
FFT	Fast Fourier Transform
FSA	Five-sample adaptive
FT	Fourier Transform
HT	Hilbert Transform
IMFs	Intrinsic mode functions
MAE	Mean absolute error
MEMS	Micro Electro Mechanical Systems
NA	Numerical Aperture
OPD	Optical path difference
PSM	Phase Shifting Microscopy
ROI	Region of interest

SG filter	Savitzky-Golay filter
SNR	Signal to noise ratio
TK	Teager-Kaiser
TKEO	Teager-Kaiser energy operator
WLSI	White Light Scanning Interferometry

GENERAL INTRODUCTION

This thesis is the result of my PhD research carried out for more than three years in fringe signal analysis in the field of Coherence Scanning Interferometry (CSI). The work has been performed in the IPP team (Photonics Instrumentation and Processes), in the ICube laboratory, University of Strasbourg-CNRS. The PhD scholarship has been funded by the Ministry of Trade, Indonesian government from 2014 to 2018. The purpose of the project was to develop new n-D approaches (2D, 3D) which are suitable for improved characterization of more complex surfaces and transparent layers using white light interferometry.

Several surface analysis techniques, such as the classical stylus probe, SEM (Scanning Electron Microscopy), AFM (Atomic Force Microscopy), confocal microscopy and interference microscopy, are important in the field of materials characterization, industrial metrology, and inspection [1],[2],[3]. It is often useful to use several techniques to elucidate the various surface characteristics, especially since there is no single technique capable of providing all the information on the morphology of a surface. The technique of interference microscopy, which makes use of light interference as the optical probe, has the advantages of being non-destructive and fast [4],[5],[6]. There are two families of techniques in interference microscopy: Phase Shifting Microscopy (PSM) and Coherence Scanning Interferometry (CSI). PSM is a mathematical method of fringe interpolation based on the introduction of known phase shifts between the two arms of the interferometer. The technique is well suited for the analysis of small surface roughness (depth < 200 nm) and commonly has a nanometric axial resolution. The dynamic range of PSM is limited to $\lambda/2$ due to the periodicity of the interference fringes that induce a 2π ambiguity in the measured surface profiles.

Due to this limitation, the second family of techniques, i.e. CSI was developed to allow the measurement of much deeper surfaces. The advantages of this technique compared to the PSM are the larger vertical depth of field and the possibility of measuring height differences of several microns and more [7],[8]. Nowadays, the use of CSI, which is also common known as white light interferometry, is widely used in various fields, including surface metrology, materials characterization, and medical imaging. For instance in the field of metrology, white light interferometry has been applied in the

characterisation of the fabrication of Micro Electro Mechanical Systems (MEMS) and other micro-component devices [9],[10],[11]. White light interferometry has also been applied for the measurement of surface roughness and microscopic structures in materials science and microelectronics [12],[13]. In another field, Dubois et al. developed full-field optical coherence tomography (FF-OCT) based on white light interferometry for high-resolution optical imaging of biological tissue [14],[15],[16]. This technique achieves a better spatial resolution than conventional OCT, without using an expensive light source, achieving a resolution of axial × transverse = 0.7 μm × 0.9 μm. Conventional OCT is usually based on a fibre Michelson interferometer illuminated by a broad-bandwidth spatially coherent source (laser). The measurement requires scanning of a point probe in the transverse direction over the sample in order to obtain the cross sectional image. The spatial resolution of OCT in the axial direction is defined by the coherence length of the illumination source, typically 10–15 μm in the case of a super luminescent diode (SLD) [16], [17], [18]. By using ultra-short femto second laser technology, the spatial resolution of OCT has improved down to ~ 1 μm. Nowadays, OCT can be applied at the cellular level [14], [17].

A schematic layout of a simplified OCT system is illustrated in Fig. 1. The light from a low coherence source is coupled into a fiber-optic Michelson interferometer. This light is then split at a fiber coupler into the reference and the sample arm. The light retroreflected from the reference mirror and the light backscattered from the sample is recombined in the coupler and generates an interference pattern, which is detected by a single point detector (a photodiode) [17], [19], [20].

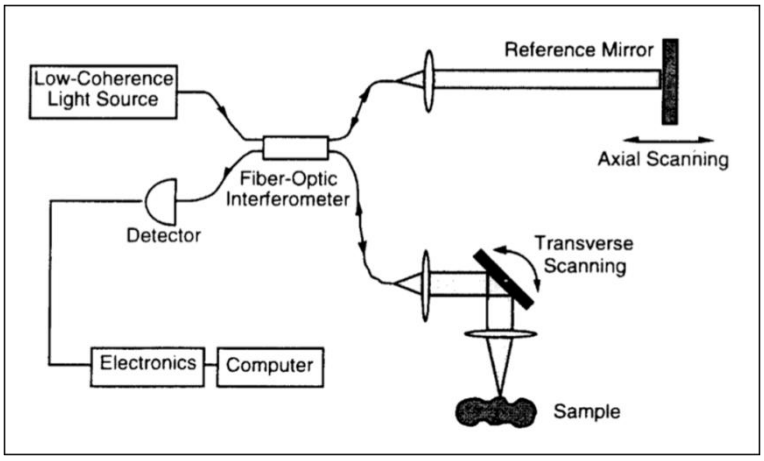

Fig. 1 Schematic of the OCT system [17]

The use of white light interference fringes as an optical probe in microscopy has a long history. In 1665, Robert Hooke investigated the coloured fringe that can be observed in white light when the two glass plates are in contact [21]. This phenomenon can be called as the starting point of optical interferometry. Coloured fringe were then studied by Isaac Newton in 1717 as an interference pattern created by the reflection of light between two surfaces (known as "Newton's rings"). Since then, the development of white light interferometry has been extended right up to the present day. The method developed for the three dimensional measurement of surface topography using white light interferometry is generally based on the analysis of fringe contrast. In this method, vertical fringe scanning (either the object or reference mirror) is carried out, followed by measuring the fringe intensity at each point of the object surface. The fringe pattern is observable when the optical path difference between the reference mirror position and the object surface is smaller than the coherence length of the used light. The zero value of the optical path difference is related to the surface position of the object (sample).

Developments in digital signal processing now allow three dimensional measurement using white light interferometry rapidly and automatically. The first automated 3D measurement using white light interferometry was reported by Balasubramanian in 1980 [22]. The variation in fringe contrast is recorded using a detector (CCD), point by point for each surface position. If the maximum fringe contrast level is observed, that point is determined as having a zero path difference that indicates the surface position. In 1987, Davidson reported the application of white light interferometry for integrated circuit inspection and metrology [23]. In this application, the use of an automated mechanical piezoelectric stage for fringe scanning was applied. The fringe intensity was captured using a detector, and then the peak of the fringe contrast was detected for profiling the object (integrated circuits). In 1990, by extending the concept of the Davidson's work and focusing on the profilometry capabilities of white light interferometry, Lee and Starnd reported the advantage of white light interferometry over the conventional microscope in lateral resolution [24]. In 1992, the work on three dimensional sensing using white light interferometry for rough objects was reported [25]. In 1990, Chim and Kino introduced another way of fringe analysis by digital filtering of the interferogram (interference data). The fringe analysis used two different algorithms based on the Fourier Transform and Hilbert transform for extracting the fringe envelope [26], [27]. In 1993, Caber used the demodulation technique adapted from

communications theory for retrieving the fringe envelope [7], [28], [29]. In 1993, Montgomery and Fillard applied the algorithm of PFSM (peak fringe scanning microscopy) [30], [31], a very efficient algorithm which was then adapted for 3D measurement in real time [32],[33]. In 1996, Larkin developed the Five Sample Adaptive (FSA) algorithm which is an efficient algorithm in computational time for retrieving the fringe contrast envelope [34]. This was then demonstrated to be a member of the wider family of very compact and efficient Teager-Kaiser Energy Operators by Salzenstein et al. (TKEO) [35], [36], [37]. The work demonstrated that the TKEO algorithms are robust and very competitive with the other types of fringe envelope detection algorithms, being very efficient in terms of computation time, and making them quicker than the other techniques when implemented on the appropriate hardware. The extended versions of this operator show that the method substantially provides the effective results in term of the surface measurement [38]. Then, another method using the wavelet transform algorithm in order to retrieve the fringe envelope in white-light interferometry was applied by Sandoz in 1997 [39]. The advantage of the wavelet transform method implemented in white light interferometry is that it is very robust to noise.

Most of the above fringe envelope detection methods are implemented on the one dimensional fringe signal (1D approach). The work in [13] used a 2D imaging processing method of the XZ images in an image stack for tomographic analysis of transparent layers. We also demonstrated in [12], [40] the ability of 2D approaches to compete with some classical methods used in the field of interferometry, in terms of robustness. Whereas most methods only take into account the 1D data, it is advantageous to take into account the spatial neighborhood using multidimensional approaches (2D, 3D). The objective of this project was therefore to study and develop new n-D approaches using Teager Kaiser energy operators for fringe analysis in CSI. This study is one part of dealing with several challenges of fringe signal processing currently in CSI. The challenges include the precision required along Z (optical axis) and XY (lateral direction), speed of processing, quantitative and qualitative aspects, noise aspects, the offset component, n-D approaches, and a formalised protocol for processing. Another challenge is the degree of complexity of the surface, that can be classified going from the simplest to the more complex, by a smooth homogenous surface, a rough surface, a transparent layer with defects, a cell in water, and skin/tissue, as shown in Fig. 2.

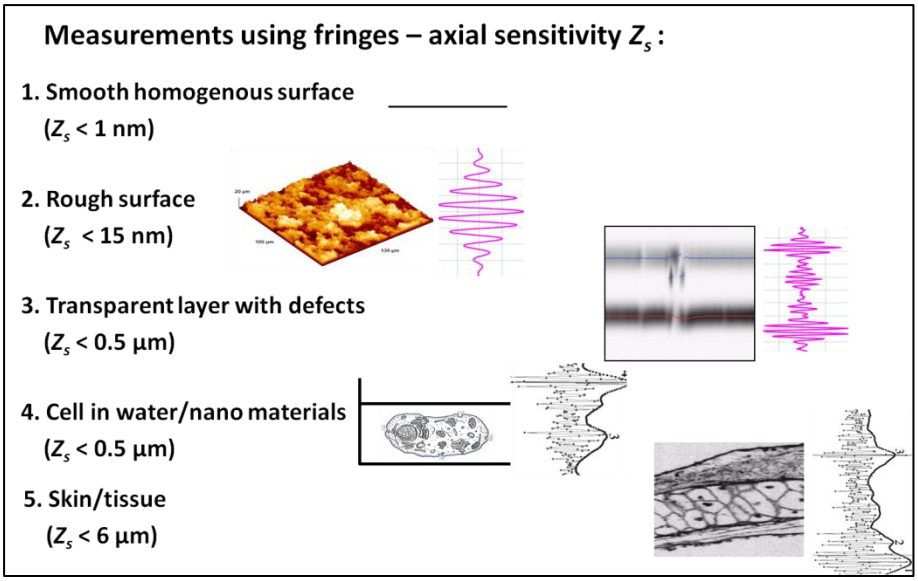

Fig. 2 Challenges of fringe signal processing in CSI

This thesis is composed of four main chapters.

The first chapter discusses the state of the art of Coherence Scanning Interferometry as related to this project. We mainly discuss the general principles of CSI and the procedure of fringe analysis. We study and observe the structure of the fringe signal and the various approaches (Z-scan and XZ-scan techniques) for fringe analysis. The study of pre-processing for the offset component removal, microscope system, and description of the samples which we use in the work are also reported.

In the second chapter, we begin our study by evaluating the performance of envelope detection using the 1D Teager Kaiser Energy Operator, which is compared to other techniques. These methods consist of the Fourier Transform (TF), wavelet, the FSA (Five-Sample-Adaptive). We have developed a simulation program (on MATLAB) that allows the comparison of the performance of different methods using a synthetic fringe signal (a synthetic transparent layer). Then, we have studied the realization of the algorithms using real data, in this case on fringe images from a resin layer on Silicon.

In the third chapter, we implement the 2D approach using Teager Kaiser for fringe analysis. In this work, the study of the robustness of the 2D approach in CSI was carried out for the characterization of a transparent polymer film. The results demonstrate that the XZ fringe envelope extracted by the 2D Teager Kaiser approaches gives more satisfactory results than the 1D approach by revealing the internal structures and the rear surface of

the transparent polymer film. The technique also results in improved details in the XZ images as well as more accurate measurements of the thickness of the polymer film.

In the fourth chapter, we present the study of the application of the 3D Teager Kaiser Energy Operator (3DTKEO), which is developed on the basis of the multi-dimensional Teager Kaiser energy operator. Through a simulation using a synthetic fringe signal, we have evaluated the robustness of the 3DTKEO's performance in fringe signal processing, which is compared to the 1D and 2D approaches. In addition, we have also used the algorithm on real data, in this case a step height standard (VLSI Standard Inc.) to evaluate the accuracy of the measurement. In addition, we have enriched the field of study by testing the algorithm on various other samples, such as graphene, DOE (Diffractive Optical Elements), resin on silicon, cable, and rock.

Chapter 1. COHERENCE SCANNING INTERFEROMETRY

In this chapter, we discuss several of the existing three dimensional surface profiling techniques, including Atomic Force Microscopy (AFM), confocal microscopy, and interference microscopy. Futhermore, we describe how the technique of Coherence Scanning Interferometry (CSI) generates an interferogram (fringe signal). We study and observe the structure of the fringe signal and the various approaches (Z-scan and XZ-scan techniques) for the fringe analysis. Then, we focus on the steps of the fringe analysis procedure which we perform in this work. The study of pre-processing for the offset component removal and determination of the surface structure of the sample which we use in the work are also reported.

1.1 3D SURFACE PROFILING

The measurement of 3D surface structures is an important field in materials characterization and industrial metrology. The existing techniques of 3D surface topography measurement consist of contact profilometers and optical profilometers. A stylus profiler is the oldest contact profiler, using a tactile probe to measure the surface profile [1], [2]. The technique works by moving the object surface in relation to the stylus tip and sensing the height variations of the stylus tip to determine the surface height profile. In the 1980's, another type of scanning probe profilometer involving near field microsopy was developed [41]. The first mode was Scanning Probe Microscopy (SPM), based on electron tunnelling, that works by moving a fine tip in close proximity to the sample surface, to within several nm to a few angstroms depending on the technique. The Atomic Force Microscope (AFM) is the most popular SPM, using Van der Waal's forces that can provide 3D images of surfaces generally at the nanometer scale. AFM is popular particularly for use in measuring non-conductive materials such as cells, bacteria, viruses and proteins [42], [43].

AFM has the advantages of nanometric resolution, but the images take in general several minutes to several tens of minutes or more to acquire. Optical profilers on the other hand have the advantage of allowing high speed surface profiling. The two most

common optical profilers are confocal microscope and white light interferometery (Coherence Scanning Interferometry).

Confocal microscope. The confocal microscope is based on focusing principle, as illustrated in Fig. 3. that uses a pinhole to ensure only light at the point of focus on the sample surface can enter the detector. Fig. 3(a) shows the sample in the focal plane of the objective, while the sample moving out of the focus is shown in Fig. 3(b). The complete image is formed through point by point scanning of the illuminating and detecting pinhole on the spot over the sample surface. The image will not be formed if the sample moves out of focus, as shown in Fig. 3(b).

Another type, the chromatic confocal microscope was then developed which the vertical scanning is not required [1],[4], as shown in Fig. 3(c). Rather than using the vertical scanning, the technique uses an objective with an axial chromatic aberration that has a different focus position for each different wavelength corresponding to the height of the surface. A spectrometer in place of CCD as a detector, detects the wavelength value. The measurement of the object focus position based on the spectrum measurement makes the measurement process much faster. The technique has the disadvantage of the optical sensitivity for the inhomogeneous materials. Similarly as the conventional confocal system, another disadvantage is the necessity of lateral scanning of the sample.

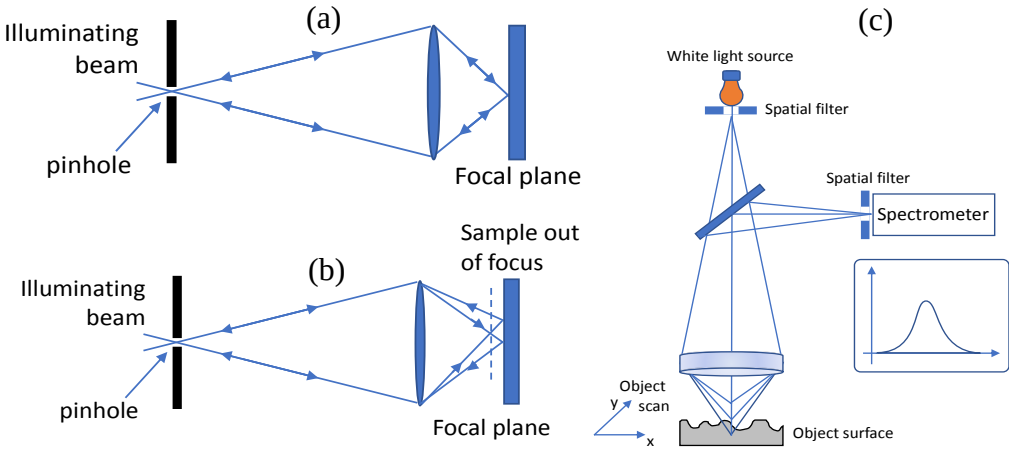

Fig. 3 Schematic of confocal microscope: showing the scanning (a) in the focal plane of the objective and (b) out of focus. (c) schematic of chromatic confocal microscopy [44]

Phase Shifting Microscopy. There are two main techniques used in interference microscopy: Phase Shifting Microscopy (PSM) and CSI [12],[8],[45]. PSM is a mathematical method of fringe interpolation based on the introduction of known phase shifts between the two arms of the interferometer. These phase shifts vary the optical path difference (OPD) which result in several interferograms. The technique is well suited for the analysis of small surface roughness (depth < 200 nm) and commonly has a nanometric axial resolution. The PSM also has the capability to deliver results with low noise and high precision for smooth optical surfaces. However, the dynamic range of PSM is limited to $\lambda/2$ due to the periodicity of the interference fringes that induce a 2π ambiguity in the measured surface profiles. Due to this limitation, the second family of techniques, i.e. CSI was developed to allow the measurement of much deeper surfaces. The advantages of this technique compared to the PSM are the larger vertical depth of field and the possibility of measuring height differences of several microns and more [7],[8].

In PSM technique, a monochromatic or quasi-monochromatic light source is used for illumination on the sample such as with Köhler illumination. During the measurement, the optical path difference (OPD) is changed by taking three or more images using the camera. The phase of the interference signal is then analyzed at each point on the image using the PSM algorithm. The altitude which represents the surface profile is calculated based on the result of the phase measurement.

The following Eq.(1.1) [46] express the intensity at a coordinate point (x,y) in an interference pattern:

$$\boldsymbol{I_i(x,y) = I_o(x,y)[1 + \gamma_0 \cos(\varphi(x,y) + \alpha_i)]} \qquad \textbf{(1.1)}$$

where $I_o(x,y)$ is the irradiance, γ_0 is the fringe visibility (also called modulation or contrast), $\varphi(x,y)$ is the signal phase, and α_i is the phase shift. Based on the Eq. (1.1) mathematically, the three unknown parameters: $I_o(x,y)$, γ_0 and $\varphi(x,y)$ can be calculated by using at least three interferograms. The precision of the measurement in PSM technique can be improved using higher numbers of interferograms.

In order to introduce the phase shifts in PSM, there are two basic modes, i.e. the discrete mode and continuous mode. For description of this phase shift in discrete and continuous mode, the algorithm of 4 steps of 120° is chosen as illustration.

Discrete mode. The discrete mode of this technique based on the discrete phase steps calculation is also known as the phase stepping microscopy. The illustration in Fig. 4 shows a phase determination from 4 discrete mode which is represented by the intensity of the interference fringes. The phase is then can be calculated using the following equation, which is usually displayed as a grayscale image of the phase:

$$\varphi = \tan\left[\frac{I_4 - I_2}{I_1 - I_3}\right] \quad \textbf{(1.2)}$$

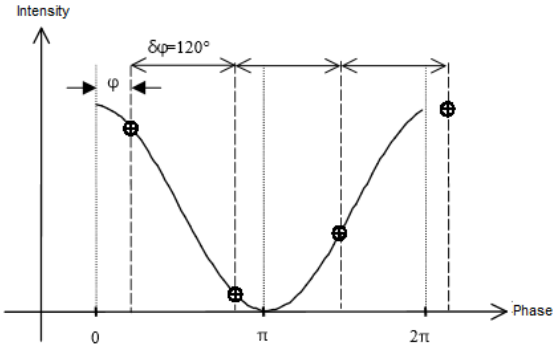

Fig. 4 Phase determination, from 4 discrete steps of 120°[47].

Continuous mode. The continuous mode of the phase change technique in PSM, also known as the technique of the phase integration. As illustrated in Fig. 5, the technique is based on a linear variation of the phase. The parameter *T* is the period time of the change of the phase, while the parameter τ, which depends on the number of interferograms, is a time of the acquisition of an image.

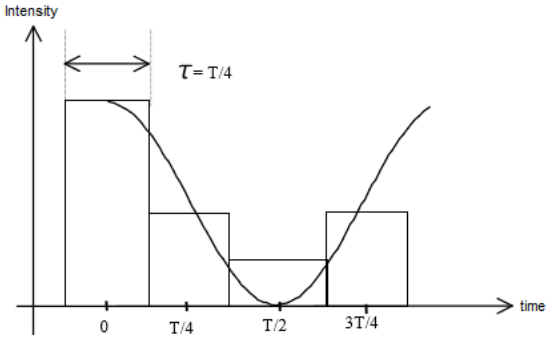

Fig. 5 The technique of the change of phase[47].

In this technique several interferograms over the period T (assuming T is continuous) are recorded in order to determine the initial phase. On the other hand, one interferogram represents each integration time τ. Fig. 5 shows the illustration of phase determination in continuous mode corresponding to the example of Fig. 4. The integration time $\tau_1 = 0\,, \tau_2 = \frac{T}{4}\,, \tau_3 = \frac{T}{2}\,, \tau_4 = \frac{3T}{4}$ represents respectively the phase determination of 4 steps of 120°.

PSM algorithms

Several phase reconstruction algorithms have been developed. The phase measurement algorithms are based on the acquisition of a series of N interferograms (N ranging generally from 3 to 7) obtained with known phase shifts. The essential parameters in these measurement techniques are the mode of variation of the phase (discrete or continuous), the frequency of acquisition of the interference fringes and the number N of interferograms used to calculate the phase at a given instant.

a. Three step technique

If a phase shift of 2π is introduced between the object and reference beams, the phase $\varphi(x,y)$ can be deduced from the intensities I_1, I_2, I_3 of the three interferograms recorded for the angular offsets $\pi/4$, $3\pi/4$, $5\pi/4$. The intensities measured are given by:

$$\begin{aligned} I_1(x,y) &= I_0(x,y)\left[1+\gamma\cos\left(\varphi(x,y)+\frac{\pi}{4}\right)\right] \\ I_2(x,y) &= I_0(x,y)\left[1+\gamma\cos\left(\varphi(x,y)+\frac{3\pi}{4}\right)\right] \\ I_3(x,y) &= I_0(x,y)\left[1+\gamma\cos\left(\varphi(x,y)+\frac{5\pi}{4}\right)\right] \end{aligned} \qquad \textbf{(1.3)}$$

The resolution of these equations gives the expressions of phase and visibility at a point of coordinates (x,y) as follows:

$$\begin{aligned} \varphi(x,y) &= arctg\left[\frac{I_3(x,y)-I_2(x,y)}{I_1(x,y)-I_2(x,y)}\right] \\ \gamma(x,y) &= \frac{\sqrt{\left(I_1(x,y)-I_2(x,y)\right)^2+\left(I_2(x,y)-I_3(x,y)\right)^2}}{2I_0(x,y)} \end{aligned} \qquad \textbf{(1.4)}$$

b. Four step technique

The intensity of the interference fringes for phase shifts of 2π is given by:

$$\begin{aligned} I_1(x,y) &= I_0(x,y)\left[1+\gamma\cos\left(\varphi(x,y)\right)\right] \\ I_2(x,y) &= I_0(x,y)\left[1+\gamma\cos\left(\varphi(x,y)+\frac{\pi}{2}\right)\right] \\ I_3(x,y) &= I_0(x,y)\left[1+\gamma\cos\left(\varphi(x,y)+\pi\right)\right] \\ I_4(x,y) &= I_0(x,y)\left[1+\gamma\cos\left(\varphi(x,y)+\frac{3\pi}{2}\right)\right] \end{aligned} \qquad \textbf{(1.5)}$$

By a combination of these equations, the phase and visibility can be calculated with the following expressions:

$$\begin{aligned} \varphi(x,y) &= arctg\left[\frac{I_4(x,y)-I_2(x,y)}{I_1(x,y)-I_3(x,y)}\right] \\ \gamma(x,y) &= \frac{\sqrt{\left(I_4(x,y)-I_2(x,y)\right)^2+\left(I_1(x,y)-I_3(x,y)\right)^2}}{2I_0(x,y)} \end{aligned} \qquad \textbf{(1.6)}$$

c. Five step technique

The intensity of the interference fringes for phase shifts of 2π is given by:

$$\begin{aligned} I_1(x,y) &= I_0(x,y)\left[1+\gamma\cos\left(\varphi(x,y)-\pi\right)\right] \\ I_2(x,y) &= I_0(x,y)\left[1+\gamma\cos\left(\varphi(x,y)-\frac{\pi}{2}\right)\right] \\ I_3(x,y) &= I_0(x,y)\left[1+\gamma\cos\left(\varphi(x,y)\right)\right] \\ I_4(x,y) &= I_0(x,y)\left[1+\gamma\cos\left(\varphi(x,y)+\frac{\pi}{2}\right)\right] \\ I_5(x,y) &= I_0(x,y)\left[1+\gamma\cos\left(\varphi(x,y)+\pi\right)\right] \end{aligned} \qquad \textbf{1.7)}$$

By a combination of these equations, the phase and visibility can be calculated by the following expressions:

$$\begin{aligned} \varphi(x,y) &= arctg\left[\frac{2\left(I_2(x,y)-I_4(x,y)\right)}{2I_3(x,y)-I_5(x,y)-I_1(x,y)}\right] \\ \gamma(x,y) &= \frac{\sqrt{\left(2\left(I_2(x,y)-I_4(x,y)\right)\right)^2+\left(2I_3(x,y)-I_5(x,y)-I_1(x,y)\right)^2}}{4I_0(x,y)} \end{aligned} \qquad \textbf{(1.8)}$$

As mentioned previously, the limited depth range of PSM led to the development of white light interferometry and a different technique altogether based on the fringe envelope detection to give unambiguous depth measurement over large depths. This is now presented in the next section.

1.2 GENERAL PRINCIPLE OF CSI

A typical layout of a CSI system is shown in Fig. 6(a) [11]. The working principle of the CSI technique is based on the cross coherence analysis between the reference beam and the reflected object beam which come from a low coherence source using a beam splitter. During the measurement of the sample surface, the reference beam is reflected from the reference mirror, whilst the reflected object beam is reflected from the sample [48].

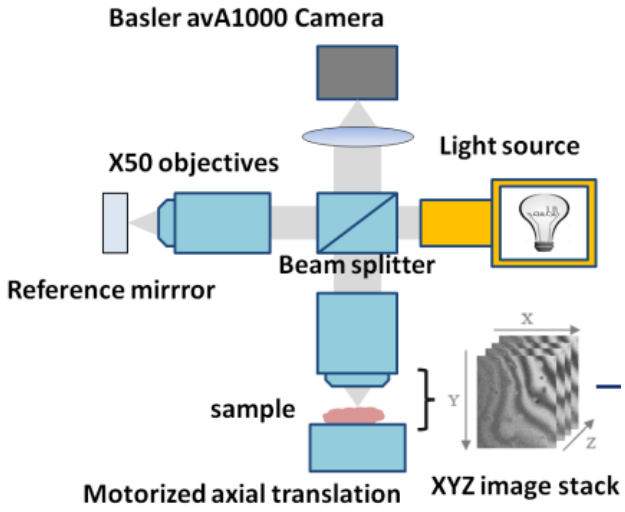

(a)

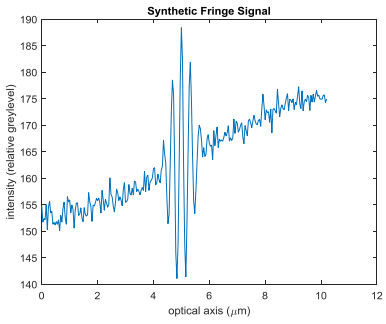

(b)

Fig. 6 (a) A schematic layout of a CSI system (Leitz-Linnik interference microscope) and (b) typical signal from a single surface [49].

The two light beams are then combined at the detector. The interference will occur when the optical path difference between the reference beam and the reflected object beam is close to zero. This is when the optical path length to the sample is nearly identical with the optical path length to the reference mirror. With the goal of finding the interference maximum, fringe scanning is carried out at each point on the sample surface, point by point. The fringe intensities, which vary according to the change in distance between the sample and the objective (in *z* axis), are captured by the detector (camera) generating the stored data signal, or interferogram. Fringe analysis is then applied in order to retrieve the peak of the fringe contrast envelope which indicates the axial position of

the surface of the sample. Fig. 7 shows how the interference is constructed at each pixel, point by point in the detector (camera).

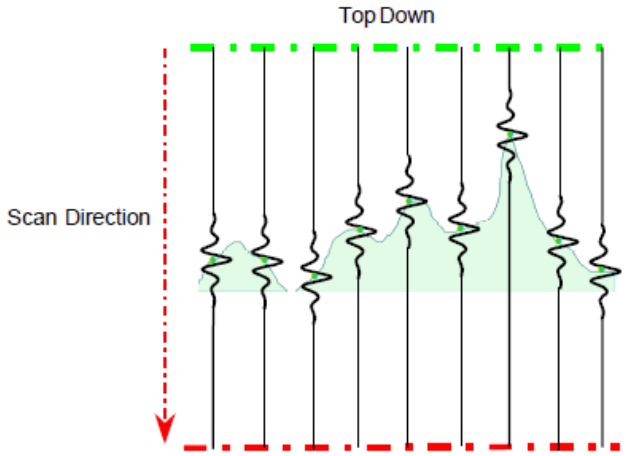

Fig. 7 The interferogram construction on a surface using CSI (source: Guide to the measurement using CSI [50]).

The advantage of white light over monochromatic light is its ability to avoid ambiguity in order to determine the fringe order due to white light having a low coherence length. On the other hand, many factors can affect the accuracy of the CSI measurements, including the camera performance, the control and linearity of the piezo-controlled vertical scanning, the metrology frame design, the environment, and the sample stability [50].

1.3 FRINGE SIGNAL

The light intensity giving rise to the fringe signal, $s(x,y,z)$, captured from a detector (CCD) as the optical path difference is varied through focus in a white light interferometer, has the following form [26], [34]:

$$s(x,y,z) = a(x,y,z) + b(x,y)\,g\left(z - z_0(x,y)\right).\cos\left(\frac{4\pi}{\lambda_0}\left(z - z_0(x,y)\right) - \alpha(x,y)\right)$$

where $z = k\Delta$

(1.9)

The function s corresponds to the intensity signal at a given point of the sample surface (x,y), where z represents a vertical scanning position in relation to the surface. The parameter z is referred to as $k\Delta$, with k the index-scanning step and Δ the value of scanning step. The height of the surface $z_0(x,y)$ is a spatial function that depends on lateral

coordinates *x* and *y*. The quantity *a(x,y,z)* is an offset intensity related to the reference and object beam intensities, *b(x,y)* is the fringe contrast, *g(z)* is the fringe envelope function related to the spectral profile of the white light source, and λ_0 is the mean wavelength of the light source. The phase offset related to the phase change on reflection is represented by *α(x,y)*. The fringe signal in Fig. 6(b) shows a synthetic fringe signal from a single surface that has been generated based on the structure of white light interferences in Eq.(1.9).

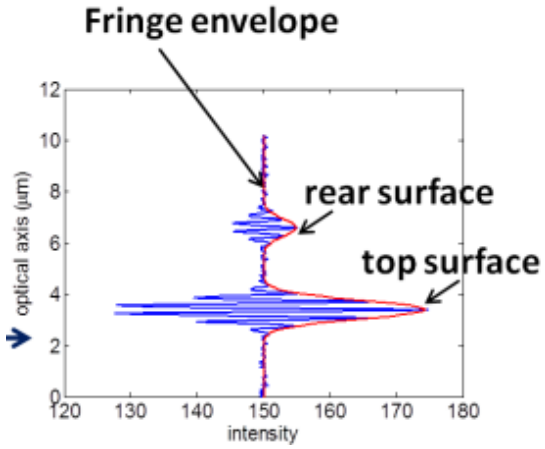

Fig. 8 Double signal of white light interference fringes from a transparent layer (synthetic signal).

Eq.(1.9) corresponds to the simple case of light propagation in air which is assumed to be equal to 1. In the case of the light passing through a transparent layer, a double signal is produced, one from each side of the layer (Fig. 8). In this case the refractive index is greater than one and wavelength dependent, thus inducing the phenomenon of dispersion for the signal from the other side of the layer. In this case the actual distance for the second signal is measured by Eq.(1.10). CSI measures the optical path difference along the optical axis Z. By measuring the distance Δ separating the peaks of the two envelopes, the actual distance *d* of the transparent layer at that point (X,Y) can be measured. If the sample displacement *d* along the optical axis (Z) and the refractive index *n* of the layer is known, the actual distance *d* is:

$$d = \frac{\Delta}{n} \qquad \textbf{(1.10)}$$

A completely description about this topic will be discussed in Chapter 2 and Chapter 3 in measurement the sample of resin on Si and Mylar polymer film.

1.4 Z-SCAN TECHNIQUE (ID)

The description of fringe analysis in CSI using the Z-scan technique is shown in Fig. 9. By means of a single vertical scan of the sample, a stack of XYZ images is generated. Signal processing is then used to obtain the fringe envelopes along Z in order to measure the positions of the peak of the fringe envelope which corresponds to the height of the surface at each pixel in the XY image [51], [52].

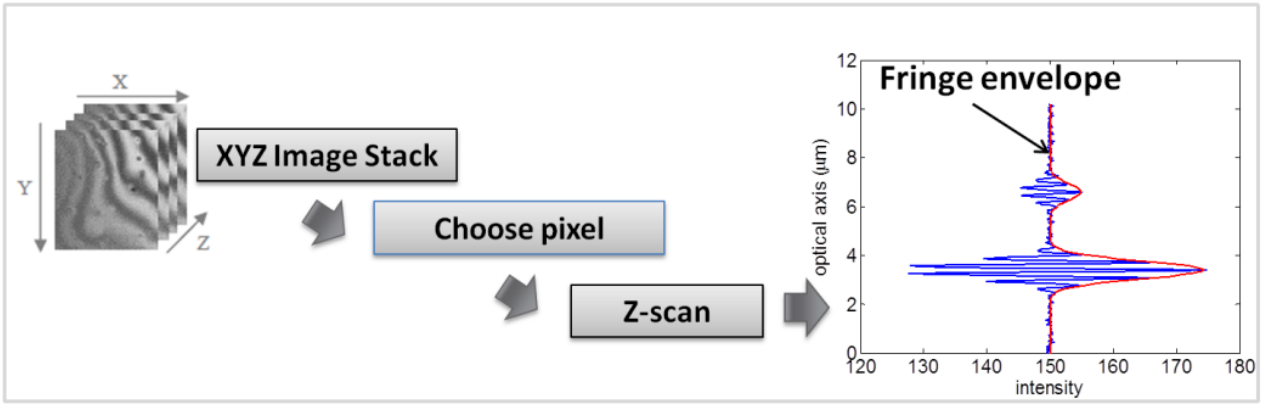

Fig. 9 Z scan technique.

Z-scan technique allows the initial manual investigation of the nature and quality of the fringe signal obtained which is generated by CSI. A priori information of the nature of the fringe signal is useful for the checking the presence of artefacts, for instance in a complex layer.

1.5 XZ-SCAN TECHNIQUE (2D)

Two dimensional fringe signal processing can be chosen using the raw XYZ data by operating on the XZY images as shown in Fig. 10. The technique is based on analyzing the XZ fringe images at a given point along the Y axis. The fringes are low pass filtered in 2D so as to find the fringe envelope. By processing a given XZ image, the cross sectional profile of a transparent sample can be obtained [52], also known as a B-scan in optical coherence tomography.

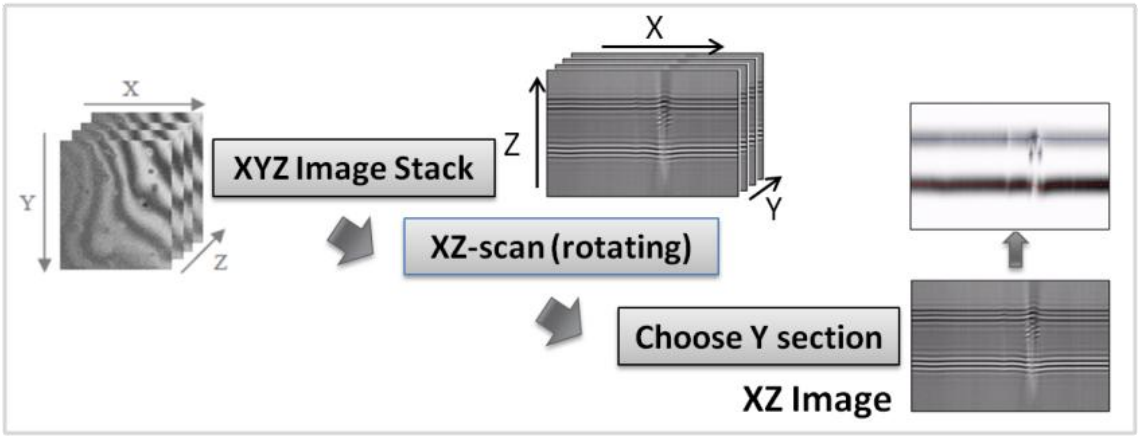

Fig. 10 XZ scan technique [49].

1.6 ANALYSIS OF WHITE LIGHT INTERFERENCE FRINGES

In general, the techniques of signal processing developed in this work consist of three main steps: pre-filtering, envelope detection and post-filtering (Fig. 11). The envelope detection is needed in order to obtain the fringe envelope of which the peak represents the surface position. Pre-filtering is used to remove the offset component and reduce the noise, while post-filtering is used to determine more precisely the measurement.

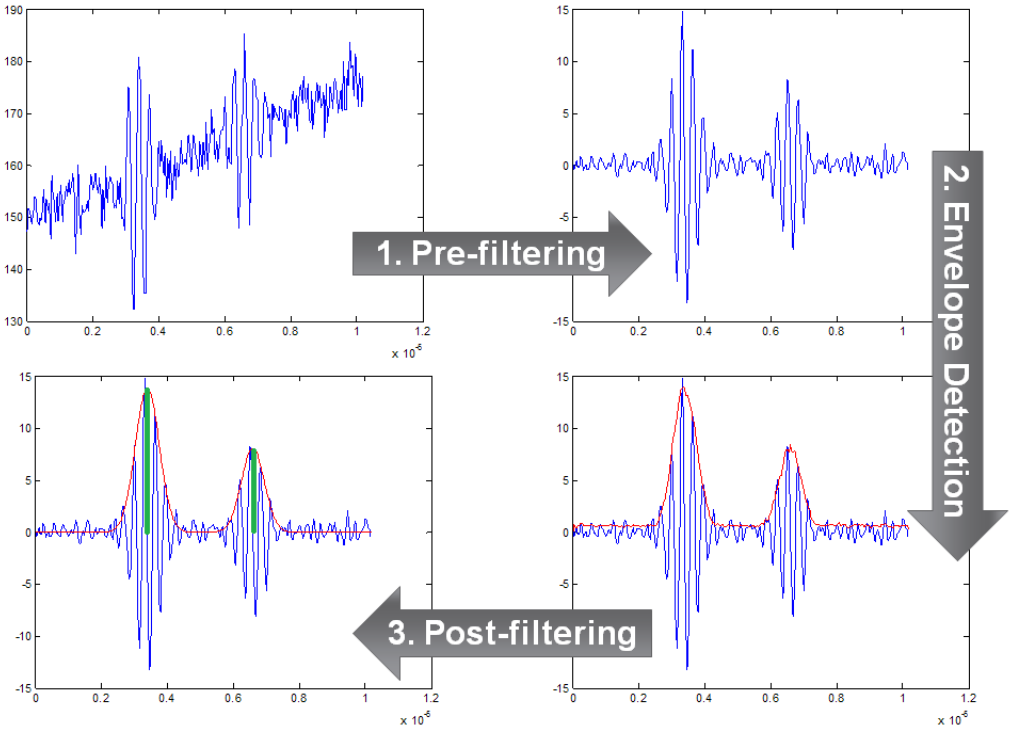

Fig. 11 The procedure of white light interference fringe analysis [53].

1.6.1 Pre-filtering

The robustness of the signal processing of fringe signals depends on the sensitivity to the different sources of signal noise and artifacts. Another problem lies in an additive offset component (background) which can appear in the fringe signals during the acquisition process, particularly over large scanning depths. In order to remove this offset component and the additive noise, it is important to filter out both of them before applying fringe envelope detection.

1.6.2 Envelope Detection

In the following we present the different techniques used to retrieve the fringe envelope in CSI.

1. Analytic Signal (Hilbert Transform)

In analytic signals, the Hilbert Transform is often used for the purpose of amplitude demodulation. If we consider a real signal $s(t)$, then the analytic signal $s_A(t)$ is defined as:

$$s_A(t) = s(t) + is_H(t) = A(t)\exp\left[i\psi(t)\right] \tag{1.11}$$

Where the Hilbert transform of a signal is given by:

$$s_H(t) = s(t) * \frac{1}{\pi t} = \frac{1}{\pi}\int_{-\infty}^{\infty}\frac{s(u)}{t-u}du \tag{1.12}$$

In the frequency domain, the analytic signal corresponds to:

$$S_A(\omega) = \left[1 + sign(\omega)\right]S(\omega) \tag{1.13}$$

In particular, for obtaining the analytic signal $s_A(t)$, the negative frequency component of the signal is suppressed, which can be performed using a Fast Fourier Transform (FFT). The main steps of the Analytic Signal (Hilbert Transform) technique using a Fast Fourier Transform (FFT) calculation are outlined in Fig. 12. The FFT is applied to the signal in Fig. 12(a), producing the spectrum of the signal (Fig. 12(b)). The FFT coefficients that correspond to negative frequencies are then replaced with zeros (Fig. 12(c)). Finally, the fringe envelope is extracted (Fig. 12(d)) by calculating the inverse FFT of the positive frequency packet in Fig. 12(c). By removing negative frequencies from the spectrum of real signal $s(t)$, the signal provided by inverse FFT becomes

complex as shown in Eq. (1.11), which gives directly the phase $\psi(t)$ and the amplitude $A(t)$.

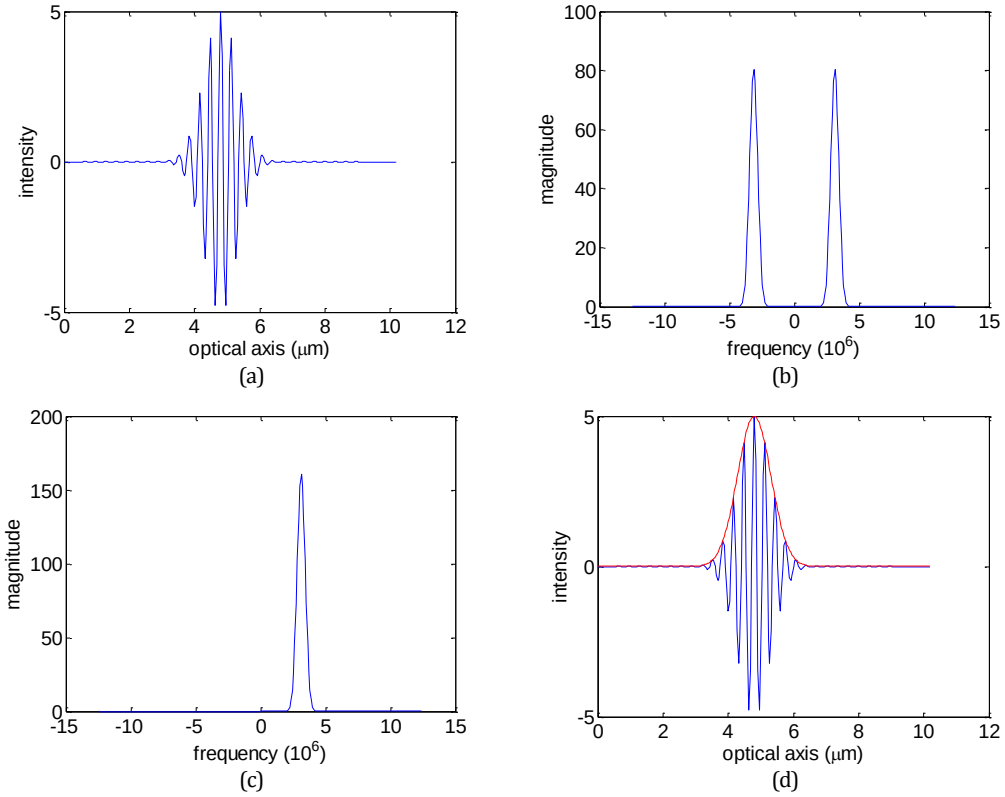

Fig. 12 Fringe envelope detection process using Hilbert Transform technique [53].

2. Five Sample Adaptive (FSA) algorithm

The FSA technique is a fast and simple algorithm which has been commonly used in CSI to retrieve the fringe envelope [34]. The main idea of the technique is the application of phase shifting algorithms for white light interferogram demodulation and to use the fringe visibility (or modulation) to calculate the fringe envelope. In the case of the FSA technique, five interferograms are captured by a digital imaging system.

At each pixel location in the image (x,y), the value of the visibility $\gamma(x,y)$ of the fringes at that point is calculated from the intensities of five sampling positions, I_{n-2} to I_{n+2}, along the optical axis z (Fig. 13):

$$A(x,y) = \frac{1}{4}\sqrt{4\left(I_2 - I_4\right)^2 + \left(-I_1 + 2I_3 - I_5\right)^2} \qquad \textbf{(1.14)}$$

where I_1 to I_5 are the interferogram intensities, giving exact values when the phase shifting between interferograms is 90°. The amplitude $A(x,y)$ can be calculated with

just two multiplications and one square root operation, which gives the advantage of efficient computation time. This well-known technique in fact corresponds to a derivative of the signal followed by the discrete Teager Kaiser operator which we discuss next.

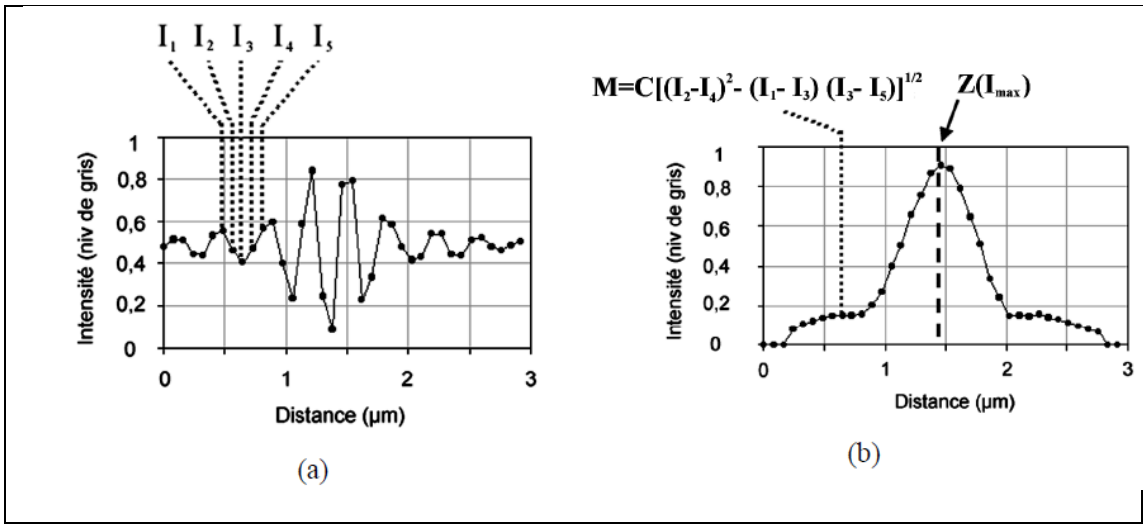

Fig. 13 FSA Algorithm

3. Teager Kaiser Energy Operator (TKEO)

The Teager Kaiser Energy Operator (TKEO) [54] is an operator that tracks the instantaneous energy of a signal. This non-linear energy operator and its 1D/2D discrete versions has found applications in various fields of signal and image processing due to its success in analysing and demodulating AM-FM signals with high resolution, simplicity, and efficiency [55]. In its discrete version, only three samples are required at each time instant. In the continuous case, the Teager Kaiser Energy Operator is defined by:

$$\psi\left[s(z)\right] = \dot{s}^2(z) - s(z)\ddot{s}(z) = \left(\frac{\partial s(z)}{\partial z}\right)^2 - s(z)\left(\frac{\partial^2 s(z)}{\partial z^2}\right) \qquad \textbf{(1.15)}$$

where $s(z)$ is the signal, $\dot{s}(z)$ and $\ddot{s}(z)$ means the first derivative and the second derivative of s respectively. A discrete forward and backward approximation of the derivatives of Eq.(1.15) leads to the discrete TKEO [56]:

$$\psi\left[s(n)\right] = s^2[n] - s[n-1]s[n+1] \qquad \textbf{(1.16)}$$

Let us consider a mono-component continuous time AM-FM signal:

$$s(t) = a(t)\cos\left(\phi(t)\right) \tag{1.17}$$

where $a(t)$ represents the spatially varying amplitude and $\phi(t)$ is the phase signal. The output of the Teager Kaiser Energy Operator applied to $s(t)$, is given by $\psi\left[s(t)\right] \approx \left[a(t)\dot{\phi}(t)\right]^2$, where $\dot{\phi}(t)$ is the instantaneous phase. Moreover, the Energy Separation Algorithm (ESA), estimates the instantaneous envelope $a(t)$ and the instantaneous phase $\dot{\phi}(t)$ as follows:

$$\left|a(t)\right| \approx \frac{\psi\left[s(t)\right]}{\sqrt{\psi\left[\dot{s}(t)\right]}}; \quad \left|\dot{\phi}(t)\right| \approx \sqrt{\frac{\psi\left[\dot{s}(t)\right]}{\psi\left[s(t)\right]}} \tag{1.18}$$

The main disadvantage of the Teager Kaiser Energy Operator lies in its sensitivity to noise, due to the successive derivations. In the context of noisy data, a filter such as the Savitzky-Golay approach, improves the robustness of TKEO.

4. Continuous Wavelet Transform (CWT)

The Wavelet transform is a time-frequency analysis technique which has been widely used in signal analysis and processing [57], [58], [59]. Due to its ability to decompose locally the signal into different scale/frequencies, the CWT highlights the region of interest, where the local frequency corresponds to the carrier frequency of the CSI signal. Moreover, the CWT method seems to be robust to noise, providing accurate measurements of the surface.

The CWT transform function of a fringe signal $s(z)$ can be expressed as:

$$W(a,b) = \frac{1}{|a|^{1/2}} \int_{-\infty}^{\infty} s(z)\psi\left(\frac{z-b}{a}\right)dz \tag{1.19}$$

where $W(a,b)$ represents the CWT coefficient function, $\psi(z)$ is a continuous function in time and frequency domain called the mother wavelet, a is the scale factor, and b is the shift factor. The well-known complex Morlet wavelet [60], [61], [62], [55], [63], [64], [65] has been chosen as the mother wavelet since its properties have strong

similarities with the fringe signal, since the wavelet function corresponds to a Gaussian envelope modulated by a sinusoidal function.

$$\psi(z) = e^{i\omega z} e^{\left(-z^2/2\right)} \tag{1.20}$$

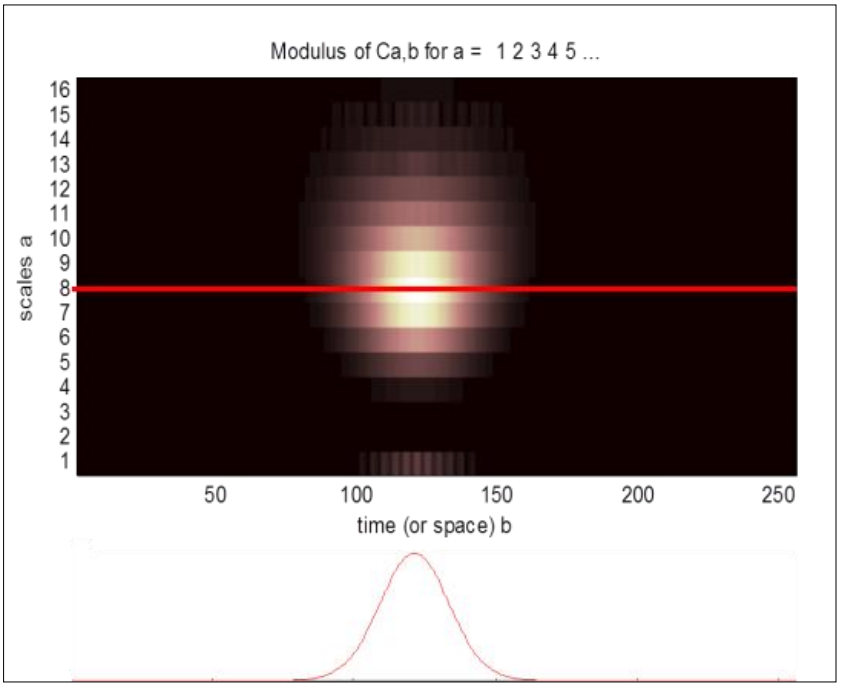

Fig. 14 The modulus of coefficient CWT of the fringe signal [53].

In order to compute each coefficient $W(a,b)$, the fringe signal is convolved with a set of complex Morlet wavelets. As a function of scale factors a and shift b, $W(a,b)$ can be represented by a scalogram, as shown in Fig. 14. The fringe envelope corresponds to the absolute modulus of the maximum correlation coefficient as shown by the red line in the scalogram.

1.6.3 Post-filtering

For noisy fringe signals, for instance as shown in Fig. 15(a) even though pre-filtering is used to remove the offset component and suppress the noise before the process of envelope detection, the noise can still appear in the resulting fringe signal, as shown in Fig. 15(b). This affects the process of envelope detection so that the fringe patterns appear in the resulting fringe envelope, as illustrated in Fig. 15(c). Because of this, a smoothing filter such as a cubic spline is needed to improve the envelope peak detection (Fig. 15(d)). Then, the curve fitting method using Gaussian fitting is implemented in order to determine more precisely the envelope peak.

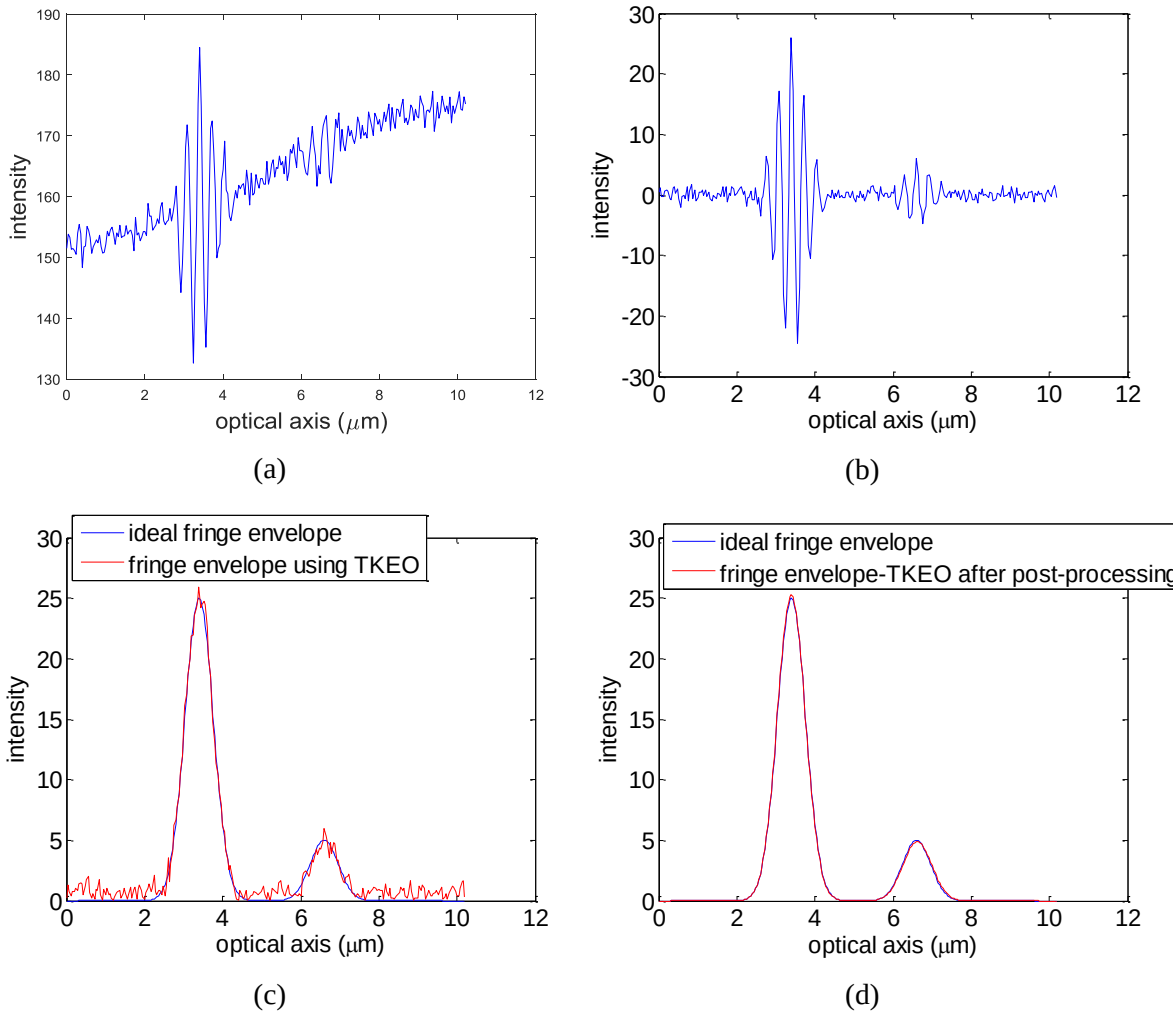

Fig. 15 The use of post-filtering in CSI: (a) fringe signal, (b) prefiltered signal, and its envelope obtained (c) without post-filtering and (d) using post-filtering.

1.7 PERFORMANCE EVALUATION OF DIFFERENT OFFSET COMPONENT REMOVAL TECHNIQUES IN CSI

Generally, when we apply signal processing, the main aim is to remove part of the noise present in the signal or to eliminate different sources of variation (e.g. background) that are not related to the measured variable. The existence of a variable background offset to the signal can be caused by the effects of defocusing (3D PSF along Z), the Köhler illumination (conical illumination at each point on the sample), contrast variations across the sample (XY) and diffraction effects at step edges. In the case of fringe signal processing, it is important to filter out the background (offset component) before applying fringe envelope detection. The background variation is more observable on rougher surfaces or edges of structures and results from the response of the imaging objective to diffraction and out of focus effects. This generally consists of a slowly varying

component along the z-axis due to optical effects and has a lower spatial frequency than the fringes, as shown by the red line in Fig. 16. In this work, we present the performance evaluation results of different offset component removal techniques as a pre-processing step in fringe signal processing.

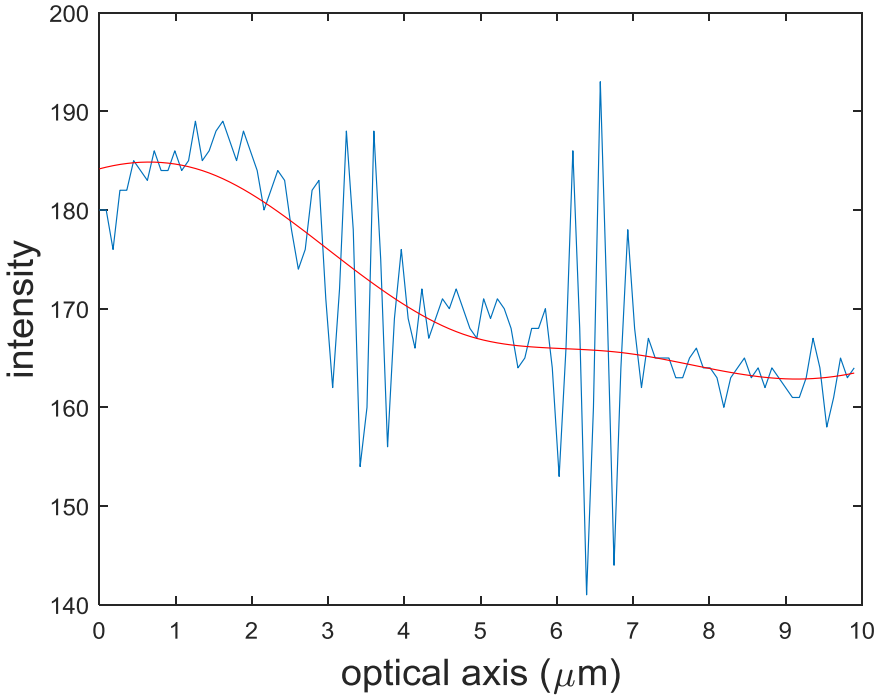

Fig. 16 An example of background variation on the fringe signal (resin on Si)

1.7.1 The Offset Component removal technique

The following are most common offset component removal techniques in CSI:

a. Global Average

The global average technique makes use of the average of the signals in order to suppress the offset component. Global averaging removes the mean value from the vector *x*, which can be expressed as:

$$x_i = x_i - \frac{1}{N}\sum_{i=1}^{N} x_i \qquad \textbf{(1.21)}$$

b. Local Average

The local averaging technique is a fast and simple algorithm which has been commonly used in signal processing to suppress the offset component. The value of the pre-filtered

signal for a single sampling position x_i is calculated from the intensities of three sampling positions, x_{i-1} to x_{i+1}, which can be expressed as:

$$x_i = x_i - \frac{\left(x_{i-1} + x_i + x_{i+1}\right)}{3} \tag{1.22}$$

c. Central Derivative

In signal processing, the derivative is a common method used to remove the background variation of a signal. The simplest form of numerical approximation of the derivative is the first order derivative based on the finite difference method, which has three form types, i.e. forward difference, backward difference, and central difference. By removing the values of the signal where their adjacent/neighbourhood values are almost equal, the first derivative effectively removes the lower frequencies of the signal, i.e. the offset component. Among the three types of the first derivative, the central difference gives the most accurate approximation, and hence it is commonly used for suppressing the trend and the offset in white light fringe analysis. The central difference formula for the first derivative of $f(x)$ which is based on the values of the function at the points $f(x+h)$ and $f(x-h)$, can be expressed as:

$$f'(x) \approx \frac{f\left(x+h\right) - f\left(x-h\right)}{2h} \tag{1.23}$$

This Eq.(1.23) expresses that the first derivative of $f(x)$ at a point x is derived by subtraction of its immediate neighboring points $(x+h)$ and $(x-h)$. It removes the values of two successive points of $f(x)$ which are the same and leaves the values which are different. When it is performed on an entire signal, the first derivative $f'(x)$ effectively removes the intensity background and suppresses the lower frequency signal, although it emphasizes the higher frequency signal which tends to accentuate the noise. The first derivative therefore works well for noiseless signals whose derivation values can be calculated precisely and is not good for high frequency suppression.

d. Empirical Mode Decomposition

After studying different techniques for supressing the background variation, as an alternative to the first derivative, we have introduced the use of the well-known decomposition technique known as Empirical Mode Decomposition (EMD). The EMD method has the ability to decompose a signal into oscillatory components, known as intrinsic mode functions (IMFs). The principle of EMD is the use of a repeated shifting

process on the analyzed signal. For a given signal x(t), all extrema (local maxima and minima) are detected and connected by an interpolation technique, such as the cubic spline, that produces respectively the upper envelope $e_{max}(t)$ and the lower envelope $e_{min}(t)$. The average of the two envelopes is then computed, $m(t) = (e_{max}(t) + e_{min}(t))/2$ and the remaining detail $d(t) = x(t) - m(t)$, is extracted. The above procedure is repeated in order to obtain the first intrinsic mode functions (IMFs), $d_1(t)$ which satisfy two conditions:

1. The number of extrema (the sum of the maxima and minima) and the number of zero-crossings must either be equal or differ at most by one.
2. At any point of an IMF the mean value of the envelopes of the local maxima and minima is zero.

After the 1st IMF is obtained, a residue $r(t) = x(t) - d_1(t)$ is computed and processed as a new signal instead of $x(t)$. The same procedure is applied to the new signal until other IMFs, $d_2(t)$, $d_3(t)$, $d_N(t)$ are obtained. Finally, the result of decomposition using the EMD method from the $x(t)$ signal yields N component of IMF's and a residue.

$$x(t) = \sum_{k=1}^{N} d_k(t) + r(t) \qquad \textbf{(1.24)}$$

The lower-order IMF's typically represents fast oscillation modes, while the higher order IMF's and the residue typically represent slow oscillation modes. Due to this characteristic, the EMD technique seems to be well adapted for suppressing the slowly varying offset. However, as with the central derivative technique, the EMD method used as a pre-filter can also fail in the presence of significant noise. For this reason, we have tested more robust filters such as the Savitzky-Golay or Wiener family in combination with the derivative and EMD methods.

In order to remove the offset and reduce the noise, three different algorithms have been studied in this work which combine the derivative/EMD technique and denoising filter (Savitzky-Golay/Wiener [66], [67], [68]). The corresponding algorithms are referred to with the following names:

i) Pre-filter 1: combination of derivative and Wiener filter.

ii) Pre-filter 2: combination of derivative and Savitzky-Golay filter.

iii) Pre-filter 3: combination of EMD and Savitzky-Golay filter.

1.7.2 The denoising technique

The following gives a description of the denoising techniques used in this work:

a. Wiener Filter

Let us consider the signal corrupted by an independent zero-mean white Gaussian noise, which is modeled as [69]:

$$y(i,j) = x(i,j) + n(i,j) \tag{1.25}$$

where $y(i,j)$ is the noisy signal, $x(i,j)$ is the original signal and $n(i,j)$ is a Gaussian noise. The aim of the technique is to remove the noise and to obtain a linear estimate $\hat{x}(i,j)$ which minimizes the mean squared error (MSE) [69].

$$MSE = \frac{1}{N}\sum_{i,j=1}^{N}\left(\hat{x}(i,j) - x(i,j)\right)^2 \tag{1.26}$$

where N is the number of elements in $x(i,j)$. When $x(i,j)$ and $n(i,j)$ are stationary Gaussian processes the Wiener filter is the optimal filter. Specifically, when $x(i,j)$ is also a white Gaussian process the Wiener filter has a very simple scalar form:

$$\hat{x}(i,j) = \frac{\sigma_x^{\,2}(i,j)}{\sigma_x^{\,2}(i,j) + \sigma_n^{\,2}(i,j)}\left(y(i,j) - u_x(i,j)\right) + u_x(i,j) \tag{1.27}$$

where σ^2, μ are the signal variances and means, respectively, and where we will normally assume the mean of the noise to be zero.

b. Savitzky-Golay Filter

The Savitzky-Golay filter is a smoothing technique for a signal that was proposed by Savitzky and Golay to increase the SNR (signal to noise ratio) without significantly distorting the signal. The filter is defined as a weighted moving average with weighting given as a polynomial of a specific degree [70],[68]. The illustration of Savizky Golay filer is shown in Fig. 17.

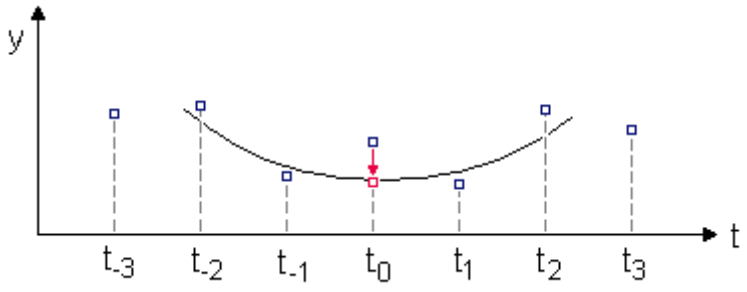

Fig. 17 Illustration of the Savitzky Golay filter

The coefficients of a Savitzky-Golay filter, when applied to a signal, perform a polynomial P of the degree k, is fitted to points of the signal, where N describes the window size (neighboring points, including the point to be smoothed). The advantage of this filter is that it tends to keep features of the distribution such as those relative to the maxima and minima which are often flattened by other smoothing techniques such as MA (moving average).

1.7.3 Simulation results

In order to test these techniques by simulation, we generate different types of synthetic fringe signals corresponding to the two fringe signals coming from the top and bottom surfaces of a transparent layer. We then used these to test all pre-processing techniques, based locally on the general model expressed by Eq. (1.9) along the optical axis Z, with a 40 nm sampling step, for each lateral position X.

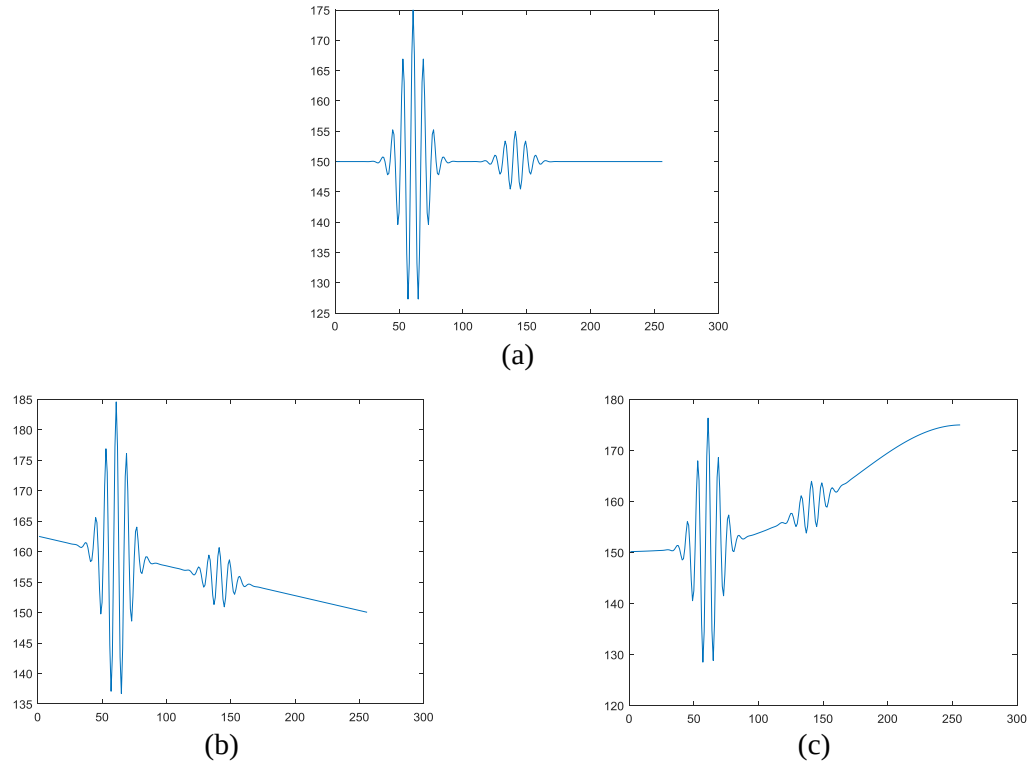

Fig. 18 Synthetic fringe signals with: (a) constant, (b) linear, (c) non-linear offset components.

The resulting synthetic signals are shown in Fig. 18 with the different types of (a) constant, (b) linear and (c) non-linear offsets added to the synthetic data that can commonly appear in the fringe signals during the acquisition process that can be due to the various optical effects.

The previously cited pre-processing techniques were then applied to the synthetic fringe signals, namely global averaging, local averaging, the central derivative and the EMD filter. The results are then shown for the constant offset (Fig. 19), linear offset (Fig. 20) and non-linear offset (Fig. 21).

Based on the results in Fig. 19, Fig. 20, and Fig. 21, it can be seen that the type of pre-processing technique required to suppress the offset component from the fringe signal depends on the nature of the signal and the computational time available and the precision required. The computation times for each of these processes are given in **Table 1** using Matlab on a PC equipped with an Intel Xeon processor (2.33 GHz, 8 Go RAM).

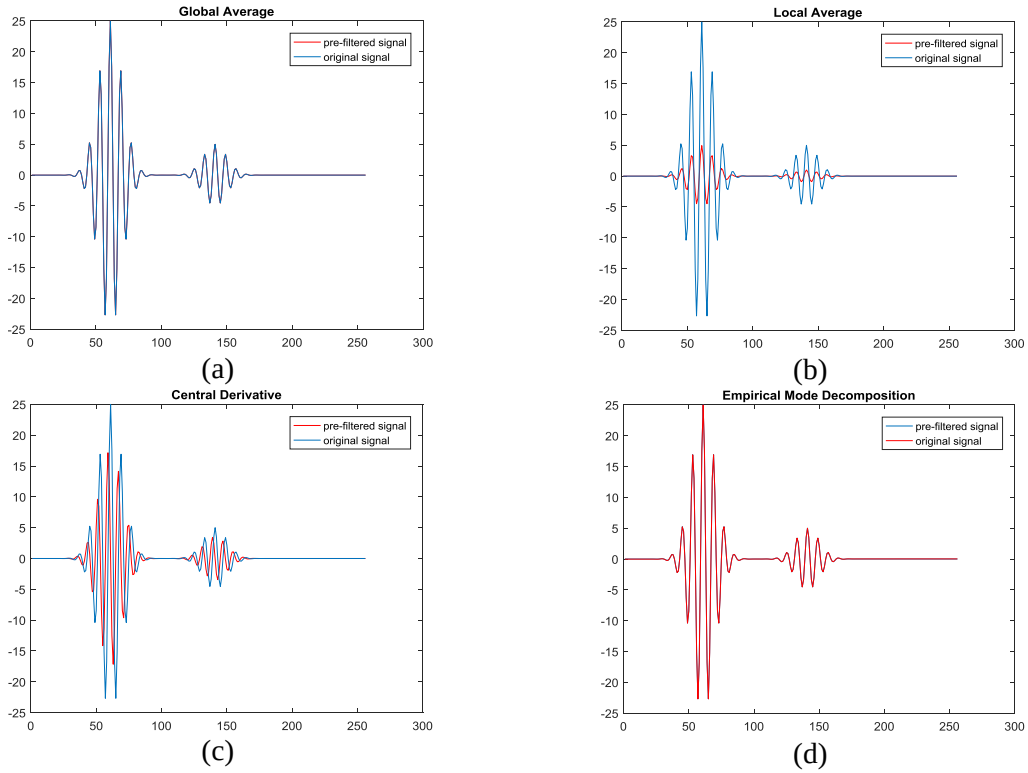

Fig. 19 Prefiltered signal obtained using: (a) Global average, (b) Local average, (c) Central derivative, (d) EMD, applied to the synthetic fringe signal with a constant offset component.

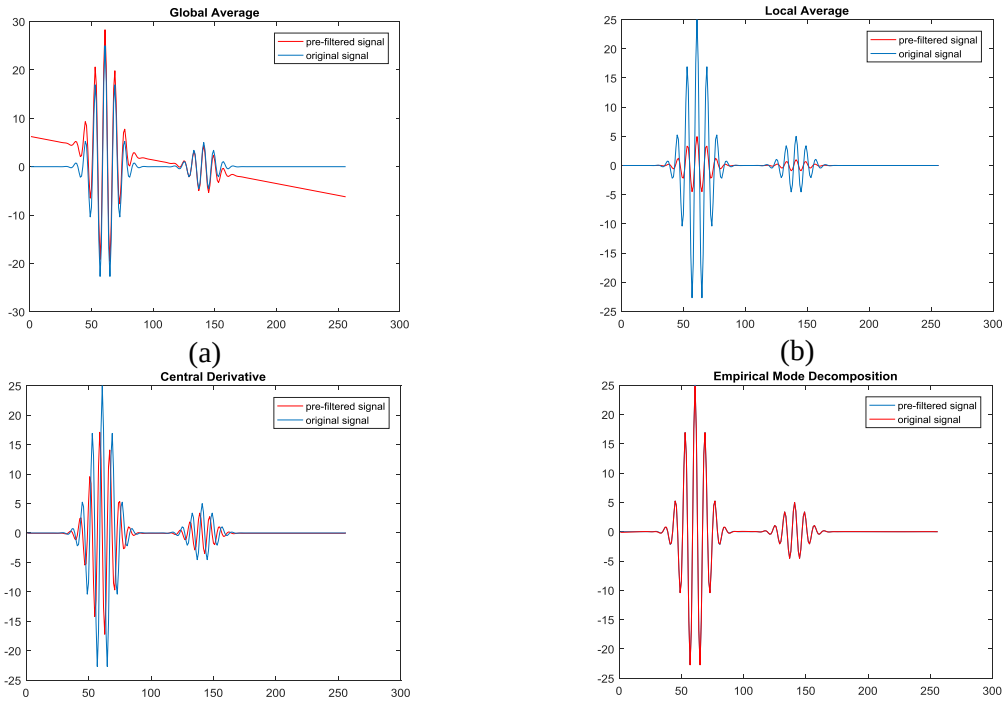

Fig. 20 Prefiltered signal obtained using: (a) Global average, (b) Local average, (c) Central derivative, (d) EMD, applied to the synthetic fringe signal with a linear offset component.

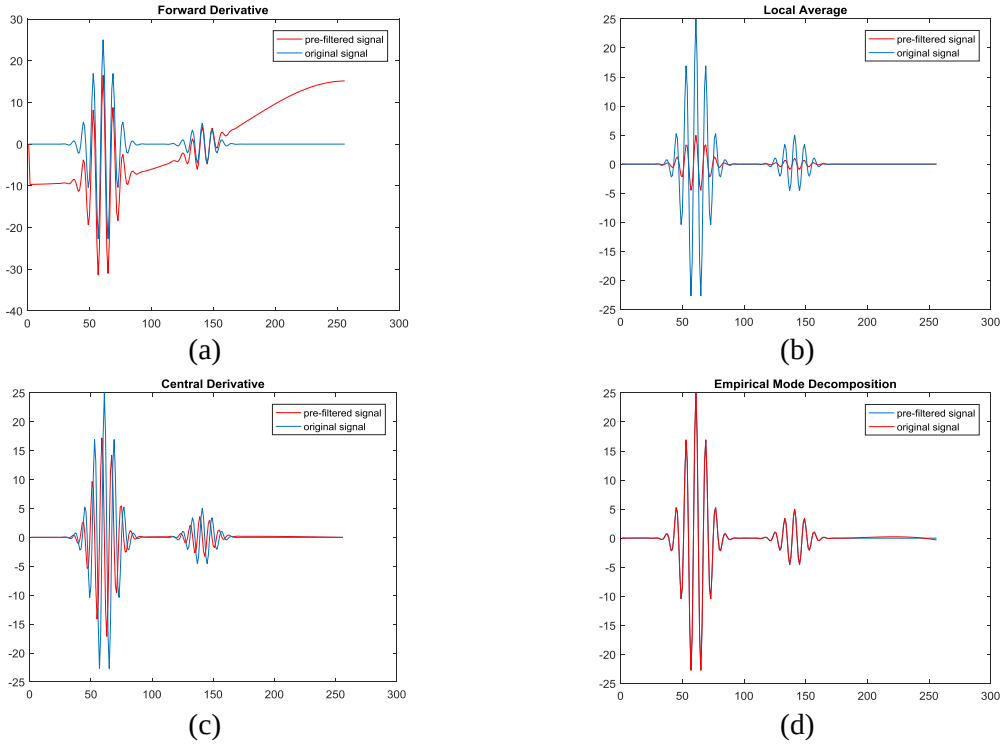

Fig. 21 Prefiltered signal obtained using: (a) Global average, (b) Local average, (c) Central derivative, (d) EMD, applied to the synthetic fringe signal with a nonlinear offset component.

Table 1 Computation times for the different pre-processing techniques applied to the synthetic fringe signals

	Global Average	Local Average	Central Derivative	EMD
Time computation (ms)	6.49	3.76	17.96	115.68

The global averaging technique only works well for fringe signals with an offset which is relatively constant, but not for the linear and nonlinear offsets. The Local averaging technique is able to maintain the symmetry of the fringe pattern and has the fastest computation time (**Table 1**). However, as illustrated in Fig. 19(b), Fig. 20(b), and Fig. 21(b), the resulting amplitude of the fringe signal is clearly lower than the ideal synthetic fringe signal (without the offset). This means that a degradation of the intensities occurs during the pre-processing process. Similar results are also obtained using the central derivative technique, as illustrated in Fig. 19(c), Fig. 20(c), and Fig. 21(c), although taking from 3 to 4 times longer than the global and local averaging. The resulting amplitude of the fringe signal is also clearly lower than the ideal synthetic fringe signal, although the decrease is not as great as that for the local averaging. A decrease in the intensity may seriously degrade the performance of the algorithm in order to extract the fringe envelope, particularly in areas where the SNR is low. The best results are provided by the EMD technique, as illustrated in Fig. 19(d), Fig. 20(d), and Fig. 21(d) which is clearly able to remove the offset, while almost maintaining the amplitude of the fringe signal. But this good result is at the expense of the computation time which takes from 6 to 31 times the time required by the three other techniques.

1.8 SURFACE MEASUREMENT ERRORS IN CSI

As with any measurement technique, while CSI has significant advantages for optical profiling, the measurements are also prone to different types of noise, artefacts and errors. These are now fairly well known and have been described in the literature over the last decade, namely: ghost steps, the batwing effect, slope dependent errors, material effects and multiple scattering effects. These are now described.

a. Ghost Steps

When measuring a perfectly flat surface with CSI, depending on the algorithm and parameters used, step artefacts can be introduced into the measurement [71], [72]. This

kind of error is commonly referred to as ghost steps. The simplest form is due to the sampling step when interpolation is not used. This results in the presence of steps corresponding to the scanning step between images. Another form of ghost step error is a type of fringe order error, which correspond to an error of the measured profile of $\lambda_0/2$ [73]. The asymmetries in CSI, which arise for instance from imperfect beam splitter, can lead to the ghost step error in the measured profile [74].

b. Batwing Effect

This measurement error is known as batwing effect due to the shape, rather like that of batwings, as illustrated in Fig. 22. The error appears in the measurement of step height, which is less than the coherence length of the light source used [75], [76]. The batwing effect generally appears for the white light vertical scanning technique due to the diffraction effect on the edges. For a typical white light interferometer, the fringe contrast envelope obtained, which is Gaussian, skews on the surface close to the edges leading to the error. The batwing effect must be considered when carrying out the measurement calibration using a step height standard. .

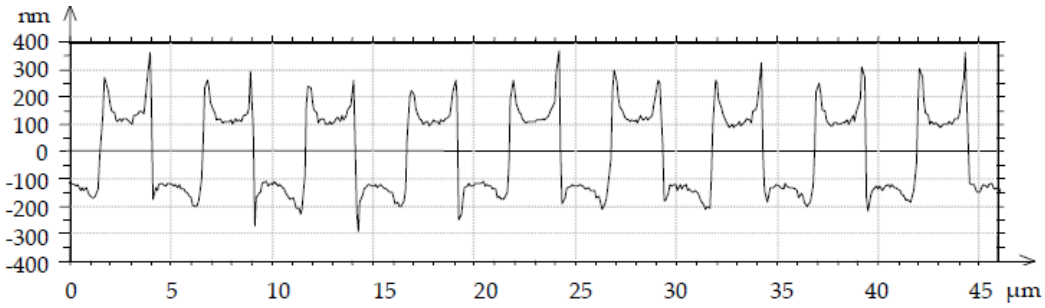

Source: Guide to the Measurement using CSI [50]

Fig. 22 A square wave grating that shows the batwing effect at the step edges

c. Multiple Scattering

For the object with the depth profile such as V-grooves, the incident light is scattered multiple times due to the geometry of the object [73], [77]. The effect of multiple scattering is discussed in [78] using a silicon V-groove specimen, as shown in Fig. 23.

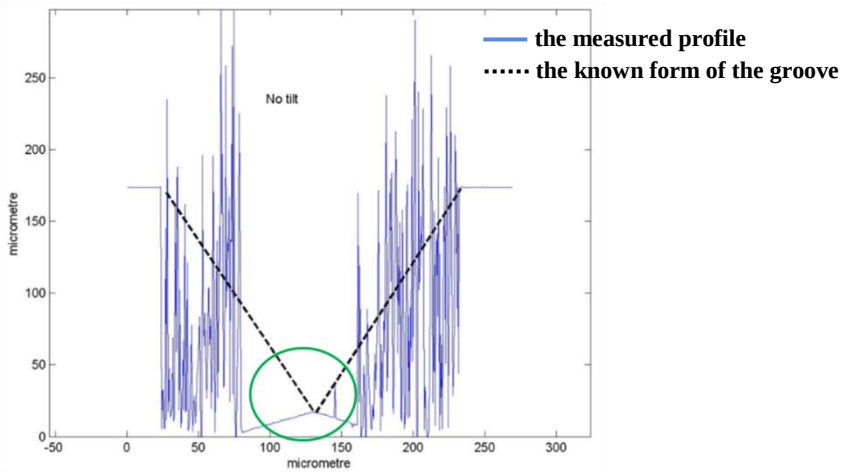

Fig. 23 Profile measurement of V-groove using white light interferometry [78]

As illustrated in the figure, at the bottom of the groove, the measured profile (blue line) and the known form of the groove (black line) only coincides at the apex, while the measured profile around the apex show the inverted form of the V-groove. Generally, in white light interferometry, multi scattering causes the over estimation for the surface roughness [73], which can be considered to be similar to small V-grooves.

d. Dispersive Effects in Dissimilar Materials

The optical properties of the object surface can also be a source of measurement error in white light interferometry [73], [79], [80]. The surface height measurement will be affected since different materials exhibit different phase changes on reflection [81]. For instance, because of the complex refractive index of metallic surface, this will lead to shifting of the position peak of the coherence envelope function which results in the measurement error. In the article [81], it is demonstrated that the largest phase dispersion on reflection is shown by metallic surfaces, shifting the peak position of the coherence envelope by 10 – 40 nm.

1.9 MICROSCOPE SYSTEM

The equipment developed for testing the developed algorithm for fringe signal processing in this thesis consists of four adapted microscopes, a Leica DMR-X microscope (Fig. 24) equipped with Mirau (x10, x40) and Michelson (x5) objectives, a Leitz-Linnik

microscope equipped with x50 (NA = 0.85) objectives (Fig. 6(a)), a modified Fogale microscope equipped with x40 immersion objectives used in water (“immersion” system) and a modified Fogale microscope equipped with a Nikon x50 Mirau objective (“Michelin” system). The sample is mounted on a piezo-controlled vertical scanning table (the PIFOC scanner from PI) for Z-scanning. The piezo actuator is controlled in a closed loop with a capacitive position sensor, having a position sensitivity of 1 nm. For the illumination, a halogen lamp is used in the Leica DMR-X, an incandescent lamp in the Leitz-Linnik (310 nm – 1100 nm) and white LED’s in the Fogale “immersion” and “Michelin” systems. Image acquisition is performed with either a digital Prosilica CCD (type EC1380) having 1360x1024 pixels and a Basler Ava1000 having 1024x1024 pixels and a Firewire connection or a Sony 3CCD (type DXC-390P) and standard color acquisition board. Acquisition and processing is carried out on a PC equipped with an Intel Xeon processor (2.4 GHz, 8 Go RAM). The measurement system is controlled with software that has been developed in LabView on Windows 7 (64-bit) [12], [52], [82], [83].

The Leica DMR-X (Fig. 24) consists of the following five main elements [83]:

a. The stand that supports and maintains various optical mechanisms and tubes.
b. The illumination source (halogen or tungsten filament lamp or LED).
c. The interference objective that makes it possible to view interference fringes superimposed on the image of the sample surface and to modify the degree of magnification.
d. The motorised sample platform for focusing and positioning the observed sample.
e. The observation head which allows both direct binocular observation by eye and image detection using a sensor such as a CCD camera to record the observed image.

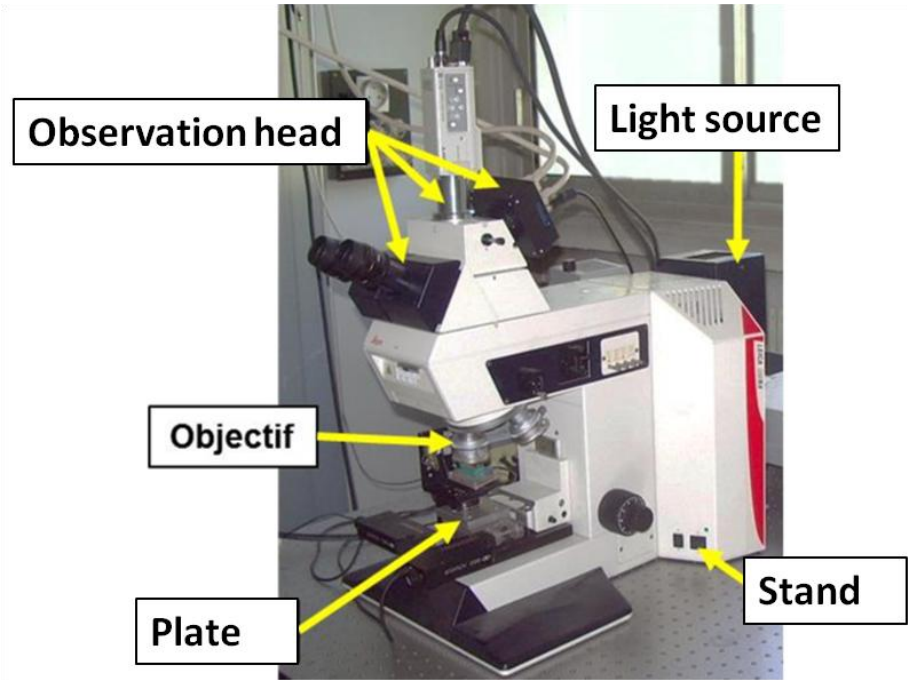

Fig. 24 The modified Leica DMR-X interference microscope developed in the IPP team [83].

1.10 STRUCTURE OF THE SAMPLES SURFACE

In order to evaluate the performance of the algorithms developed in this work, the following samples that have different structures were used. They were chosen because they vary from a simple smooth surface through to increasingly complex structures.

a. Single surface

The samples that have a single surface which are used in the thesis consist of two types of structures: (i) a sample having a smooth surface, such as a step height standard (SHS), with a step having a height of 1.7803 ± 0.011 µm [76], [84] and (ii) a sample having a rough surface, such as a rock surface, i.e. limestone, in which the fringes are very noisy [85]. The sample of SHS is used to calibrate and test the precision of the measurement using the developed algorithm, while the rock sample is used to test the robustness of the algorithm on the noisy data of the rough sample (Chapter 4). The interferograms of the samples are shown in Fig. 25.

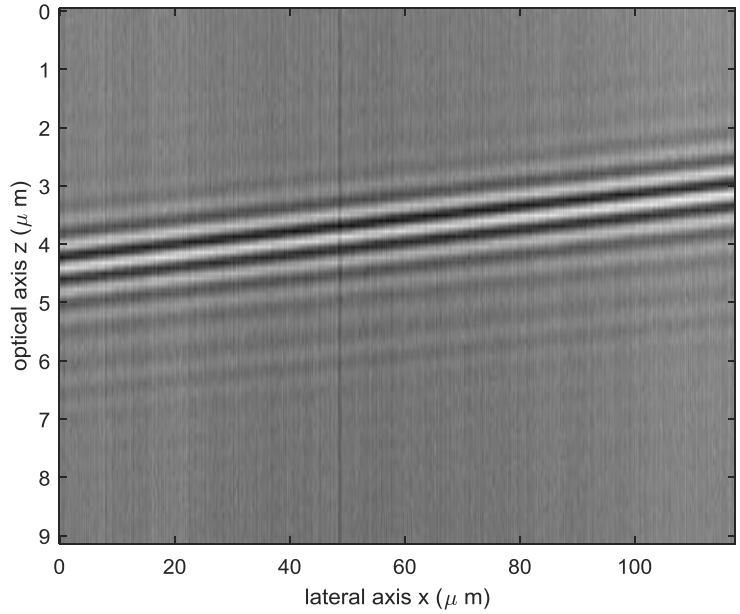

(a)

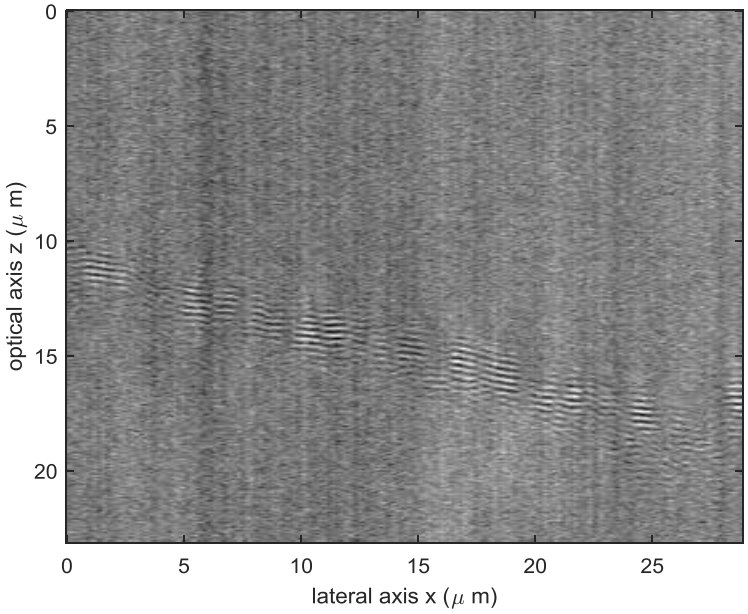

(b)

Fig. 25 XZ images showing the interferograms from (a) a Step Height Standard and (b) a rock surface [85].

b. Transparent layer on substrate

The next sample consists of a layer of resin on silicon used for making diffractive optical elements (Fig. 26) [86]. The description of acquisition data of resin on Si obtained by the microscope system is given in Appendix-1: Data of Sample. This sample is of interest because it produces two interferograms in each signal from the air/resin surface and resin/silicon interface, the distance between them indicating the optical thickness of the layer. Interference microscopy can thus also be used to non-

destructively analyze a surface buried under a transparent layer. However, several factors can contribute to the degradation of the wavefront reflected from the interface, for instance the aberrations due to the presence of the transparent layer, the variations of the refractive index of the transparent layer, the shape and geometry of the transparent layer and interface, the edges of the layer etc. In Chapter 2, the transparent layer on substrate sample is used to evaluate the performance of certain algorithms to measure the thickness profile of the transparent layer and to analyze the layer/substrate interface.

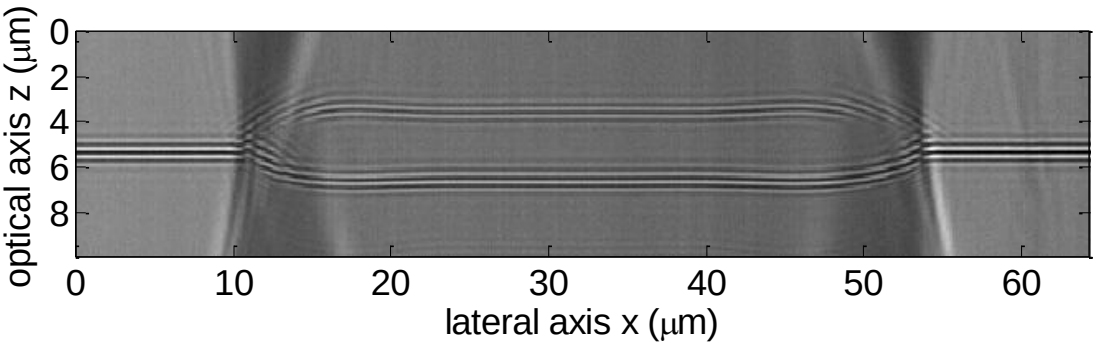

Fig. 26 An XZ image showing the interferogram on a transparent layer on a substrate consisting of a resin layer on a silicon substrate

c. Transparent polymer film

The transparent polymer film sample consists of a Mylar film used as an insulator in microelectronics (Fig. 27) [87], [88]. The description of acquisition data of Mylar polymer film obtained by the microscope system is given in Appendix-1: Data of Sample. This sample is of interest because as well as the upper and lower reflecting surfaces, it is a bit more complex since it contains low contrast buried structures which are not easily observable using classical optical techniques. The sample is used to test the performance of the developed algorithms in detecting the rear surface position and the presence of the buried structures (Chapter 3).

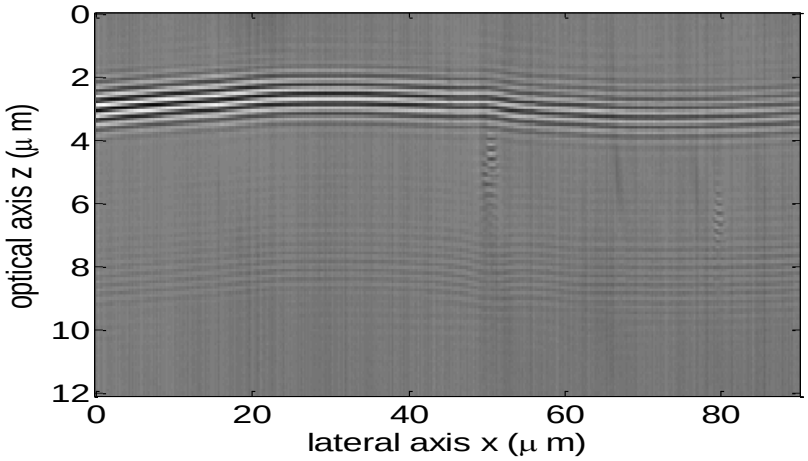

Fig. 27 An XZ image showing the interferogram of the transparent polymer film sample.

1.11 RESOLUTION

The spatial resolution of an optical technique refers to the smallest value that can be measured along the spatial dimension. In other words, the spatial resolution is the minimum distance that can be measured between two points of space. In this section, we will discuss the spatial resolutions of optical microscopes, i.e. lateral and axial resolution.

1.11.1 Lateral resolution

The optical microscope is limited by the diffraction of light, which leads to the spatial resolution of a microscope [89], [90]. In 1873, Ernst Abbe defined the resolution limit of an optical microscope as the minimum lateral distance between two objects allowing them to be observed separately. This distance is given by $d = \lambda / (2NA)$, where λ is the wavelength of the light and *NA* is the numerical aperture of the objective. The *NA* as applied to a microscope objective is a measure of the ability to gather light and resolve fine specimen detail at a fixed object distance. The higher the numerical aperture of the total system, the better the resolution.

Two-point resolution

The two-point resolution criterion corresponds to the ability of an imaging system (an eye or an optical instrument) to distinguish two point sources of equal luminosity and separated by a minimum distance. When two distinct points are very close, they will have a spots (Airy spots) which overlap and if they are not sufficiently separated, may therefore no longer be distinguished from each other. These point sources are represented by two well separated diffraction patterns, or Airy disks. Experimentally, the normalized

intensity of an Airy spot corresponds to the PSF (Point Spread Function) of the system. The two-point resolution criteria are based on the observation of PSF recovery from two point sources of equal intensity. Several the types of this criteria for example are the Rayleigh, Abbe, and Sparrow criteria. The distance between the two spots from the point sources is given by the following relation:

$$R_K = K \cdot \frac{\lambda}{NA} \tag{1.28}$$

with the numerical aperture of the objective microscope $NA = n \times \sin\theta$ where θ is the half angle of the cone of light that can enter the objective and n is the refractive index of the medium between the objective and the object, λ is the wavelength of the light source and K is a constant, between 0.47 and 1, according to the criterion and the illumination type of the light source used [91].

Table 2 The lateral resolution criteria based on the illumination type

Criteria	Illumination type	
	Incoherent	**Coherent**
Rayleigh	$R_R = 0.61 \cdot \frac{\lambda}{NA}$	-
Sparrow	$R_S = 0.47 \cdot \frac{\lambda}{NA}$	$R_S = 0.73 \cdot \frac{\lambda}{NA}$
Abbe	$R_A = 0.5 \cdot \frac{\lambda}{NA}$	$R_A = \frac{\lambda}{NA}$

Point Spread Function (PSF)

The incoherent impulse response or PSF (Point Spread Function) is the response of the microscope to a point source and therefore corresponds to the intensity of an Airy spot if we consider a perfect optical system, i.e. without aberrations. The ideal point spread function (PSF) is the diffraction pattern of light emitted from an infinitely small point source and transmitted through a high NA objective.

According to the Rayleigh criterion, the distance of the maxima of the PSF is an essential value in the determination of the resolution and it is therefore important that the maxima are well separated from each other. This implies that the resolution is all the better as the diameter of the Airy spot is small. So another way to determine the resolving

power of an optical instrument is to measure the PSF's FWHM (Full Width at Half Maximum) [92], as shown in Fig. 28.

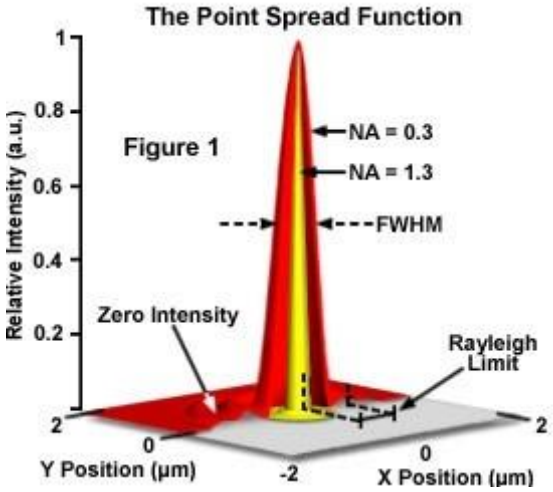

Fig. 28 The illustration of 3D PSF

1.11.2 Axial resolution

The axial resolution of a microscope corresponds to the depth resolution and depends on the temporal coherence length of the illumination source and the numerical aperture of the lenses used. As for lateral resolution, the axial resolution can be determined from the system of PSF (point spread function) by measuring its width at half-height along the optical axis [14] and can be defined by the following relationship:

$$R_{axial} = \frac{2\ln 2}{n\pi} \cdot \frac{\lambda^2}{\Delta\lambda} \qquad \textbf{(1.29)}$$

where n is the refractive index of the medium, λ is the central wavelength of the source and $\Delta\lambda$ is the total spectral width at mid-height of the source (FWHM) [16]. The temporal coherence length of the source is given by $Lc = v / \Delta\lambda$ where v is the speed of propagation of the wave. Therefore, the use of an illumination source with a wide spectrum, having a low coherence length, can improve the axial resolution of the system.

When objectives have large numerical apertures, the axial resolution of the system depends mainly on the *NA* of the objectives [16] and can be approximated by the following relation:

$$R_{axial} \approx \frac{0.44\lambda}{n\left(1-\cos\alpha\right)} \qquad \textbf{(1.30)}$$

with α the half-angle of the opening cone and λ the central wavelength of illumination.

1.12 RÉSUMÉ DU CHAPITRE 1

Dans ce chapitre, nous décrivons comment la technique de l'interférométrie à balayage de cohérence (CSI) génère un interférogramme (signal des franges). Nous étudions et observons la structure du signal des franges et les différentes approches (techniques Z-scan et XZ-scan) pour l'analyse des franges. Ensuite, nous nous concentrons sur les étapes de la procédure d'analyse des franges que nous effectuons dans ce travail. L'étude du pré-traitement pour enlever les composants "offset" et la détermination de la structure de surface de l'échantillon que nous utilisons dans le travail sont également rapportés.

Le principe de la technique CSI est basé sur l'analyse de cohérence croisée de deux faisceaux lumineux de faible cohérence, le faisceau objet étant réfléchi par l'échantillon, tandis que le faisceau de référence est réfléchi par un miroir de référence. Les deux faisceaux lumineux sont ensuite combinés au niveau du détecteur. L'interférence se produit lorsque la différence de chemin optique entre le faisceau de référence et le faisceau d'objet réfléchi est proche de zéro. C'est-à-dire lorsque la longueur du trajet optique vers l'échantillon est presque identique à la longueur du trajet optique par rapport au miroir de référence. Dans le but de trouver le maximum d'interférence, un balayage de frange est effectué sur chaque point de la surface de l'échantillon, point par point. Les intensités de contraste des franges qui tiennent compte du changement de distance entre l'échantillon et l'objectif (en axe z) sont captées par le détecteur (caméra) générant le signal de frange, également connu sous le nom d'interférogramme. L'analyse des franges est alors nécessaire pour récupérer le pic d'enveloppe de contraste de frange qui indique la position de surface de l'échantillon.

L'intensité lumineuse donnant lieu au signal de frange, s (x, y, z), capté à partir d'un détecteur (CCD) lorsque la différence de trajet optique varie par focalisation dans un interféromètre de lumière blanche, a la forme suivante:

$$s(x,y,z) = \quad a(x,y,z) + b(x,y)\,g\left(z - z_0(x,y)\right).\cos\left(\frac{4\pi}{\lambda_0}\left(z - z_0(x,y)\right) - \alpha(x,y)\right)$$

$$\text{where} \quad z = k\Delta$$

La fonction *s* correspond au signal d'intensité à un point donné de la surface de l'échantillon (*x*,*y*), où *z* représente une position de balayage vertical par rapport à la surface. La quantité *a*(*x*,*y*,*z*) est une intensité de décalage liée aux intensités de faisceau de référence et d'objet, *b*(*x*,*y*) est le contraste de frange, *g*(*z*) est la fonction d'enveloppe de

frange liée au profil spectral du source de lumière blanche, et λ_0 est la longueur d'onde moyenne de la source lumineuse. Le déphasage lié au changement de phase à la réflexion est représenté par $\alpha(x,y)$.

En général, les techniques de traitement du signal développées dans ce travail se composent de trois étapes principales: un pré-filtrage, la détection d'enveloppe et un post-filtrage. La détection d'enveloppe est nécessaire pour obtenir l'enveloppe de franges dont le pic représente la position de surface. Le pré-filtrage est utilisé pour supprimer le composant de décalage et réduire le bruit, tandis que le post-filtrage est utilisé pour déterminer plus précisément la mesure. Dans ce chapitre, nous présentons les différentes techniques utilisées pour extraire l'enveloppe de frange dans la CSI, à savoir la Transformée de Hilbert (HT), l'algorithme Adaptatif à cinq échantillons (FSA), la Transformée en ondelettes continue (CWT) et l'Opérateur de Teager Kaiser-Energy (TKEO). Par contre, nous avons également rapporté notre étude de la comparaison des performances de différents pré-traitements afin d'éliminer la composante de décalage du signal de frange (moyenne globale, moyenne locale, dérivée centrale, décomposition en mode empirique).

L'équipement développé pour exécuter l'algorithme pour le traitement des signaux de frange dans cette thèse consiste en deux microscopes adaptés, un microscope Leica DMR-X équipé d'objectifs Mirau (x10, x40) et Michelson (x5) et un microscope Leitz-Linnik équipé d'objectifs de x50 (NA = 0,85). L'échantillon est monté sur une table de balayage vertical piézo-contrôlée pour le balayage en Z. L'actionneur piézoélectrique est commandé en boucle fermée avec un capteur de position capacitif, ayant une sensibilité de position de 1 nm. Une lampe à halogène est utilisée dans le Leica DMR-X et une lampe à incandescence est utilisée pour l'éclairage du Leitz-Linnik avec une lumière blanche (310 nm - 1100 nm). L'acquisition d'image est réalisée avec un CCD Prosilica numérique ayant 1360x1024 pixels et un Aval1000 Basler ayant 1024x1024 pixels.

Afin d'évaluer la performance des algorithmes développés dans ce travail, les échantillons suivants qui ont différentes structures ont été utilisés. Ils ont été choisis parce qu'ils varient d'une simple surface lisse à des structures de plus en plus complexes, y compris une surface unique, une couche transparente sur le substrat et un film de polymère transparent.

Chapter 2. COMPARISON OF PRE-FILTERING AND ENVELOPE DETECTION TECHNIQUES

In this chapter, we describe the Teager-Kaiser Energy Operator which we use as the proposed multidimensional algorithm (1D, 2D, 3D) for envelope detection in CSI. Then the study of the performance comparison of the different pre-filtering and envelope detection techniques in fringe signal processing is described. For comparison, results using the algorithms are presented on the synthetic fringe signal and on real data, i.e. the resin on silicon sample. In addition, a study of the selection of the mother wavelet for the Continuous Wavelet Transform is presented in its use for obtaining the fringe envelope.

2.1 TEAGER KAISER ENERGY OPERATOR

2.1.1 Signal energy

The estimation of signal energy is commonly used to characterize a signal. In traditional signal processing, the energy of a signal is defined as the square of the signal magnitude, or the envelope of the squared signal magnitude or the integral of the squared signal magnitude.

Let us consider a signal $x(t)$. With a time period $2T$, the signal $x(t)$ has the energy E which is defined as follows:

$$E = \int_{t=-T}^{T} \left|x(t)\right|^2 dt \qquad \textbf{(2.1)}$$

while the total energy is defined by

$$E = \int_{t=-\infty}^{\infty} \left|x(t)\right|^2 dt \quad , \qquad \textbf{(2.2)}$$

Note that the total energy of the signal in Eq.(2.2) is not the same as the instantaneous energy which is what we need to seek. Then the instantaneous amplitude can be found for fringe analysis. In the case of simple harmonic motion, i.e. fundamental sinusoidal oscillation, this expression shows that the energy required to produce a simple

sinusoidal signal is a function of the frequency and amplitude. This observation was used by Kaiser to define the Teager Kaiser-Energy Operator [54].

2.1.2 Teager Kaiser Energy Operator

The above observation of the signal energy in light is discussed in the article by Kaiser [54]. Here, Kaiser derives the equation of energy for a simple oscillator from the basic physics of motion.

The energy is presented as being directly corresponding to the square of the product of the pulsation frequency and amplitude. The second order differential equation in the case of using the basic physics of motion for a simple spring and mass oscillator is used as the beginning of the development of the operator, as illustrated in the following equation:

$$\frac{d^2x}{dt^2} + \frac{k}{m}x = 0 \qquad \textbf{(2.3)}$$

The Eq.(2.3) represents the law of motion of a system consisting of a mass m that is suspended from a spring with force constant $k > 0$. The system can be regarded as a model of a simple mechanical acoustical system, in which the object oscillates, generating the pressure wave in the neighbouring medium.

The solution of Eq.(2.3) is the simple harmonic motion, which can be defined as $x(t) = A\cos(\omega t + \phi)$ where A corresponds to the oscillation amplitude, ω represents the oscillation frequency, that is given by $\omega = \sqrt{\frac{k}{m}}$, and ϕ is the arbitrary initial phase.

The simple harmonic motion has the energy E that is defined as the total energy coming from the kinetic energy of the mass and the potential energy in the spring, as follows:

$$E = \frac{1}{2}kx^2 + \frac{1}{2}m\dot{x}^2 \qquad \textbf{(2.4)}$$

By substituting the equation of $x = A\cos(\omega t + \varphi)$ and its derivative, $\dot{x} = \frac{dx}{dt}$, we can obtain the equation of energy:

$$E = \frac{1}{2}m\omega^2A^2 \quad \text{or} \quad E \approx \omega^2A^2 \qquad \textbf{(2.5)}$$

Based on this equation, we can observe that the energy of the simple harmonic system is proportional to the squared of the product of the frequency ω and the amplitude A, and varies as function of time t, while the $x^2(t)$ only takes into account the potential energy of the signal source.

2.1.3 Discrete Teager Kaiser Energy Operator

Let us consider a discrete-time signal x_n representing the motion of the oscillator body, given by:

$$x_n = A\cos(\Omega n + \phi) \tag{2.6}$$

Where A corresponds to the oscillation amplitude, Ω corresponds to the frequency and is given by $\Omega = 2\pi f/F_s$, where f represents the oscillation frequency, F_s represents the sampling frequency, while the parameter φ corresponds to the arbitrary initial phase.

In Eq.(2.6), there are three parameters A, Ω, and φ, with unknown values. This means that mathematically, it is necessary to construct three different equations based on the formula in Eq.(2.6) in order to obtain the values of these parameters from three samples of the signal x_n.

$$\begin{aligned} x_n &= A\cos(\Omega n + \phi) \\ x_{n-1} &= A\cos(\Omega(n-1) + \phi) \\ x_{n+1} &= A\cos(\Omega(n+1) + \phi) \end{aligned} \tag{2.7}$$

Through the trigonometric formulas, then we obtain:

$$x_{n-1}x_{n+1} = A^2\cos^2(\Omega + \phi) - A^2\sin^2(\Omega) \tag{2.8}$$

$$A^2\sin^2(\Omega) = x_n^{\,2} - x_{n-1}x_{n+1} \tag{2.9}$$

The solution to Eq.(2.9) with respect to Ω is specific and singular provided that Ω is restricted to be less than π/2 and has a positive value. The approximated approach of this equation can be carried out by noting that if Ω is small, sin (Ω) ≈ Ω. If we limit the value of Ω to $\Omega < \pi/4 = 0.7854$, i.e. $f/f_s < 1/8$ then the relative error is always below 11 %.

Thus the discrete version of Teager Kaiser-Energy Operator can be defined as the following equation:

$$\psi_d\left[x(n)\right] = x^2(n) - x(n-1)\,x(n+1) \tag{2.10}$$

Based on the Eq.(2.10), the instantaneous energy ψ_d of a signal $x(n)$ can be estimated by substituting x in the formula of the TK energy operator. This operator is nonlinear and has the following properties [36], [93]:

- $\psi_d[\cdot]$ is independent of the initial phase φ_0.
- $\psi_d[x(n)] = \psi_d[x(-n)]$.
- $\psi_d[x(n)]$ is robust to the division by zero error even when the signal passes through zero, as no division operation is required.
- $\psi_d[x(n)]$ is capable of responding rapidly to changes in both frequency and amplitude (instantaneous operator).

2.1.4 Continuous Teager Kaiser Energy Operator

The discrete version of the Teager-Kaiser Energy Operator has been defined in the previous section. In the continuous time domain, the Teager-Kaiser Energy Operator is then defined as:

$$\psi_c\left[x(t)\right] = \left(\frac{dx}{dt}\right)^2 - x(t)\left(\frac{d^2x}{dt^2}\right) \tag{2.11}$$

Let us consider a signal $x(t) = A\cos(\omega t)$ and substitute it into the Eq.(2.11), yielding:

$$\begin{aligned}\psi_c\left[x(t)\right] &= \left(-A\omega\sin(\omega t)\right)^2 - A\cos(\omega t)\left(-\omega^2 A\cos(\omega t)\right)\\ &= \omega^2A^2\left(\sin^2(\omega t) + \cos^2(\omega t)\right)\\ &= \omega^2A^2\end{aligned} \tag{2.12}$$

As illustrated in Eq.(2.12), the energy of the signal $x(t) = A\cos(\omega t)$ is defined by the squared product of the frequency ω and the amplitude A. In fringe analysis, the main disadvantage of the Teager-Kaiser Energy Operator is its sensitivity to the signal noise that appears during the acquisition process. In the application of a noisy fringe signal, a denoising filter, such as the Savitzky-Golay filter can be applied in combination with the operator to make the envelope detection more robust to noise.

2.2 Performance Comparison Of Different Mother Wavelet In Continuous Wavelet Transform Algorithm On Fringe Signal Processing

2.2.1 Application wavelet analysis in fringe signal processing

The wavelet transform is a relatively robust mathematical tool for signal analysis and processing. In optical measurement, wavelet analysis has been widely used for fringe signal processing. In 1997, Sandoz applied the wavelet transform to the analysis of white light interferometry [39]. In this application, the accurate phase measurements are obtained from simple correlation computations which are used to accurately identify the local fringe peak, which indicates the surface height of a sample. Meanwhile, similar work was reported in 1997 [94] which also applied wavelets for the analysis of white light interferometry. In this application, the fringe envelope of a white light interferogram corresponds to the absolute modulus of the maximum correlation coefficient. The fringe analysis based on a local fringe peak can provide a higher resolution than current methods that are is based on a global envelope peak. Moreover, the wavelet analysis seems to be robust to noise [57],[95], providing accurate measurements of the surface.

2.2.2 Mother wavelet selection

The success of the CWT for retrieving the fringe envelope depends on the selection of a mother wavelet [64]. In order to obtain satisfactory results, the mother wavelet should be of the same form as the signal. The fringe signal which will be analysed is characterized by a high frequency sinusoid that is modulated by a Gaussian function. As regards the characterization, wavelet families that visually have a similar shape to that of the fringe signal are the Morlet, complex Morlet, Gaussian, complex Gaussian, and Mexican hat[96],[97],[98] as shown in Fig. 29. In this study, all these wavelets were tested and performed using a synthetic fringe signal.

The synthetic signal we used in this simulation to test all the wavelets is based locally on the general model expressed by equation (1.9) along the optical axis Z, with a 40 nm sampling step, for each lateral position X. The resulting XZ image is shown in Fig. 30. The synthetic images represent a wavy transparent layer on a substrate i.e., a surface and an interface giving two fringe signals. An additive non-linear offset and Gaussian noise are added onto this synthetic data which commonly appear in a fringe signal during the acquisition process and results in reduced precision of surface measurement. The

Gaussian noise value is of 20%, which means that the mean value of the Gaussian noise is 20% of the maximum of intensity of the buried interface fringe signal.

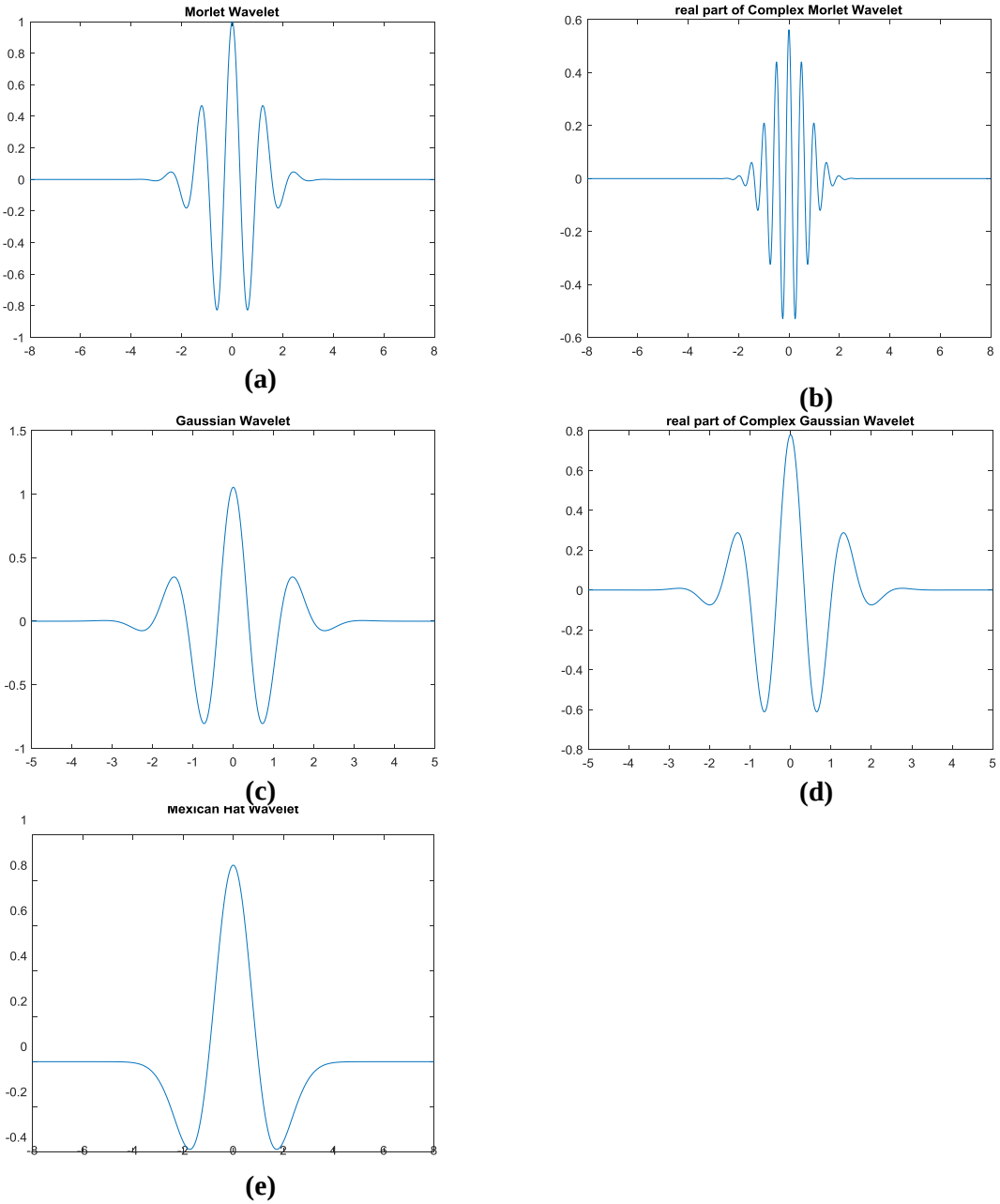

Fig. 29 Wavelet familes: (a) Morlet, (b) complex Morlet, (c) Gaussian, (d) complex Gaussian, and (e) Mexican hat

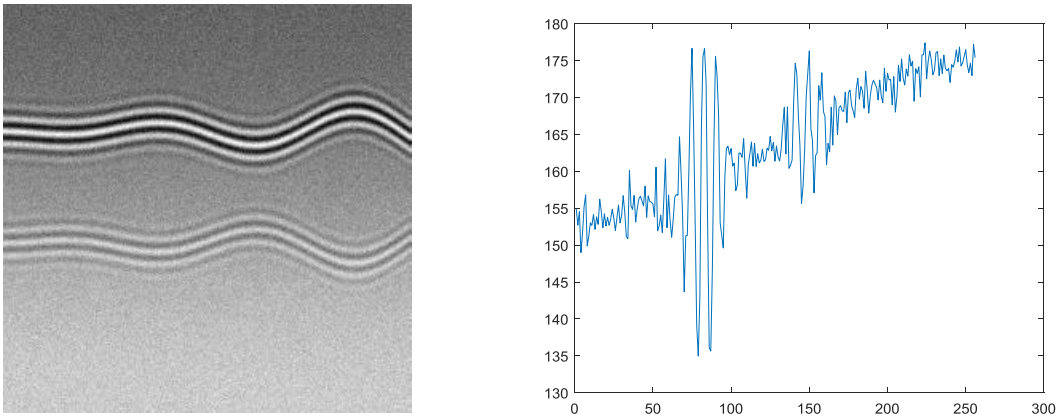

(a) **(b)**

Fig. 30 Synthetic fringe signal in (a) XZ image and (1D)

The results in Fig. 31 show the fringe envelopes obtained using wavelet families: (a) Morlet, (b) complex Morlet, (c) Gaussian, (d) complex Gaussian, and (e) Mexican hat. In this simulation, we adjust the scale frequency of 0.1 in the CWT algorithm, as refered to in article [99]. Based on these figures, it can be seen that only one of the wavelet families is suitable, i.e. the complex Morlet, which provides a well-defined fringe envelope, as shown in Fig. 31(b). The other wavelets: Morlet, Gaussian, Mexican hat provide a significantly noisier fringe envelope, as shown in Fig. 31(a-c-e). The fringe envelope obtained using these mother wavelets contain a fringe pattern. Meanwhile, the fringe envelope obtained using a complex Gaussian provides a well-defined envelope without containing a significant fringe pattern, as shown in Fig. 31(d). However, the envelope amplitude increases by almost twice as much as the original fringe envelope. Further evaluation is required to see whether the increase in amplitude produces an effect on the height surface information contained in the peak of the fringe envelope. In this work, we therefore tested the use of the complex Gaussian as a mother wavelet in the CWT algorithm in order to obtain the envelope for fringe analysis, which is then compared to the complex Morlet.

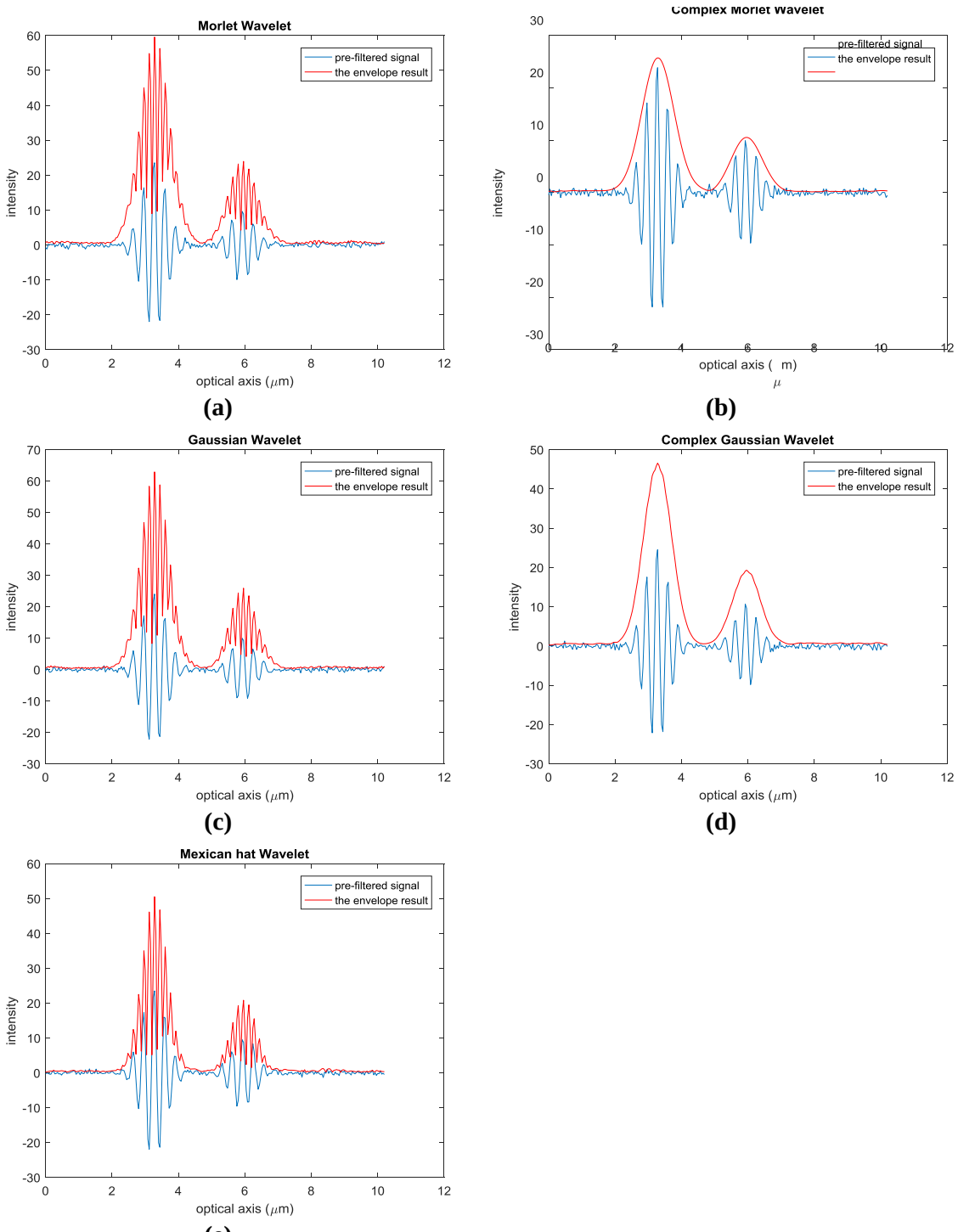

Fig. 31 Fringe envelope obtained using wavelet familes: (a) Morlet, (b) complex Morlet, (c) Gaussian, (d) complex Gaussian, and (e) Mexican hat

2.2.3 Simulation results

For further observation of the use of the complex Gaussian and complex Morlet as mother wavelets in the CWT algorithm, we carried out the simulation using the procedure described in section 2.4.1, as shown in Fig. 35. In the simulations, we use the EMD and

Savitsky-Golay filters in the prefiltering step in order to remove the offset component and to suppress the noise. In the post-processing step, we only use the Gaussian estimation and interpolation to correct the peak curve, without smoothing due to the fringe envelope obtained using the CWT algorithms (complex Gaussian and complex Morlet) that already provides a well-defined fringe envelope without containing significant noise and fringe pattern. Fig. 32 and Fig. 33 show examples of the results of signal processing for the wavy transparent layers obtained using the CWT algorithms (complex Gaussian and complex Morlet).

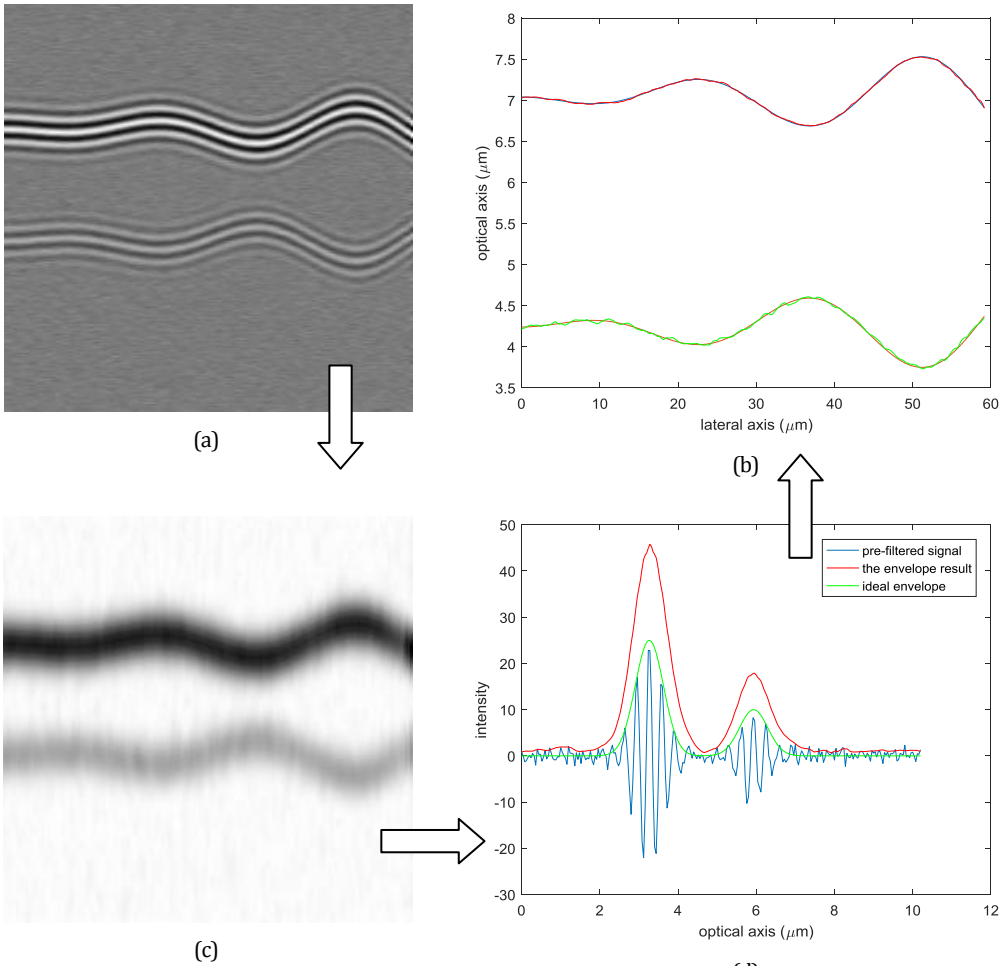

Fig. 32 Signal processing analysis for a wavy synthetic transparent surface: (a) output of pre-filtering using the EMD-SGolay filter; (b) surface profile, (c) 2D and (d) 1D fringe envelope obtained by CWT(complex Gaussian).

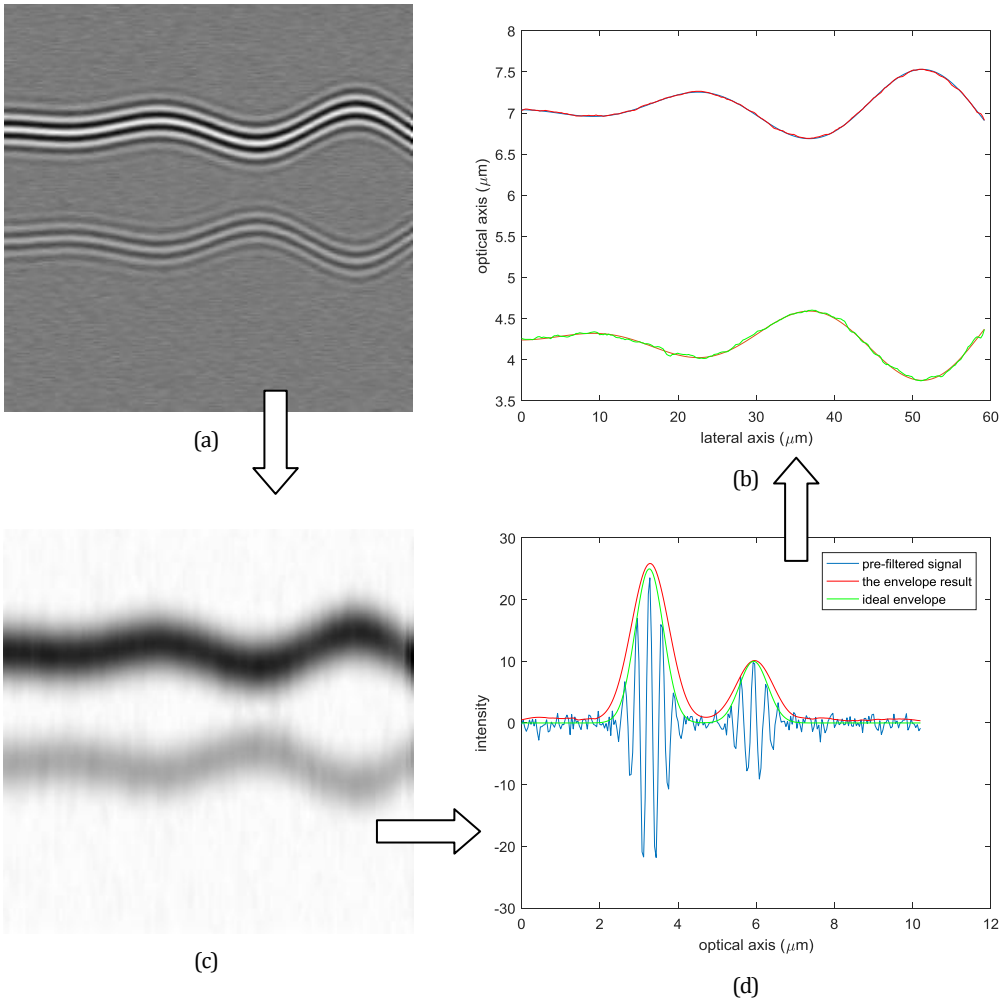

Fig. 33 Signal processing analysis for a wavy synthetic transparent surface: (a) output of pre-filtering using the EMD-SGolay filter; (b) surface profile, (c) 2D and (d) 1D fringe envelope obtained by CWT (complex Morlet).

Table 3 summarizes the results of the performance comparison of the complex Morlet and complex Gaussian in the CWT algorithm on fringe signal processing. The table shows the mean absolute error (*mae*) of surface extraction obtained using the CWT algorithm (complex Gaussian and complex Morlet wavelet), as illustrated in Fig. 32(b) and Fig. 33(b). The value of mean absolute error shows the precision of the measurement results using the fringe signal processing used. Comparing the results in the table, both the CWT using the complex Gaussian and complex Morlet wavelet are similar in terms of performance in the casees of the noiseless signal (σ=0%) and a noisy signal (σ=10% and σ=20%), providing a maximum difference of *mae* = 0.24 nm. Based on these results, it can be observed that the use of the complex Gaussian wavelet in the CWT algorithm is as competitive as the complex Morlet wavelet as the mother wavelet in fringe signal

processing. This means that even though the fringe envelope obtained using the CWT (Gaussian complex morlet) has the envelope amplitude that is twice the original envelope, this algorithm is still able to maintain the height surface information in its fringe envelope peak.

Table 3 Mean absolute error (mae) of surface extraction obtained using the CWT algorithm (complex Gaussian and complex Morlet wavelet)

Pre-filt.	Suppress the offset: EMD Suppress the noise: Savitzky-Golay filter			
Env. Det.	CWT (complex Morlet)		CWT (complex Gaussian)	
Post-filt.	Correct the peak curve using Gaussian estimation and interpolation			
mean absolute error (nm)				
noise(σ)	1st surf.	2nd surf.	1st surf.	2nd surf.
0%	1.02	1.04	1.02	1.02
10%	3.32	7.04	3.37	7.22
20%	5.80	14.0	5.86	14.24

2.3 COMPARISON OF PRE-FILTERING TECHNIQUES

In order to remove the offset and reduce the noise, in this section we compare three different algorithms which combine the derivative/EMD technique and denoising filter (Savitzky-Golay/Wiener). The corresponding algorithms are referred to with the following names:

- Pre-filter 1: combination of derivative and Wiener filter,
- Pre-filter 2: combination of derivative and Savitzky-Golay filter,
- Pre-filter 3: combination of EMD and Savitzky-Golay filter.

For the performance evaluation of the above different pre-filters, we carry out the simulation by performing them on a synthetic fringe signal, with a 40 nm sampling step, as shown in Fig. 34(a). It can be noted that the scanning step height chosen in interference microscopy during the data acquisition is a fixed step both for PSM and the FSA algorithm ($\pi/2$, linked to the effective wavelength). The reason for this is that the phase used for the algorithm is fixed at $\pi/2$. Even though this step can be variable for other TKEO algorithms, since the same fixed scanning step height is used for FSA, it will also

be used for the performance comparison. An additive non-linear offset and Gaussian noise are added onto the synthetic data (20%) which means that the root mean square (rms) of the added Gaussian noise is 20% of the maximum amplitude of the second layer fringe signal. Regarding the removal of the offset, two procedures are considered: a) the classical centered derivative, which has been chosen for its stability [100], and b) as an alternative method, the EMD which helps to remove the low frequency component given by the higher order IMF's and the residue [101]**.** On the other hand, to process the noisy data, the Savitzky-Golay filter is compared with the classic Wiener filter**,** using a local window around each sample. Based on empirical data, the window length of 5 seems to optimize the performance for this approach (with a 40 nm sampling step). Concerning the Savitzky-Golay filter, we have applied it along the lateral axis using a third order polynomial. Based, on our data, this parameter seems to ensure the better robustness to noise.

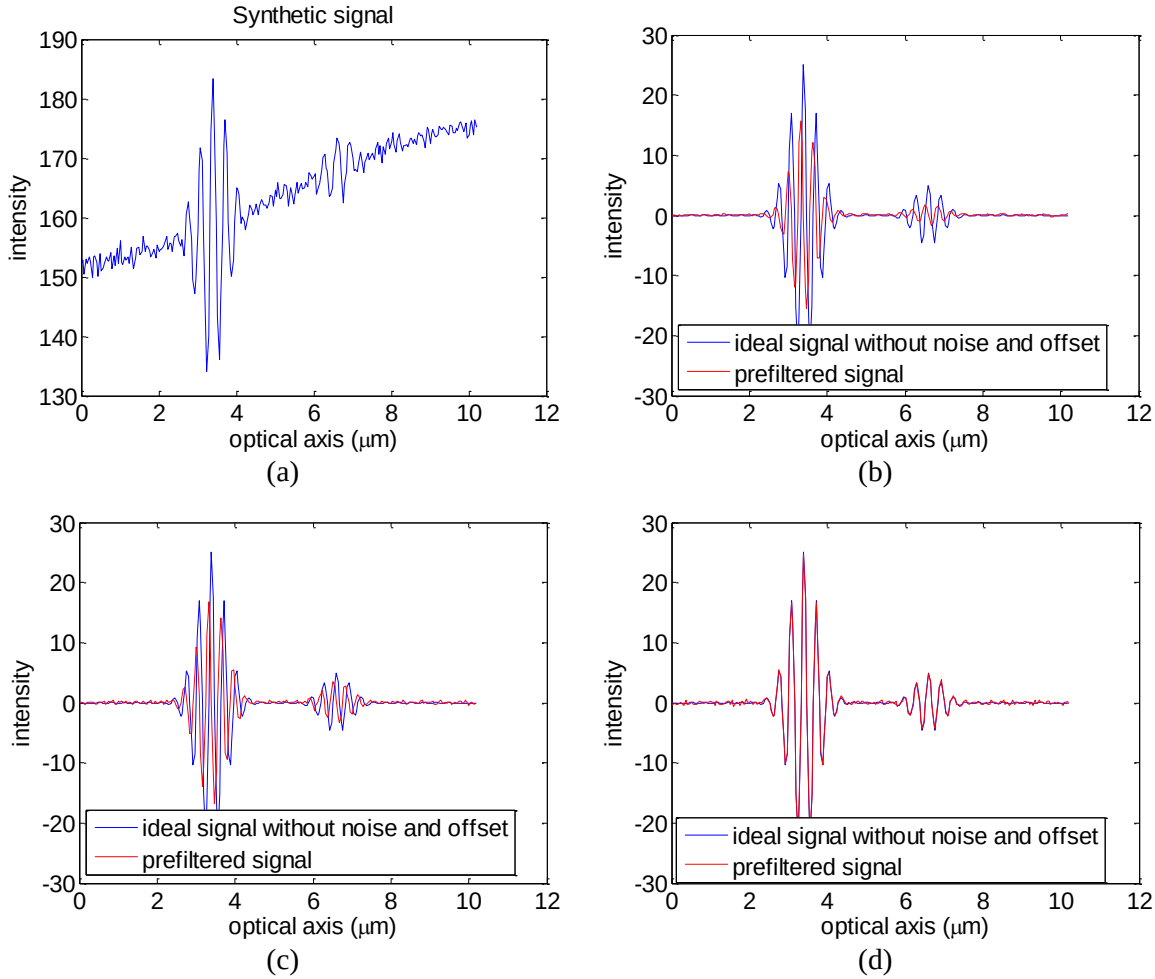

Fig. 34 (a) Synthetic signal with noise σ =20% and prefiltered signal resulting from: (b) pre-filter 1; (c) pre-filter 2; (d) pre-filter 3.

The simulation results of performance comparison of pre-filter 1, pre-filter 2, and pre-filter 3, are shown in Fig. 34(b,c,d). It can be observed in Fig. 34, that the three algorithms provide competitive results for the offset removal and noise reduction. However, they have different capabilities for maintaining the fringe signal intensities. Comparisons are made between the fringe signal intensities of the pre-filtered (red line, Fig. 34) and the ideal signals i.e. without the offset and noise (blue line, Fig. 34). As illustrated in Fig. 34(b), the resulting amplitude of the fringe signal using pre-filter 1, is clearly lower than the ideal synthetic fringe signal (without the offset or the noise). This means that a degradation of the intensities occurs during the pre-filtering process.

Similar results are also obtained using pre-filter 2 (Fig. 34(c)), although it maintains better the fringe signal intensities of the second layer. This means that the use of the Savitzky-Golay filter is better at maintaining the amplitude of the fringe signal than the wiener filter in the pre-filtering step. A decrease in the intensity may seriously degrade the performance of the algorithm in order to extract the fringe envelope, particularly in the area where the SNR is low**.** Meanwhile, as illustrated in Fig. 34(d), the pre-filter 3 is able to remove the offset and reduce the noise, while almost maintaining the amplitude of the fringe signal. Based on the simulation, we observe that pre-filter 3 using a combination of the EMD and Savitzky-Golay provides a better result than the others in removing the offset, suppressing the noise and particularly in maintaining the fringe amplitude.

2.4 COMPARISON OF ENVELOPE DETECTION TECHNIQUES

2.4.1 Comparison Procedure

In this section, results are presented of simulations performed using a Matlab program in order to compare the performance of the envelope detection techniques. The simulation procedure is illustrated in Fig. 35. In the simulation, we used a synthetic fringe signal corresponding to the known profile of the reference surface (h_{ref}). Then we perform the fringe analysis procedure on the synthetic fringe signal. This consist of a first step of pre-filtering for removing the offset component and suppressing the noise, a second step of fringe contrast envelope detection and a third step of post-filtering using smoothing and Gaussian fitting for determining more precise the envelope peak position, which indicates to the surface height (h). Finally, we calculate the error of the surface height estimation

(h) in respect to the reference surface (h_{ref}). A smaller value of the error rate (*mae*) represents a higher accuracy.

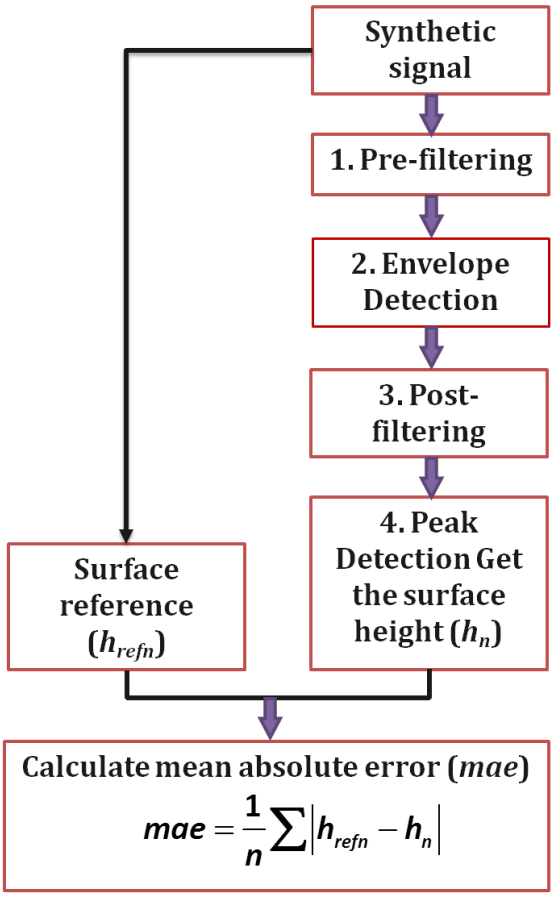

Fig. 35 The comparison procedure to evaluate the performance of the different algorithms[53].

2.4.2 Synthetic Samples

The synthetic signal we used in this simulation to test all the cited algorithms is based locally on the general model expressed by Eq.(1.9) along the optical axis Z, with a 40 nm sampling step, for each lateral position X. The resulting XZ image is shown in Fig. 36. The two synthetic images used represent flat and wavy transparent layers on a substrate, giving two fringe signals along Z corresponding to the air/layer surface and layer/substrate interface. In this case, an additive non-linear offset and Gaussian noise are added onto the synthetic data (10% and 20%). The Gaussian noise value of 10% means that the root mean square (*rms*) of the added Gaussian noise is 10% of the maximum amplitude of the second layer fringe signal. Considering the synthetic fringe signal, the rms of 10% is equal to 19 dB, while the *rms* of 20% is equal to 13 dB.

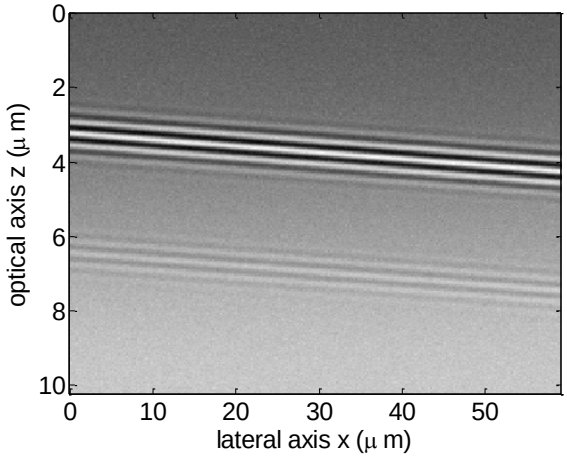

(a)

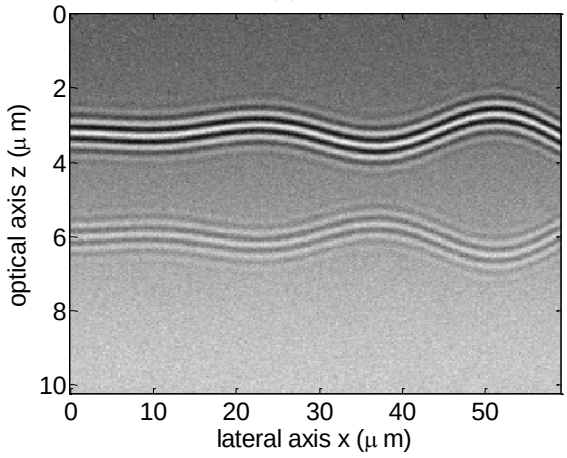

(b)

Fig. 36 Synthetic fringe signal with a non-linear offset and 10% Gaussian noise (XZ image) 256 x 256 pixel on a (a) flat transparent layer and (b) wavy transparent layer.

2.4.3 Simulation Results

Fig. 37 and Fig. 38 show an example of the results of fringe analysis for the flat and wavy transparent layers as shown in Fig. 36 using the procedure as described in section 2.4.1. In detail, Fig. 37(a) and Fig. 38(a) show the pre-filtered signal in two dimensions (XZ image) after carrying out the pre-filtering process. In these figures, it can be seen that the pre-filter which we used has successfully removed the offset component and suppresses the noise (compare with the XZ image in Fig. 36). After the pre-filtering process, then we carry out the envelope detection on the pre-filtered signal, obtaining the fringe contrast envelope in two dimensional (XZ image), as shown in Fig. 37(b) and Fig. 38(b). The clearer observation of the pre-filtered signal and the fringe contrast envelope is illustrated in Fig. 37(d) and Fig. 38(d) in one dimension (the optical axis Z).

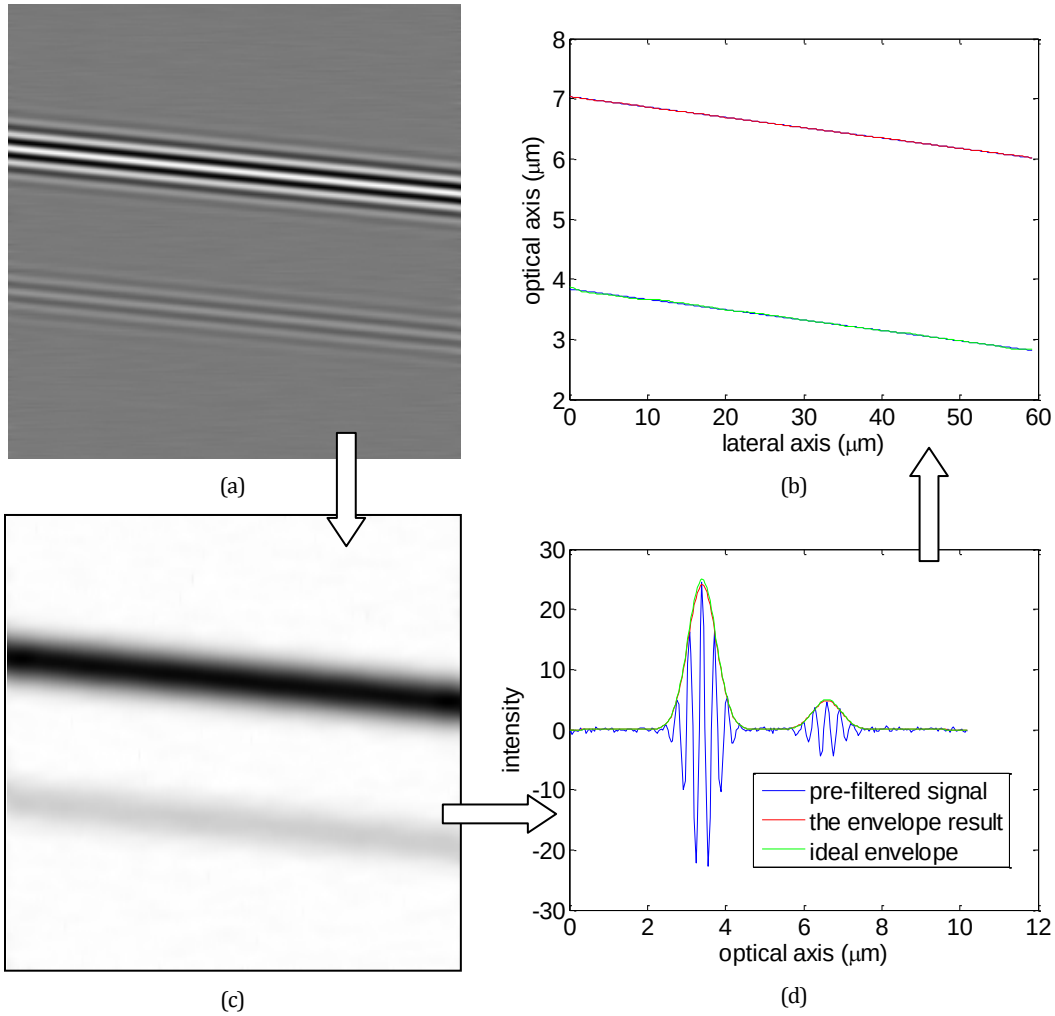

Fig. 37 Signal processing analysis for synthetic flat transparent surface: (a) output of pre-filtering using EMD-SGolay filter; (b) surface profile, (c) XZ image of envelope and (d) 1D fringe envelope obtained by TKEO.

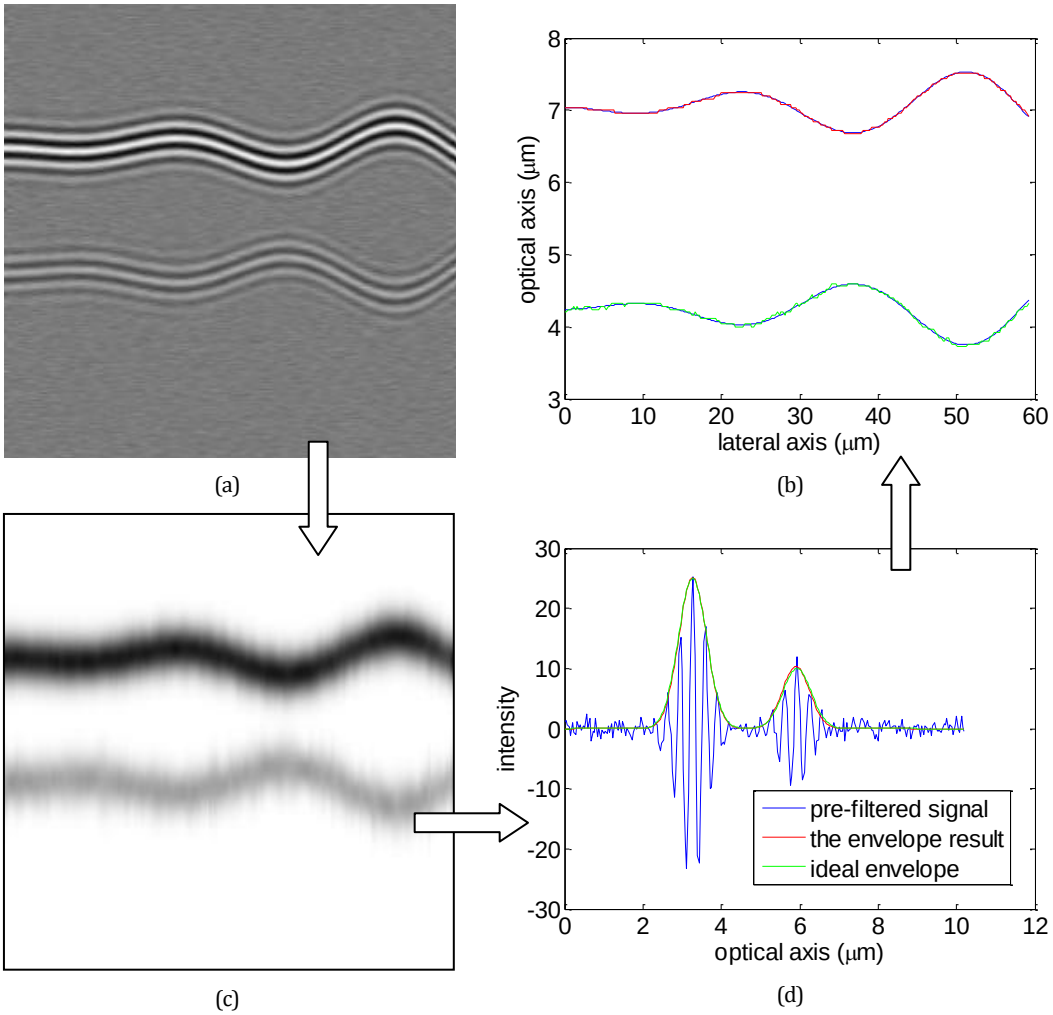

Fig. 38 Signal processing analysis for a wavy synthetic transparent surface: (a) output of pre-filtering using EMD-SGolay filter; (b) surface profile, (c) XZ image of envelope and (d) 1D fringe envelope obtained by TKEO.

After the pre-filtering and envelope detection process, we then perform the post-processing using a cubic smoothing spline and Gaussian fitting on the fringe contrast envelope obtained in order to determine more precisely the peak of the envelope that indicates the height of the object surface. Fig. 37(b) and Fig. 38(b) show the measured surface profile (red line for the air/layer surface and green line for the layer/substrate interface) as the final result obtained by the fringe analysis using the procedure as described in section 2.4.1. In these figures, it can be seen that the measured profiles (red and green line) coincide with the reference surface (blue line) of the synthetic transparent layers which we used in the simulation. For quantitative evaluation, then the error rate (mean absolute error) of the measured profile is calculated in respect to the surface reference, as shown in **Table 4**, **Table 5** and **Table 6**.

In this simulation, we carry out the procedure as described in the section 2.4.1 in order to compare the performance of fringe analysis using a combination of different pre-filtering as described in the section 2.3 and different envelope detection as described in the section 1.6.2. The results of performance comparison using this procedure are summarized in the following **Table 4** – **Table 6**.

Table 4 Experiment result using pre-filter 1 and different envelope detection techniques (nm)

	A		B		C		D	
Pre-filt.	Suppress the offset: 1st order central derivative Suppress the noise: Wiener filter							
Env. Det.	HT		FSA		TKEO		CWT	
Post-filt.	Smooth the amplitude envelope using cubic smoothing spline Correct the peak curve using Gaussian estimation and interpolation							
mean absolute error (nm)								
noise(σ)	1st surf.	2nd surf.	1st surf.	2nd surf.	1st surf.	2nd surf.	1st surf.	2nd surf.
flat transparent layer								
0%	0.00	0.05	0.00	0.05	0.00	0.05	0.01	0.05
10%	3.07	7.27	4.21	7.09	3.08	7.11	2.44	6.65
20%	5.35	14.52	7.55	14.40	5.19	14.58	4.29	13.31
time	2.6 s		1.6 s		3.2 s		27.3 s	
wavy transparent layer								
0%	1.12	2.17	1.18	3.95	1.15	2.31	1.14	1.39
10%	5.58	10.20	7.56	11.42	5.49	11.31	4.57	8.15
20%	10.54	19.48	15.23	21.90	10.25	18.73	8.39	15.71
time	2.6 s		1.6 s		3.2 s		27.3 s	

Table 4, **Table 5** and **Table 6** correspond respectively to the pre-filter 1, 2 and 3, the related algorithms being respectively denoted by A, B, C, D (**Table 4**), E, F, G, H (**Table 5**) and I, J, K, L (**Table 6**). For each table, the envelope technique associated with each procedure is indicated. For instance: A, E, and I are related to the Hilbert Transform; B, F, and J are related to the FSA, C, G, and K are related to the TKEO, while

D, H, and L use CWT). The same post-processing mentioned in section 1.5.3, has been applied. For each procedure, the simulations have been calculated with different levels of noise ($\sigma = 0\%, 10\%, 20\%$). The performance of each procedure has been quantitatively evaluated by the measurement of the calculation time and the error rate (mean absolute error) between the reference surface and the estimated one (for both surface layers).

Table 5 Experiment result using pre-filter 2 and different envelope detection techniques (nm)

	E		F		G		H	
Pre-filt.	Suppress the offset: 1st order central derivative Suppress the noise: Savitzky-Golay filter							
Env. Det.	HT		FSA		TKEO		CWT	
Post-filt.	Smooth the amplitude envelope using cubic smoothing spline Correct the peak curve using Gaussian estimation and interpolation							
mean absolute error (nm)								
noise(σ)	1st surf.	2nd surf.	1st surf.	2nd surf.	1st surf.	2nd surf.	1st surf.	2nd surf.
flat transparent layer								
0%	0.00	0.00	0.00	0.00	0.00	0.00	0.00	0.00
10%	0.59	4.31	0.92	6.05	0.59	4.19	2.51	4.23
20%	1.67	9.50	2.24	13.01	1.60	8.72	2.50	7.27
time	2.6 s		1.6 s		3.2 s		27.3 s	
wavy transparent layer								
0%	1.02	1.03	1.02	1.02	1.03	1.06	1.02	1.04
10%	3.96	8.68	5.05	12.00	3.79	8.75	3.91	7.53
20%	7.03	17.81	10.06	28.03	7.03	16.74	6.08	14.33
time	2.6 s		1.6 s		3.2 s		27.3 s	

Table 6 Experiment result using pre-filter 3 and different envelope detection techniques (nm)

	I		J		K		L	
Pre-filt.	Suppress the offset: EMD Suppress the noise: Savitzky-Golay filter							
Env. Det.	HT		FSA		TKEO		CWT	
Post-filt.	Smooth the amplitude envelope using cubic smoothing spline Correct the peak curve using Gaussian estimation and interpolation							
mean absolute error (nm)								
noise(σ)	1st surf.	2nd surf.	1st surf.	2nd surf.	1st surf.	2nd surf.	1st surf.	2nd surf.
flat transparent layer								
0%	0.00	0.00	0.00	0.00	0.00	0.00	0.00	0.00
10%	0.56	4.25	0.80	5.06	**0.51**	4.01	1.05	**3.73**
20%	1.66	8.35	1.96	10.45	**1.58**	8.32	1.65	**7.28**
time	5.9 s		4.9 s		6.5 s		30.6 s	
wavy transparent layer								
0%	1..07	1.06	1.02	1.02	1.05	1.03	1.02	1.05
10%	3.71	8.62	4.26	10.41	3.61	8.57	**3.46**	**7.26**
20%	6.89	17.07	9.04	23.18	6.54	16..35	**5.84**	**14.02**
time	5.9 s		4.9 s		6.5 s		30.6 s	

Based on the *mae* in the case of a noiseless signal (σ = 0%), all algorithms perform similarly providing an average value of *mae* = 0 nm for the flat transparent layer and average value of *mae* = 1 nm for the wavy transparent layer. In the presence of noisy data (σ =10% or σ =20%), the *mae* values significantly differ from each other. More precisely the *mae* values of E, F, G, and H in **Table 5** are lower than the *mae* values of algorithms A, B, C, and D in **Table 4**, which indicates that the use of the pre-filter 2 provides a better performance than the pre-filter 1 in terms of precision. Thus, the Savitzky-Golay filter is more effective than the Wiener filter regarding the noise. However, the combination of EMD and the Savitzky-Golay filter (pre-filter 3) provides the best performance for removing the offset and reducing the noise which improves the precision of surface measurement, as shown by the smaller value of *mae* in **Table 6**.

In regard to the main step in the procedure of fringe analysis, i.e. envelope detection process, it can be observed that the TKEO algorithm (called "K") is a competitive algorithm in terms of robustness and computational time compared with the other techniques. TKEO provides better surface extraction than the Hilbert Transform (algorithm called "I") and FSA (algorithm called "J"). In the case of the flat transparent layer, TKEO provides the most precise results for the 1st surface extraction and close to the performance of CWT (called "L") for the buried interface (2nd surface) extraction, having the smallest mean absolute error value as shown in Table 3. For the wavy transparent layer, the most precise measurement is provided by CWT, while the performance of TKEO is closer to CWT than the others. However, TKEO has the advantage of being more compact computationally so TKEO is far better in terms of computational time than CWT. For instance, TKEO taking 6.5 s while CWT taking 30.6 s in the context of a noisy fringe signal with σ = 20%.

Table 7 Improvement of axial sensitivity of measurement obtained using Gaussian fitting (nm)

Pre-filt.	Suppress the offset: EMD Suppress the noise: Savitzky-Golay filter							
Env. Det.	HT		FSA		TKEO		CWT	
Post-filt.	Smooth the amplitude envelope using cubic smoothing spline							
mean absolute error (nm)								
noise(σ)	1st surf.	2nd surf.	1st surf.	2nd surf.	1st surf.	2nd surf.	1st surf.	2nd surf.
flat transparent layer – without interpolation on Gaussian fitting								
0%	10.06	10.06	10.06	10.06	10.06	10.06	10.06	10.06
10%	10.07	10.68	10.07	11.07	10.07	10.62	10.07	10.53
20%	10.12	12.90	10.17	14.28	10.11	12.34	10.16	12.14
flat transparent layer – using interpolation on Gaussian fitting								
0%	0.00	0.00	0.00	0.00	0.00	0.00	0.00	0.00
10%	0.56	4.25	0.80	5.06	0.51	4.01	1.05	3.73
20%	1.66	8.35	1.96	10.45	1.58	8.32	1.65	7.28

On the other hand, we have also evaluated the performance of post-processing that we used in our procedure of fringe analysis. **Table 7** shows the performance comparison between the fringe analysis with and without interpolation on Gaussian fitting. Based on these results, we have demonstrated that the use of interpolation with Gaussian fitting successfully improves the axial sensitivity of the profile measurement. The results provide a significant improvement in terms of precision of surface extraction, as represented by the smaller value of *mae* in **Table 7**, compared without the use of interpolation with Gaussian fitting as post-processing. The value of *mae* obtained for fringe analysis using interpolation with Gaussian fitting being 2 to 3 times smaller, corresponds to a higher precision.

2.5 RESULTS USING MEASUREMENTS ON RESIN LAYER ON SILICON

The performance of the algorithms using real data, i.e. a fringe image XZ measured on a resin layer on Si with (570 x 111) pixels, is shown in Fig. 39(a). This real data was taken on the Leitz-Linnik interference microscope with the following optical parameters: objective x50, numerical aperture 0.85, pixel size of 0.113 µm, and effective average wavelength of 720 nm. The step height of the piezo scanner in order to scan the sample along the optical axis was 90 nm over a dynamic range of 10 µm. A description of the acquisition data of the resin on Si sample obtained by the microscope system is given in Appendix-1: Data of Sample.

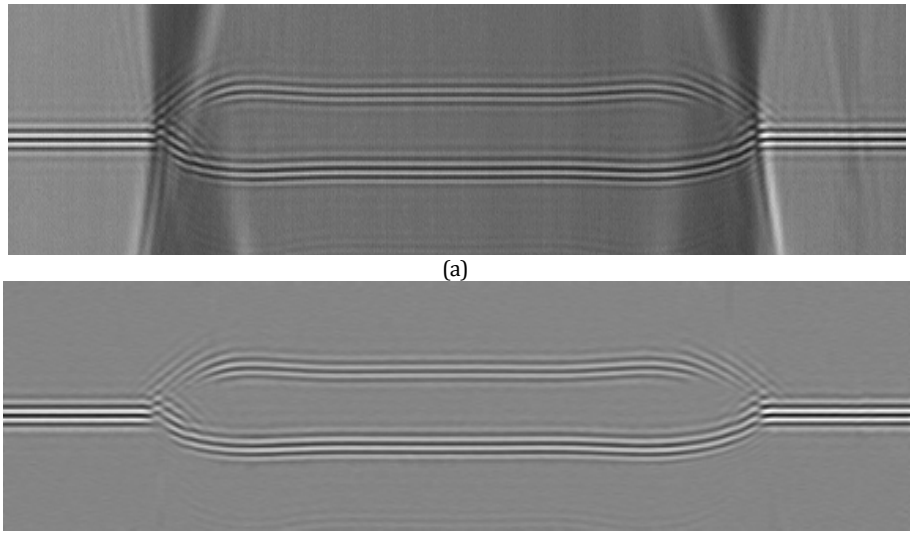

(a)

(b)

Fig. 39 Real fringe measurements on the resin on silicon sample: (a) raw XZ image data and (b) output of pre-filtering of (a) using the EMD-SGolay filter.

The image in Fig. 39(a) clearly shows the presence of large variations in the offset along the optical axis near to the edges of the resin layer due to optical effects. In order to eliminate this background on the fringe image, pre-filtering is performed using the EMD technique combined with the Savitzky-Golay filter, as used in the previous simulation in section 2.3. The results in Fig. 39(b) shows how this pre-filtering approach effectively eliminates the variation in background intensity, while the intensity values of the fringe signals have not been degraded.

Then, the different envelope detection techniques were performed to obtain the fringe envelope of the pre-filtered fringe signals. Fig. 40(a-d) compares the surface profiles extracted by HT, FSA, CWT, and TKEO. It can be observed that the performance of each technique is different, especially concerning the details near to the resin layer edges, which are particularly difficult to measure.

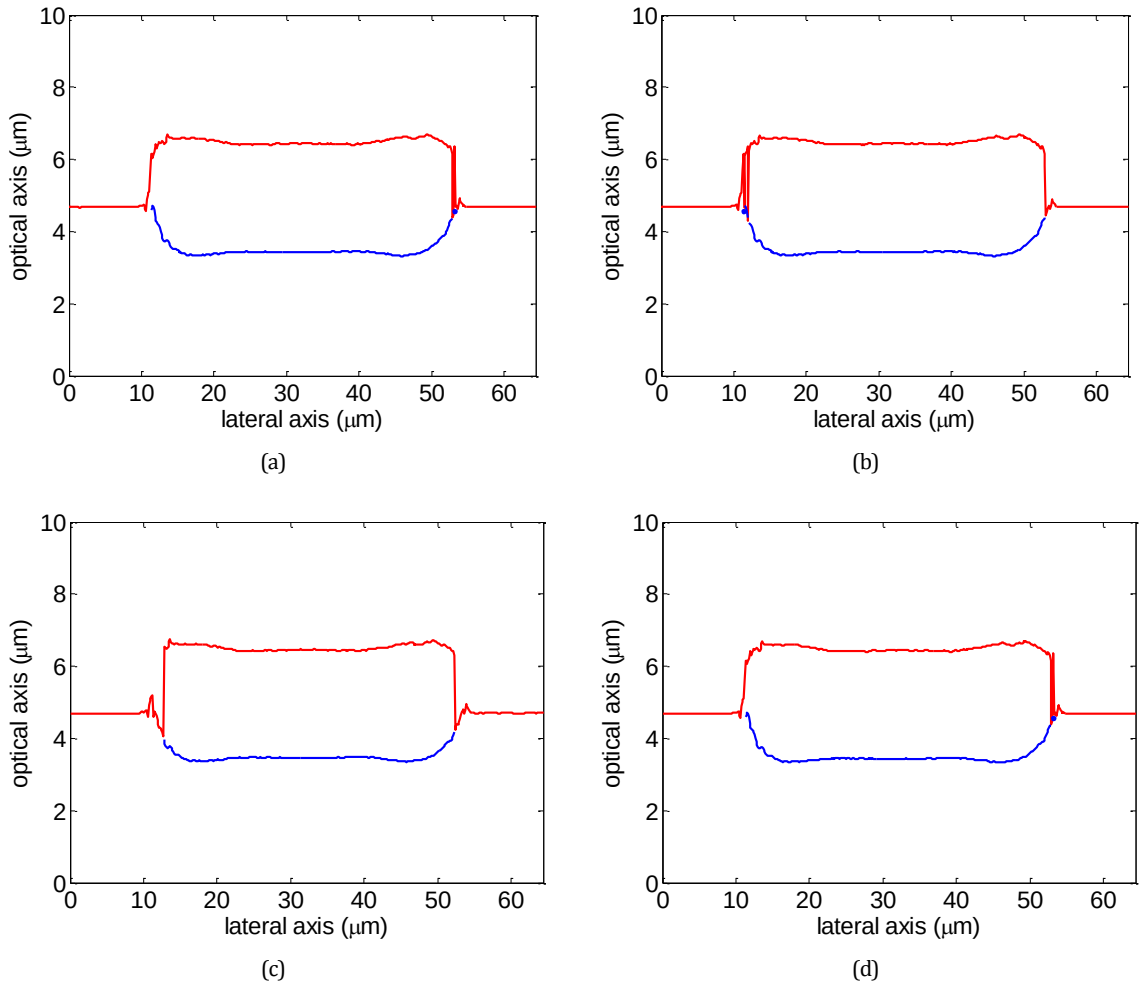

Fig. 40 2D envelope peak detection obtained by: (a) HT, (b) FSA, (c) CWT, (d) TKEO.

For the results of the measurements on this sample, the performance is evaluated by measuring the total (or peak-valley) roughness R_t and arithmetic roughness R_a of the profiles from each algorithm. The maximum height of the profile R_t, is computed as follows [102]:

$$R_t = \left| z_{\max} - z_{\min} \right| \tag{2.13}$$

Where z_{max} (resp. z_{min}) represents the highest (resp. the lowest) peak of the surface profile. R_a is the average deviation of the roughness profile height z_j from a mean line $\bar{z}$ over the evaluation length N [103].

$$R_a = \frac{1}{N} \sum_{j=1}^{N} \left| z_j - \bar{z} \right| \tag{2.14}$$

Then we propose to evaluate four different regions of interest (ROI) of the surface profile (Fig. 41):

- ROI-1 = 0 – 9 µm on the left hand part of the bare silicon substrate.
- ROI-2 = 20 – 45 µm on the air/layer surface.
- ROI-3 = 55 – 64 µm on the right hand part of the bare silicon substrate.
- ROI-4 = 20 – 45 µm on the layer/silicon interface.

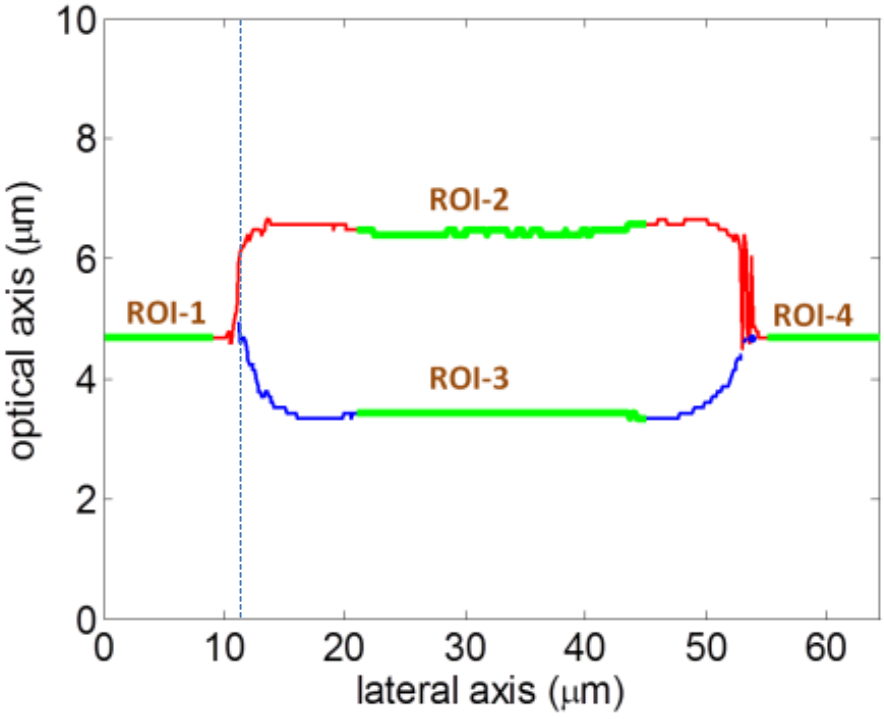

Fig. 41 Region of interest (ROI).

The smaller is the value of this roughness parameter, the better is the performance of the algorithm, in terms of sensitivity. The results comparing the different algorithms are given in **Table 8**.

Based on the results in **Table 8**, for the single surfaces (ROI-1 and ROI-3), all the algorithms show excellent performance, as illustrated by the very small value of R_t = 18.0–27.0 nm and R_a = 2.8–6.2 nm (which is below the sampling step of 90 nm). Then for the transparent surface regions (ROI-2 and ROI-4), the algorithms seem to provide comparable results according to the value of the roughness parameters R_t and R_a, where the maximum difference is 9 nm. The different envelope techniques provide similar performance for the single substrate surface as well as for the transparent layer, since the fringe image is slightly noisy. In accordance with the results of the performance comparison based on synthetic images, the performance of the different envelope detection techniques depends on the SNR in the fringe image, while they are similar for the noiseless fringe images.

Table 8 Experiment result using pre-filter 3 and different envelope detection techniques (nm)

	ROI-1	ROI-2	ROI-3	ROI-4
axis/length	(0 – 9 μm)	(20 – 45 μm)	(55 – 64 μm)	(20 – 45 μm)
	HT			
Rt (nm)	18.0	99.0	27.0	63.0
Ra (nm)	4.8	16.5	5.7	8.8
	FSA			
Rt (nm)	18.0	108.0	27.0	63.0
Ra (nm)	4.6	15.8	5.3	8.6
	CWT			
Rt (nm)	18.0	108.0	27.0	63.0
Ra (nm)	2.9	16.7	6.2	8.2
	TKEO			
Rt (nm)	18.0	108.0	27.0	63.0
Ra (nm)	2.8	17.3	5.9	8.3

However, let us now focus on the surface profile in the region located between 10 and 13 µm, corresponding to the resin step. The results in Fig. 40(a)-(d), highlight the different capabilities of the envelope detection techniques to identify two adjacent peak positions. In such a region, an accurate discrimination of close neighboured positions may be required, in order to discriminate between the two surfaces. Fig. 42(a)-(d) show the fringe envelopes of the fringe signals near to the edge of the resin layer where the thickness of the layer is 0.87 µm at a distance of 11.41 µm (dotted line in Fig. 41) which has been obtained by HT, FSA, CWT, and TKEO. The capability to discriminate between two adjacent surfaces using the envelope detection technique is measured by the contrast value Δi, which represents the difference in the intensity values between the smallest peak intensity and the neighbouring valley intensity (green vertical line). Thus, the higher is the contrast value Δi, the better is the performance of the envelope detection technique in the presence of two adjacent peaks.

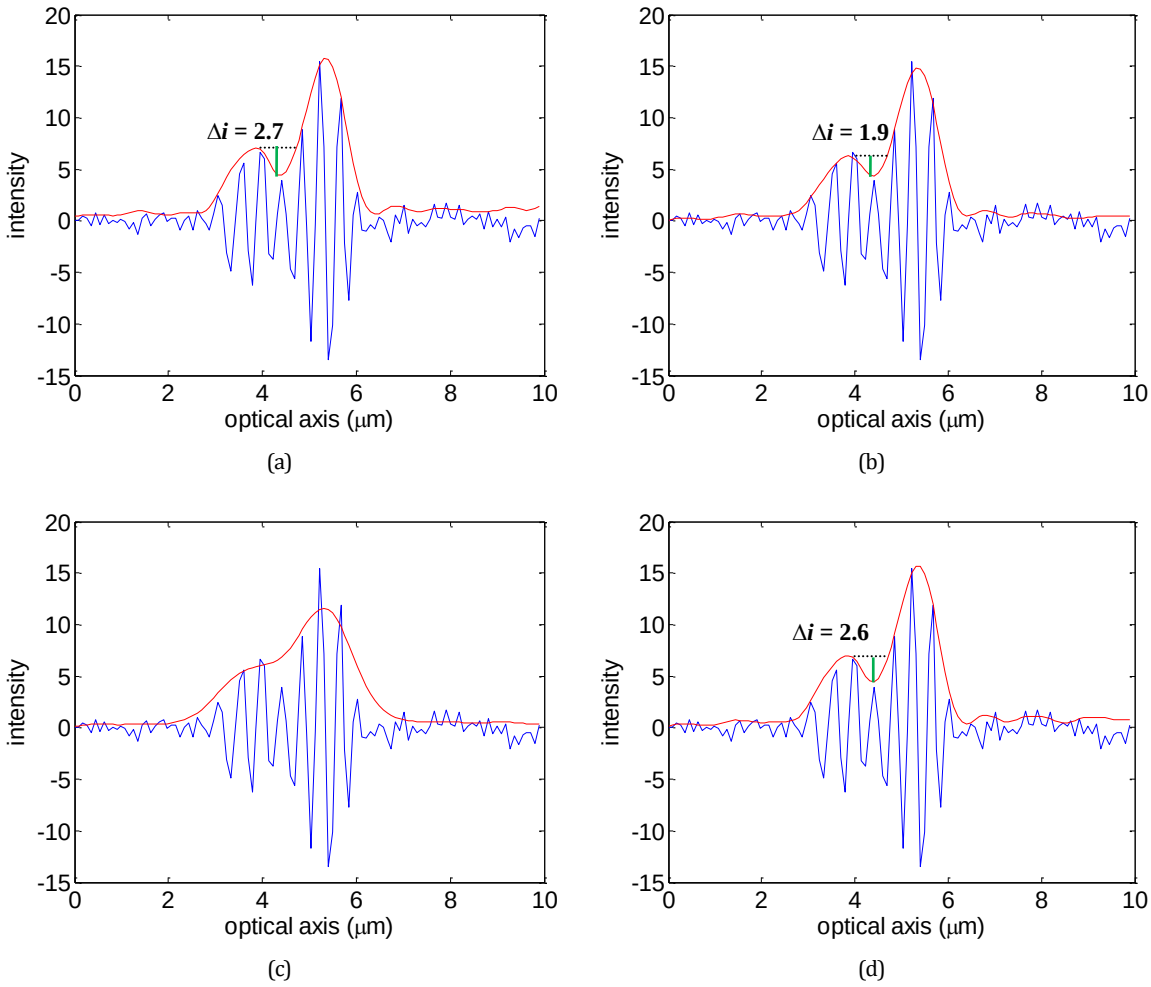

Fig. 42 1D fringe envelopes obtained by: (a) HT, (b) FSA, (c) CWT, and (d) TKEO at x = 11.41 µm near the resin edge where the two surfaces are closer together.

The best performance is provided by HT (Fig. 42(a)) and TKEO (Fig. 42(d) with nearly similar values of 2.7 and 2.6 respectively. The value for FSA (Fig. 42(b)) is slightly worse, at 1.9, but nonetheless capable of discriminating the two surfaces. The parameter ΔI derived from the CWT approach, (see Fig. 42(c)) cannot be calculated since it fails to distinguish between the envelopes.

In this work, the CWT algorithm actually used is not able to distinguish between two successive fringe envelopes, due to the non-optimal use of the CWT. Further work involving the testing of the trade-off between space and frequency to find the optimal value would most likely have made it possible to allow this distinction, but the wavelets technique was considered not to be central to the actual work in hand.

The altitude (Z axis) measurement of resin on SI

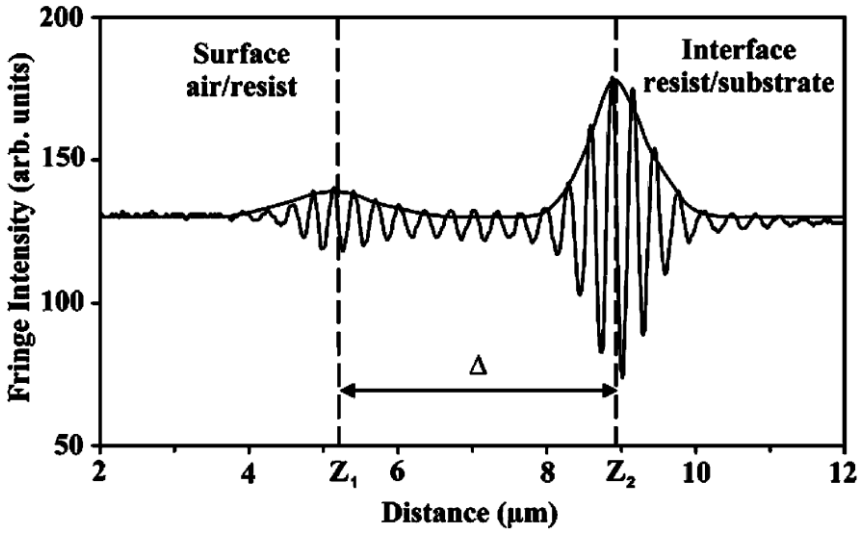

Fig. 43 Typical fringe signals from a sample of a resin layer on Silicon

Fig. 43 illustrates a typical axial intensity profile of fringe signals on the sample of a layer of resin on Si. Two signals are observed, one due to the upper air surface and the other due to the buried substrate interface. The fringes corresponding to the air surface have a lower contrast than that of the fringes corresponding to the buried interface since the reflectivity of the silicon is higher than that of the resin. By measuring the distance Δ separating the peaks of the two envelopes, the thickness d of the transparent layer at that

point (X,Y) can be measured. If the sample displacement *d* along the optical axis (Z) and the refractive index *n* of the resin is known, the thickness *d* is given by Eq.(2.15):

$$d = \frac{\Delta}{n} \tag{2.15}$$

For each point (X,Y), the identification of the position of the first envelope peak (Fig. 43) gives the posiiton of the surface (Z_1) and the peak of the second envelope gives the positon along Z of the interface (Z_2). If this procedure is carried out for each point, the (XZ) profile of the corresponding points on the surface and the buried interface can be made. A correction to the position of the interface profile needs to be performed due to the value of the refractive index of the resist layer (n = 1.644) being greater than unity, the corrected value of Z being:

$$Z = Z_1 - \frac{Z_1 - Z_2}{n} \tag{2.16}$$

Approximate empirical expression of the refractive index

The Cauchy formulas are valid for media whose absorption bands are all in the ultraviolet. The resin verifies this condition which favored this choice of formulas:

$$n = A + \frac{B}{\lambda^2} + \frac{C}{\lambda^4} \tag{2.17}$$

Resin is a transparent material in the visible region: it is therefore far from the absorption bands, which allows on the one hand, to consider that its refractive index is real and on the other hand, to make a limited development based on the wavelength.

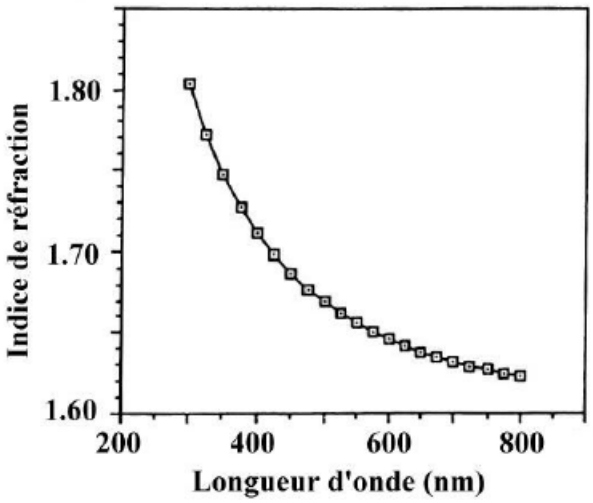

Fig. 44 The dispersion curve corresponding to the resin layer

In these areas of transparency, the refractive index follows a function that decreases with wavelength (Fig. 44), or, which amounts to the same, a function that increases with frequency. Such a law of dispersion is called the law of normal dispersion. Media used in optics, which are obviously transparent in the visible, have larger indices of refraction in the blue than in the red: $n_{blue} > n_{red}$.

The dispersion curve (Fig. 44) and the Cauchy equation (Eq.2.17) describe how the refractive index of the photosensitive resin changes as a function of the wavelength of the light incident on the film. The Cauchy equation is given by:

$$n(\lambda) = A + \frac{B}{\lambda^2} + \frac{C}{\lambda^4} \qquad \textbf{(2.18)}$$

where λ corresponds to the wavelength, n corresponds to the refractive index, while A, B, C represent the coefficients. By performing the fitting using the data provided in Fig. 44, the coefficient values for resin can be obtained:

B = 1.5935
C = 1.8854 x10^6
D = 4.1211 x10^{10}

Thus, the refractive index of resin for λ = 610 nm is calculated as n = 1.644. By using this refactive index value and the Eq.(2.16), the altitude (Z axis) of the sample of resin on Si can be obtained, as illustrated by Fig. 45.

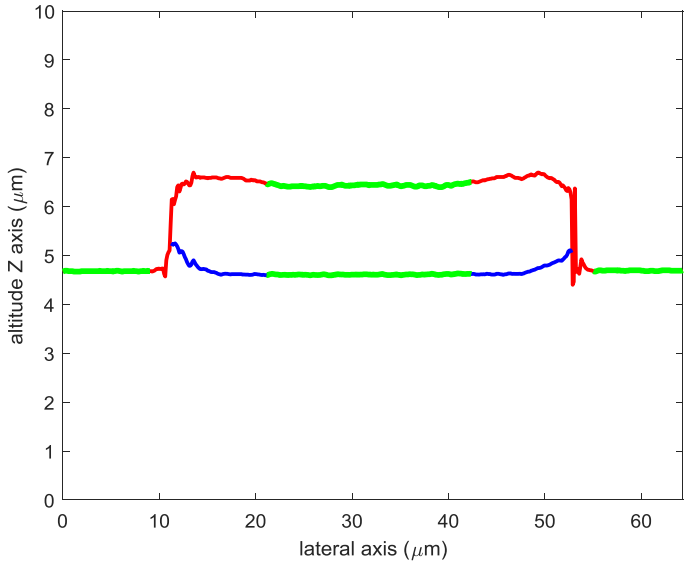

Fig. 45 The altitude Z (axis) of resin on Si

2.6 CONCLUSION

A study has been made on the comparison of different pre-processing and different envelope detection techniques in CSI using synthetic images and real measurements of different types of thin transparent films, resulting in the following conclusions:

- The combination of EMD and Savitzky-Golay filters provides the best performance for suppressing noise and the offset component while maintaining the original signal intensity.
- The CWT and TKEO are both competitive for providing surface extraction:
  - TKEO is slightly better in terms of computational time.
  - CWT is slightly better for the wavy transparent layer, but TKEO is quicker in terms of computational time.
  - In this work, TKEO is more competitive than CWT for resolving two close layers although this may be due to a non optimal use of the CWT used. The ability of CWT to allow different space frequency trade-offs that provides the opportunity to prioritize either space resolution or frequency resolution could lead to distinguishing between closely spaced layers.
- The use of an interpolation method with Gaussian fitting as the post-processing has been successfully used to improve the the axial sensitivity of the measurement, with the error rate (*mae*) being from 2 to 3 times smaller than if it was not used, corresponding to a higher precision.

2.7 RÉSUMÉ DU CHAPITRE 2

Dans ce chapitre, nous décrivons l'opérateur d'énergie Teager-Kaiser que nous utilisons comme algorithme multidimensionnel proposé (1D, 2D, 3D) pour la détection d'enveloppe dans la CSI. Ensuite, l'étude de la comparaison des performances des différentes techniques de pré-filtrage et de détection d'enveloppe dans le traitement des signaux de franges est décrite. A titre de comparaison, des résultats utilisant les algorithmes sont présentés sur le signal de frange synthétique et sur des données réelles, c'est-à-dire l'échantillon de résine sur silicium. En outre, une étude de sélection de l'ondelette mère sur la transformée en ondelettes continue est présentée dans son utilisation pour l'obtention de l'enveloppe de franges.

Afin de supprimer le décalage et réduire le bruit, nous comparons dans ce chapitre trois algorithmes différents qui combinent la technique dérivée / EMD et le filtre de

débruitage (Savitzky-Golay / Wiener). Les algorithmes correspondants sont référencés avec les noms suivants:

- Pré-filtre 1: combinaison de dérivée et filtre de Wiener,
- Pré-filtre 2: combinaison de dérivée et filtre Savitzky-Golay,
- Pré-filtre 3: combinaison d'EMD et filtre Savitzky-Golay.

Pour l'évaluation des performances de différents pré-filtres ci-dessus, nous effectuons la simulation en les effectuant sur un signal de franges synthétiques, avec un pas d'échantillonnage de 40 nm. Un décalage non linéaire additif et un bruit gaussien sont ajoutés aux données synthétiques (20%), ce qui signifie que le carré moyen (rms) du bruit gaussien ajouté est égal à 20% de l'amplitude maximale du signal de frange de la seconde couche. Sur la base de la simulation, nous observons que le préfiltre 3 utilisant la combinaison d'EMD et Savitzky-Golay fournit le meilleur résultat que d'autres afin de supprimer le décalage et le bruit, en particulier dans le maintien de l'amplitude des franges.

Une autre simulation a été réalisée afin d'évaluer notre procédure d'analyse des franges, en utilisant une combinaison de pré-filtrage différent et de détection d'enveloppe différente. En ce qui concerne l'étape principale de notre procédure, à savoir la détection de l'enveloppe des franges, nous observons que le TKEO est un algorithme compétitif en termes de robustesse et de temps de calcul. TKEO fournit une meilleure extraction de surface que la transformée de Hilbert et FSA. Dans le cas d'une couche transparente plate, TKEO fournit les résultats les plus précis pour l'extraction de la surface (1^e surface) et plus proche de la performance de CWT pour l'extraction de l'interface enterrée (2^e surface), donnant la valeur la plus petite d'erreur absolue moyenne. Pour la couche transparente ondulée, la mesure la plus précise est fournie par CWT, tandis que la performance de TKEO est la plus proche de CWT que les autres. Cependant, TKEO a l'avantage d'être plus compact en termes computationnels et ainsi bien meilleur en termes de temps de calcul que le CWT. Par exemple, TKEO prend 6,5 s tandis que CWT prend 30,6 s dans le contexte d'un signal de frange bruyant avec $\sigma = 20\%$.

D'autre part, nous avons également évalué les performances de post-traitement que nous avons utilisées dans notre procédure d'analyse des franges. Sur la base des résultats, nous avons démontré que l'utilisation de l'interpolation sur l'ajustement gaussien améliore la sensibilité axiale de la mesure du profil. Les résultats donnent une amélioration

significative en termes de précision de l'extraction de surface, comme représenté par la plus petite valeur de *mae*, en tant que critère de comparaison, lorsque nous n'avons pas effectué l'interpolation sur l'ajustement gaussien comme post-traitement. La valeur de *mae* de l'analyse de frange en utilisant une interpolation sur un ajustement gaussien est 2 à 3 fois plus petit, ce qui correspond à une plus grande précision.

Ensuite, les algorithmes sont réalisés sur des données réelles, c'est-à-dire d'une couche de résine sur Si. L'interférogramme venant de l'échantillon montre clairement la présence de grandes variations du décalage le long de l'axe optique près des bords de la couche de résine en raison d'effets optiques. Afin d'éliminer ce fond sur l'image des franges, le pré-filtrage est réalisé en utilisant la technique EMD en combinaison avec le filtre Savitzky-Golay. Ensuite, les différentes techniques de détection d'enveloppe ont été réalisées pour obtenir l'enveloppe de frange des signaux de franges pré-filtrés. Basé sur les résultats, on peut observer que la performance de chaque technique est différente, notamment en ce qui concerne les détails proches des bords de la couche de résine, particulièrement difficiles à mesurer. Dans la région des bords de la couche de résine, les meilleures performances sont fournies par HT et TKEO que par les autres pour distinguer clairement entre deux couches proches.

Chapter 3. 2D FRINGE PROCESSING IN CSI

In this chapter, we study the performance of 2D fringe processing in CSI developed based on the two dimensional Teager Kaiser Energy Operator [104] on a transparent film sample containing defects. A robust fringe analysis is needed for improved characterization of the transparent polymer film, i.e. a Mylar, which is complex and contains buried layers with low contrast. The algorithms are compared to the classical two dimensional Hilbert Transform [62],[105],[106],[107] and the 1D Fringe Processing using the well-known FSA algorithm. In addition, we also report the study of the developed algorithm for the detection of the layer number in multiple layers using Gaussian curve fitting.

But first we discuss the notion of the independence of neighboring pixels, which is an assumption made in the CSI technique that leads to the ability to measure larger steps than in PSM. But in reality, as we shall see, there is a certain dependence between pixels due to the experimental conditions, which motivates the use of 2D and 3D processing.

The dependence of neighbouring pixels in PSM processing

As mentioned in chapter 1, the technique of PSM is limited to the measurement of small surface roughness or sample surfaces that are assumed to present height differences of less than λ/2 between neighbouring image points, as illustrated in Fig. 46(a). In the case of this surface type, representing a small step, PSM can be used to measure the height of each point independently of its neighbours.

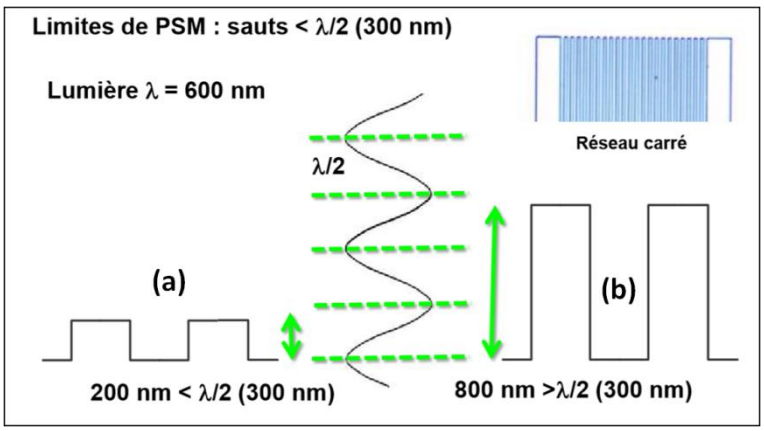

Fig. 46 The limitation of the PSM technique in height measurement

But in the case of a sample surface having a deeper smooth and continuous surface, for instance in the case of a spherical surface such as a microlens (Fig. 47), it is well known that the 2π phase discontinuities can be corrected as shown in Fig. 48. The use of phase unwrapping in the PSM technique therefore takes into account the neighbourhood values of pixels. This means that measurements using the PSM technique in this case are not independent of their neighbours.

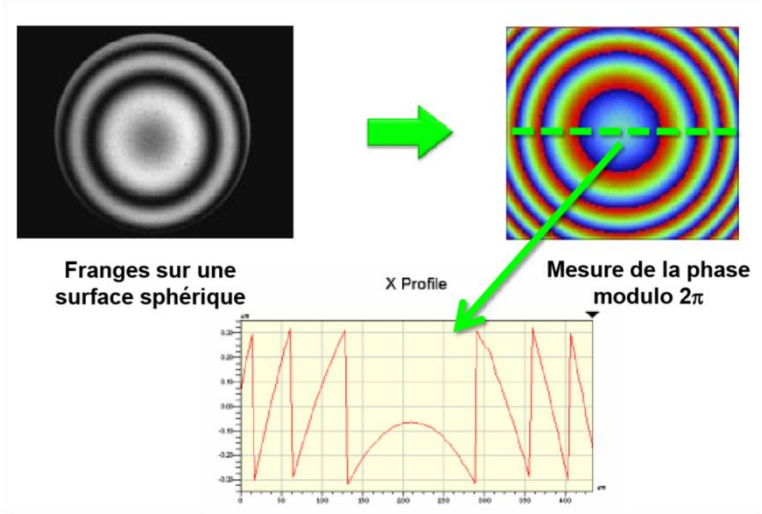

Fig. 47 The measurement of a spherical surface using the PSM technique resulting in phase discontinuities

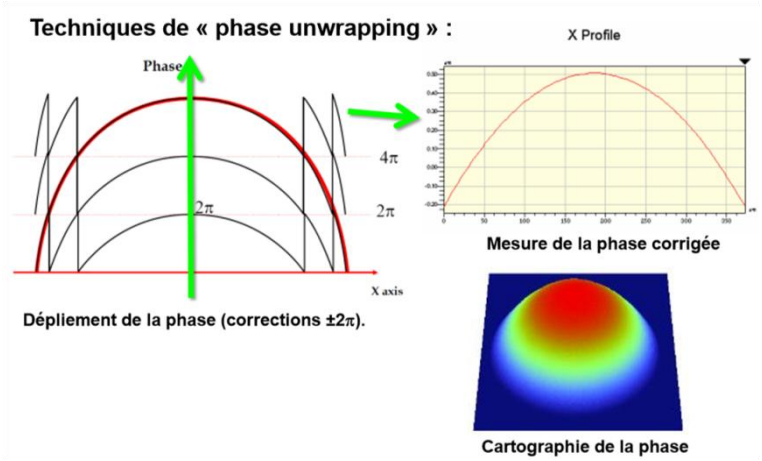

Fig. 48 The technique of phase unwrapping in PSM to measure deeper structures

But in the case of sample surfaces having a step height difference of more than λ/2 between neighboring pixels, the PSM technique is unable to measure the height due to the ambiguity of the number of 2π values for the correction as illustrated in Fig. 46(b).

The dependence of neighbouring pixels in CSI processing

In the history of the development of interference microscopy, white light interferometry (CSI) was therefore proposed as a solution to measuring large step heights. Making the assumption that CSI allows the measurement of the absolute height of a surface at each point independently of its neighbours by localizing each point along Z in relation to the scanning performed by the piezoelectric actuator, in principle any step height can be measured. This is the reason why we can categorize this signal processing as 1D fringe signal processing.

However, in practice, in an experimental system, the measurement at a given pixel is not absolutely independent of its neighbours for several reasons. Firstly, we can consider the effects of diffraction at a step or on details of a very rough surface, where we need to consider the 3D PSF (Point Spread Function) as sampled by the individual photodiodes on the camera sensor. The image in Fig. 49 illustrates the central Airy spot of a point source at infinity being correctly sampled by the camera according to the Nyquist criterion at twice the signal spatial frequency, a typical condition for microscope imaging. This means that there is a link between neighbouring pixels and that the measurement of the height of a surface at each point is not absolutely independently of its neighbours.

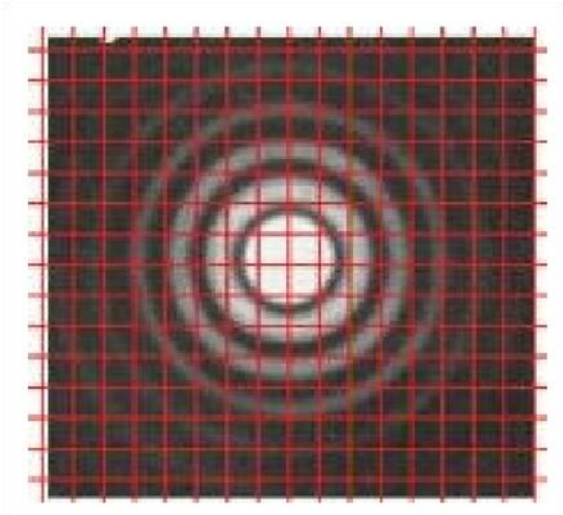

Fig. 49 The illustration of airy spot on the pixels

The neighbourhood link is also present in the measurement of certain step heights, as shown in Fig. 50 where there is over and undershoot near to the step instead of a square step when the height is close to the coherence length of the light illumination [75], [76]. This is known as the “batwing” effect on the edge of the step caused by the mixing

of signals from the top and bottom of the step, demonstrating again the dependence of neighboring pixels.

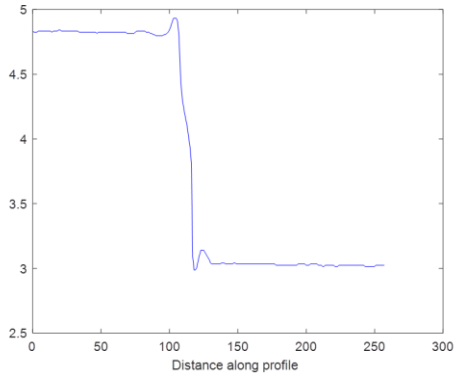

Fig. 50 The batwing effect on the measurement of a step

A third reason is that for most surfaces where there are no holes present, it can be assumed to be continuous laterally, whatever the roughness. The measurement of the surface roughness is always an approximation of the real surface topography, limited by the various parameters of the measurement system, so that the assumption needs to be made that a neighbouring point is linked to its neighbour.

In the present work, we therefore propose performing 2D and 3D fringe processing that takes into account the spatial neighbourhood, so that the independence of measurements between neighboring pixels is therefore lost, at least on a small scale of several pixels. Taking into account diffraction, step effects and the assumption that the surface is locally continuous justifies the use of 2D/3D algorithms and their assumptions (that neighbouring pixels are linked) and the estimation of the local slope.

3.1 2D FRINGE ENVELOPE DETECTION

3.1.1 Analytic signal-Hilbert Transform (HT2D)

The one dimensional form of the Hilbert transform of a signal is given by:

$$s_H(x) = s(x) * \frac{1}{\pi x} = \frac{1}{\pi} \int_{-\infty}^{\infty} \frac{s(u)}{x-u} du \qquad \textbf{(3.1)}$$

This Hilbert transform is often used in analytic signals and is useful for the purpose of amplitude demodulation [108],[109]. In particular, for obtaining the analytic signal, the

negative frequency component of the signal is suppressed [110]. The analytic signal $s_A(x)$ is defined as:

$$s_A(x) = s(x) + is_H(x) = A(x)\exp\left[i\psi(x)\right] \tag{3.2}$$

In the frequency domain, the analytic signal corresponds to:

$$S_A(\omega) = \left[1 + sign(\omega)\right]S(\omega) \tag{3.3}$$

Based on Equation (17), it can be seen that we can obtain the instantaneous amplitude (envelope) of a real signal $s(t)$ from the absolute value of $s_A(t)$. Meanwhile for the 2D signal, the technique is extended by a basic approach of the 2D Hilbert Transform $H\{s(x,y)\}$:

$$s_H(x,y) = s(x,y) * \frac{1}{\pi^2 xy} = \frac{1}{\pi^2}\int_{-\infty}^{\infty}\frac{s(u,v)}{(x-u)(x-v)}dudv \tag{3.4}$$

which leads to the 2D analytic signal $s_A(x,y)$, which is given by:

$$s_A(x,y) = s(x,y) + is_H(x,y) \tag{3.5}$$

In the frequency domain, the 2D analytic signal $s_A(x,y)$ corresponds to:

$$S_A(\varsigma,\eta) = \left[1 - i\ sign(\varsigma)sign(\eta)\right]S(\varsigma,\eta) \tag{3.6}$$

Notice with this equation, that we can understand that Eq. (3.6) could be obtained by multiplying the transformed image and the appropriate mask in the frequency domain. If the 2D analytical signal $s_A(x,y) = A(x,y)\exp\left[i\varphi(x,y)\right]$ has been constructed, the phase and the amplitude of the signal $s(x,y)$ could be obtained based on the following equation [106]:

$$\nabla\varphi = \mathrm{Re}\left[\frac{\nabla s_A(x,y)}{i\ s_A(x,y)}\right] \tag{3.7}$$

$$A(x,y) = \left|s_A(x,y)\right| \tag{3.8}$$

3.1.2 Teager Kaiser Energy Operator (TKEO2D)

For local energy tracking measurement, the Teager-Kaiser Energy Operator (TKEO) is well known in digital signal processing, particularly on oscillatory signals due to the fact that the operator is simple to implement and is computationally very efficient. In the one

dimensional and continuous version of the Teager Kaiser Energy Operator, the energy of a signal $x(t)$ is defined by the following equation [104]:

$$\psi\left[s(t)\right]=\left[s^{(1)}(t)\right]^2-s^{(0)}(t)s^{(2)}(t) \tag{3.9}$$

When applied to a signal $s(t) = a(t)\cos(\omega t)$, the TKEO formula yields: $a(t)^2\omega(t)^2$. It is assumed that the instantaneous amplitude $a(t)$ and the instantaneous frequency $\omega(t)$ do not vary too much or too fast with respect to the average value of $\omega(t)$. Given the simplicity of the TKEO (and the extended versions of TKEO) and the broad applicability of the AM-FM model in signal processing and communication systems, this operator leads to the Energy Separation Algorithm (ESA) defined by [111]:

$$\omega(t)\approx\sqrt{\frac{\psi\left[\dot{x}(t)\right]}{\psi\left[x(t)\right]}};\qquad \left|a(t)\right|\approx\frac{\psi\left[x(t)\right]}{\sqrt{\psi\left[\dot{x}(t)\right]}} \tag{3.10}$$

The TK operator, which is usually called as TKEO limited to the second order, has been extended into higher-order differential operators (DEOs) [112]:

$$\psi_k\left[x(t)\right]=x^{(1)}(t)x^{(k-1)}(t)-x^{(0)}(t)x^{(k)}(t) \tag{3.11}$$

Practically, the operators (DEOs) have been implemented to the 2D case of fringe signals in the article [40],[113] in order to improve the fringe envelope extraction to detect the surface height of the sample.

The generalization of the higher order differential operators (DEOs) is as follows [114]:

$$\psi_{p,q,m,l}\left[x(t)\right]=x^{(p)}(t)x^{(q)}(t)-x^{(m)}(t)x^{(l)}(t) \tag{3.12}$$

with integers $p+q = m+l$, $(p,q) \neq (m,l)$. For (p=1, q=1, m=0, l=2), the generalized operator is reduced to the TK operator. Finally, all these operators can be extended to the multidimensional case as k^{th}-order tensors H (H stands for higher) [104]:

$$\psi_{H_{k,p,m}}\left[s(\mathrm{u})\right]=\frac{\mathrm{d}^m s}{\mathrm{du}^m}\otimes\left(\frac{\mathrm{d}^l s}{\mathrm{du}^l}\right)^T-\frac{\mathrm{d}^p s}{\mathrm{du}^p}\otimes\left(\frac{\mathrm{d}^q s}{\mathrm{du}^q}\right)^T \tag{3.13}$$

with $k=p+q=m+l$, $(m,l)=(p,q)$. Vector $\mathrm{u} = (x_1\ x_2\ \ldots\ x_n)$ is n-dimensional, $s(\mathrm{u})$ is a multidimensional signal, and $\otimes$ means the Kronecker product. The second-order operator (k=2) provides the directional TKEO, which extends one dimensional classical TKEO using directional derivatives along any vector v as follows:

$$\Phi_{2,\mathrm{v}}\left[s(\mathrm{u})\right]=\mathrm{v}^{T}\psi_{2}\left[s(\mathrm{u})\right]^{T}\mathrm{v}=\left(\frac{\partial s}{\partial \mathrm{v}}(\mathrm{u})\right)^{2}-s(\mathrm{u})\frac{\partial^{2}s}{\partial \mathrm{v}^{2}}(\mathrm{u}) \qquad \textbf{(3.14)}$$

The Eq. (3.14) can be applied for the AM-FM signal demodulation. For any *n*-dimensional local AM-FM signal defined by:

$$s(\mathrm{u})=A(\mathrm{u})\cos\left(\phi(\mathrm{u})\right) \qquad \textbf{(3.15)}$$

We have the following approximation [104]:

$$\Phi_{2,\mathrm{v}}\left[s(\mathrm{u})\right]=A(\mathrm{u})^{2}\left(\frac{\partial\phi}{\partial \mathrm{v}}(\mathrm{u})\right)^{2}=A(\mathrm{u})^{2}\left(\mathrm{w}(\mathrm{u})^{T}\mathrm{v}\right)^{2} \qquad \textbf{(3.16)}$$

w is the local frequency w = $(w_1,w_2,...,w_n)^T$, which is the gradient of the phase $\nabla\phi$, where $\nabla\phi=\mathrm{w}(\mathrm{u})\simeq\mathrm{w}$, when the local amplitude A(u) does not vary too fast compared to the carrier [115]. The vector v is a normalized vector v = $(v_1, v_2,...,v_n)^T$. The choose of the directional derivative has been discussed in article [116].

It is then possible to compute the instantaneous envelope:

$$A(\mathrm{u})^{2}=\frac{\left|\Phi_{2,\mathrm{v}}^{2}\left[s(\mathrm{u})\right]\right|}{\left|\Phi_{2,\mathrm{v}}^{2}\left[\frac{\partial s(\mathrm{u})}{\partial \mathrm{v}}\right]\right|}=\frac{\left|\Phi_{2,\mathrm{v}}^{2}\left[s(\mathrm{u})\right]\right|}{\left|\Phi_{4,\mathrm{v}}^{2}\left[s(\mathrm{u})\right]\right|} \qquad \textbf{(3.17)}$$

3.2 THE ROBUSTNESS EVALUATION OF 2DTKEO AND 2DHT

To evaluate the robustness of 2DTKEO [104] and 2DHT [62],[105],[106],[107], it has been applied respectively to a noiseless signal (σ=0%) and noisy signals (σ=10% and σ=20%) using a synthetic signal as shown in Fig. 51. In order to improve the axial sensitivity and precision regarding the peak detection, cubic spline smoothing followed by a Gaussian interpolation has been used, which is adapted to the physical model of the envelope. Fig. 52 and Fig. 53 show the results obtained.

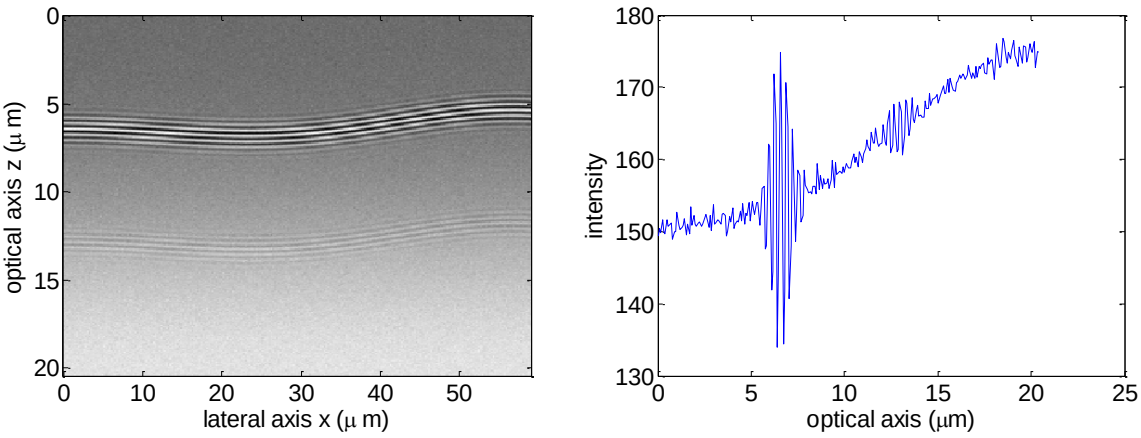

(a) (b)

Fig. 51 (a) Synthetic XZ fringe image 256 x 256 pixel and (b) profile of fringe signal along the optical axis Z.

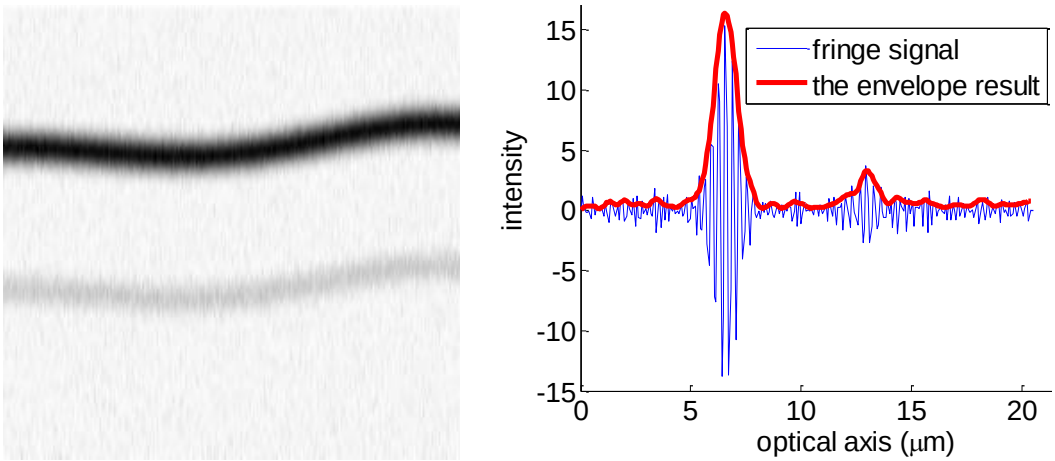

(a) (b)

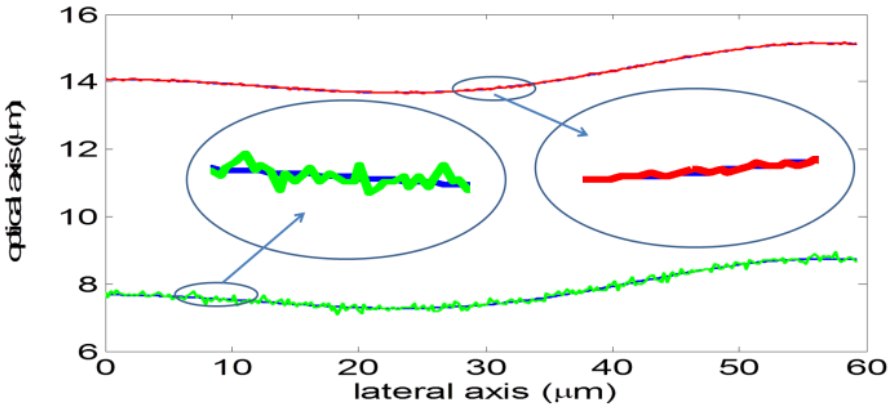

(c)

Fig. 52 Analysis of a noisy synthetic fringe signal (σ=20%): (a) 2D and (b) 1D fringe envelope obtained by Z-scan technique (FSA), (c) surface profile.

Based on the surface profiles shown in Fig. 52(c) and Fig. 53(c), the qualitative performance comparison can be observed between the XZ-scan technique using 2DTKEO and the Z-scan technique using the FSA algorithm**.** In the figures the red line, green line and blue line represent respectively the top surface extraction (1st surface), the bottom surface extraction (2nd surface), and the reference surface. It can be observed that the XZ-scan technique (2DTKEO) provides better surface extraction than the FSA both on the top and bottom surfaces. In addition, the mean absolute error rate (*mae*) has been computed, in relation to the reference surface, as shown in **Table 9**.

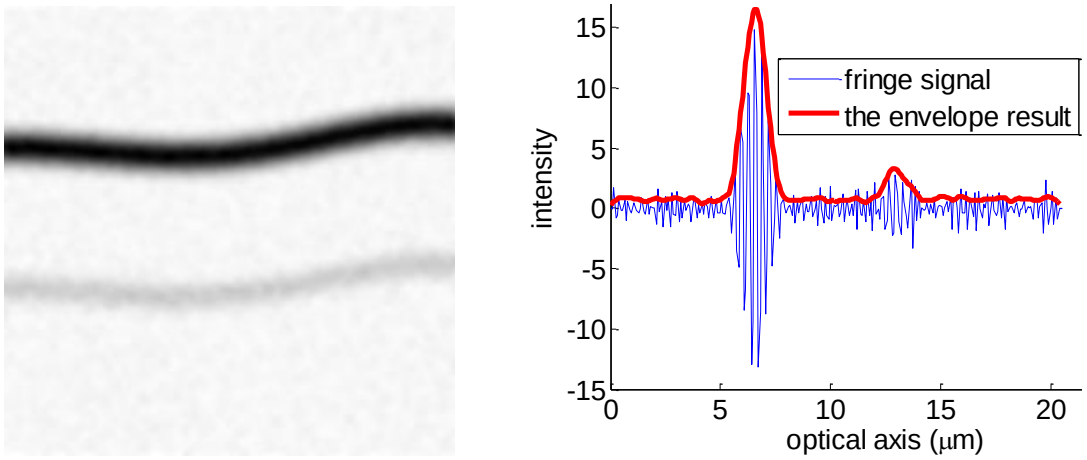

(a) (b)

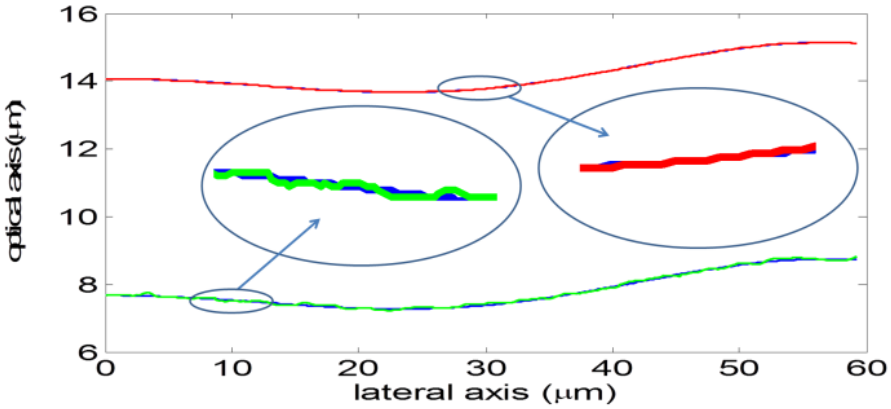

(c)

Fig. 53 Analysis of a noisy synthetic fringe signal (σ=20%): (a) 2D and (b) 1D fringe envelope obtained by XZ-scan technique (2DTKEO), (c) surface profile.

Table 9 Mean absolute error (mae) of surface extraction corresponding to synthetic fringe image

Methods	noise=0%		noise=10%		noise=20%	
	Surf1	Surf2	Surf1	Surf2	Surf1	Surf2
	mean absolute error (nm)					
1DFSA	2.1	2.1	6.0	27.9	11.5	57.3
2DTKEO	2.1	2.1	**3.2**	**12.3**	**5.1**	**25.2**
2DHT	2.1	2.1	3.2	13.0	5.2	28.5

Comparing the results in **Table 9**, both the Z-scan technique (FSA) and XZ-scan technique (2DTKEO and 2DHT) are similar in terms of performance in the case of the noiseless signal (σ=0%) providing an average value of *mae* = 2.1 nm. Meanwhile for a noisy signal (σ=10% and σ=20%), the XZ-scan technique is generally more robust than the FSA. Moreover, it can also be observed that the use of 2DTKEO is as competitive as classical 2DHT in terms of performance for a noisy signal. The error rate value (*mae*) of surface measurement extracted by both of 2DTKEO and the 2DHT is nearly similar for a noisy signal (σ = 10% and σ = 20%). The reason that 2DTKEO is more robust than the FSA algorithm is due to the use of a 2D gradient smooth by two-dimensional Gaussian filter.

3.3 DETECTION OF THE LAYERS NUMBER ON A TRANSPARENT LAYERS

One of the benefits of CSI is the ability to separate multiple reflections from a transparent layer structure. Fig. 54 shows the scheme of the interferogram construction on a transparent layer using CSI. As illustrated in Fig. 54, we found that there are three clearly identifiable modulation envelopes corresponding to surface reflections from the transparent layer boundaries (top surface, rear surface, and structure). In the case of a transparent layer as shown in the figure, the interferogram has two conditions: (i) an interferogram has two modulation envelopes corresponding to the top and rear surfaces; (ii) an interferogram has more than two modulation envelopes due to the presence of the structures. In this case of the sample with multiple layers, an adaptive algorithm in fringe signal processing is required to identify the layers number on an interferogram.

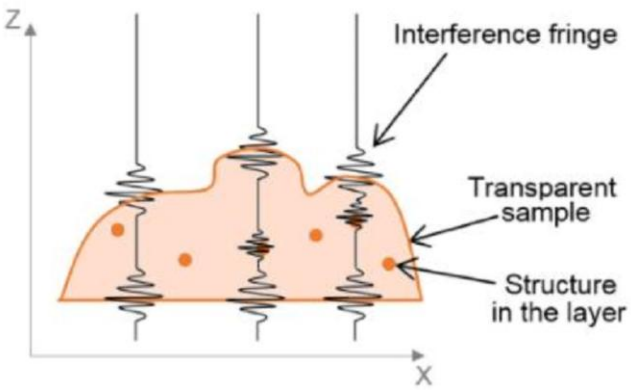

Fig. 54 Scheme of the interferogram construction on a transparent layer using CSI [83]

In this work, in order to find the layer number on an interferogram, we perform threshold filtering using Gaussian curve fitting on the fringe envelope, which is applied after the step of envelope detection. The Gaussian curve fitting is performed on the number of points around the identifiable local maximum on the fringe envelope during the peak detection process. Through this Gaussian curve fitting, we can obtain the characteristics of each of the Gaussian functions, such as its height, position, and width. Fig. 55(a) shows how this procedure has been tested on synthetic data which contains multiple Gaussian functions. As illustrated in Fig. 55(a), by using this procedure, we obtain the four identifiable Gaussian functions as the candidates. In order to identify the number of Gaussian function which indicates the different layers of the sample, we make use of the height and width obtained using Gaussian curve fitting to filter the Gaussian functions which are not suitable for the characteristics of the Gaussian functions that we seek to define. For example, we seek the Gaussian function with a width > 10 and a height (amplitude) > 2. By defining this threshold value of the height and width, then we obtain only two Gaussian functions which are suitable (red colour), as shown in Fig. 55(b). The number of Gaussian functions (envelopes) on an interferogram indicates the number of layers in the sample.

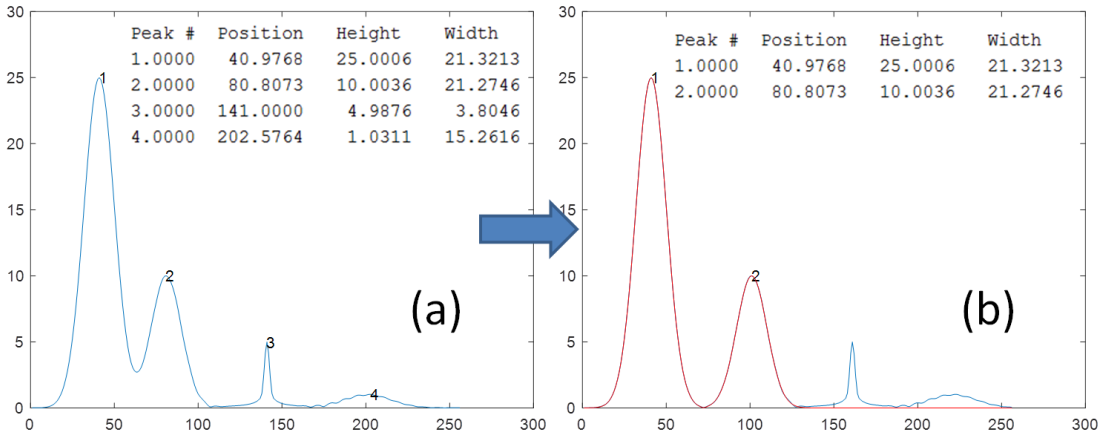

Fig. 55 Identify the number of Gaussian function using curve fitting

For further evaluation, we have tested the algorithm with the detection of the layer number on a synthetic fringe signal of transparent layers and real data, i.e. a transparent polymer film.

a. Simulation results on synthetic data

In the simulation, the synthetic signal we have used to test the algorithm is based locally on the general model expressed by equation (1) along the optical axis Z, with a 80 nm sampling step, for each lateral position X. The resulting synthetic signal is shown in Fig. 56. An additive offset and Gaussian noise (15%) is added onto this synthetic data which commonly appear in the fringe signal during the acquisition process. The value of 15% means that the root mean square (rms) of the added Gaussian noise is 15% of the maximum amplitude of the fringe signal of rear surface.

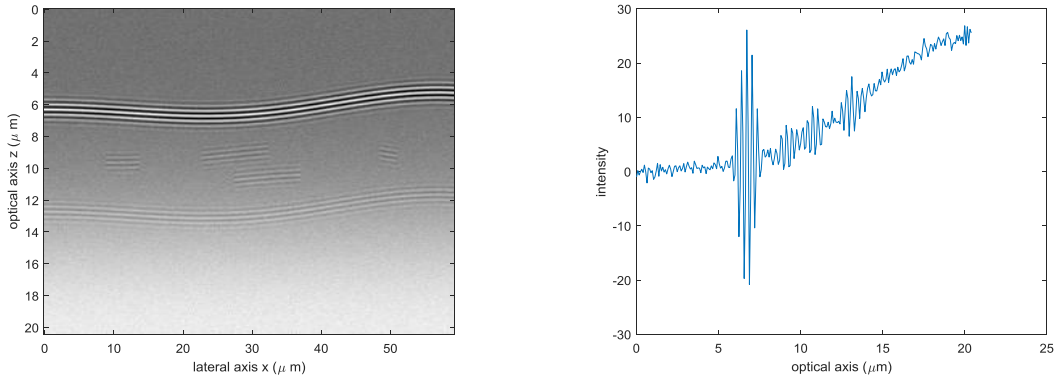

(a) (b)

Fig. 56 (a) Synthetic XZ fringe image 256 x 256 pixel and (b) profile of fringe signal along the optical axis Z of transparent multilayer.

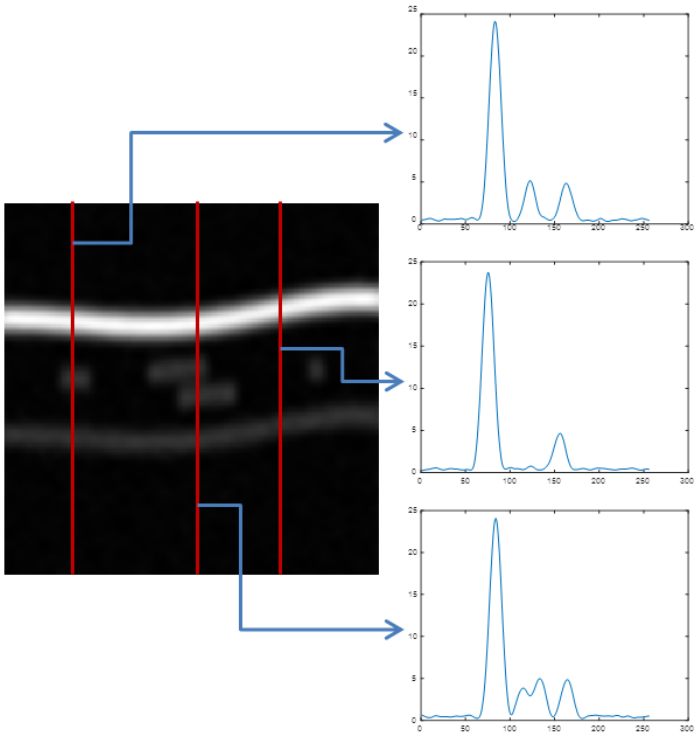

Fig. 57 Fringe envelope of a synthetic transparent layers

As illustrated by the interferogram in Fig. 56, we have generated the synthetic fringe signal corresponding to multiple layers (top surface, rear surface, and some structures). We perform the algorithm for the detection of the layer number as post-processing after applying the process of envelope detection. Fig. 57 shows the fringe envelope of the synthetic fringe signal of the transparent layers. As illustrated in the figure, an adaptive algorithm is required as post-processing to identify whether an interferogram has two, three, or four modulated envelopes corresponding to the different positions of the layer/surface.

In this simulation, the width of the Gaussian has been identified for our constructed synthetic fringe signal. We can adjust the minimum width threshold value corresponding to 0.75 times the identified width of the Gaussian based on the coherence length of the fringe signal. We did not choose the exact identified width threshold due to the fact that the fringe contrast envelope (Gaussian) which we seek could be distorted by the noise. Meanwhile, for the amplitude threshold, we adjust it by 3* the standard deviation of the noise. This amplitude threshold is obtained empirically and corresponds to the fringe amplitude being higher than 3* the standard deviation of the noise. The standard deviation of the noise is estimated on the region of the interferogram which does not have a fringe pattern (the background region). By using the adjusted threshold, this makes it

possible to detect the layer number and obtain the different positions of the layer and surface, as shown in Fig. 58.

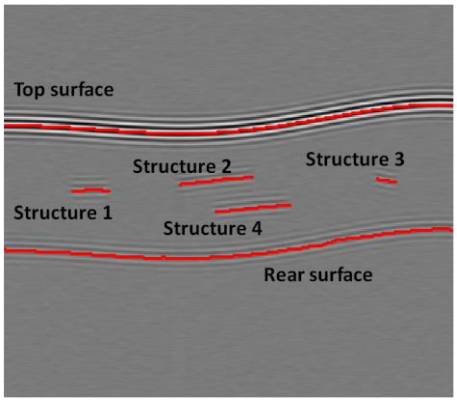

(a)

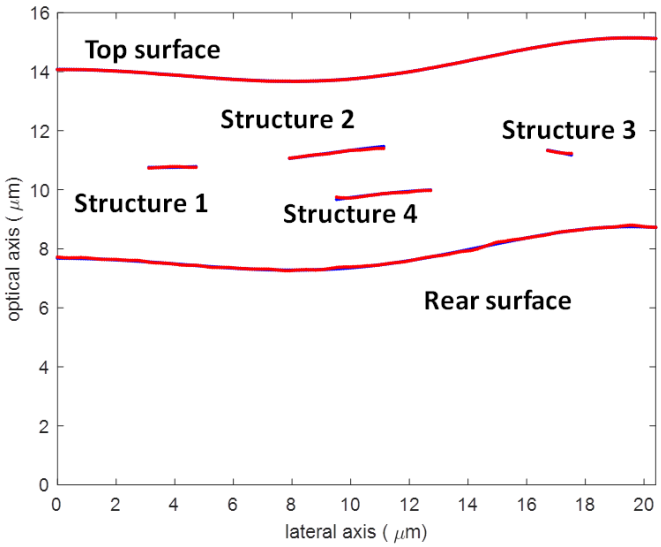

(b)

Fig. 58 (a) Surface detection on the synthetic transparent layers and (b) detected surface profile

In order to evaluate the algorithm performance in term of accuracy, we used the statistical parameter, i.e. mean absolute error (*mae*). The error rate (*mae*) of the measurements in Fig. 58(b) for the top surface, internal structures (1-4), and rear surface is respectively 3.19 nm, 14.49 nm, 16.86 nm, 16.59 nm, 14.16 nm, 14.20 nm. It seems that the surface extraction of the top surface is more precise than the other surfaces due to the fringe contrast of the top surface being far higher than the others, as shown in Fig. 57. Besides that, we also used another parameter, i.e. the ratio of number of the detected surface and number of the reference surface. Based on the Fig. 59, it seems that the ratio value is 100%, which means that our algorithm is able to detect correctly the entire assembly of reference structures.

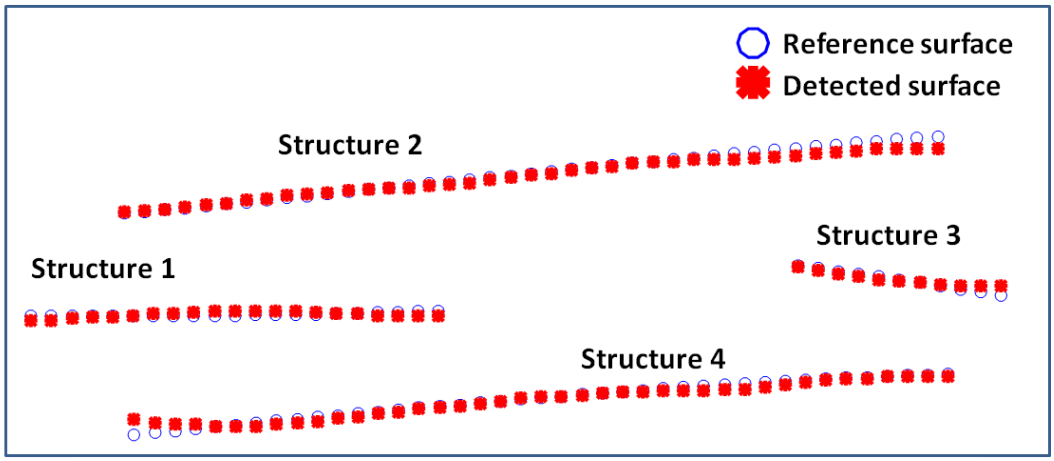

Fig. 59 Comparison of the measured structures with the reference structures

For the results of the measurements on this sample, the performance is also evaluated by measuring the local total (or peak-valley) roughness R_t and arithmetic roughness R_a of the profiles after removing the slopes. By using Eq.(2.13) and Eq.(2.14), it seems that the total roughness R_t for the top surface, internal structures (1-4), and rear surface has the same value, i.e. 5.33 nm, while the arithmetic roughness R_a also has the same value, i.e. 1.21 nm. The small value of roughness parameter indicates that the measured profiles has represent well the homogeneous reference structures.

b. Real data (transparent polymer film)

The performance of the algorithm was tested using real data, i.e. a transparent polymer film, of which the interferogram is shown in Fig. 60 and the envelope is illustrated in Fig. 61. The description of acquisition data of the measurement of a transparent polymer film obtained by the microscope system is given in Appendix-1: Data of Sample. As shown in Fig. 61, it is apparent that there are three clearly identifiable envelopes in the interferogram which indicate the top surface, rear surface, and some internal structures. In order to apply our algorithm to this data, it was necessary to adjust the threshold value. As with the synthetic data, the amplitude threshold is adjusted by 3* the standard deviation of the noise, which is estimated on the region of interferogram without fringes. Meanwhile, the width threshold is adjusted based on the coherence length of the fringe signal. The width (variation) w of Gaussian function considering to the fringe envelope of the signal can then be calculated based on the following equation [117],[118]:

$$w = \sqrt{8\ln 2}\cdot L_c = 2.3548\cdot\left(\frac{2\ln 2}{\pi}\frac{{\lambda_0}^2}{\Delta\lambda}\right) \qquad \textbf{(3.18)}$$

Where λ_0 is the mean of wavelength from the light source, while $\Delta\lambda$ is the spectral bandwidth of the camera that will limit $\delta\lambda$ (which is smaller than the wider spectral bandwidth of the black body emission of the light source) for the illumination actually used in the microscope.

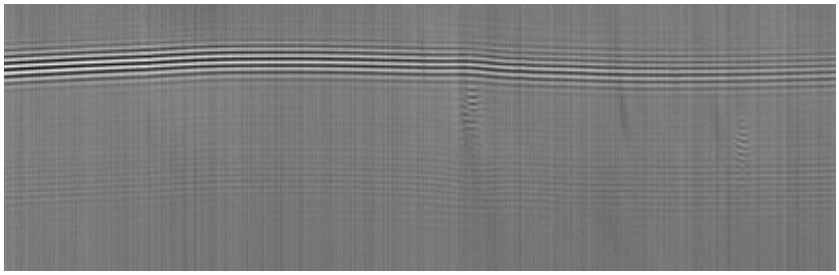

Fig. 60 Interferogram of a transparent polymer film

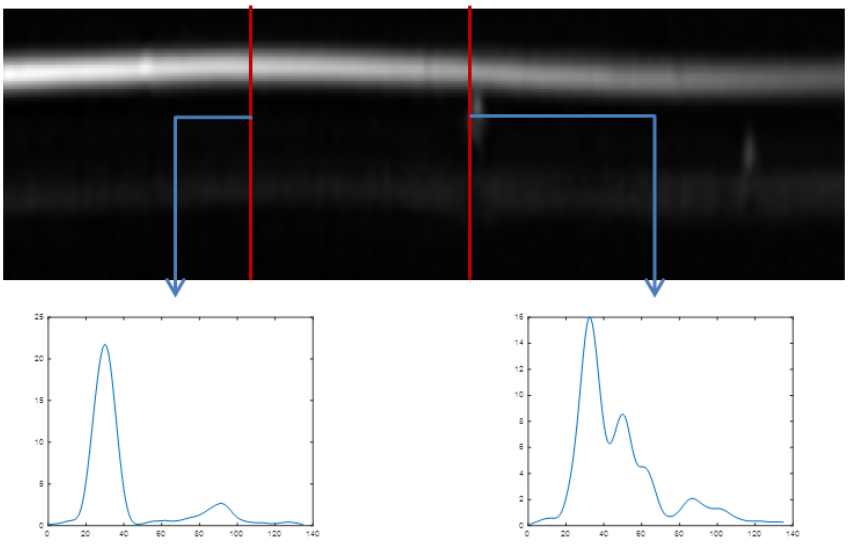

Fig. 61 Fringe envelope of the interferogram from a transparent polymer film

Fig. 62(a) shows the result of surface detection using the adjusted threshold (amplitude and width of Gaussian). As illustrated in Fig. 62(a), the algorithm succeeded in finding the layer number of the transparent polymer film, hence making it possible to identify the position of the top surface, the rear surface, and the presence of internal structures. However, it is apparent that there is still an artefact that appears during the processing of surface detection, as shown with the blue line in Fig. 62(a). In order to suppress the artefact, the neighbourhood number is added to the identifiable surface as a threshold parameter in the algorithm. This filters out the identifiable surface that has less than three surface neighbours to remain within the size of the Airy disc so as not to lose lateral information. The result is shown in Fig. 62(b).

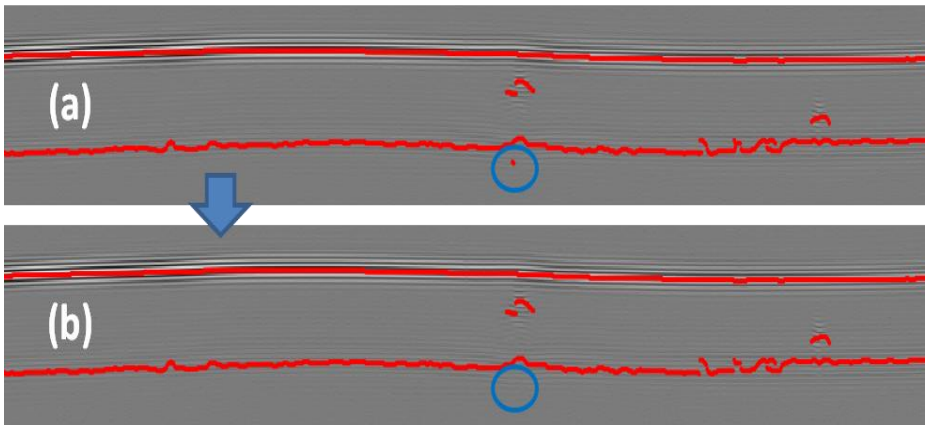

Fig. 62 Result of surface detection using the neighborhoods number as the threshold

3.4 RESULTS OF MEASUREMENTS ON MYLAR POLYMER FILM USING Z-SCAN AND XZ-SCAN TECHNIQUE

The fringe signals from the Mylar polymer film (Fig. 63) were obtained using the adapted Leitz-Linnik interference microscope. The description of the acquisition data of the measurement of the Mylar polymer film obtained by the microscope system is given in Appendix-1: Data of Sample. The method using the averaging technique with dark and flat corrections was performed in order to reduce the noise [88]. The previously described techniques were then used to measure the position of the surface, the internal structures, and the rear surface. As illustrated in Fig. 63(b), the fringes corresponding to the top surface have a high contrast, contrarily to the fringes on the rear surface, due to imaging in air. Even though the averaging technique increases the SNR, the noise can still appear in the resulting fringe signals of the film.

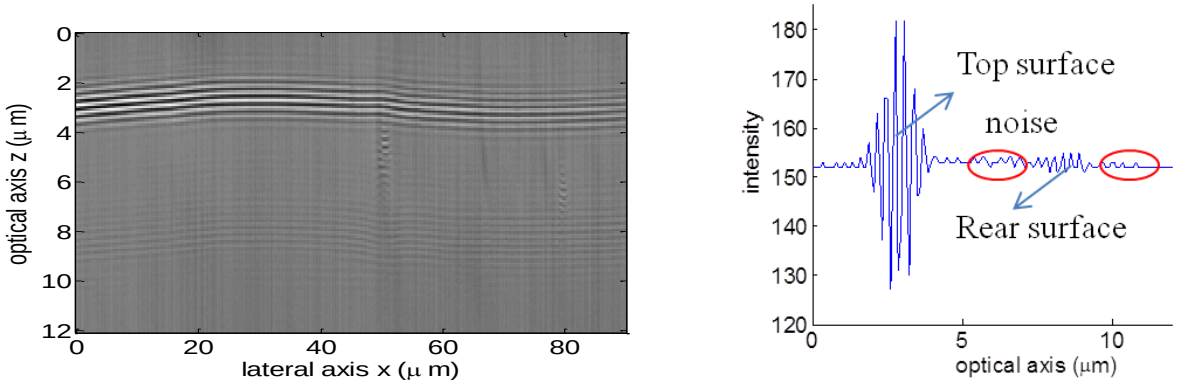

(a) (b)

Fig. 63 (a) XZ fringe image of a Mylar polymer and (b) the fringe signal along the optical axis Z.

3.4.1 Z-scan technique (1D Fringe Processing) results

Performing the Z-scan FSA approach on the fringe signal of the Mylar polymer film leads to the fringe envelope image shown in Fig. 64(a). The fringe envelope is shown as a logarithmic transformation in order to facilitate the identification of the presence of the structures and the rear surface. This XZ image is sufficient to provide the information regarding the structures and the rear surface. Fig. 64(b) shows the post-processing result using cubic spline smoothing. Positional measurements of the surface profiles and internal structures extracted by the Z-scan technique are shown in Fig. 65. It can be observed that the technique provides satisfactory results for measuring the top surface, but it is not sufficient for the accurate measurement of the depths of the internal structures nor of the rear surface.

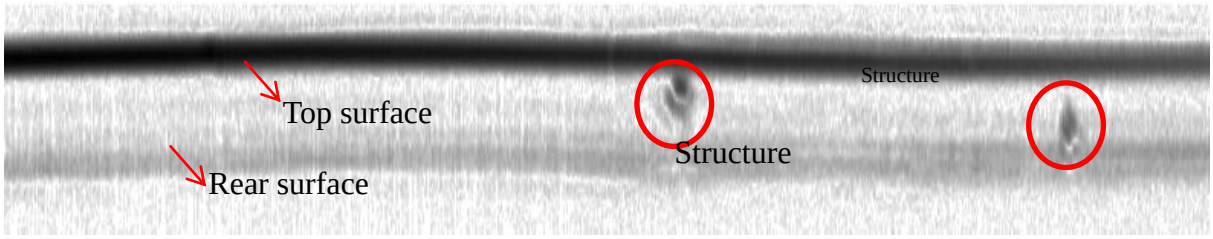

(a)

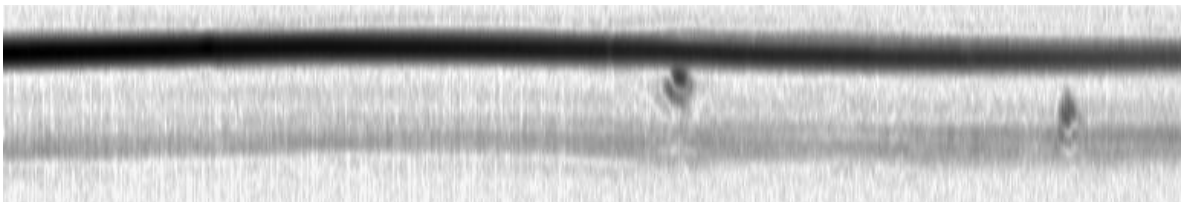

(b)

Fig. 64 Logarithmic transformation[1] of fringe envelope obtained by (a) FSA, (b) post-processing result using cubic spline smoothing.

[1] Logarithmic transformation: $T_i^{\log} = \dfrac{\log(i+1)*(i_{\max}-1)}{\log(i_{\max}-1)}$

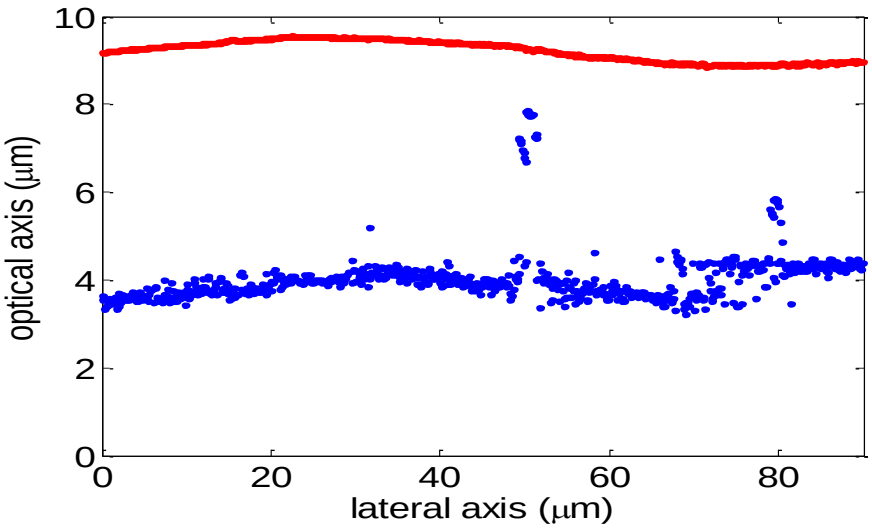

Fig. 65 Surface extraction of Mylar polymer obtained by Z-scan technique using FSA algorithm.

3.4.2 XZ-scan technique (2D Fringe Processing) results

In order to obtain better results on the Mylar polymer film, the XZ-scan technique was performed with the previously mentioned post-processing techniques. Fig. 66(a) and Fig. 67(a) show respectively the fringe envelope obtained by 2DTKEO and 2DHT. Fig. 66(b) and Fig. 67(b) then show the post-processing results using cubic spline smoothing which have been performed on the 2D fringe envelope. A slight improvement compared to the post-processing results in the Z-scan technique can be observed since it takes into account the lateral axis X and optical axis Z in the reduction of the noise. By performing such a technique, the rear surface depth can be measured with more precision as shown in Fig. 68.

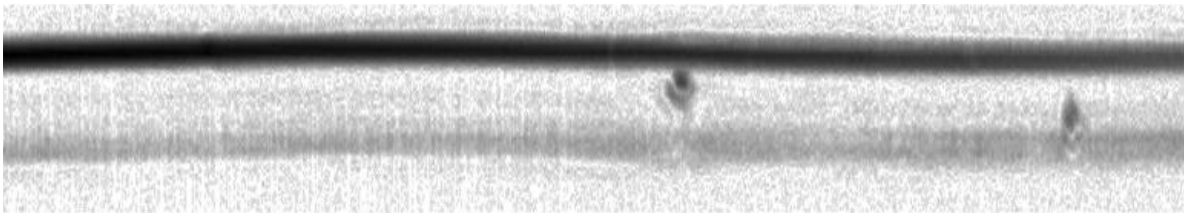

(a)

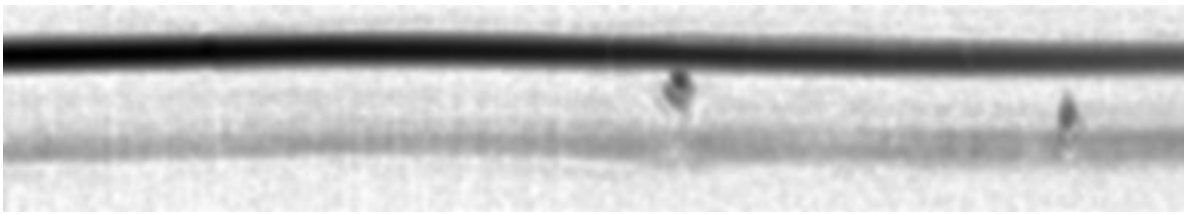

(b)

Fig. 66 Logarithmic transformation of fringe envelope obtained by (a) 2DTKEO, (b) its post-processing result using cubic spline smoothing.

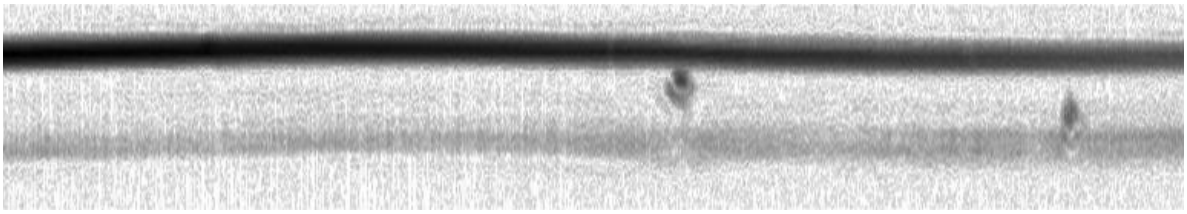

(a)

(b)

Fig. 67 Logarithmic transformation of fringe envelope obtained by (a) 2DHT, and (b) its post-processing result using cubic spline smoothing.

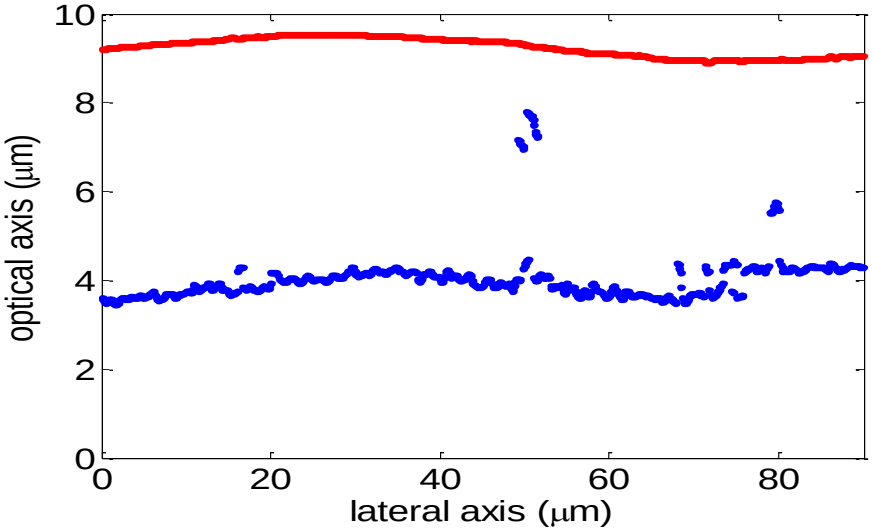

(a)

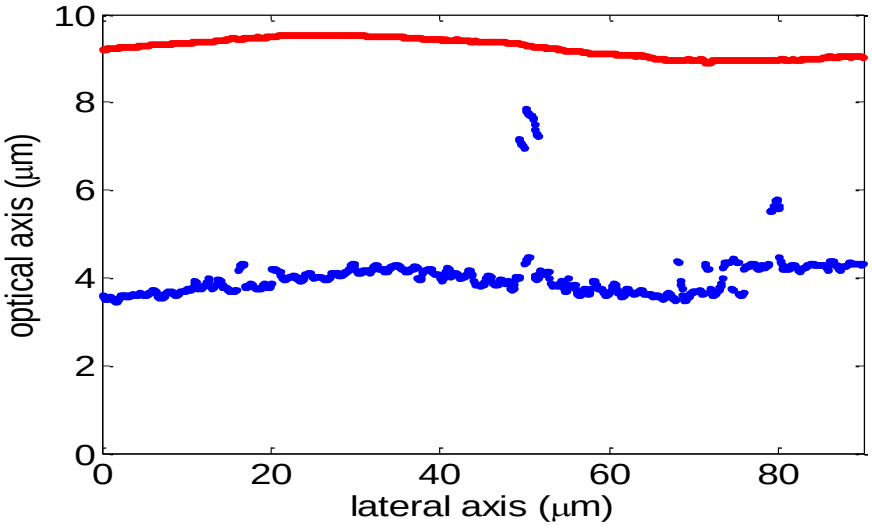

(b)

Fig. 68 Surface extraction of Mylar polymer obtained by XZ-scan technique using (a) 2DTKEO and (b) 2DHT.

3.4.3 Measurement of thickness of Mylar polymer film

The surface extraction using the XZ-scan technique can be used for the thickness measurement of the Mylar polymer film, known to be between 3 µm and 3.6 µm. **Table 10** and Fig. 70 show the mean values of the thickness for a given Region of Interest (ROI). The ROI is taken every lateral span of 10 µm along the lateral axis X. The thickness of the Mylar polymer film at the point X can be measured by calculating the distance Δ separating the surface position along the optical axis Z [47], [119]. By using the value of refractive index (n) of the Mylar polymer film which is known (1.63 for λ = 700 nm), the thickness d is:

$$d = \frac{\Delta}{n} \tag{3.19}$$

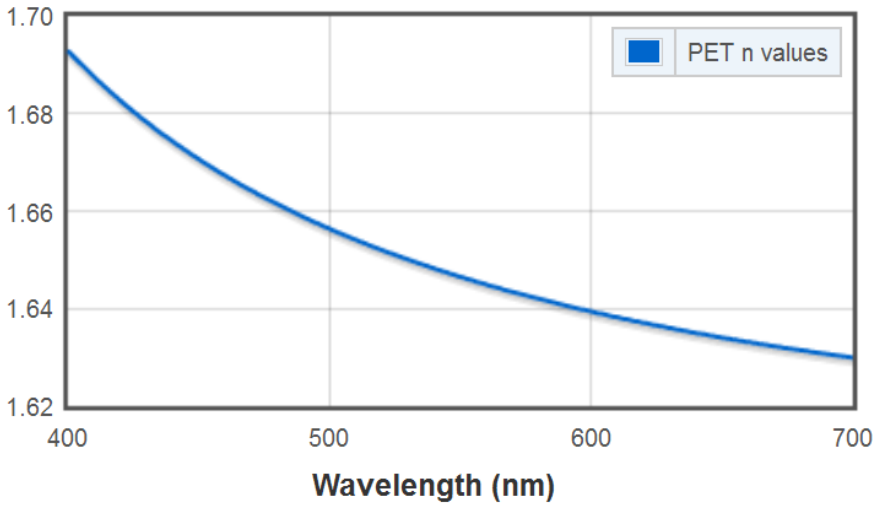

Fig. 69 The refractive index of the Mylar

Fig. 69 shows the refractive index of the Mylar polymer film. Based on this figure, it can be seen that its value vary as a function of the wavelength. In order to calculate the index value of $n(\lambda)$ of the Mylar polymer film, we applied the Cauchy equation, which shows the empirical relationship between the wavelength and the refractive index. The Cauchy equation is given by:

$$n(\lambda) = B + \frac{C}{\lambda^2} + \frac{D}{\lambda^4} \tag{3.20}$$

where λ corresponds to the wavelength, n corresponds to the refractive index, while B, C, D represent the coefficients. Through the information concerning the measured refractive index of Mylar at known wavelengths, as illustrated in Fig. 69, the values of the

coefficient can be computed by fitting the equation. By performing the fitting using the data provided in Fig. 69, the coefficient values for Mylar can be obtained:

B = 1.6073

C = 9.7817 x10^3

D = 6.2689 x10^8

Thus, the refractive index of Mylar polymer film for λ_{eff} = 720 nm is calculated as follows:

$$n_1(720) = 1.6073 + \frac{9.7817 \times 10^3}{720^2} + \frac{6.2689 \times 10^8}{720^4} = 1.628$$

The inhomogeneity of the refractive index of the Mylar is a factor that can accentuate the degradation of the wavefront reflected by the interface, which introduces an additional measurement error. It was assumed in our study that the index is homogeneous and constant across the depth of the layer. In reality, several variations are possible: random, linear or quadratic. Each variation has a different effect on the value of the measurement.

Table 10 Mean value of mylar polymer thickness

Mylar thickness (μm) for each of ROI								
0-10	**10-20**	**20-30**	**30-40**	**40-50**	**50-60**	**60-70**	**70-80**	**80-90**
3.48	3.44	3.36	3.27	3.32	3.24	3.28	2.98	2.90

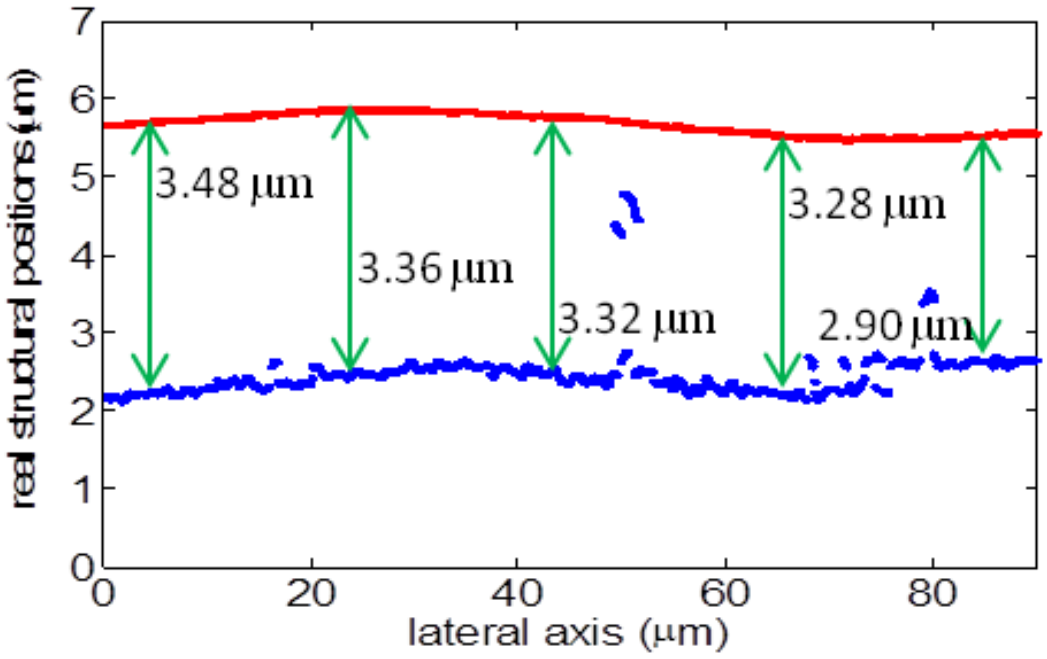

Fig. 70 Thickness measurements of Mylar polymer film.

3.4.4 Error Approximation of Thickness Measurement of Mylar Film

The error approximation of the thickness measurement is given by:

$$\delta d = \frac{\delta \Delta}{n_1} + \frac{\Delta \delta n_1}{n_1^{\,2}} \tag{3.20}$$

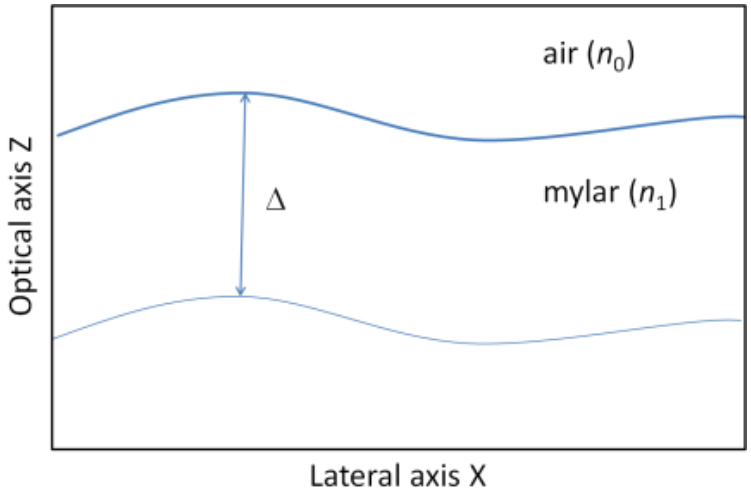

Fig. 71 Thickness of Mylar polymer film.

The main sources of error are:

- The variation of the refractive index n_1 of the medium,
- The variation in the measurement of Δ.

a. Error n_1 (δ_n)

The main contribution of refractive index error comes from the light source used (white light), δ_λ:

$$\delta_n = \frac{n_1(\lambda_1) - n_1(\lambda_2)}{2} \tag{3.21}$$

If we take into account the spectral response of the CCD sensor, that extends from λ_1 = 350 nm to λ_2 = 1100 nm, the value of this error can be estimated by:

$$\delta_n = \frac{n(350\text{ nm}) - n(1100\text{ nm})}{2} \tag{3.22}$$

The refractive index of Mylar polymer film for λ_{eff} = 720 nm is calculated as follows:

$$n_1(720) = 1.6073 + \frac{9.7817\times10^3}{720^2} + \frac{6.2689\times10^8}{720^4} = 1.628$$

Meanwhile the refractive index for white light over the range of λ_1 = 350 nm to λ_1 = 1100 nm, is given by:

$$n_1(350) = 1.6073 + \frac{9.7817\times10^3}{350^2} + \frac{6.2689\times10^8}{350^4} = 1.729$$

$$n_1(1100) = 1.6073 + \frac{9.7817\times10^3}{1100^2} + \frac{6.2689\times10^8}{1100^4} = 1.616$$

By using Equation (31), we obtain the error approximation of the thickness contributed by the refractive index error, to be 0.0565.

b. Error Δ (δ_Δ)

Inaccuracies in the position of the central fringe and systematic errors cause an error that affects the values of the scanning steps. The error contribution of δ_Δ comes from the imperfection of the piezoelectric stepper calibration (δ_e) and the resolution of its plate displacement (δ_p). Using the values of δ_e = 5 nm and δ_p = 1 nm for the piezo stepper used, the error value of δ_Δ is given by:

$$\delta_{\Delta} = \delta_e + \delta_p$$
$$= (0.005 + 0.001)\mu m = 0.006\ \mu m$$

Finally, we can obtain the error approximation of the thickness measurement of the Mylar to be:

$$\delta d = \frac{\delta\Delta}{n_1} + \frac{\Delta\delta n_1}{n_1^{\,2}}$$
$$= \frac{0.006}{1.628} + \frac{(3.25)(0.0565)}{1.628^2} = \pm\ 0.07\mu m$$

3.5 CONCLUSION

The study of the robustness of 2D fringe processing in CSI has been presented for the characterization of a transparent Mylar polymer film. We have demonstrated the ability of 2D approaches to compete with some classical methods (1D approaches) used in the field of interferometry, in terms of robustness. These results demonstrate that the XZ fringe envelope extracted by the 2D fringe processing provides more satisfactory results than the 1D fringe processing in revealing the internal structures and the rear surface, which is contained in Mylar polymer film. The technique also allows an improvement in the details in the XZ images as well as more accurate measurements of the thickness of the polymer film.

3.6 RÉSUMÉ DU CHAPITRE 3

Dans ce chapitre, nous étudions les performances du traitement des franges 2D en CSI développé basé sur deux dimensions-Teager Kaiser Energy Operator sur un échantillon multicouche. Une analyse de franges robuste est nécessaire pour une caractérisation améliorée du film de polymère transparent, c'est-à-dire un film de Mylar, qui est complexe et contient des structures internes et une couche enterrées avec un faible contraste. Les algorithmes sont comparés à la transformée de Hilbert bidimensionnelle classique et au traitement frange 1D en utilisant l'algorithme FSA bien connu. En outre, nous rapportons également l'étude de l'algorithme développé pour la détection du nombre

de couches dans un échantillon multicouche en utilisant l'ajustement de la courbe gaussienne.

Pour évaluer la robustesse de 2DTKEO, comparée à la 1DFSA, nous avons effectué des simulations, qui étaient appliquées respectivement à un signal sans bruit ($\sigma = 0\%$) et à des signaux bruyants ($\sigma = 10\%$ et $\sigma = 20\%$) en utilisant un signal synthétique. Afin d'améliorer la sensibilité axiale et la précision de la détection de crête, un lissage spline cubique suivi d'une interpolation gaussienne a été utilisé, qui est adapté au modèle physique de l'enveloppe. Basé sur des profils de surface des résultats, la comparaison des performances qualitatives peut être observée entre la technique XZ-scan utilisant 2DTKEO et la technique Z-scan utilisant l'algorithme FSA. On peut observer que la technique XZ-scan (2DTKEO) fournit une meilleure extraction de surface que la FSA à la fois sur les surfaces supérieure et arrière. De plus, le taux d'erreur absolu moyen (*mae*) a été calculé par rapport à la surface de référence. En comparant les résultats de l'évaluation quantitative, la technique Z-scan (FSA) et la technique XZ-scan (2DTKEO) sont similaires en termes de performance dans le cas du signal sans bruit ($\sigma = 0\%$) fournissant une valeur moyenne de mae = 2,1 nm. La raison de 2DTKEO devrait être plus robuste que la FSA est l'utilisation d'une dérivée 2D par le biais du filtre gaussien, en présence de surfaces lisses. Pendant ce temps, pour un signal bruyant ($\sigma = 10\%$ et $\sigma = 20\%$), la technique XZ-scan utilisant 2DTKEO est généralement plus robuste que la FSA, ce qui est montré par le taux d'erreur (*mae*) 2 fois plus petit, correspondant au une plus grande précision.

Ensuite, nous évaluons ces deux algorithmes sur des données réelles, c'est-à-dire un film de Mylar qui a une couche multiple constituée de la surface supérieure, des structures internes et de la surface arrière. Les signaux de franges provenant du film de polymère Mylar ont été obtenus en utilisant le microscope interférentiel Leitz-Linnik adapté. La méthode utilisant la technique de moyennage avec des corrections champ sombre et plate a été réalisée afin de réduire le bruit. Les franges de Mylar correspondant à la surface supérieure ont un contraste élevé, contrairement aux franges sur la surface arrière, en raison de l'imagerie dans l'air. Même si la technique de moyennage a augmenté le SNR, le bruit peut encore apparaître dans les signaux de franges résultants du film. Basé sur du profil de surface obtenu en utilisant le traitement du signal frange 1D (FSA), nous avons observé que la technique fournit des résultats satisfaisants pour mesurer la surface supérieure, mais qu'elle n'est pas suffisante pour la mesure précise des

profondeurs des structures internes ou des surface arrière. Afin d'obtenir de meilleurs résultats sur le film polymère Mylar, la technique XZ-scan (2DTKEO) a été réalisée. Les résultats démontrent que l'enveloppe de frange XZ extraite par le traitement du signal de frange 2D fournit des résultats plus satisfaisants que le traitement du signal frange 1D en révélant les structures internes et la surface arrière, qui est contenue dans un film de polymère Mylar. La technique permet également une amélioration des détails dans les images XZ ainsi que des mesures plus précises de l'épaisseur du film polymère.

Chapter 4. 3D FRINGE PROCESSING IN CSI

In the previous chapter 2 and 3, we report the study of 1D fringe signal processing (Z-scan technique) and 2D fringe signal processing (XZ-scan technique) in CSI. We have demonstrated the ability of 2D approaches to compete with some classical methods (1D approaches) used in the field of interferometry, in terms of robustness. In addition, whereas most methods only take into account the 1D data, it would seem advantageous to take into account the spatial neighbourhood using multi-dimensional approaches (2D, 3D).

In this chapter, we present the study of the application of the 3D Teager Kaiser Energy Operator (3DTKEO), which is developed based on the multi-dimensional energy operator (2009, Salzenstein and Boudraa) [104], [116]. Through a simulation using a synthetic fringe signal, we evaluated the robustness of the 3DTKEO performance in fringe signal processing, which is compared to the 1D and 2D approaches. Moreover, we also used the algorithm on real data, i.e. a step height standard (VLSI Standard Inc.) in order to evaluate the measurement accuracy. In addition, we enrich the field of study by testing the algorithm on measurements from different samples: Graphene, DOE (Diffractive Optical Elements), Resin on Silicon, Cable and Rock.

4.1 XYZ-SCAN TECHNIQUE (3D)

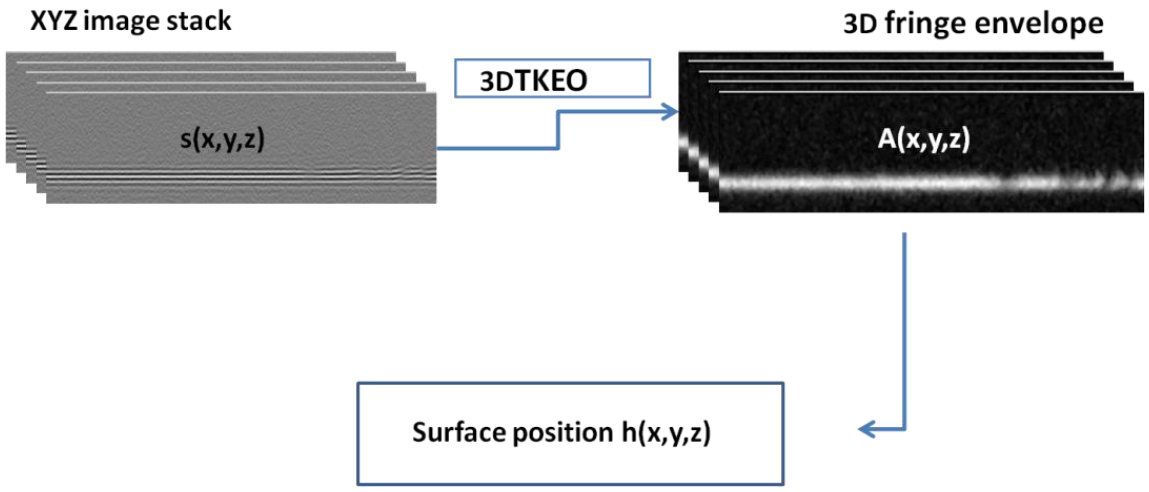

Fig. 72 The technique of 3D fringe processing using 3DTKEO

Three dimensional fringe signal processing can be chosen using the raw XYZ data by operating on the XZY images as shown in Fig. 72. The technique is defined as an "XYZ-scan" which consists in analyzing the XYZ fringe signals (three dimensional signals). By processing a given XYZ fringe signals, we can obtain the 3D fringe envelope directly.

4.2 3D TEAGER KAISER ENERGY OPERATOR

In this work, we have applied the developed algorithm for continuous 3D Teager Kaiser Energy Operator based on the multi-dimensional energy operator [104], [116], for fringe signal analysis using white light interferometry. In addition, we have also introduced the mathematical model and its application of the discrete 3D Teager Kaiser Energy Operator in the same field of fringe signal processing in CSI.

We now introduce the general image processing model of 3D Teager Kaiser Energy Operator for the three dimensions of AM-FM signal *f(x,y,z)* as follows:

$$f(x,y,z) = \quad a(x,y,z) + c(x,y,z).\cos(ux + vy + wz + \alpha_0) \tag{4.1}$$

where *a*(x,y,z) is the offset component, *c*(*x*,*y*,*z*) is the envelope function as a function of the variable ordinate *x*, *y*, *z*, α_0 is the phase offset, and *ux*,*vy*,*wz* are respectively the phase along the *x*, *y* and *z*-axes.

In this work we apply the 3D TKEO algorithm in order to identify the instantaneous amplitude on an optical physical recording model of fringe signals *s(x,y,z)*, i.e. XYZ stack image, as for example as that shown in Fig. 73. The reason we apply the 3D TKEO to the XYZ image stack of fringe signals is the assumption that it physically corresponds to the local orientation of the continuous surface.

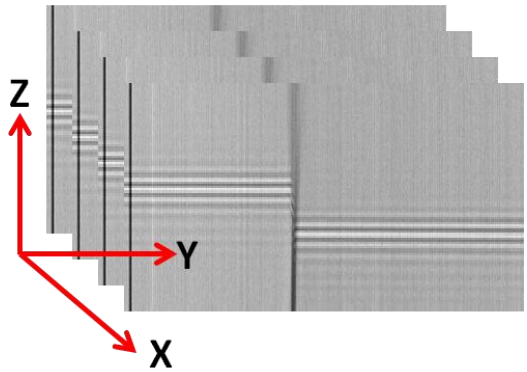

Fig. 73 Stack image XYZ of fringe signals *s(x,y,z)*

In this work, we make the hypothesis that the XYZ image stack of the fringe signals generated by CSI follows the model of a three dimensional AM-FM signal. It is obviously intrinsically difficult to represent the 3D signal. We consider this three dimensional AM-FM of XYZ fringe signal as a reconstruction of the projection of the XZ slices and YZ slices. For example, we have the 3D AM-FM signal of the fringe signal as follows:

$$s(x,y,z) = a(x,y,z) + g\left(z - z_0(x,y)\right).\cos\left(ux + vy + wz + \alpha_0\right) \quad \text{where} \quad z = k\Delta \tag{4.2}$$

where a(x,y,z) is the offset component, $g(z - z_0(x,y))$ is the envelope function, which contains intrinsically a 1D Gaussian function, α_0 is the phase offset, and ux,vy,wz are respectively the phase along the x, y, and z-axes. The parameter z is referred to as $k\Delta$, with k the index-scanning step and Δ the value of scanning step. As an illustration, Fig. 74 shows the stack image of XYZ fringe signals generated by CSI on the step height sample.

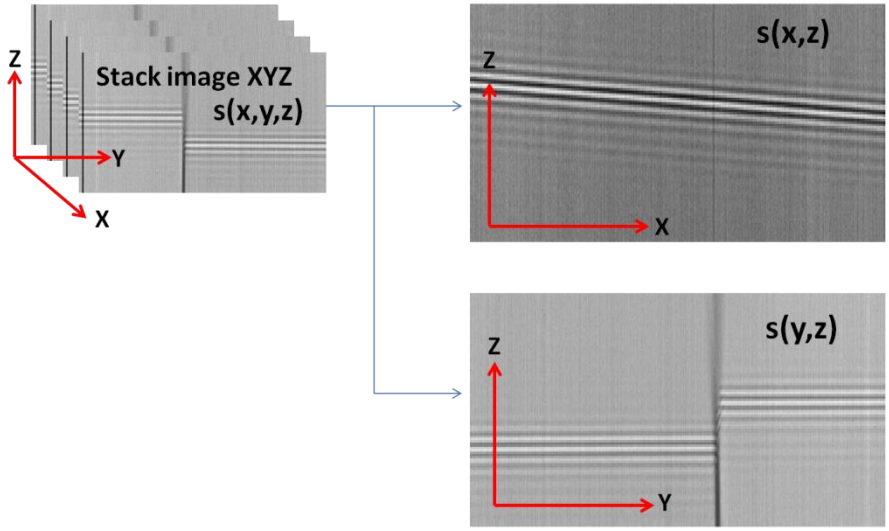

Fig. 74 The stack image XYZ of fringe signal corresponds as reconstruction of the projection XZ slices and YZ slices

Based on Eq.(4.2) and as illustrated in Fig. 74, fixing a slice x_0 yields the 2D AM-FM signal (YZ slice), which is represented by the following equation:

$$s(y,z) = a(x_0,y,z) + g\left(z - z_0(x_0,y)\right).\cos\left(vy + wz + \alpha_1\right) \quad \text{where} \quad z = k\Delta \tag{4.3}$$

where α_1 depends on x_0, u, and α_0. The component $g(z - z_0(x_0,y))$ is the envelope function, which contains intrinsically a 1D Gaussian function, as illustrated in Fig. 75(a). The parameter z is referred to as $k\Delta$, with k the index-scanning step and Δ the value of

scanning step. By using the 3D TKEO, we also can obtain the local frequency/orientation of the signal. If we choose a fixed slice y_0, we obtain the 2D AM-FM signal (XZ slice), which is represented by the following equation:

$$s(x,z) = a(x,y_0,z) + g\left(z - z_0(x,y_0)\right).\cos\left(ux + wz + \alpha_2\right) \quad \text{where} \quad z = k\Delta \tag{4.4}$$

where α_2 depends on y_0, v, and α_0. The component $g(z - z_0(x,y_0))$ is the envelope function, which contains intrinsically a 1D Gaussian function, as illustrated in Fig. 75. The parameter z is referred to as $k\Delta$, with k the index-scanning step and Δ the value of scanning step. This hypothesis seems to justify that the model of the developed 3D fringe processing is suitable for the XYZ image stack of the fringe signals. Therefore, we can obtain the surface profile which is the height of surface $z_0(x,y)$ of the sample, as illustrated in Fig. 76.

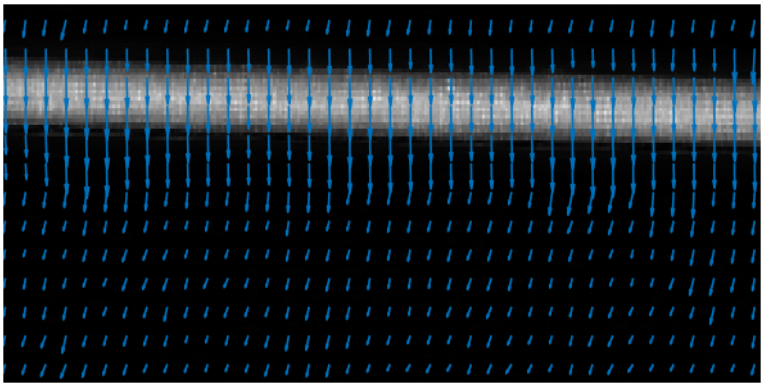

(a)

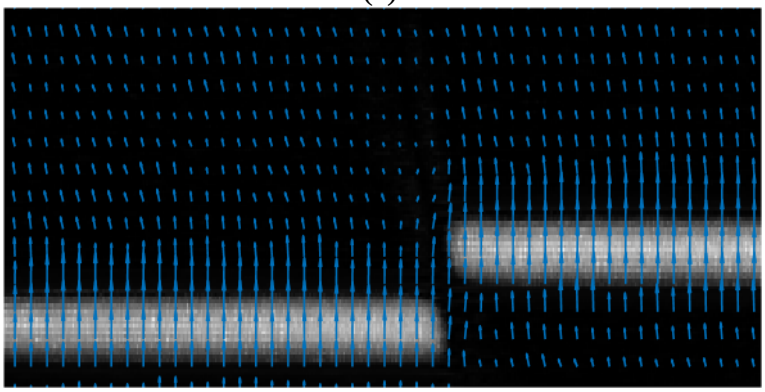

(b)

Fig. 75 The fringe envelope and the local frequency/orientation

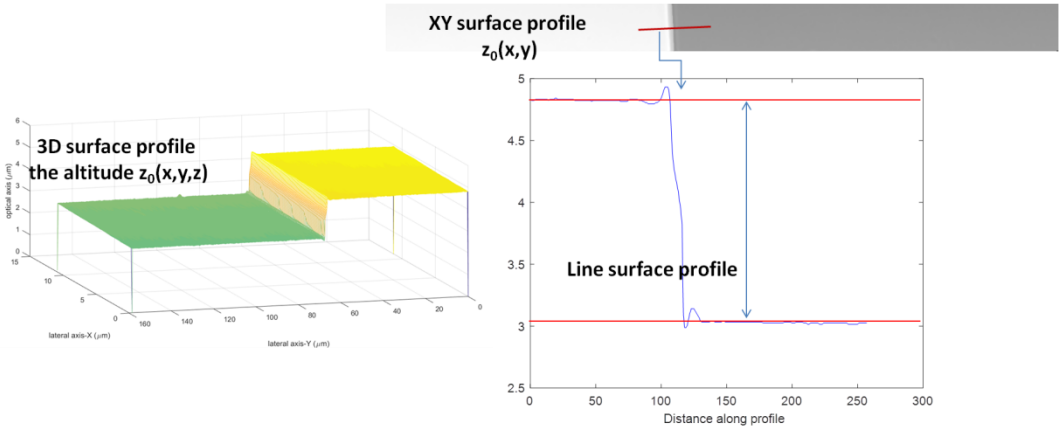

Fig. 76 3D surface profile, XY surface profile $z_0(x,y)$, and the line surface profile

4.2.1 Continuous 3D Teager Kaiser Energy Operator

The techniques of 2DTKEO and 3DTKEO are extended versions of the mono-dimensional TKEO. The different operators extending mono-dimensional TKEO to 2D signals have been developed by Maragos and Bovik in 1995, Boudraa et al. in 2005, and Larkin in 2005. These operator outputs are proportional to the square of the product of the frequency and the amplitude of the input 2D signal, which is useful for AM-FM signal demodulation. In the case of the 2D signal, the operators can be expressed by a tensor as follows in Eq.(4.5):

$$
\begin{aligned}
\Phi\left[s(x,y)\right] &= \left[\nabla s(x,y)\right]^2 - s(x,y)\Delta s(x,y) \\
&= \left[\frac{\partial s}{\partial x} + \frac{\partial s}{\partial y}\right]^2 - s\left[\frac{\partial^2 s}{\partial x^2} + \frac{\partial^2 s}{\partial y^2} + 2\frac{\partial^2 s}{\partial x \partial y}\right] \\
&= \left[\left(\frac{\partial s}{\partial x}\right)^2 + \left(\frac{\partial s}{\partial y}\right)^2 + 2\left(\frac{\partial s}{\partial x}\frac{\partial s}{\partial y}\right)\right] - s\left[\frac{\partial^2 s}{\partial x^2} + \frac{\partial^2 s}{\partial y^2} + 2\frac{\partial^2 s}{\partial x \partial y}\right] \\
&= \left[\left(\frac{\partial s}{\partial x}\right)^2 - s\frac{\partial^2 s}{\partial x^2}\right] + \left[\left(\frac{\partial s}{\partial y}\right)^2 - s\frac{\partial^2 s}{\partial y^2}\right] + 2\left[\left(\frac{\partial s}{\partial x}\frac{\partial s}{\partial y}\right) - s\frac{\partial^2 s}{\partial x \partial y}\right] \\
&\Rightarrow \begin{pmatrix} \psi_{11} & \psi_{12} \\ \psi_{21} & \psi_{22} \end{pmatrix}
\end{aligned}
\qquad \textbf{(4.5)}
$$

The following relations are the different operators developed by Maragos and Bovik, Boudraa, and Larkin for 2D signal $s(x,y)$. These operators are denoted respectively by Φ_B, Φ_C and Φ_D [40], [104].

$$\Phi_B\left[s(x,y)\right] = \psi_{11} + \psi_{22} = trace\left[\psi_t\left[s(x,y)\right]\right] \quad \Rightarrow \text{(Maragos and Bovik 1995)}$$

$$\Phi_C\left[s(x,y)\right] = \psi_{11} + \psi_{22} + \psi_{12} + \psi_{21} \quad \Rightarrow \text{(Boudraa et al. 2005)}$$

$$\Phi_D\left[s(x,y)\right] = \psi_{11} - \psi_{22} + j\psi_{12} + j\psi_{21} \quad \Rightarrow \text{(Larkin 2005)}$$

In for the case of a 3D signal, the operators can be expressed by an energy tensor as follows [104], [116]:

$$\begin{aligned}
\Phi\left[s(x,y,z)\right] &= \left\|\nabla s(x,y,z)\right\|^2 - \left(s(x,y,z)\Delta s(x,y,z)\right) \\
&= \left[\frac{\partial s}{\partial x} + \frac{\partial s}{\partial y} + \frac{\partial s}{\partial z}\right]^2 \ldots \\
&\ldots - s\left[\frac{\partial^2 s}{\partial x^2} + \frac{\partial^2 s}{\partial y^2} + \frac{\partial^2 s}{\partial z^2} + 2\frac{\partial^2 s}{\partial x \partial y} + 2\frac{\partial^2 s}{\partial x \partial z} + 2\frac{\partial^2 s}{\partial y \partial z}\right] \\
&= \left[\left(\frac{\partial s}{\partial x}\right)^2 + \left(\frac{\partial s}{\partial y}\right)^2 + \left(\frac{\partial s}{\partial z}\right)^2 + 2\left(\frac{\partial s}{\partial x}\frac{\partial s}{\partial y}\right) + 2\left(\frac{\partial s}{\partial x}\frac{\partial s}{\partial z}\right) + 2\left(\frac{\partial s}{\partial y}\frac{\partial s}{\partial z}\right)\right] \ldots \\
&\ldots - s\left[\frac{\partial^2 s}{\partial x^2} + \frac{\partial^2 s}{\partial y^2} + \frac{\partial^2 s}{\partial z^2} + 2\frac{\partial^2 s}{\partial x \partial y} + 2\frac{\partial^2 s}{\partial x \partial z} + 2\frac{\partial^2 s}{\partial y \partial z}\right]
\end{aligned} \tag{4.6}$$

$$\begin{aligned}
\Phi\left[s(x,y,z)\right] &= \left[\left(\frac{\partial s}{\partial x}\right)^2 - s\frac{\partial^2 s}{\partial x^2}\right] \\
&\ldots + \left[\left(\frac{\partial s}{\partial y}\right)^2 - s\frac{\partial^2 s}{\partial y^2}\right] \\
&\ldots + \left[\left(\frac{\partial s}{\partial z}\right)^2 - s\frac{\partial^2 s}{\partial z^2}\right] \\
&\ldots + 2\left[\left(\frac{\partial s}{\partial x}\frac{\partial s}{\partial y}\right) - s\left(\frac{\partial^2 s}{\partial x \partial y}\right)\right] \\
&\ldots + 2\left[\left(\frac{\partial s}{\partial x}\frac{\partial s}{\partial z}\right) - s\left(\frac{\partial^2 s}{\partial x \partial z}\right)\right] \\
&\ldots + 2\left[\left(\frac{\partial s}{\partial y}\frac{\partial s}{\partial z}\right) - s\left(\frac{\partial^2 s}{\partial y \partial z}\right)\right] \quad \Rightarrow \begin{pmatrix} \psi_{11} & \psi_{12} & \psi_{13} \\ \psi_{21} & \psi_{22} & \psi_{23} \\ \psi_{31} & \psi_{32} & \psi_{33} \end{pmatrix}
\end{aligned} \tag{4.7}$$

For a 3D signal, we have the following relations:

$$\Phi_B\left[s(x,y,z)\right] = \psi_{11} + \psi_{22} + \psi_{33} = trace\left[\psi_t\left[s(x,y,z)\right]\right]$$
$$\Phi_C\left[s(x,y,z)\right] = \psi_{11} + \psi_{22} + \psi_{33} + \psi_{12} + \psi_{21} + \psi_{13} + \psi_{31} + \psi_{23} + \psi_{32} \quad \textbf{(4.8)}$$

4.2.2 Discrete 3D Teager Kaiser Energy Operator

In this section, we recall the mathematical model of discrete 3D Teager Kaiser Energy Operator, which was introduced in the article [120]. As far as we know, no one has applied this discrete model to fringe signal processing, nor compared it with the performance of the algorithm of the continuous 3D Teager Kaiser Energy Operator. In a 3D context, let us give a local discrete AM-FM signal $s(i,j,k) = A(i,j,k)\cos(\Omega_x i + \Omega_y j + \Omega_z k)$ where $\Omega_x = \omega_x x_e$, $\Omega_y = \omega_y y_e$, $\Omega_z = \omega_z z_e$. The variable x_e (resp. y_e and z_e) represents the sampling period along the x-axis (resp. the y-axis and z-axis). The discrete counterpart of the operator Φ_2 denoted by Φ_2^d applied to the signal $s(u)$ is obtained in the same way, by performing the sum of the absolute values of the matrix elements, as follows:

$$\begin{aligned}
\Phi_2^d\left[s(x,y,z)\right] &= \psi_{11} + \psi_{22} + \psi_{33} + \psi_{12} + \psi_{21} + \psi_{13} + \psi_{31} + \psi_{23} + \psi_{32} \\
&= \left|s^2(i,j,k) - s(i-1,j,k)s(i+1,j,k)\right| \\
&+ \left|s^2(i,j,k) - s(i,j-1,k)s(i,j+1,k)\right| \\
&+ \left|s^2(i,j,k) - s(i,j,k-1)s(i,j,k+1)\right| \\
&+2\left|s_x(i,j,k)s_y(i,j,k) - s(i,j,k)s_{xy}(i,j,k)\right| \\
&+2\left|s_x(i,j,k)s_z(i,j,k) - s(i,j,k)s_{xz}(i,j,k)\right| \\
&+2\left|s_y(i,j,k)s_z(i,j,k) - s(i,j,k)s_{yz}(i,j,k)\right|
\end{aligned} \quad \textbf{(4.9)}$$

Where $s_x(i,j,k)$, $s_y(i,j,k)$ and $s_z(i,j,k)$ represent the first order derivative along x (resp. y and z). The parameter $s_{xy}(i,j,k)$ represents the second order derivatives according to x and y (resp. $s_{xz}(i,j,k)$ and $s_{yz}(i,j,k)$). The first part of (4.8) corresponds to the 2D discrete energy operator described in by Maragos and Bovik [121] and is identical to discrete energy operator developed in [122] for digital image edge detection.

Consider a 3-dimensional an AM–FM signal defined by:

$$\begin{aligned}
&s(i,j,k) = A(i,j,k)\cos\left(\Omega_x i + \Omega_y j + \Omega_z k\right) \\
&\text{where } \Omega_x = \omega_x x_e \;; \qquad \Omega_x = \omega_x x_e \;; \qquad \Omega_x = \omega_x x_e
\end{aligned} \quad \textbf{(4.10)}$$

The variable x_e (resp. y_e and z_e) represents the sampling period along the x-axis (resp. the y-axis and z-axis). The assumption that the amplitude $A(i,j,k)$ varies more slowly than the carrier signal cos ($\Omega_x\, i + \Omega_y\, j + \Omega_z\, k$), (locally constant), yields immediately:

$$
\begin{aligned}
s_x(i,j,k) &= \frac{s(i+1,j,k)-s(i-1,j,k)}{2} \simeq -A(i,j,k)\sin\Omega_x \sin\left(\Omega_x i+\Omega_y j+\Omega_z k\right)\\
s_y(i,j,k) &= \frac{s(i,j+1,k)-s(i,j-1,k)}{2} \simeq -A(i,j,k)\sin\Omega_y \sin\left(\Omega_x i+\Omega_y j+\Omega_z k\right)\\
s_z(i,j,k) &= \frac{s(i,j,k+1)-s(i,j,k-1)}{2} \simeq -A(i,j,k)\sin\Omega_z \sin\left(\Omega_x i+\Omega_y j+\Omega_z k\right)\\
s_{xy}(i,j,k) &= \frac{s_y(i+1,j,k)-s_y(i-1,j,k)}{2} \simeq -A(i,j,k)\sin\Omega_x \sin\Omega_y \cos\left(\Omega_x i+\Omega_y j+\Omega_z k\right)\\
s_{xz}(i,j,k) &= \frac{s_z(i+1,j,k)-s_z(i-1,j,k)}{2} \simeq -A(i,j,k)\sin\Omega_x \sin\Omega_z \cos\left(\Omega_x i+\Omega_y j+\Omega_z k\right)\\
s_{zy}(i,j,k) &= \frac{s_y(i,j,k+1)-s_y(i,j,k-1)}{2} \simeq -A(i,j,k)\sin\Omega_z \sin\Omega_y \cos\left(\Omega_x i+\Omega_y j+\Omega_z k\right)
\end{aligned}
$$

(4.11)

Finally, a discrete version of the C2TKEO, where the amplitude $A(i,j,k)$ is locally constant, is given by:

$$
\begin{aligned}
\Phi_2\left[s(x,y,z)\right] &= \left|s^2(i,j,k)-s(i-1,j,k)s(i+1,j,k)\right|+\left|s^2(i,j,k)-s(i,j-1,k)s(i,j+1,k)\right|\\
&+\left|s^2(i,j,k)-s(i,j,k-1)s(i,j,k+1)\right|+2\left|s_x(i,j,k)s_y(i,j,k)-s(i,j,k)s_{xy}(i,j,k)\right|\\
&+2\left|s_x(i,j,k)s_z(i,j,k)-s(i,j,k)s_{xz}(i,j,k)\right|+2\left|s_y(i,j,k)s_z(i,j,k)-s(i,j,k)s_{yz}(i,j,k)\right|\\
&= A^2(i,j,k)\sin^2\Omega_x + A^2(i,j,k)\sin^2\Omega_y + A^2(i,j,k)\sin^2\Omega_z\\
&+2\left|A^2(i,j,k)\sin\Omega_x\sin\Omega_y\right|+2\left|A^2(i,j,k)\sin\Omega_x\sin\Omega_z\right|+2\left|A^2(i,j,k)\sin\Omega_y\sin\Omega_z\right|\\
&= A^2(i,j,k)\left(\left|\sin\Omega_x\right|+\left|\sin\Omega_y\right|+\left|\sin\Omega_z\right|\right)^2
\end{aligned}
$$

(4.12)

The same discrete gradient approximations and recurrence formula lead to:

$$
\begin{aligned}
\Phi_4\left[s(x,y,z)\right] &= \Phi_4\left[s_x(i,j,k)\sin\Omega_x + s_y(i,j,k)\sin\Omega_y + s_z(i,j,k)\sin\Omega_z\right]\\
&= A^2(i,j,k)\left(\left|\sin\Omega_x\right|+\left|\sin\Omega_y\right|+\left|\sin\Omega_z\right|\right)^4
\end{aligned}
$$

(4.13)

Thus (2) and (3) provide an estimation of the envelope. Note that using the formula (2) or (3), one can directly demodulate a local AM signal, provided that the factor |sin Ω_x| + |sin

Ω_y| + |sin Ω_z| equals one. According to this remark, there are particular values of ($\omega_x,\omega_y,\omega_z$) and (xe,ye,ze) for which we expect more efficient demodulations. Finally, applying the transforms to the partial derivatives of an AM signal leads to the following results:

$$\begin{aligned}
&\Phi_2\left[s_x(i,j,k)\right] = A^2(i,j,k)\sin^2\Omega_x\left(\left|\sin\Omega_x\right|+\left|\sin\Omega_y\right|+\left|\sin\Omega_z\right|\right)^2\\
&\Phi_2\left[s_y(i,j,k)\right] = A^2(i,j,k)\sin^2\Omega_y\left(\left|\sin\Omega_x\right|+\left|\sin\Omega_y\right|+\left|\sin\Omega_z\right|\right)^2\\
&\Phi_2\left[s_z(i,j,k)\right] = A^2(i,j,k)\sin^2\Omega_z\left(\left|\sin\Omega_x\right|+\left|\sin\Omega_y\right|+\left|\sin\Omega_z\right|\right)^2\\
&\Phi_2\left[s_x(i,j,k)\pm s_y(i,j,k)\right] = A^2(i,j,k)\left(\sin\Omega_x\pm\sin\Omega_y\right)^2\left(\left|\sin\Omega_x\right|+\left|\sin\Omega_y\right|+\left|\sin\Omega_z\right|\right)^2\\
&\Phi_2\left[s_x(i,j,k)\pm s_z(i,j,k)\right] = A^2(i,j,k)\left(\sin\Omega_x\pm\sin\Omega_z\right)^2\left(\left|\sin\Omega_x\right|+\left|\sin\Omega_y\right|+\left|\sin\Omega_z\right|\right)^2\\
&\Phi_2\left[s_z(i,j,k)\pm s_y(i,j,k)\right] = A^2(i,j,k)\left(\sin\Omega_z\pm\sin\Omega_y\right)^2\left(\left|\sin\Omega_x\right|+\left|\sin\Omega_y\right|+\left|\sin\Omega_z\right|\right)^2
\end{aligned} \qquad \textbf{(4.14)}$$

The previous equations provide flexible ways to detect the carrier frequencies and the envelope, such as:

$$\sin\Omega_x = \left|\sqrt{\frac{\Phi_2\left[s_x(i,j,k)\right]}{\Phi_2\left[s(i,j,k)\right]}}\right| \qquad \textbf{(4.15)}$$

$$\begin{aligned}
\sin\Omega_y &= sign\left(\sin\Omega_x\sin\Omega_y\right)\sqrt{\frac{\Phi_2\left[s_y(i,j,k)\right]}{\Phi_2\left[s(i,j,k)\right]}}\\
&= sign\left(\frac{\left(\Phi_2\left[s_x+s_y\right]-\Phi_2\left[s_x-s_y\right]\right)}{4\Phi_2\left[s(i,j,k)\right]}\right)\sqrt{\frac{\Phi_2\left[s_y(i,j,k)\right]}{\Phi_2\left[s(i,j,k)\right]}}
\end{aligned} \qquad \textbf{(4.16)}$$

$$\begin{aligned}
\sin\Omega_z &= sign\left(\sin\Omega_x\sin\Omega_z\right)\sqrt{\frac{\Phi_2\left[s_z(i,j,k)\right]}{\Phi_2\left[s(i,j,k)\right]}}\\
&= sign\left(\frac{\left(\Phi_2\left[s_x+s_z\right]-\Phi_2\left[s_x-s_z\right]\right)}{4\Phi_2\left[s(i,j,k)\right]}\right)\sqrt{\frac{\Phi_2\left[s_z(i,j,k)\right]}{\Phi_2\left[s(i,j,k)\right]}}
\end{aligned} \qquad \textbf{(4.17)}$$

$$\left|A(i,j,k)\right| = \left|\sqrt{\frac{\Phi_2\left[s(i,j,k)\right]^2}{\Phi_4\left[s(i,j,k)\right]}}\right| \qquad \textbf{(4.18)}$$

4.3 PROCEDURE OF 3D FRINGE PROCESSING

In general, the techniques of 3D fringe processing developed in this work consist of three main steps: (i) pre-processing for offset removal and suppressing the noise, (ii) envelope detection and (iii) post-processing in order to determine the measurement results of surface height more accurately. In order to describe more clearly this procedure of 3D fringe signal processing, we use the measurements on the sample of Graphene, consisting of an image stack XYZ of 99 x 338 x 50 pixels. The description of the acquisition data of measurements on the Graphene obtained by the microscope system is given in Appendix-1: Data of Sample.

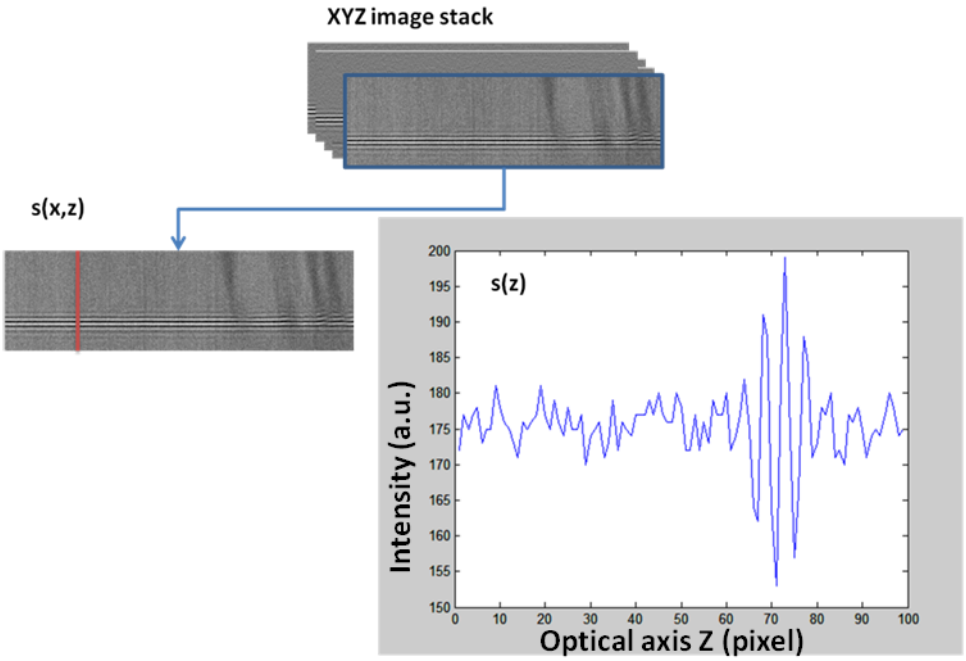

Fig. 77 Fringe signals of Graphene

a. Pre-processing

During the acquisition process in CSI, the different sources of signal noise and an additive offset component (background) can appear in the fringe signals. In order to remove this offset component and the additive noise, it is important to filter out both

of them before applying the fringe envelope detection. In CSI, it is common to use a prefilter, such as the Global average, Local average or Derivative. In this work, we have proposed using the EMD in order to remove the offset component which is applied with a denoising filter such as the wiener filter or Savitsky Golay filter. The selection of the type of pre-processing technique to perform fringe signal processing depends on the nature of the signal, the computation time available and the precision of the result required.

In Fig. 77, the fringe signals from the Graphene can be seen to have an offset component which is relatively constant. Through the pre-processing step, we obtain the pre-filtered fringe signals of Graphene, as illustrated in Fig. 78. In the figure, it can be seen that the background of the fringe signals has been removed and its noise reduced.

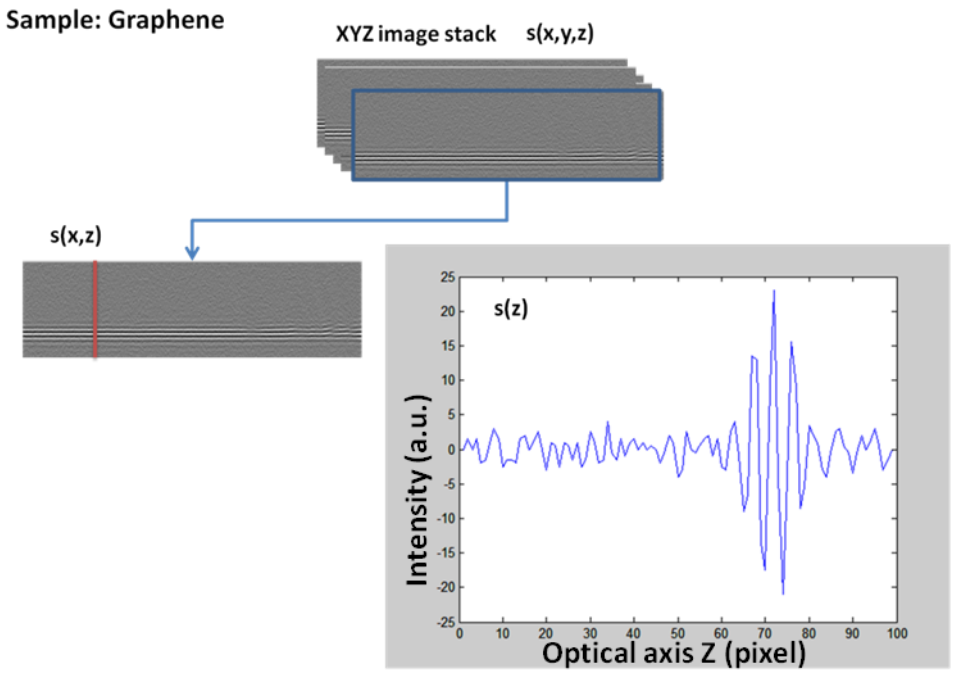

Fig. 78 Pre-filtered fringe signals of Graphene after pre-processing step

b. Envelope Detection

In 1D fringe signal processing, through the envelope detection technique, we obtain the fringe envelope in one dimension (optical axis-*z*), while in 2D fringe signal processing, we can obtain the cross sectional profile of a sample, also known as a B-scan in optical coherence tomography (two dimensional: lateral axis-*x* and optical axis-*z*). Meanwhile, in 3D fringe signal processing, we can obtain directly the 3D

fringe envelope in volume (three dimensional: lateral axis-*x*, lateral axis-*y* and optical axis-*z*). Fig. 79 shows the volume of amplitude $A(x,y,z)$ of fringe signals obtained using 3D fringe envelope detection.

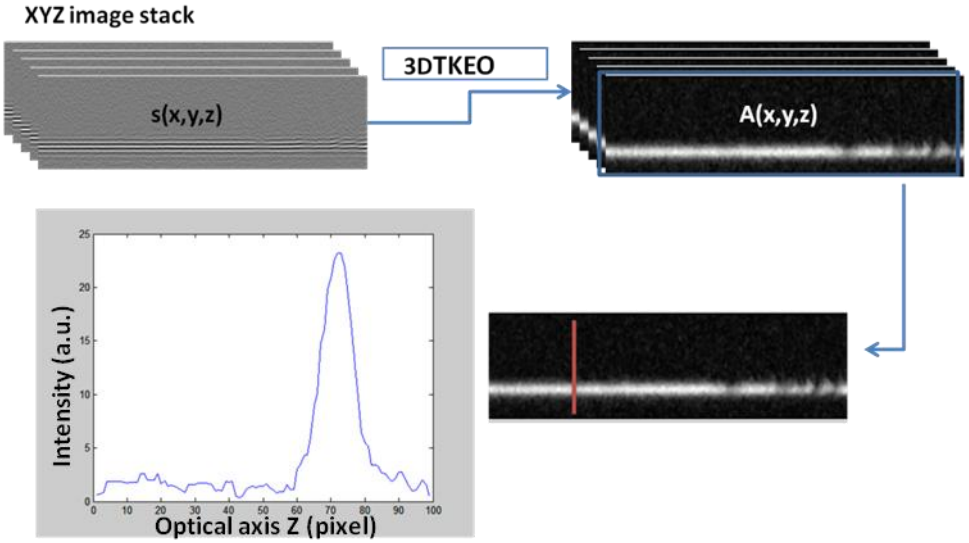

Fig. 79 The volume of amplitude $A(x,y,z)$ of fringe signals obtained using 3D fringe envelope detection

c. Post-processing

In the case of noisy fringe signals, the fringe patterns can still appear in the resulting fringe envelope even though a pre-filtering process has been used before applying the fringe envelope detection. For this reason, a smoothing filter such as a cubic spline is used to suppress the fringe patterns on the envelope, hence allowing an improvement in the accuracy of the envelope peak detection. The peak position obtained is then used as an initial value along with the neighbourhood at the peak for the next process, i.e. Gaussian fitting. The curve fitting method using Gaussian fitting is implemented in order to determine more precisely the envelope peak and to improve the axial sensitivity.

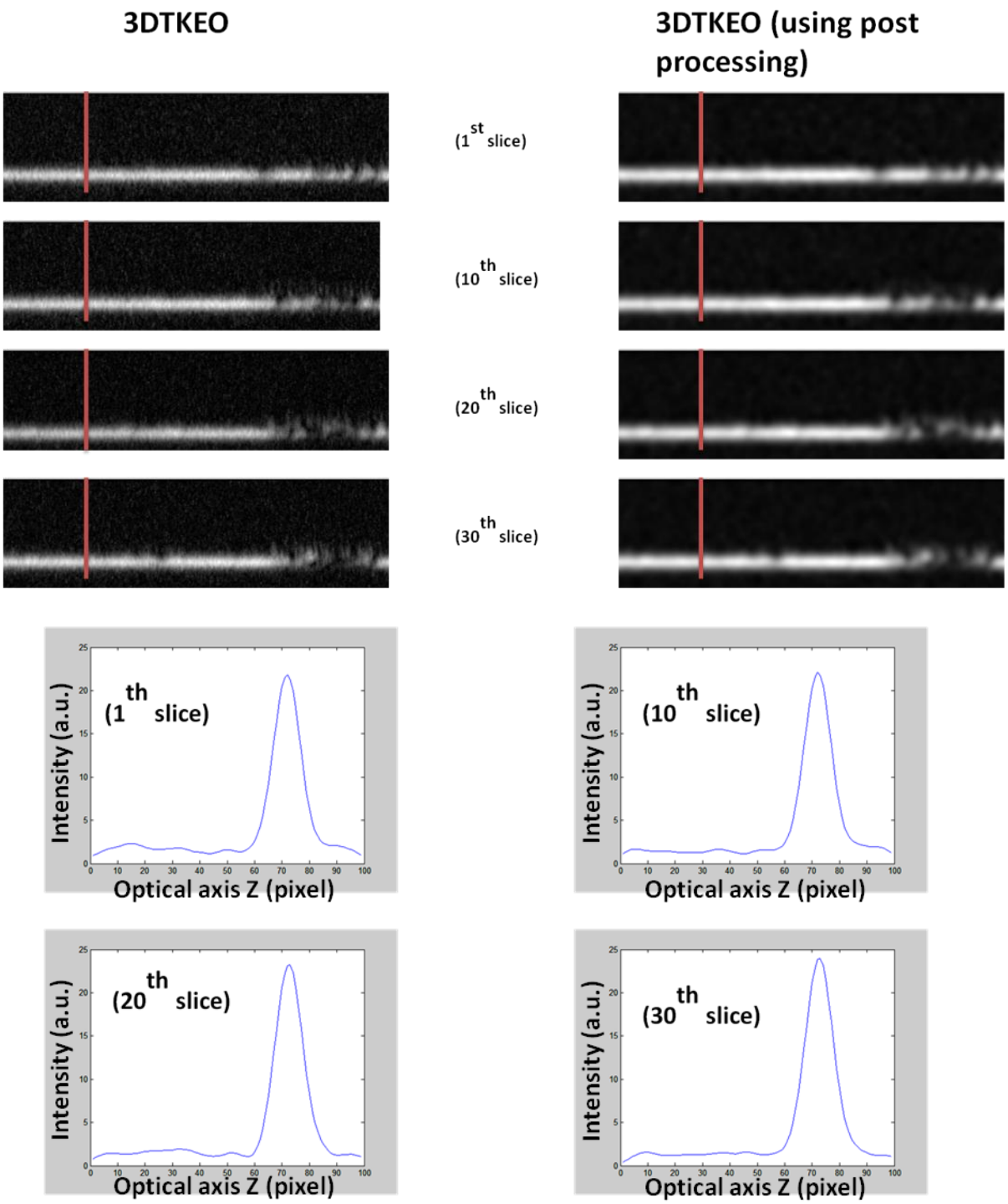

Fig. 80 Improvement results of 3D envelope detection using post-processing

Then, the final step of peak detection of the fringe envelope along the optical axis *z* at each point (*x*,*y*) along lateral axis is required since its peak represents the surface position of the sample. Fig. 81 shows the surface extraction of a sample of Graphene obtained using 3D fringe signal processing.

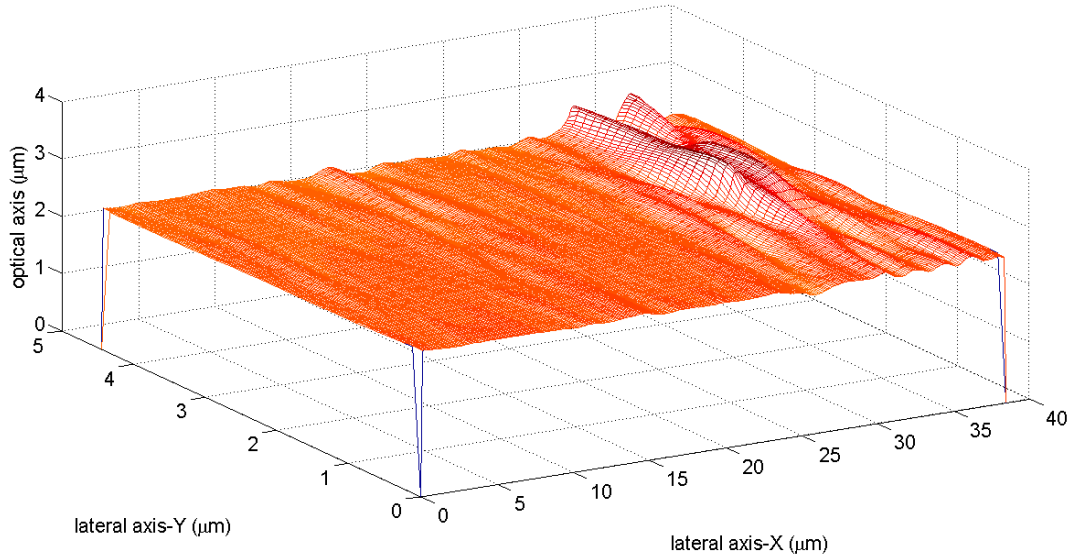

Fig. 81 Surface extraction of a sample of Graphene obtained using 3D fringe signal processing

4.4 PERFORMANCE COMPARISON OF ENVELOPE DETECTION USING 1D, 2D, 3D FRINGE PROCESSING

Some simulations have been performed using a Matlab program in order to compare the performance of the envelope detection techniques using the Z-scan technique (1D Fringe Processing), XZ-scan technique (2D Fringe Image Processing), and XYZ-scan technique (3D Fringe Processing).

The synthetic surface and the associated fringe signals we have used in this simulation to test all the 1D, 2D, 3D Fringe Processing algorithms is based locally on the general model expressed by equation (1) along the optical axis Z, with a 40 nm sampling step, for each lateral position X. The resulting XYZ image of the synthetic surface is shown in Fig. 82. The synthetic surfaces and the associated fringe signals represent a flat and a wavy transparent layer on a substrate i.e, two surfaces. An additive non-linear offset and Gaussian noise are added onto this synthetic data (10% and 20%) which commonly appear in the fringe signal during the acquisition process and result in a reduced precision of the surface measurement.

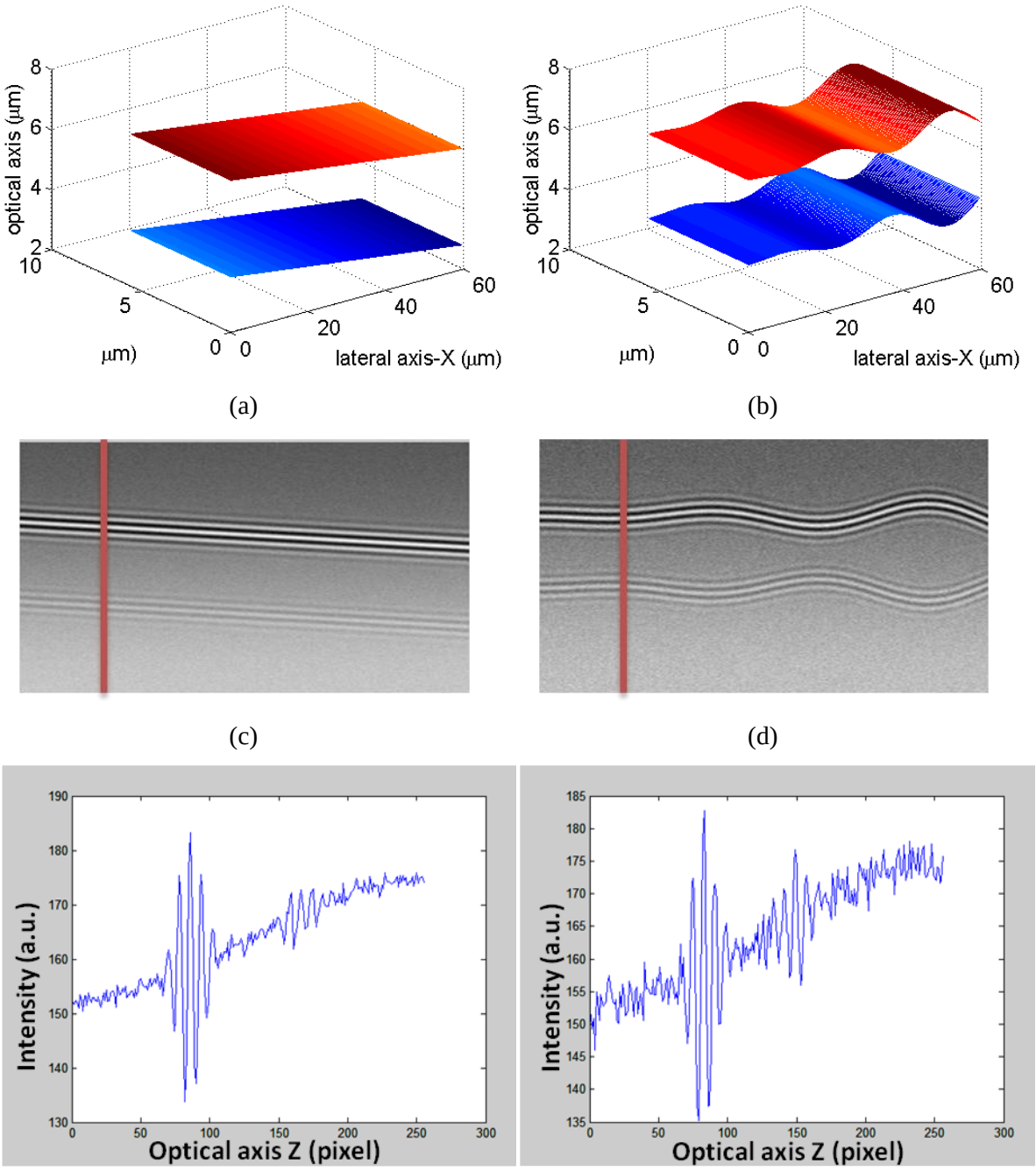

Fig. 82 Synthetic surface (XYZ image) 256 x 256 x 25 pixel and it's fringe signals: (a), (c), (e) flat transparent layer and (b), (d), (f) wavy transparent layer.

Fig. 83 and Fig. 84 show the example of the results of signal processing for the flat and wavy transparent layers. Fig. 83(a) and Fig. 84(a) show the fringe envelope obtained, while Fig. 83(b) and Fig. 84(b) show the surface extracted by performing signal processing using 3D fringe processing. Meanwhile, Fig. 85 shows the results of surface

extraction obtained using 1D, 2D, and 3D fringe processing on a transparent and wavy synthetic fringe signal.

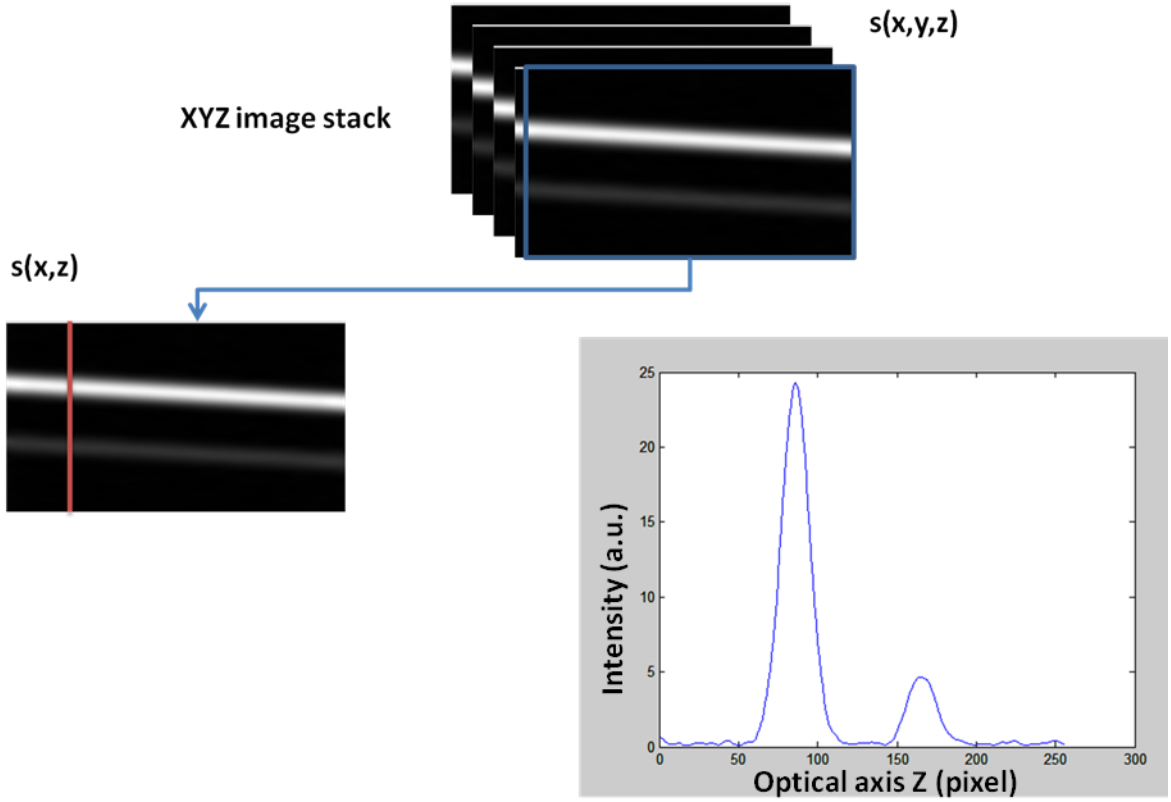

(a)

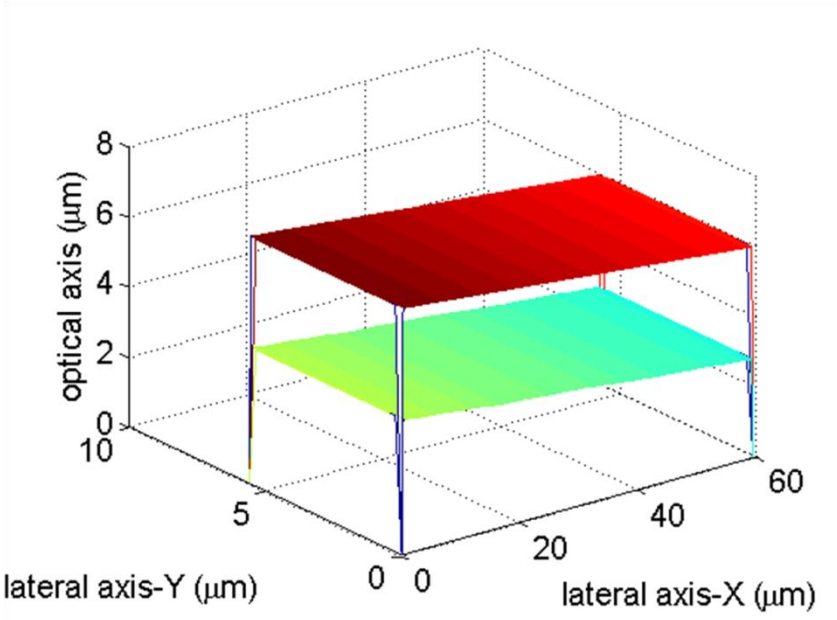

(b)

Fig. 83 Signal processing analysis for synthetic flat transparent surface

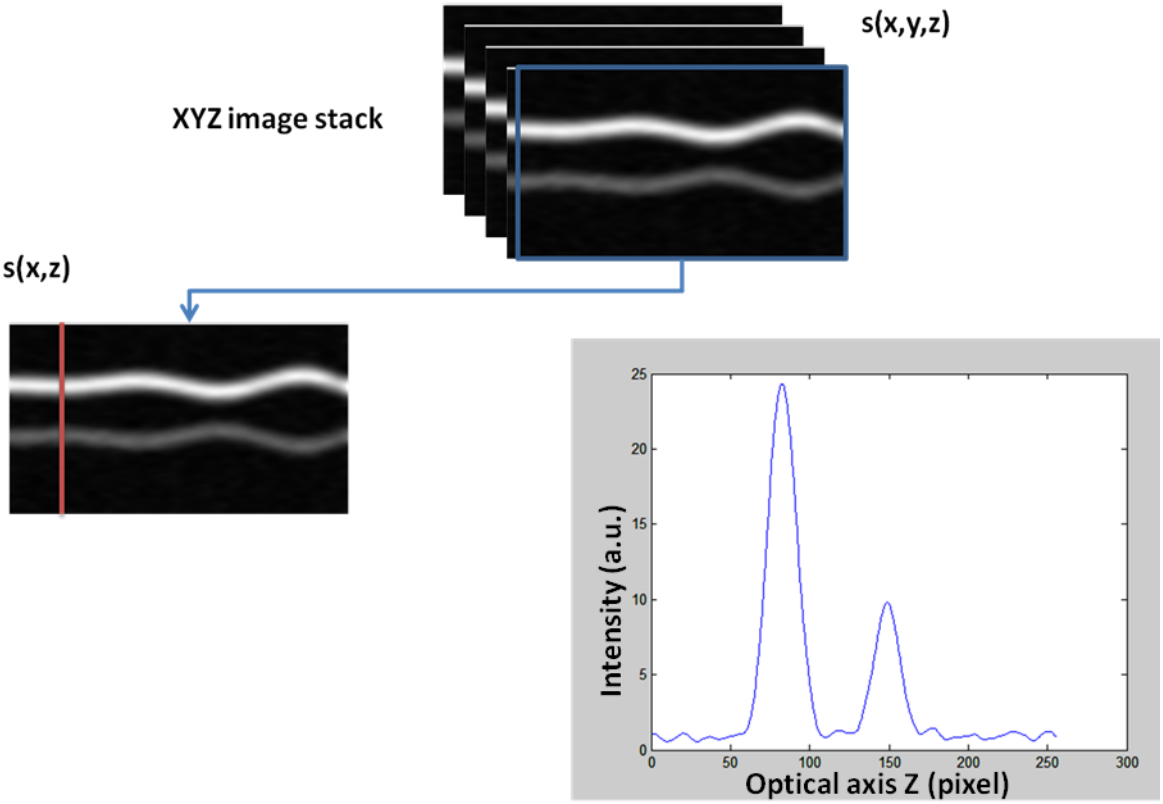

(a)

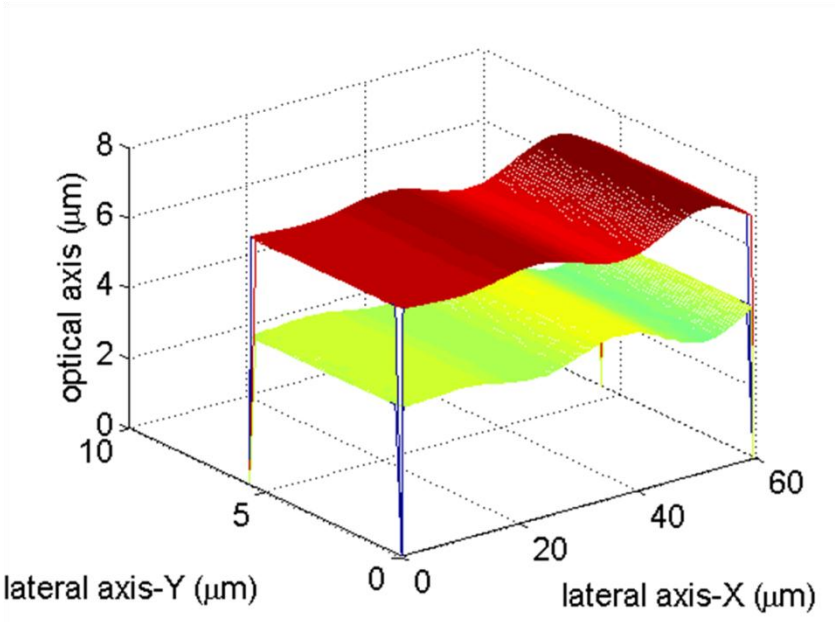

(b)

Fig. 84 Signal processing analysis for synthetic wavy transparent surface

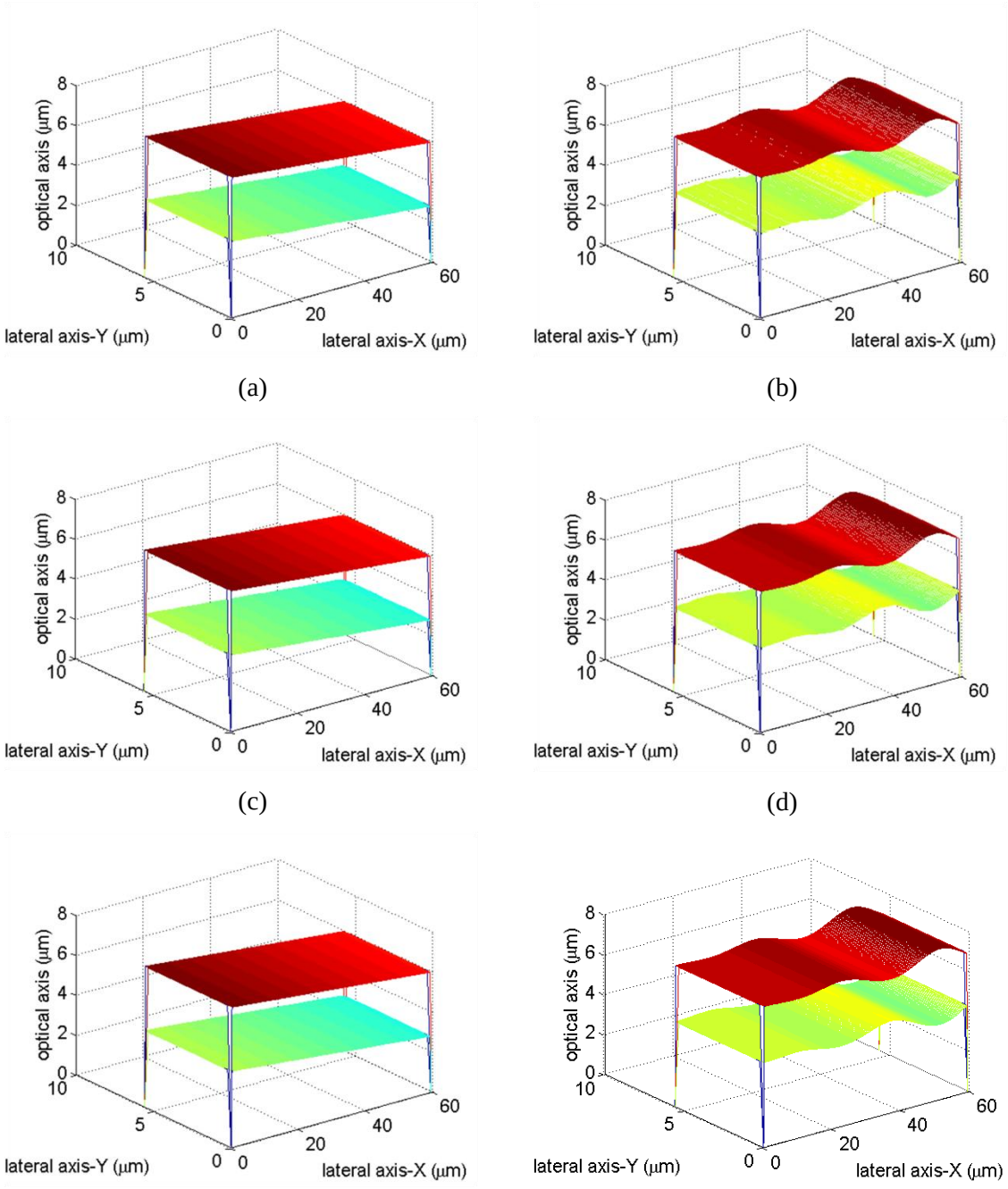

Fig. 85 Surface extracted obtained using: (a) and (b) Z-scan Technique (1DTKEO), (c) and (d) XZ-scan Technique (2DTKEO), (e) and (f) XYZ-scan Technique (3DTKEO).

Based on Fig. 86, the qualitative performance comparison for obtaining the fringe envelope can be observed for the different types of fringe signal processing. As illustrated in the figure, it can be observed that the fringe envelope obtained using 2D and 3D fringe processing (taking into account the spatial neighbourhood) is better than 1D fringe processing. The shape of the envelope obtained using 2D and 3D fringe signal processing

is closer to a Gaussian function than with 1D fringe signal processing. This result makes it easier to determine the peak of envelope more precisely.

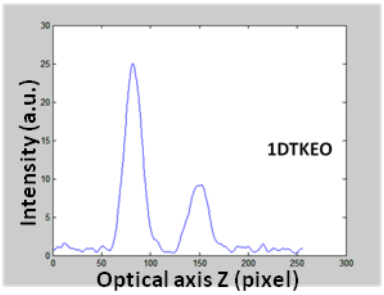

(a)

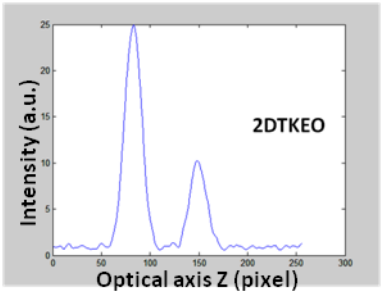

(b)

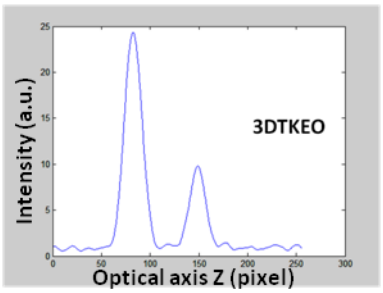

(c)

Fig. 86 1D Fringe envelope obtained using (a) 1DTKEO, (b) 2DTKEO, (c) 3DTKEO

Table 11 Performance Comparison of Envelope Detection using 1D TKEO, 2D TKEO and 3D TKEO (nm)

Pre-filt.	Suppress the offset: EMD Suppress the noise: Savitzky-Golay filter					
Env. Det.	Z-Scan Technique (1D Fringe Processing using 1DTKEO)		XZ-Scan Technique (2D Fringe Processing using 2DTKEO)		XYZ-Scan Technique (3D Fringe Processing using 3DTKEO)	
Post-filt.	Smooth the amplitude envelope using cubic smoothing spline Correct the peak curve using Gaussian estimation and interpolation					
mean absolute error (nm)						
noise(σ)	1st surf.	2nd surf.	1st surf.	2nd surf.	1st surf.	2nd surf.
flat transparent layer						
10%	**0.71**	**4.55**	**0.52**	**3.94**	**0.33**	**1.47**
20%	**2.05**	**8.75**	**1.39**	**8.19**	**0.41**	**3.49**
wavy transparent layer						
10%	**3.51**	**8.63**	**3.10**	**6.41**	**1.87**	**2.91**
20%	**6.08**	**18.17**	**5.51**	**13.06**	**2.42**	**4.83**

Table 11 summarizes the results of the performance comparison of fringe signal processing using 1D TKEO, 2D TKEO and 3D TKEO. Based on the table, we observe that the fringe signal processing which takes into account the spatial neighbourhood (2D, 3D) has the advantage of better measurements in the terms of precision. This can be observed by the smaller mean absolute error value. The smaller is the value of this mean absolute error, the better is the performance of the algorithm, in terms of precision.

4.5 EVALUATION OF THE MEASUSUREMENT ACCURACY USING STEP HEIGHT STANDARD

For further evaluation of the developed algorithm of continuous 3DTKEO, the measurement accuracy is calibrated using a calibration standard, i.e. Step Height Standard (SHS). These standards are common used for measurement calibration of mechanical or optical profilers, including interference microscopy. For the traceability of the standard, it is certified by a National Metrology Institute (NMI). The feature of SHS that we used for this calibration is the step height parameter. In this work, we used a step height standard fabricated by VLSI Standard Inc, consisting of a 25 mm x 25 mm x 3 mm and has step height value of **1.7803 ± 0.011 µm**. Fig. 87 shows the camera image of the step-height standard (VLSI Standard Inc.).

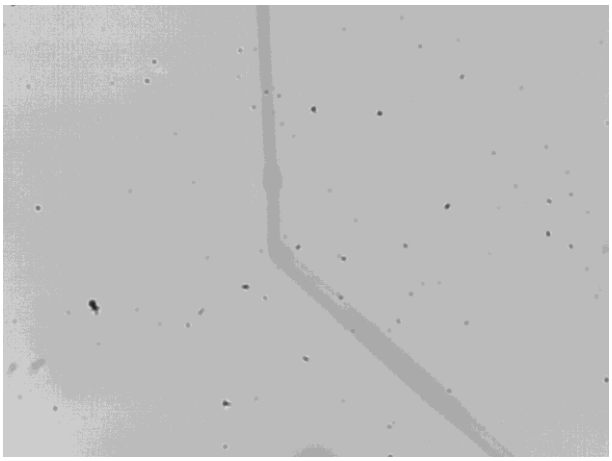

Fig. 87 Camera image (XY slice) of the step-height standard (VLSI Standard Inc.)

For the calibration, three different microscopes in the IPP team were used to provide measurements for performing the technique of 3D fringe processing. They are the modified Leitz-Linnik microscope, the new Fogale microscope ("Michelin"), and the

modified (immersion) Fogale microscope. The description of acquisition data of the measurements on the SHS sample obtained by the microscope system is given in Appendix-1: Data of Sample.

a. Measurement results obtained by the Leitz-Linnik microscope

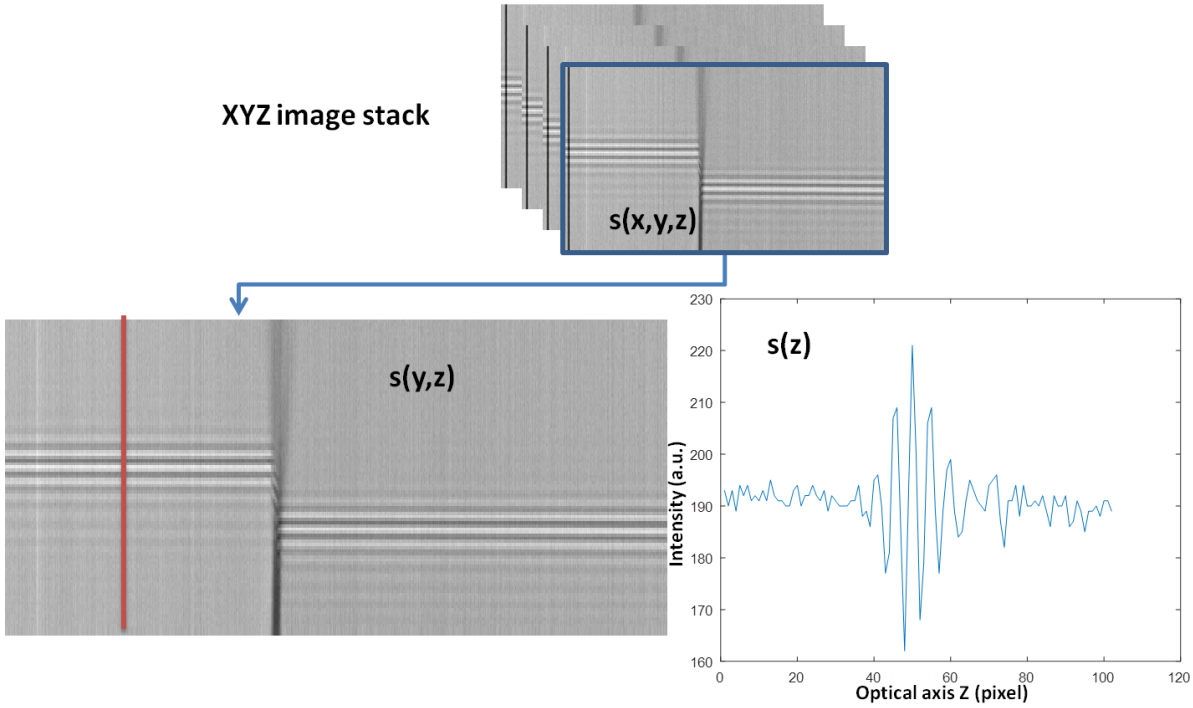

Fig. 88 Fringe signal processing of Step Height Standards (SHS) by the modified Leitz-Linnik microscope

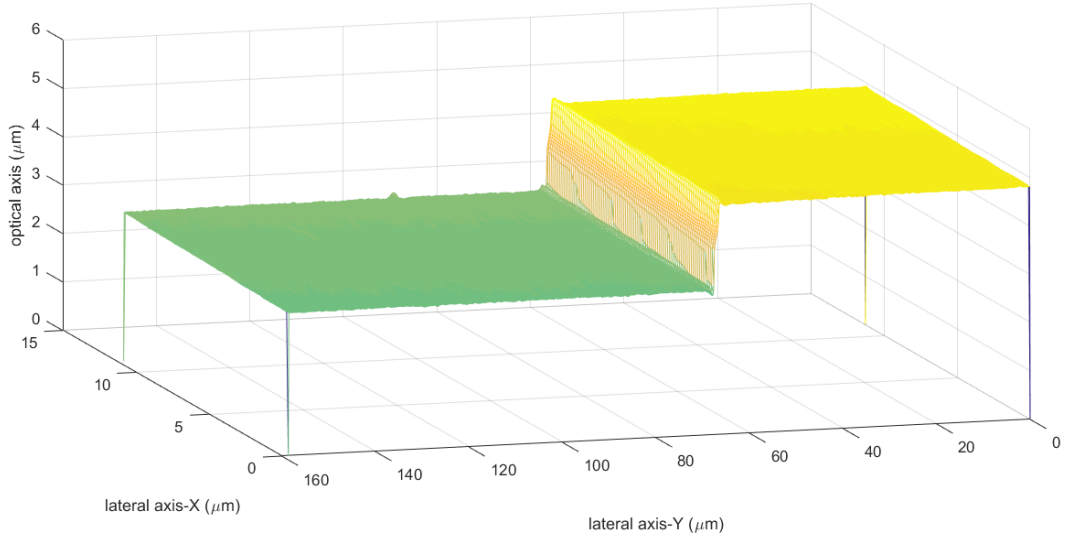

Fig. 89 Surface extracted of the Step Height Standards (SHS) obtained using 3D fringe signal processing on measurements from the modified Leitz-Linnik microscope

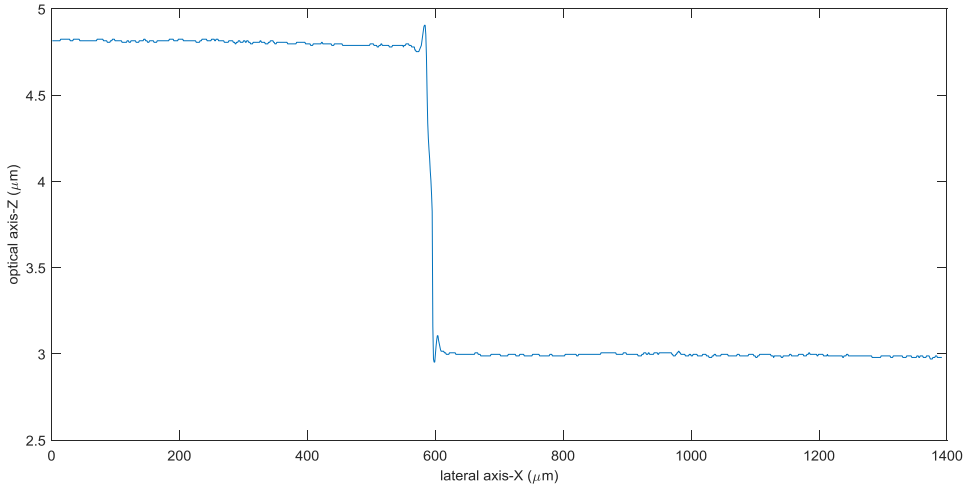

Fig. 90 Line profile of the Step Height Standards (SHS) obtained using 3D fringe signal processing on measurements with the modified Leitz-Linnik microscope

b. Measurement results obtained by the new Fogale microscope ("Michelin")

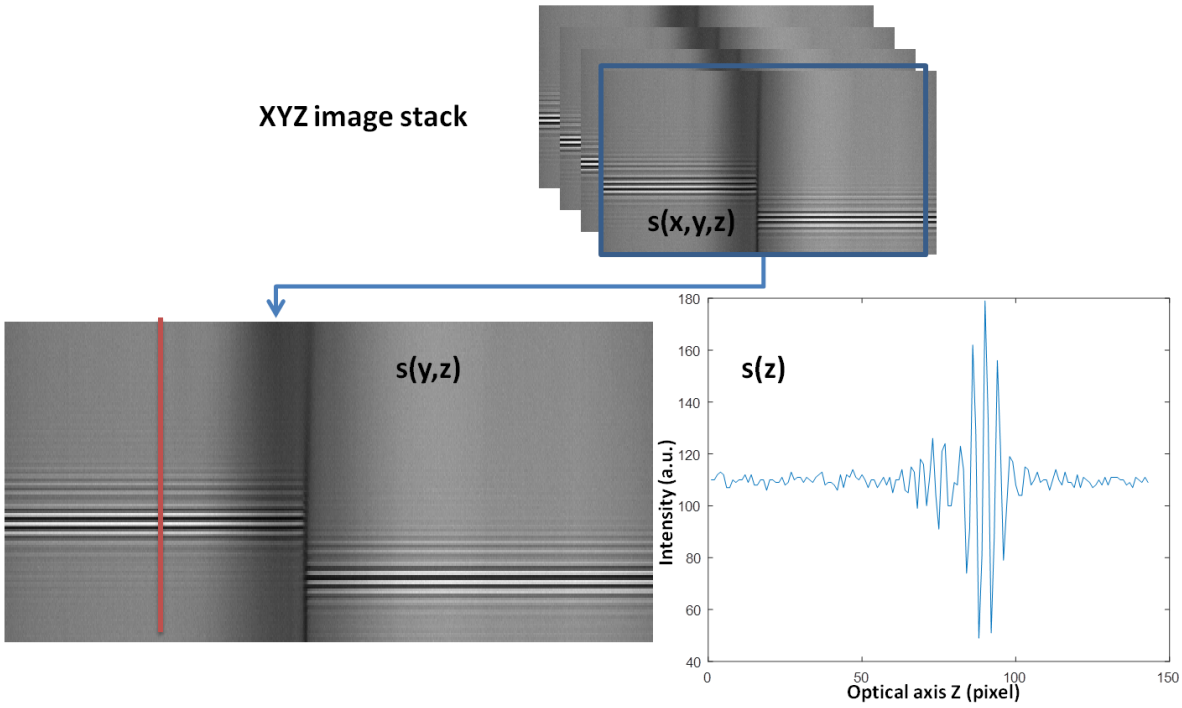

Fig. 91 Fringe signal processing of the Step Height Standards (SHS) from measurements on the new Fogale microscope ("Michelin")

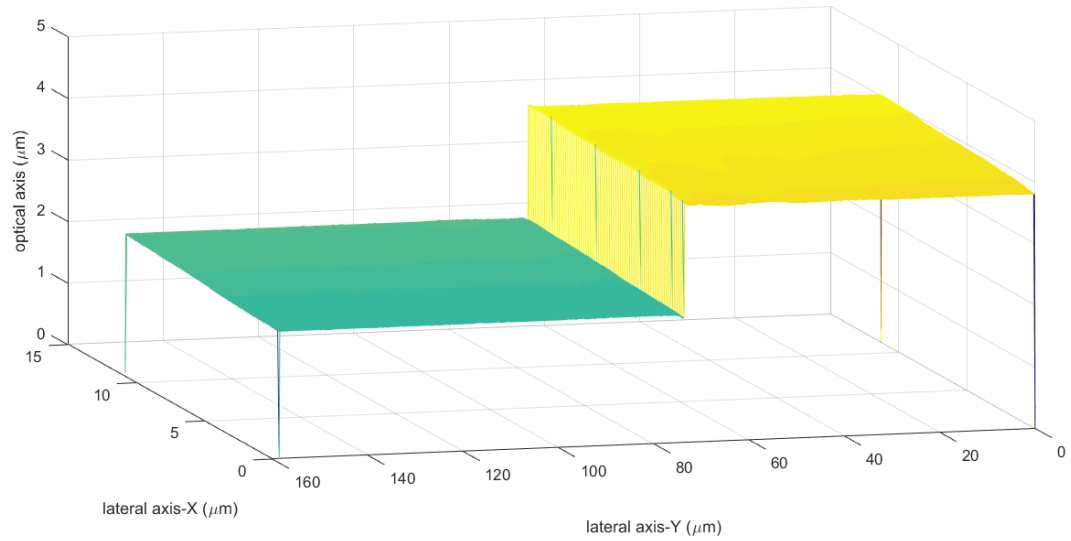

Fig. 92 Surface extracted of the Step Height Standard (SHS) obtained using 3D fringe signal processing from measurements with the new Fogale microscope ("Michelin")

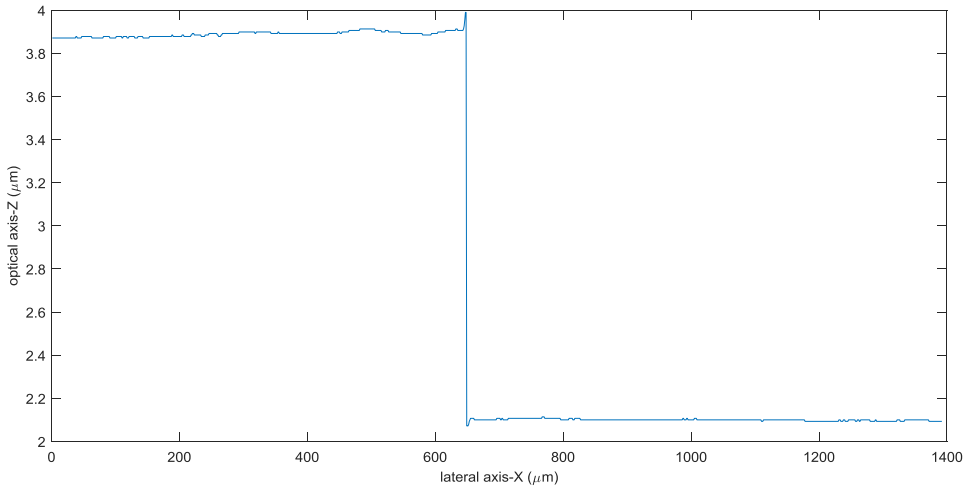

Fig. 93 Line profile of the Step Height Standards (SHS) obtained using 3D fringe signal processing from measurements with the new Fogale microscope ("Michelin")

c. Measurement results obtained by the "immersion" Fogale microscope

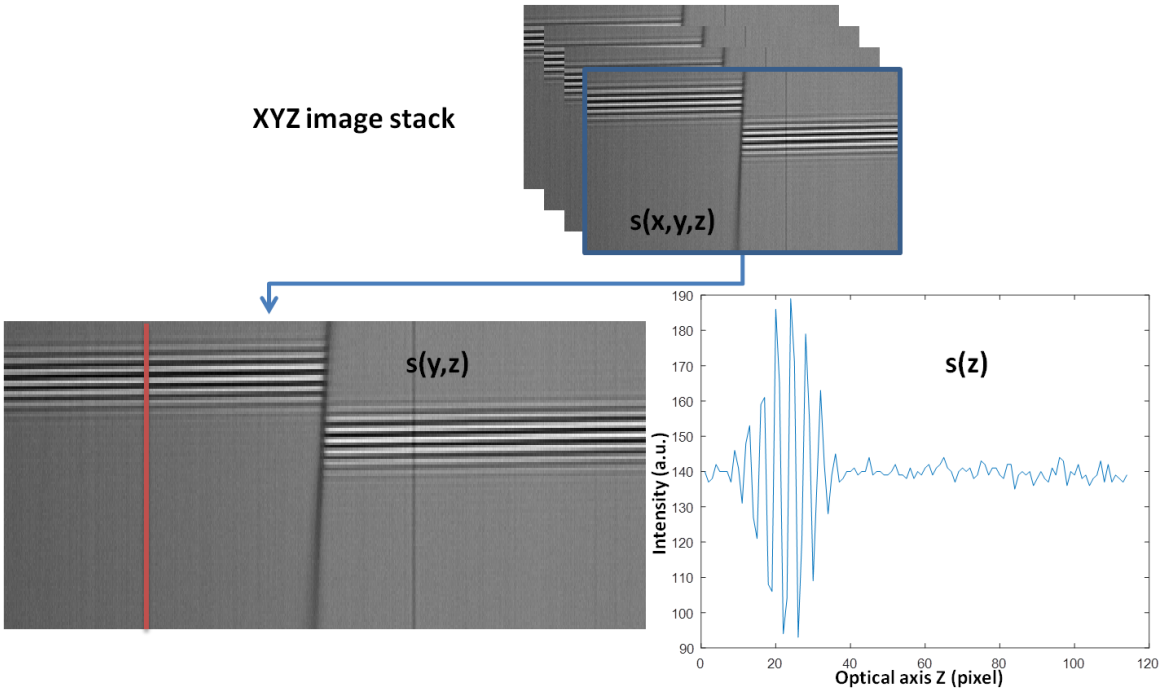

Fig. 94 Fringe signal processing of the Step Height Standard (SHS) from measurements with the "immersion" Fogale microscope

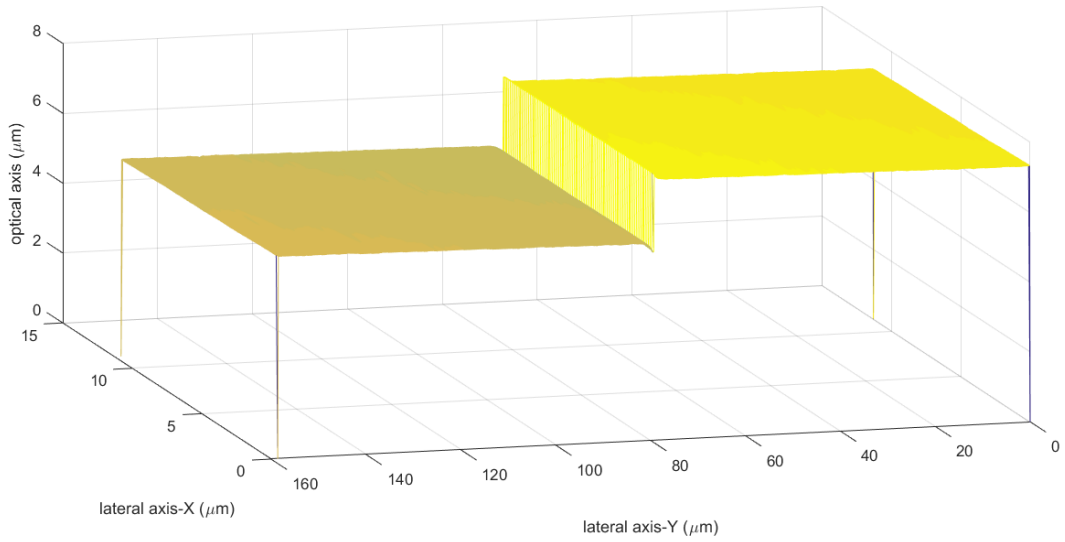

Fig. 95 Surface extracted of the Step Height Standard (SHS) obtained using 3D fringe signal processing on measurements with the "immersion" Fogale microscope

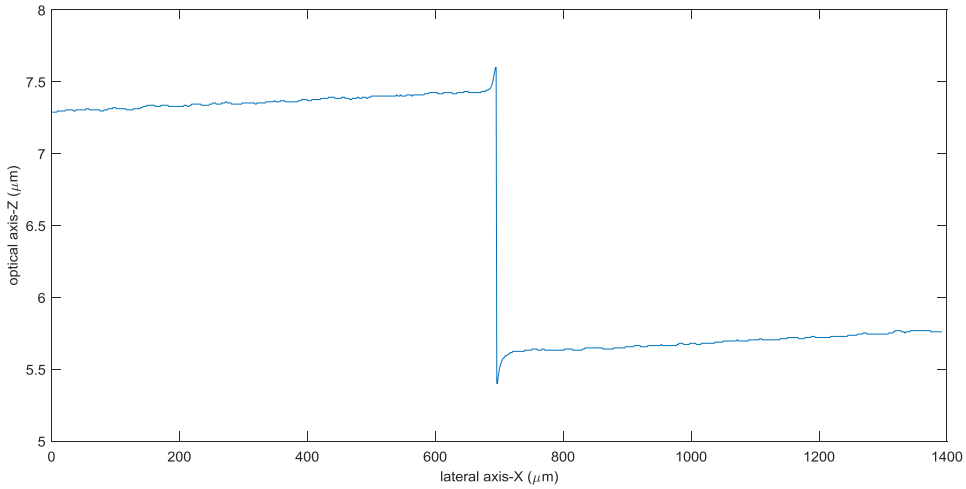

Fig. 96 Line profile of the Step Height Standard (SHS) obtained using 3D fringe signal processing on measurements with the "immersion" Fogale microscope

Table 12 Calibration results of 3D fringe signal processing (3D TKEO) using Step Height Standards (SHS)

Microscope type	Step Height Standard (µm)	Measurement results (µm)	Error (µm)
Leitz-Linnik Mic.	**1.7803 ± 0.011**	1.79	0.009
"Michelin" Fogale Mic.		1.778	0.002
"Immersion" Fogale Mic.		1.776	0.004

Table 12 and Fig. 97 show the calibration results of 3D fringe signal processing (3D TKEO) using the Step Height Standard (SHS). Based on the table, we observe that the measurement error generated by the Leitz-Linnik microscope, the new Fogale (Michelin) Microscope, and the "immersion" Fogale microscope using 3D fringe signal processing is still below the tolerance limit of the Step Height Standard (SHS) error, having a value of 0.011 µm. The results show that the 3D fringe signal processing (3D TKEO) algorithm developed is compatible with the 3D microscopes in the IPP team and give accurate results.

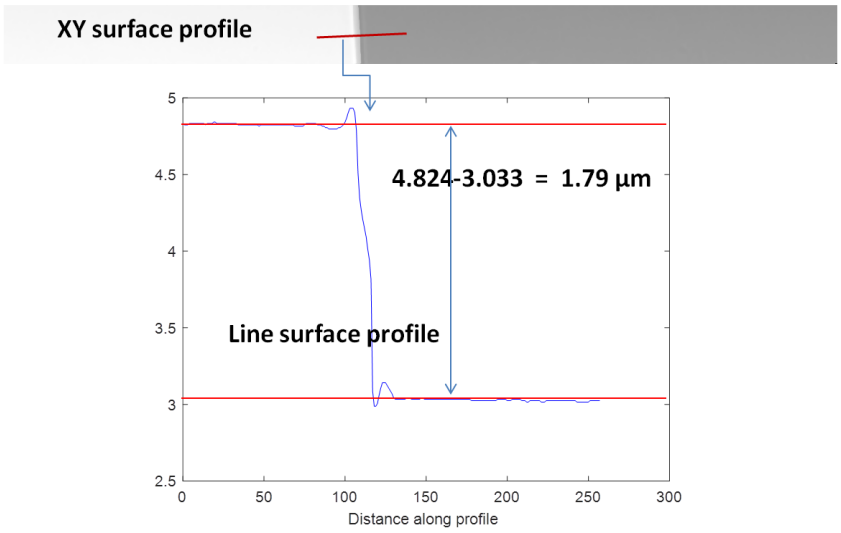

(a)

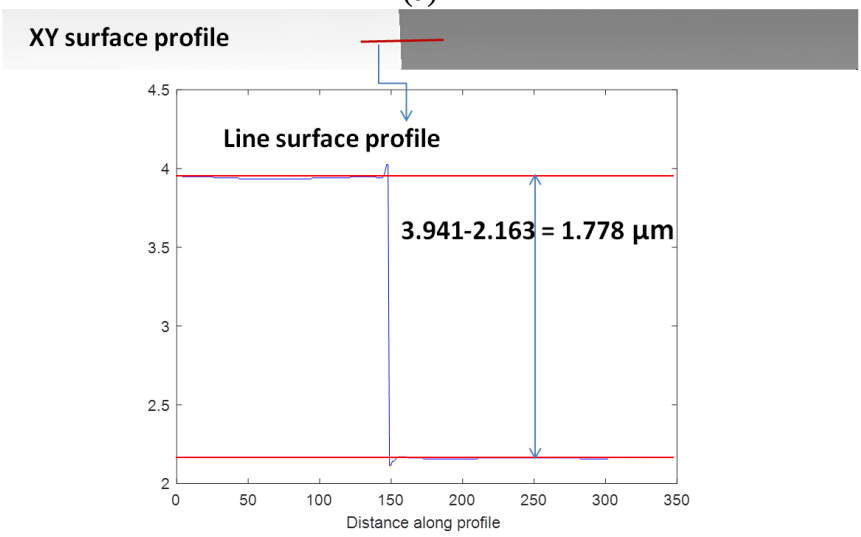

(b)

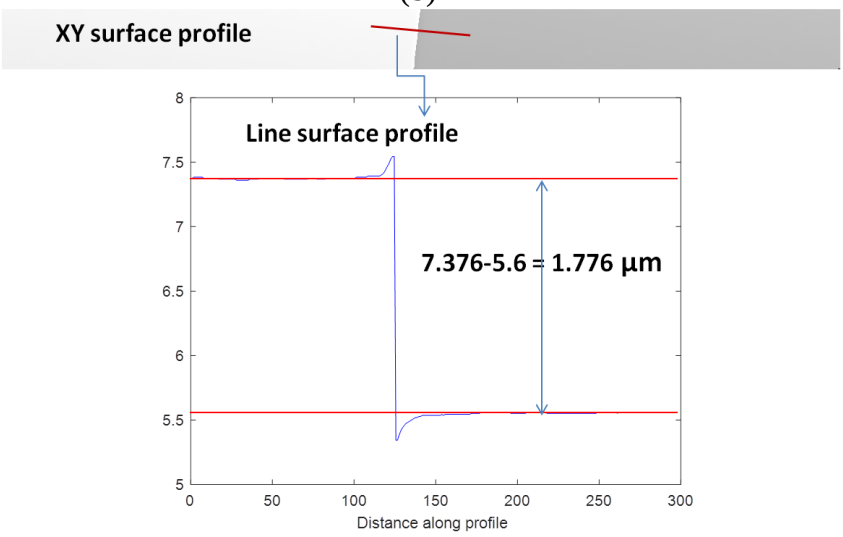

(c)

Fig. 97 The measured step height obtained using: (a) Leitz-Linnik microscope; (b) "Michelin" Fogale Microscope; (c) "immersion" Fogale microscope

4.6 PERFORMANCE OF 3D FRINGE PROCESSING ON DIFFERENT REAL SAMPLES

We have also applied the algorithm to other real data, i.e. DOE (Diffractive Optical Elements), Resin on Silicon, Cable and Rock. The description of acquisition data of the mentioned samples obtained by the microscope system is given in Appendix-1: Data of Sample.

a. DOE (80x 512 x 40)

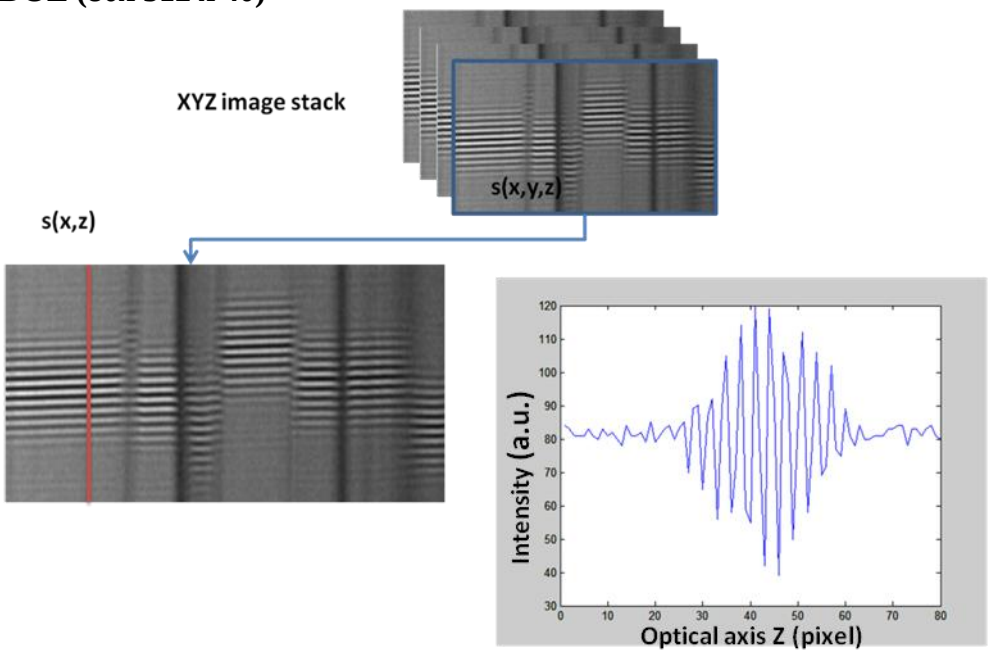

Fig. 98 Fringe signals of DOE (Diffractive Optical Elements)

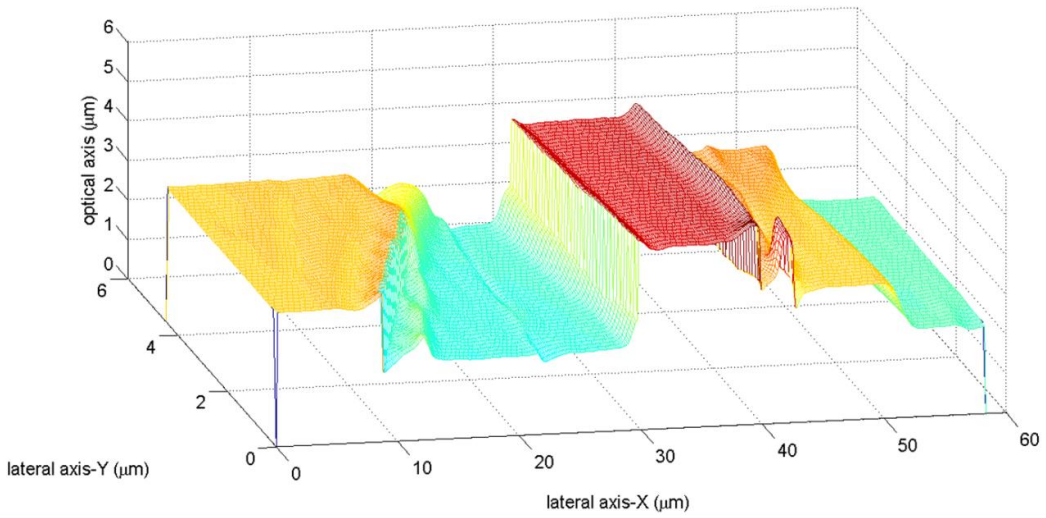

Fig. 99 Surface extraction of a sample of DOE (Diffractive Optical Elements) obtained using 3D fringe signal processing

These first results on a real sample, in this case a DOE, show very good measurement, indicated by the surface being continuous and containing less unmeasured points.

b. Resin on Si (166 x 908 x 20)

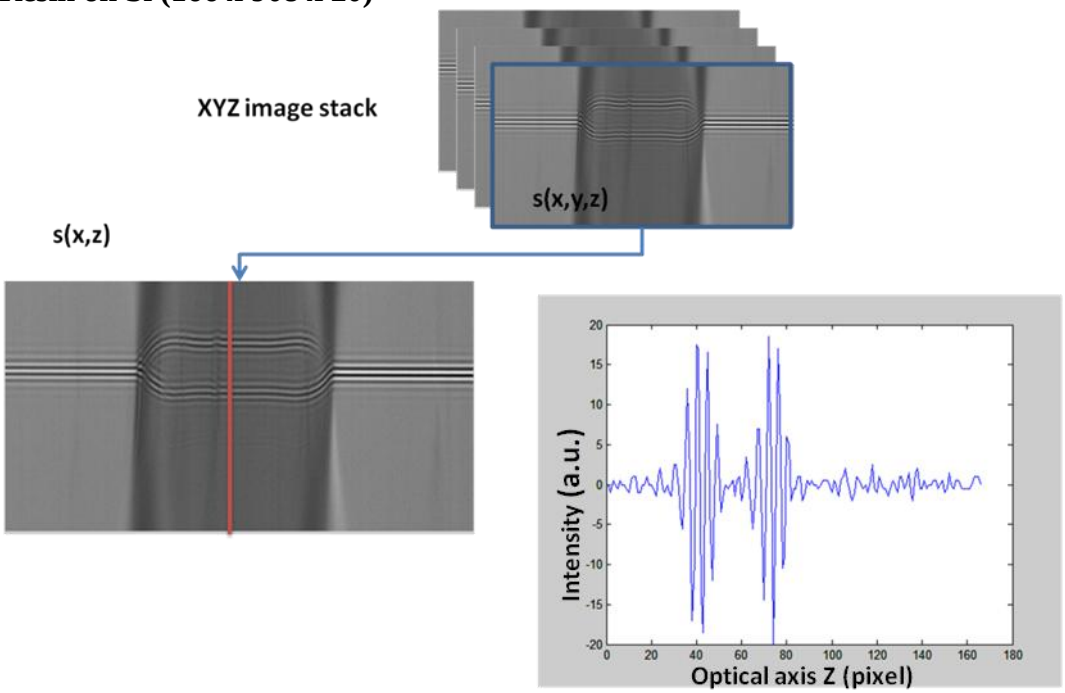

Fig. 100 Fringe signals of Resin on Silicon

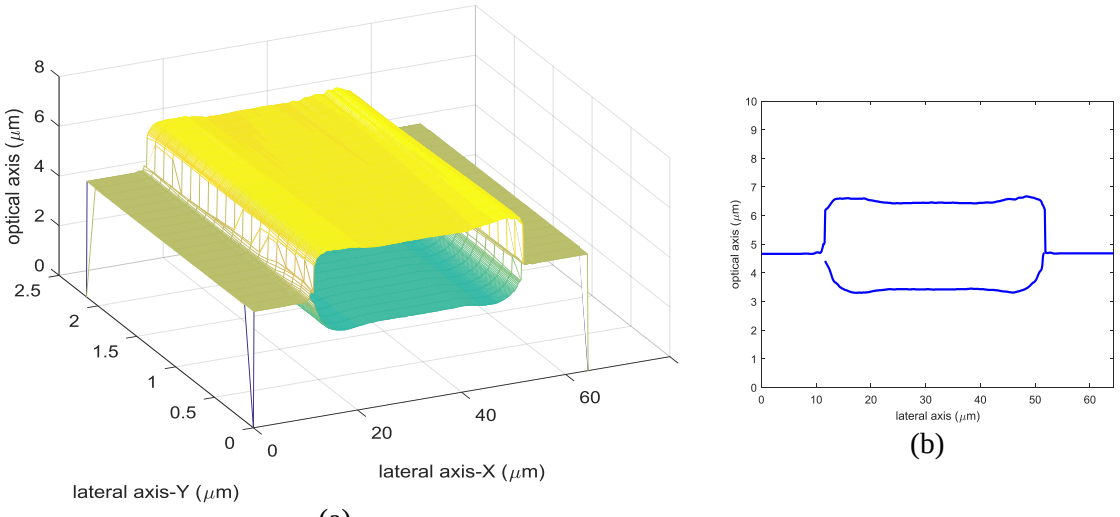

(a) (b)

Fig. 101 (a) Surface extraction of a sample of Resin on Silicon obtained using 3D fringe signal processing and (b) the line profile

In the case of the Resin on Silicon, the measurement is particularly successful, indicated by the improved measurement at the edges of the resin layer.

c. Cable (669 x 100 x 100)

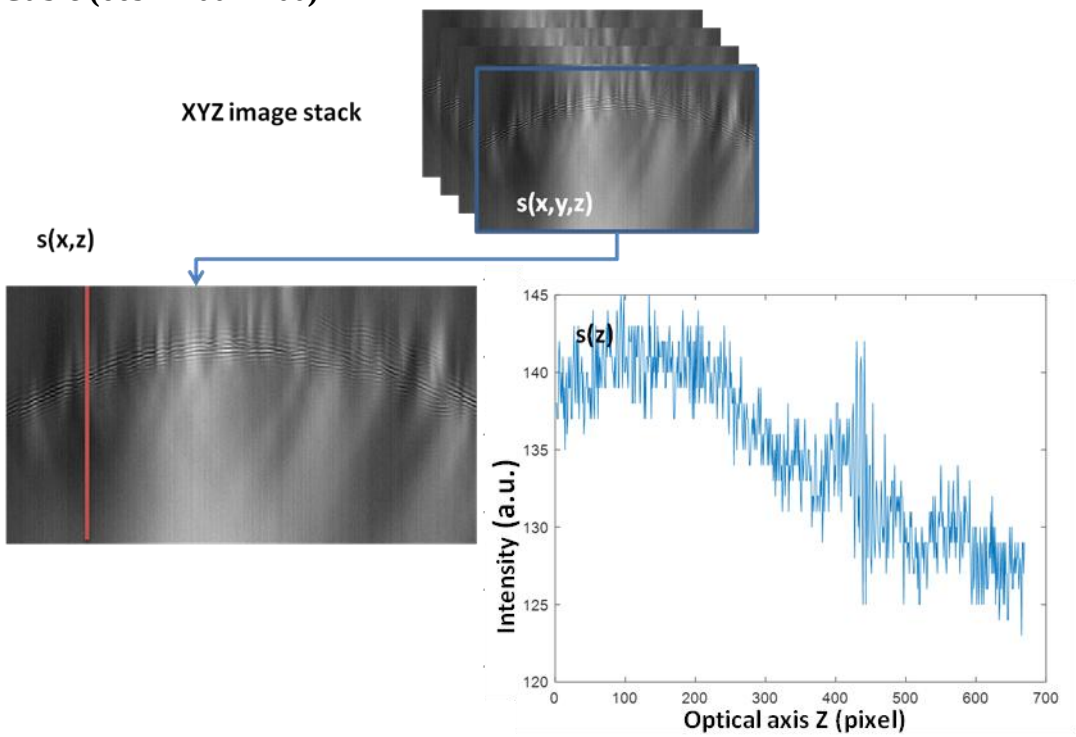

Fig. 102 Fringe signals from measurements on a Cable

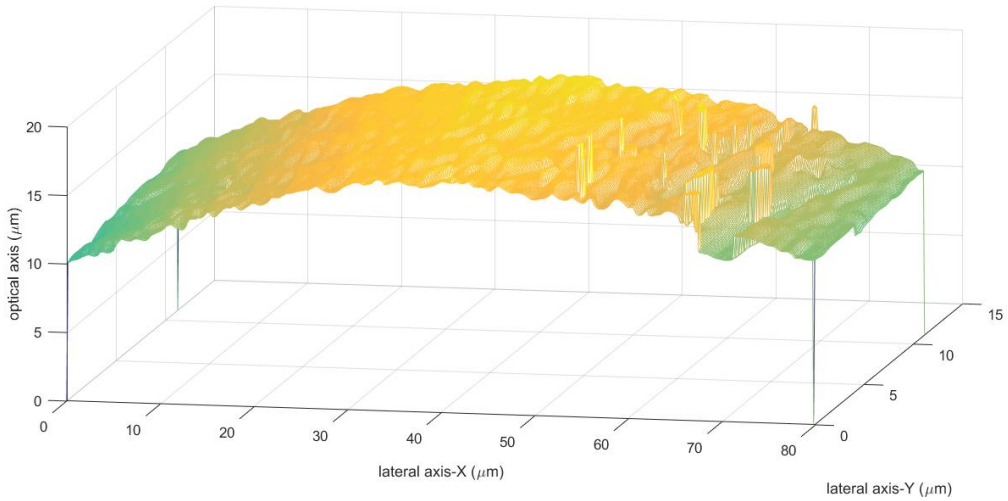

Fig. 103 Surface extraction of a sample of Cable obtained using 3D fringe signal processing

In the case of the Cable, the measurement using 3DTKEO also show very good result, indicated by the surface being continuous and containing less unmeasured points.

d. Rock (322 x 256 x 256)

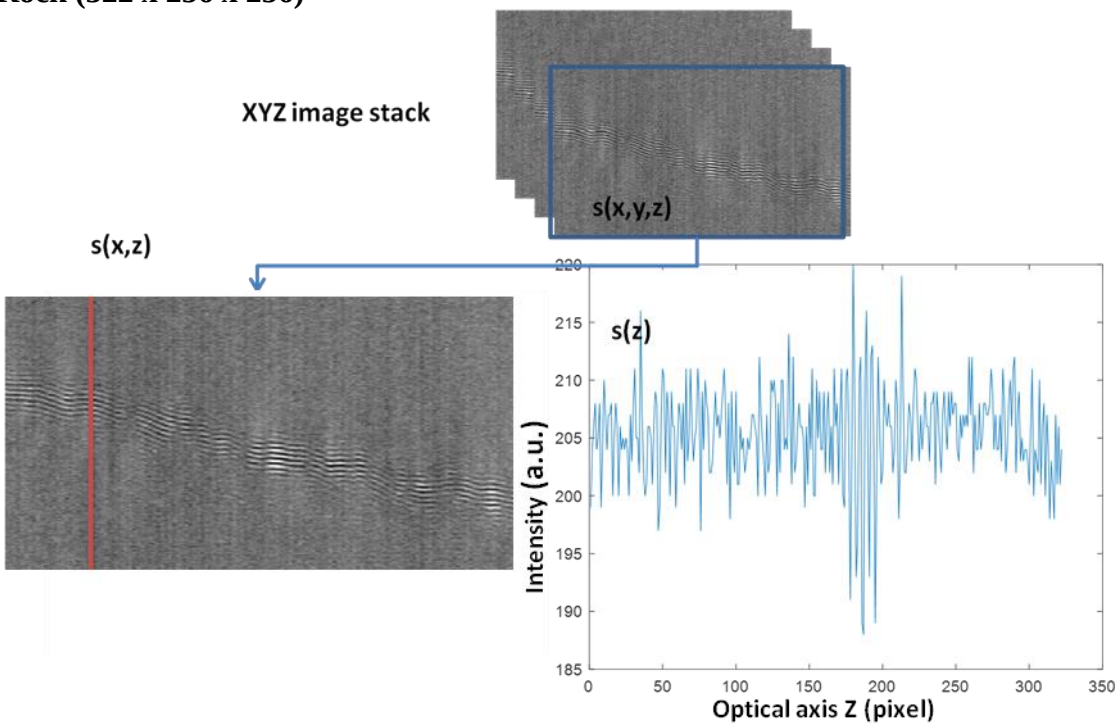

Fig. 104 Fringe signals of measurements on a Rock surface

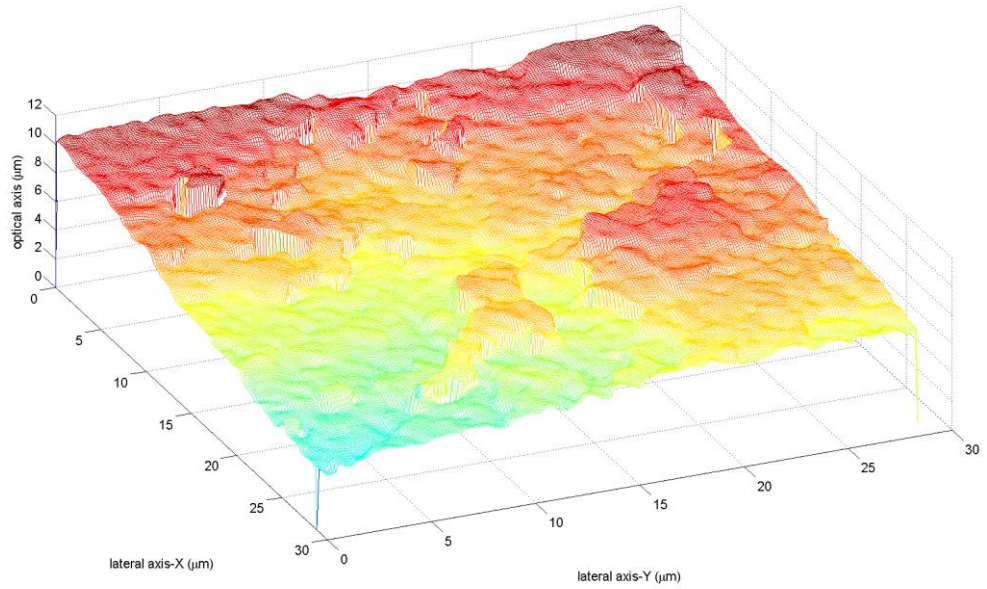

Fig. 105 Surface extraction of a sample of Rock obtained using 3D fringe signal processing

In the case of the Rock surface, this is the most difficult surface to measure precisely because of the present of many step and possibly transparent layers. The measurements using 3DTKEO also show very good results, indicated by the surface

being continuous and containing less unmeasured points than if we had measured with the classical algorithm.

4.7 PERFORMANCE COMPARISON OF 3D FRINGE PROCESSING USING CONTINUOUS 3DTKEO AND DISCRETE 3DTKEO

In the previous section, we have described the developed mathematical model of discrete 3DTKEO in order to analyse directly the stack image of the fringe signal. It is obvious that we hope this discrete approach of 3DTKEO will give the advantageous in terms of computational time. In this section, we report the study of the application of the discrete 3DTKEO on fringe signal processing in a comparison with the results from the continuous 3DTKEO. For this purpose, we use a real data sample, i.e. measurements made on the Cable, which has the fringe signals, as illustrated in Fig. 106.

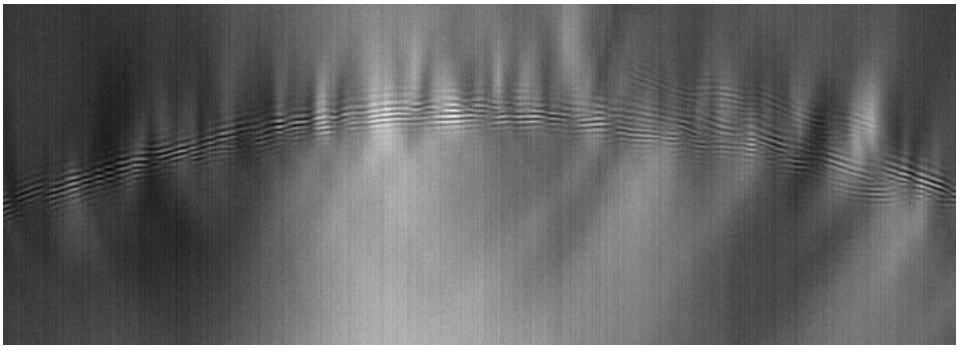

(a)

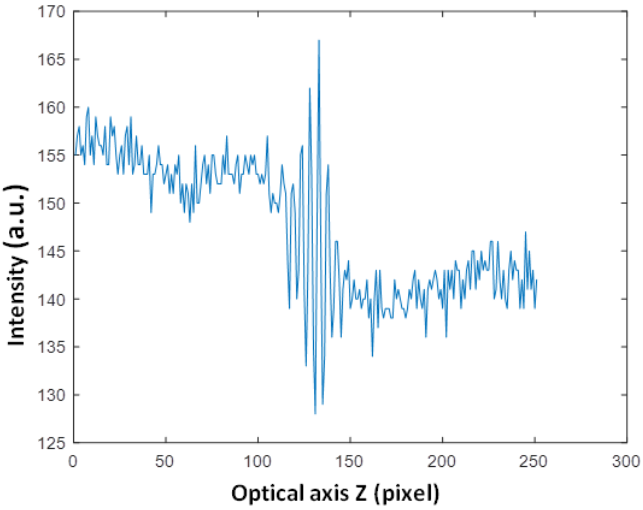

(b)

Fig. 106 (a) Fringe image of a Cable and (b) its fringe profile in 1D

As illustrated in Fig. 106, it seems that before applying the envelope detection, the pre-processing step is needed in order to remove the offset and to suppress the noise. Fig. 107 shows the pre-filtered fringe image and its fringe profile in 1D after the pre-processing step.

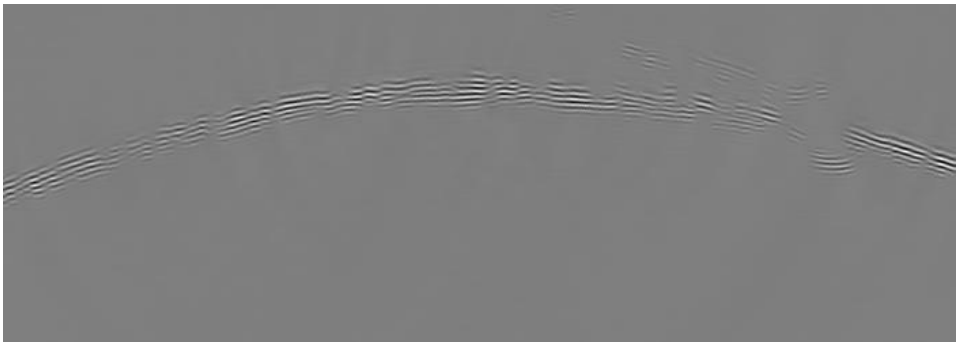

(a)

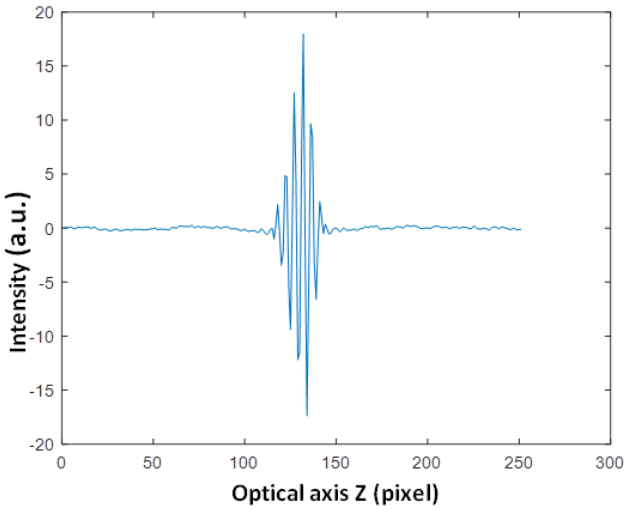

(b)

Fig. 107 Prefiltered fringe image of a measurements from the Cable after the pre-processing step and (b) its prefiltered fringe profile in 1D

The following shows the comparison of the results of the fringe analysis between the continuous 3DTKEO and discrete 3DTKEO algorithms:

a. Fringe envelope detection

Fig. 108 shows the position of the fringe envelope obtained using the Continuous 3DTKEO and Discrete 3DTKEO. As illustrated in the figure, both of the fringe envelopes obtained using the algorithms provide satisfactory results with good contrast, the fringe envelopes being clearly observable in the images. But if the amplitude of the envelopes is considered, the fringe envelope obtained using the Discrete 3DTKEO is found to have a better contrast than that using the Continuous

3DTKEO, as shown in Fig. 109. As illustrated in the figure, the fringe envelope amplitude has twice the fringe envelope amplitude obtained using the Continuous 3DTKEO. Then by further observation, we found that very small artefacts (almost unobservable by eye) appear on the fringe envelope obtained using the Discrete 3DTKEO, as illustrated by the red rectangular in Fig. 108(b). In comparison, there are no artefact that appear in the fringe envelope obtained using the Continuous 3DTKEO, as illustrated by the red rectangular in Fig. 108(a).

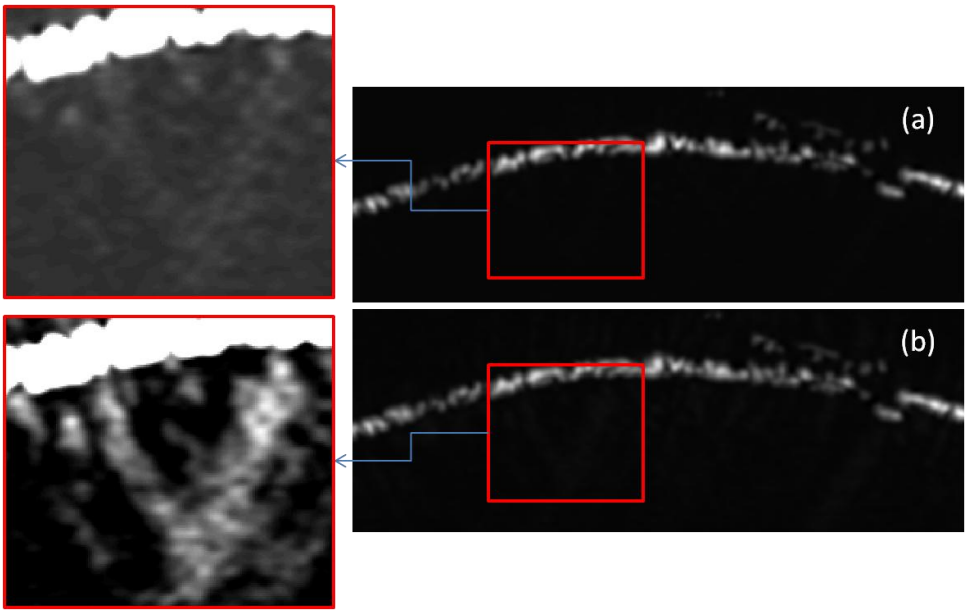

Fig. 108 XZ fringe envelope obtained using (a) Continuous 3DTKEO and (b) Discrete 3DTKEO

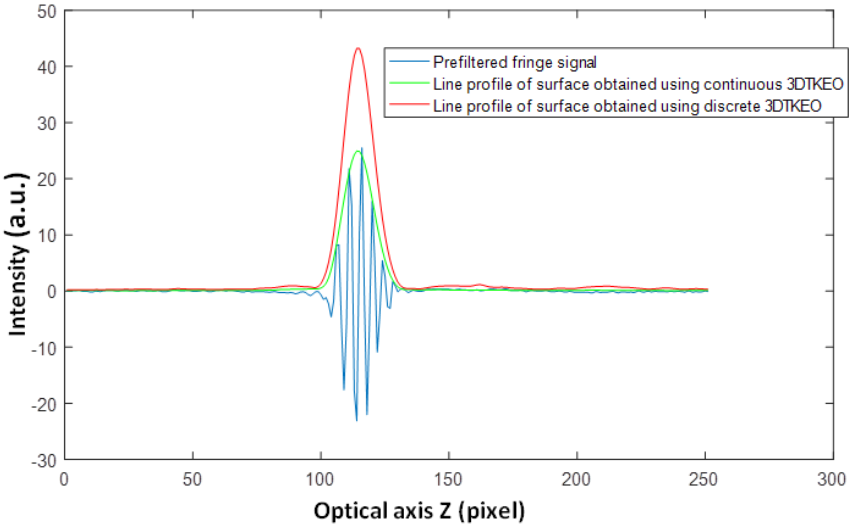

Fig. 109 Comparison fringe envelope profile in 1D obtained using (a) Continuous 3DTKEO and (b) Discrete 3DTKEO

b. Surface extraction

As illustrated in Fig. 109, it can be observed that both of the algorithms provide fringe envelopes which have the structure of a Gaussian function. This gives the advantage in the process of peak detection to indicate the surface height. The difference between the envelopes is the amplitude. Further studies are required to find out whether this difference in amplitude could lead to a difference information of the surface height. The following shows the results of surface extraction obtained using the algorithms. Fig. 110 shows the three dimensional profile of the surface of the Cable sample obtained using (a) Continuous 3DTKEO and (b) Discrete 3DTKEO, while Fig. 111 shows the image version of the surface profile in two dimensions.

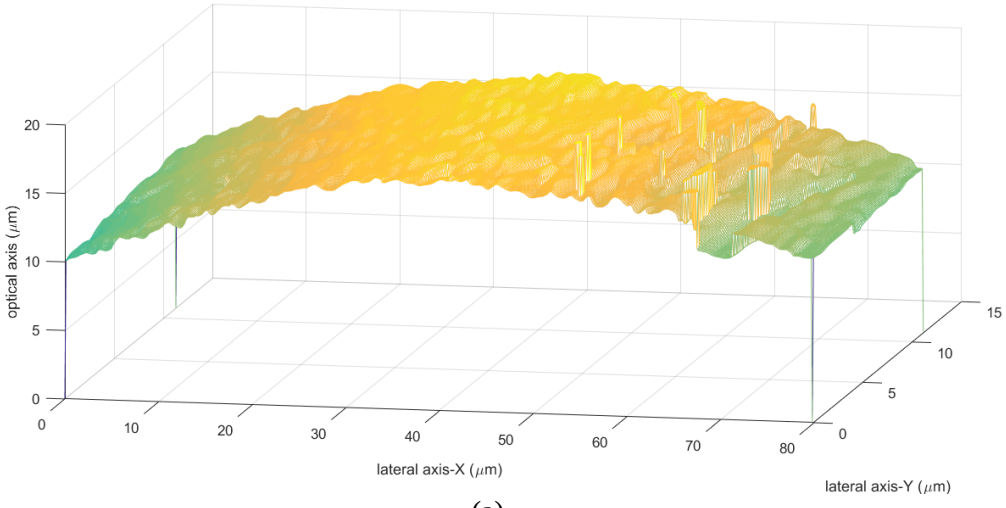

(a)

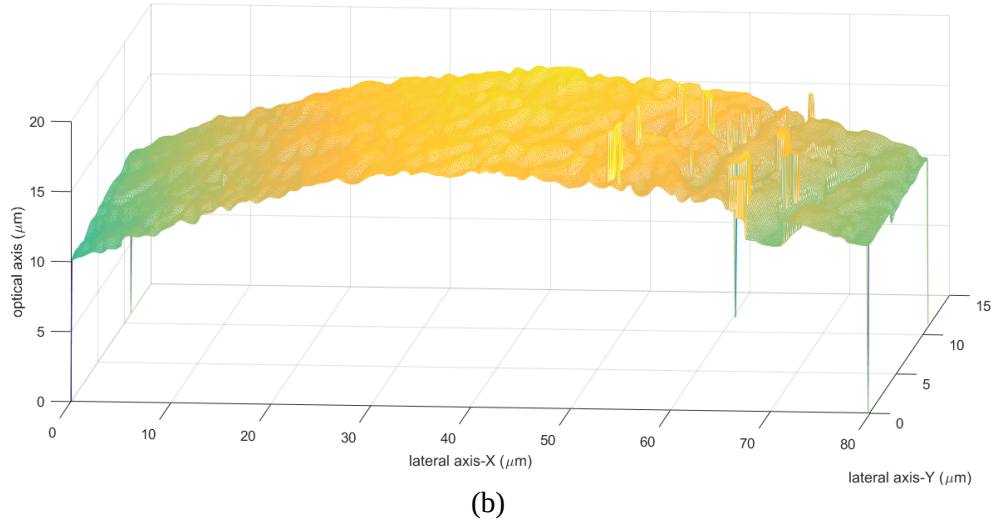

(b)

Fig. 110 3D Surface extraction obtained using (a) Continuous 3DTKEO and (b) Discrete 3DTKEO

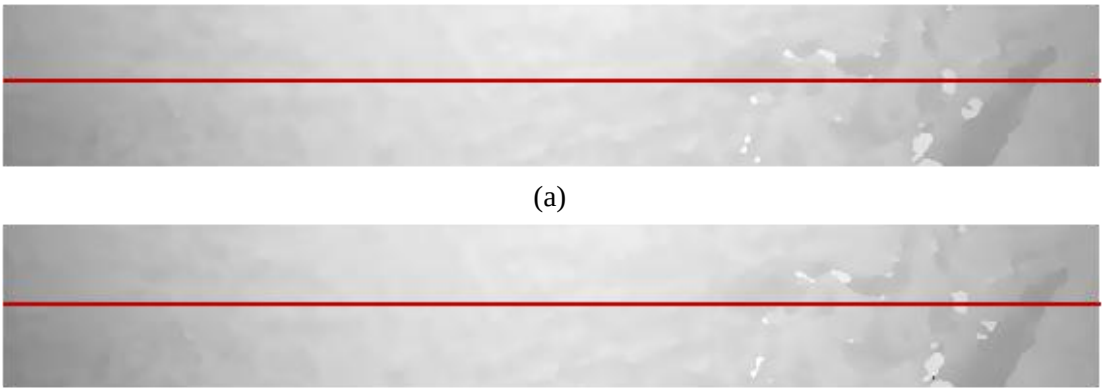

(a)

(b)

Fig. 111 Image of surface profile obtained using (a) Continuous 3DTKEO and (b) Discrete 3DTKEO

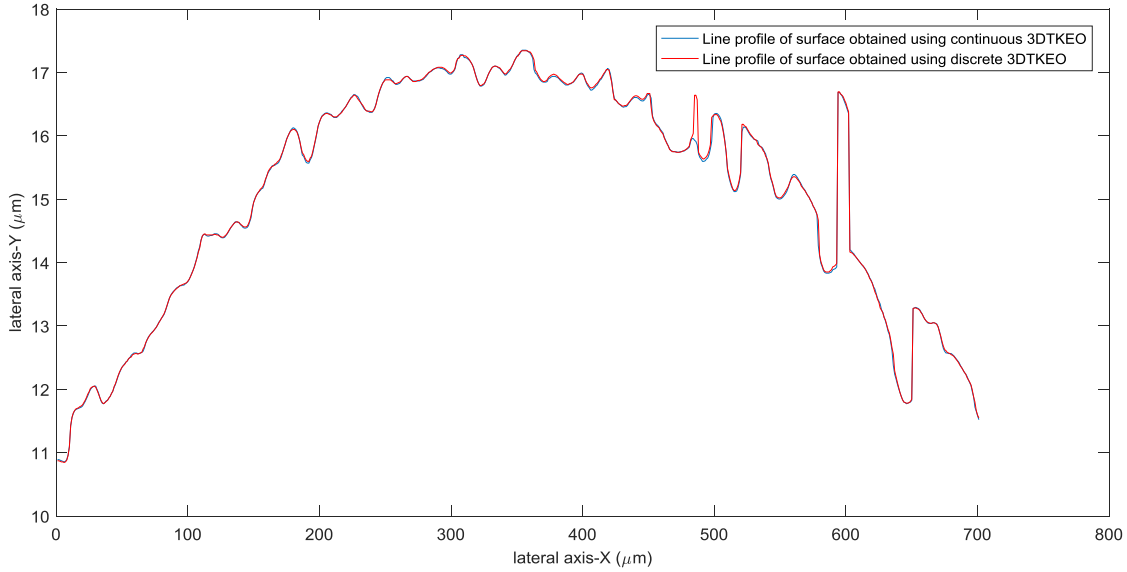

Fig. 112 Line profile comparison of Cable surface obtained using (a) Continuous 3DTKEO and (b) Discrete 3DTKEO

Fig. 112 shows the line profiles of the surface of the Cable sample obtained using (a) Continuous 3DTKEO and (b) Discrete 3DTKEO from the positions of the red lines in the images of the surface profile in Fig. 111. Based on this figure, it can be observed that the characteristics/structure of the surface profile obtained using the Continuous 3DTKEO (blue line) and Discrete 3DTKEO (red line) are relatively similar. Then the results are compared quantitatively by calculating the deviation of the surface profiles, as shown in Fig. 113. The average value of the deviation for this line profile is 9.9 nm (with a sampling step of 90 nm).

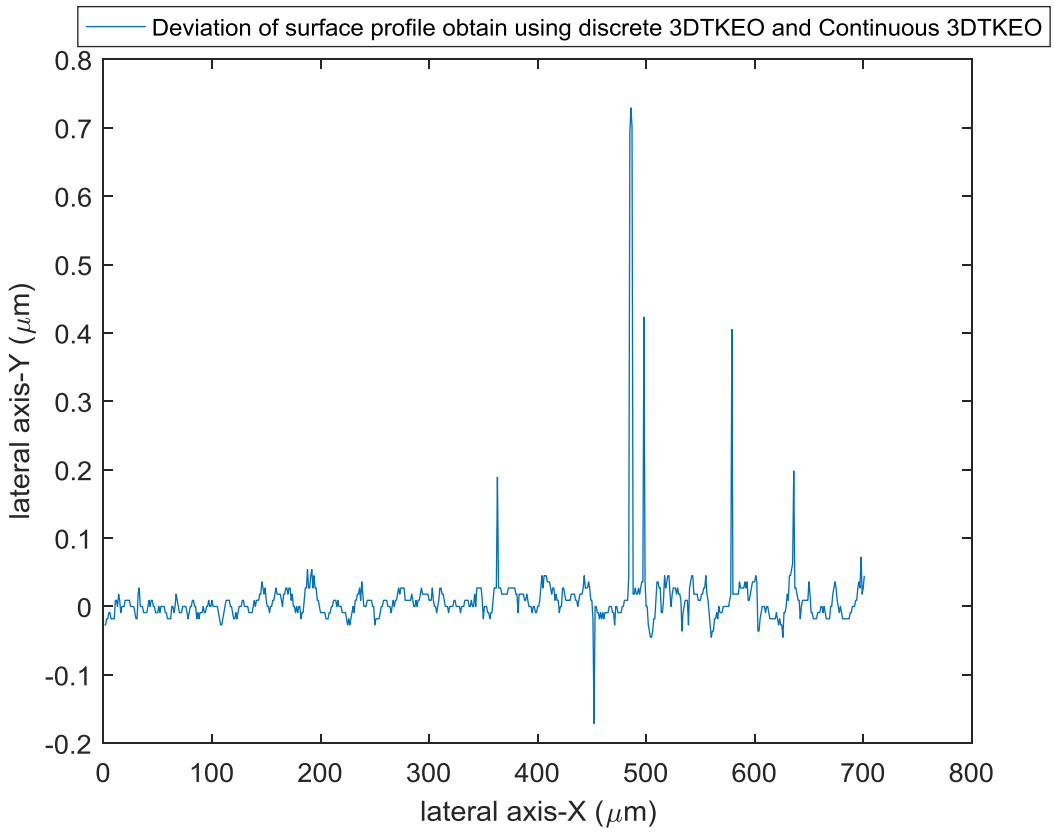

Fig. 113 Deviation value[2] of surface extraction obtained using (a) Continuous 3DTKEO and (b) Discrete 3DTKEO

c. Computation time

As regards the computation time of the 3D fringe signal processing, the Discrete 3DTKEO has the advantage of being more compact computationally due to the partial differential variables required for the energy computation being already provided in the signal itself. For the application of the algorithms on the Cable sample, this results in the Discrete 3DTKEO taking 16.53 s compared with the Continuous 3DTKEO taking 246.19 s in the context of a fringe signal with a data size of 251×701×100 pixels. The Discrete 3DTKEO is therefore far better in terms of computational time than the Continuous 3DTKEO.

[2] Deviation is the difference value of surface height obtain using Continuous 3DTKEO and Discrete 3DTKEO.

4.8 CONCLUSION

An application of the 3D-Teager Kaiser Energy Operator (3DTKEO), which is developed based on the multi-dimensional energy operator has been carried out for fringe analysis in CSI. Through simulation using a synthetic fringe signal, we have demonstrated the competitiveness of 3DTKEO performance, compared with the 1D and 2D approaches. Moreover, we have also performed the algorithm on real data, i.e. a step height standard (VLSI Standard Inc.) for measurement calibration in order to evaluate the accuracy. Based on the results, we observe that the error rate of our measurement on a calibration standard is still below the tolerance limit of the Step Height Standards (SHS) error (< 0.011 µm). In addition, we have tested the algorithm on different samples, such as Graphene, DOE (Diffractive Optical Elements), Resin on Silicon, Cable and Rock. The algorithm works very satisfactorily and provides very good surface profiles of the samples. On other hand, we have also developed and applied the discrete version of 3DTKEO in order to analyse directly the 3D fringe signal. Compared with the continuous 3DTKEO, we found that the discrete approach of 3DTKEO gives the additional advantage of computational time, while the continuous 3DTKEO is more robust to noise than the discrete 3DTKEO.

4.9 RÉSUMÉ DU CHAPITRE 4

Dans ce chapitre, nous présentons l'étude de l'application de 3D-Teager Kaiser Energy Operator (3DTKEO), qui est développé basé sur l'opérateur d'énergie multi-dimensionnel. Grâce à une simulation utilisant un signal de frange synthétique, nous avons évalué la robustesse de la performance 3DTKEO dans le traitement des signaux des franges, et comparé les résultats à l'approche 1D et 2D. De plus, nous avons également appliqué l'algorithme sur des données réelles, c'est-à-dire un étalon de hauteur (VLSI Standard Inc.) afin d'évaluer la précision de la mesure. De plus, nous enrichirons le domaine d'étude en testant l'algorithme sur différents échantillons, tels que le graphène, les DOE (Diffractive Optical Elements), la résine sur silicium, le câble et la roche.

Les 2DTKEO et 3DTKEO continus peuvent être développés comme une version étendue de TKEO monodimensionnel. Les différents opérateurs qui étendent les signaux TKEO mono-dimensionnels aux signaux 2D ont été développés par Maragos et Bovik en 1995, Boudraa et al. en 2005, et Larkin en 2005. L'application de l'opérateur à un signal AM-FM correspond au carré du produit de la fréquence et de l'amplitude du signal 2D

d'entrée, ce qui est utile pour la démodulation du signal AM-FM. Dans le cas d'un signal TKEO à 3D tridimensionnel, les opérateurs peuvent être exprimés par un tenseur d'énergie:

$$\Phi\left[s(x,y,z)\right] = \left\|\nabla s(x,y,z)\right\|^2 - \left(s(x,y,z)\Delta s(x,y,z)\right)$$

En outre, nous avons également introduit le modèle mathématique de discret 3D Teager Kaiser Energy Operator dans le même domaine de traitement des signaux des franges en CSI. Dans un contexte 3D, un signal AM-FM discret local a la forme $s(i,j,k) = A(i,j,k) \cos(\Omega_x i + \Omega_y j + \Omega_z k)$ où $\Omega_x = \omega_x x_e$, $\Omega_y = \omega_y y_e$, $\Omega_z = \omega_z z_e$. La variable xe (respectivement ye et ze) représente la période d'échantillonnage le long de l'axe des x (respectivement l'axe des y et l'axe des z). La contrepartie discrète de l'opérateur Φ_2 notée par Φ_2^d appliquée au signal $s(u)$ est obtenue de la même manière, en effectuant la somme des valeurs absolues des éléments de la matrice.

$$\Phi_2^d\left[s(x,y,z)\right] = \left|s^2(i,j,k) - s(i-1,j,k)s(i+1,j,k)\right| + \left|s^2(i,j,k) - s(i,j-1,k)s(i,j+1,k)\right|$$
$$+ \left|s^2(i,j,k) - s(i,j,k-1)s(i,j,k+1)\right| + 2\left|s_x(i,j,k)s_y(i,j,k) - s(i,j,k)s_{xy}(i,j,k)\right|$$
$$+2\left|s_x(i,j,k)s_z(i,j,k) - s(i,j,k)s_{xz}(i,j,k)\right| + 2\left|s_y(i,j,k)s_z(i,j,k) - s(i,j,k)s_{yz}(i,j,k)\right|$$

Pour l'évaluation de l'algorithme développé de 3DTKEO continu en termes de précision, la mesure 3D est étalonnée en utilisant une norme d'étalonnage, c'est-à-dire une norme de hauteur de pas (SHS). Ces normes sont couramment utilisées pour l'étalonnage de mesure de profileur mécanique ou optique, y compris la microscopie interférentielle. Pour la traçabilité de la norme, il est certifié par l'Institut National de Métrologie. La caractéristique de SHS que nous avons utilisée pour cet étalonnage est le paramètre de hauteur de pas. Dans ce travail, nous avons utilisé une norme de hauteur de pas qui est fabriquée par VLSI Standard Inc, consistant en 25 mm x 25 mm x 3 mm, et qui a une valeur de hauteur de pas de 1,7803 ± 0,011 μm. Sur la base des résultats de l'étalonnage utilisant notre traitement de signal de frange 3D développé, nous observons que le taux d'erreur de notre mesure sur un étalon est toujours en dessous de la limite de tolérance de de l'erreur SHS (< 0.011 μm).

D'autre part, nous avons également développé et appliqué la version discrète de 3DTKEO afin d'analyser directement le signal de frange 3D. L'intérêt espéré de cette approche discrète de 3DTKEO est un avantage en termes de temps de calcul. Dans ce

chapitre, nous rapportons l'étude de l'application de 3DTKEO discrète sur le traitement des signaux de franges, qui est comparée à la 3DTKEO continue. A titre de comparaison, nous utilisons des données réelles, c'est à dire un câble, comme échantillon. Nous commençons par l'observation de la topographie de l'enveloppe des franges obtenue en utilisant le 3DTKEO continue et le 3DTKEO discret. Les enveloppes de franges obtenues en utilisant les deux algorithmes fournissent des résultats satisfaisants qui ont un contraste élevé, les enveloppes de frange étant clairement visibles sur l'image. En regardant de plus prêt, l'enveloppe de franges obtenue en utilisant le 3DTKEO discret a un meilleur contraste que ce du 3DTKEO continu. L'amplitude d'enveloppe de frange a deux fois l'amplitude de l'enveloppe de frange obtenue en utilisant le 3DTKEO continu. Ensuite, avec une observation plus approfondie, nous avons constaté la présence de petits artéfacts (presque inobservables) qui apparaissent dans l'image obtenue en utilisant le 3DTKEO discret. Par contre, aucun artefact apparaît sur l'image obtenue en utilisant le 3DTKEO continue.

Ensuite, nous observons les profils de surface obtenus par les deux algorithmes. Basé sur de ceux-ci, nous avons observé que la caractéristique / structure du profil de surface obtenue en utilisant le 3DTKEO Continu et Discret sont relativement similaires. Puis nous avons comparé les résultats quantitativement en calculant la déviation des profils de surface. La valeur moyenne de la déviation pour ce profil de ligne est de 9,9 nm (avec un pas d'échantillonnage de 90 nm). En ce qui concerne le temps de calcul du traitement du signal des franges 3D, le 3DTKEO discret a l'avantage d'être plus compact en termes de calcul. Par exemple, en appliquant les algorithmes sur des mesures d'un échantillon de câble, le 3DTKEO discret prend 16,53 s alors que le 3DTKEO Continu prend 246,19 s pour un signal de frange avec une taille de données de 251×701×100 pixels. Le 3DTKEO discret est bien meilleur en termes de temps de calcul que ce du 3DTKEO continu.

GENERAL CONCLUSION

In this thesis, we have presented the study of the use of Teager Kaiser Signal processing for fringe analysis in CSI. The main aim of the research project was to develop new n-D approaches (1D, 2D, 3D) which are suitable for improved characterization of more complex surfaces and transparent layers using white light interferometry.

We begin our study by evaluating the performance of envelope detection using the 1D Teager Kaiser Energy Operator, which is compared to other techniques. These methods consist of the Fourier Transform (TF), wavelet and the FSA (Five-Sample-Adaptive) algorithm. We have developed a simulation program (in MATLAB) that allows the comparison of the performance of the different methods using a synthetic fringe signal (a synthetic transparent layer). Further comparison was then carried out using real data, i.e. the fringe image of a resin layer on Silicon. In addition, we also evaluated the performance of different types of pre-processing in order to remove the offset component and suppress the noise in the fringe analysis. This study yields the following conclusions:

- The combination of EMD and Savitzky-Golay filters provides the best performance for suppressing the noise and the offset component while maintaining the original signal intensity.
- CWT and TKEO are both competitive for providing surface extraction:
  - TKEO is slightly better in terms of computational time.
  - CWT is slightly better for the wavy transparent layer, but TKEO is quicker in terms of computational time.
  - TKEO is more competitive than CWT for resolving between two close layers.

After a study of 1D fringe signal processing, we implement the 2D approach using Teager Kaiser for fringe analysis. The study of the robustness of 2D fringe processing in CSI has been carried out for the characterization of a transparent Mylar polymer film. We have demonstrated the ability of 2D approaches to compete with some classical methods (1D approaches) used in the field of interferometry, in terms of robustness. These results demonstrate that the XZ fringe envelope extracted by the XZ-scan technique provides more satisfactory results than the Z-scan approach in revealing the internal structures and the rear surface. The technique also allows an improvement in the details in the XZ images as well as more accurate measurements of the thickness of the polymer film.

The final part of this thesis work reports an application of the 3D-Teager Kaiser Energy Operator (3DTKEO), based on the multi-dimensional energy operator for fringe analysis in CSI. Through a simulation using a synthetic fringe signal, we have demonstrated the competitiveness of the 3DTKEO performance, compared with the 1D and 2D approaches. Furthermore, we tested the algorithm on real data, i.e. a step height standard (VLSI Standard Inc.) for measurement calibration in order to evaluate the accuracy. Based on these results, we observed that the error rate of the measurements on a calibration standard is still below the tolerance limit of the Step Height Standards (SHS) error (< 0.011 μm). In addition, we have tested the algorithm on different samples, such as Graphene, DOE (Diffractive Optical Elements), Resin on Silicon, Cable and Rock. The algorithm works very well and provides satisfactory surface profiles of the samples. On the other hand, we have also developed and applied the discrete version of 3DTKEO in order to analyse directly the 3D fringe signal. Comparing this with the continuous 3DTKEO, we found that the discrete approach of 3DTKEO gives the advantage of shorter computational time, while the continuous 3DTKEO is more robust to noise than the discrete 3DTKEO.

CONCLUSION GÉNÉRALE

Dans cette thèse, nous avons présenté l'étude de l'utilisation du traitement du signal de Teager Kaiser pour l'analyse des franges dans CSI. L'objectif principal du projet de recherche était de développer de nouvelles approches n-D (1D, 2D, 3D), qui conviennent à la caractérisation améliorée de surfaces plus complexes et de couches transparentes utilisant l'interférométrie à lumière blanche.

Nous commençons notre étude en évaluant la performance de la détection d'enveloppe en utilisant l'opérateur 1D Teager Kaiser Energy, qui est comparé à d'autres techniques. Ces méthodes consistent en la Transformée de Fourier (TF), ondelettes, la FSA (Five-SampleAdaptive), Opérateur d'énergie de Teager Kaiser (TKEO). Nous avons développé un programme de simulation de franges blanches (sur MATLAB) qui permet de comparer les résultats de mesures synthétiques (une couche transparente) effectués par différentes techniques de traitement de signal. D'autre comparaison a ensuite été réalisée en utilisant des données réelles, c'est-à-dire l'image de frange de la couche de résine sur Silicium. En outre, nous avons également évalué les performances de différents types de pré-traitement afin de supprimer la composante de décalage et supprimer le bruit dans l'analyse des franges. Cette étude conduit les conclusions suivantes:

- La combinaison des filtres EMD et Savitzky-Golay permet d'obtenir les meilleures performances pour supprimer le bruit et supprimer le composant de décalage tout en maintenant l'intensité du signal original.
- CWT et TKEO sont compétitifs pour fournir l'extraction de surface:
  - TKEO est légèrement meilleur en termes de temps de calcul.
  - CWT est légèrement meilleur pour la couche transparente ondulée, mais TKEO est plus rapide en termes de temps de calcul.
  - TKEO est plus compétitif que CWT pour résoudre entre deux couches proches.

Après une étude du traitement du signal frange 1D, nous implémentons l'approche 2D en utilisant Teager Kaiser pour l'analyse des franges. L'étude de la robustesse du traitement des franges 2D en CSI a également été réalisée pour la caractérisation d'un film de polymère Mylar transparent. Nous avons démontré la capacité des approches 2D Teager Kaiser à concurrencer certaines méthodes classiques (approches 1D) utilisées dans le domaine de l'interférométrie, en termes de robustesse. Ces résultats démontrent que

l'enveloppe de frange XZ extraite par les approches 2D Teager Kaiser donne des résultats plus satisfaisants que l'approche 1D en révélant les structures internes et la surface arrière. La technique permet également une amélioration des détails dans les images XZ ainsi que des mesures plus précises de l'épaisseur du film polymère.

La dernière partie de ce travail de thèse rapporte une application de 3D Teager Kaiser Energy Operator (3DTKEO), basée sur l'opérateur d'énergie TK multi-dimensionnel. pour l'analyse des franges dans CSI. Grâce à une simulation utilisant un signal de frange synthétique, nous avons démontré la compétitivité de la performance de 3DTKEO par rapport aux approches 1D et 2D. De plus, nous avons testé l'algorithme sur des données réelles, c'est-à-dire une norme de hauteur de pas (VLSI Standard Inc.) pour l'étalonnage de mesure afin d'évaluer la précision. Sur la base de ces résultats, nous avons observé que le taux d'erreur des mesures sur une norme d'étalonnage est encore inférieur à la limite de tolérance de l'erreur de norme de hauteur de pas (<0,011 μm). De plus, nous avons testé l'algorithme sur différents échantillons, tels que le graphène, les DOE (Diffractive Optical Elements), la résine sur silicium, le câble et la roche. L'algorithme fonctionne très bien et fournit des profils de surface satisfaisants des échantillons. D'autre part, nous avons également développé et appliqué la version discrète de 3DTKEO afin d'analyser directement le signal de frange 3D. En comparant cela avec le 3DTKEO continu, nous avons trouvé que l'approche discrète de 3DTKEO donne l'avantage d'un temps de calcul plus court, tandis que le 3DTKEO continu est plus robuste au bruit que le 3DTKEO discret.

LIST OF PUBLICATIONS AND COMMUNICATIONS

International peer-reviewed journals

1. **G. Gianto**, F. Salzenstein, and P. Montgomery, "Comparison of envelope detection techniques in coherence scanning interferometry," *Appl. Opt.*, vol. **55**, no. 24, pp. 6763–6774, 2016.
2. H. Mukhtar, P.C. Montgomery**, G. Gianto** & K. Susanto, "Rock surface roughness measurement using CSI technique and analysis of surface characterization by qualitative and quantitative results", *IOP Conference Series: Earth and Environmental Science*, IOP Publishing, **29**, p. 012028, 2016.

International conferences

1. **G. Gianto**, P. Montgomery, and F. Salzenstein, "Study of Robustness of 2D Fringe Processing in Coherence Scanning Interferometry for the Characterization of a Transparent Polymer Film," , IEEE Xplore (The 4th International Conference on Instrumentation, Control and Automation 2016, Bandung, Indonesia), no. 1, pp. 60–65, 2016.
2. P.C. Montgomery, F. Salzenstein, **G. Gianto**, K.L. Apedo, N. Serres, C. Fond, F. Feugeas, Multi-scale roughness measurement of cementitious materials using different optical profilers and window resizing analysis, Proc. SPIE, "Europe Optical Metrology, Optical Measurement Systems for Industrial Inspection", Eds. P. Lehmann, W. Osten, A.A. Gonçalves, 22-25 June 2015, Munich, Germany, **9525**, 95250Z, DOI: 10.1117/12.2184711, 2015.
3. H. Mukhtar, P.C. Montgomery**, G. Gianto** & K. Susanto, "Rock surface roughness measurement using CSI technique and analysis of surface characterization by qualitative and quantitative results", Padjadjaran Earth Dialogues : International Symposium on Geophysical Issues, Jatinangor, Indonesian, 8-10 June, 2015, published in IOP Conference Series: Earth and Environmental Science (EES).

Other conferences

1. Montgomery P.C., **Gianto G**., Salzenstein F., Apedo K.L., Serres N., Fond C., Feugeas F., "Analyse multifenêtrage de la rugosité d'échantillons de ciment mesurée par différents profilomètres optiques", 10e Journées "Imagerie optique non conventionnelle", GDR ISIS et ONDES, 2015 (poster).

SUPPLEMENTARY WORK

For doctoral training program, I have participated in:

- Scientific training:
  - 42 hours of master's level lectures: Formation des Images, Microphotonique, Composant Optiques Diffractifs, Biophotonics
  - 21 scientific seminars

- Professional training:
  - 31 hours of professional courses: protéger par le brevet, Formation en FLE débutant, First steps with Zotero, Initiation à la bibliométrie avec le Web of Science
  - 22.5 hours of "scientific communication and research culture"

APPENDIX-1: DATA OF SAMPLE

Resin on Si (Chapter 2)

Sample = Resin on Si

Piezo parameters
Nb steps = 111
step height = 0,090 µm
Dynamic range = 10,000 µm

Image parameters
X size = 570 Pixels
Y size = 111 Pixels
Img size X = 64,473 µm
Img size Y = 12,578 µm
Img size Z = 1 nm

Optical parameters
NA = 0,850 µm
Pixel X = 0,113 µm
Pixel Y = 0,113 µm
Lateral Resol = 0,438 µm
Lambda eff = 720,0 nm
Lambda eff/8 = 90,0 nm
Camera = Basler AVA 1000 Couleur
Objective = x50 Linnik
Filter = 350 - 1000 nm
Zoom = x1,0

Mylar Polymer film (Chapter 3)

The system developed to carry out the experiment is an adapted Leitz-Linnik interference microscope composed of x50 objectives (NA = 0.85). The image acquisition is performed with a Basler avA1000-100gc GigE CCD camera having 1024x1024 pixels and a Giga Ethernet connection. The sample is mounted on a piezoelectric table (PIFOC, from PI) for Z-scanning. The piezo actuator is controlled in a closed loop with a capacitive position sensor, having a position sensitivity of 1 nm. Acquisition and processing is carried out on a PC equipped with an Intel® Xeon® CPU processor (2.40 GHz, 8 Go RAM) with a Windows 7 (64 bits) operating system.

Graphene FLG ABL ETCH 20 ml (Chapter 4)

Sample = Graphene FLG ABL ETOH 20 ml

Piezo parameters
Nb steps = 111
step height = 0,090 µm
Dynamic range = 10,000 µm

Image parameters
X size = 1352 Pixels
Y size = 111 Pixels
Img size X = 181,893 µm

Img size Y = 53,761 µm
Img size Z = 1 nm

Optical parameters
NA = 0,850 µm
Pixel X = 0,135 µm

Pixel Y = 0,134 µm
Lateral Resol = 0,438 µm
Lambda eff = 720,0 nm
Lambda eff/8 = 90,0 nm
Camera = Mono - Prosilica DCAM 1.31
Objective = x50 Linnik
Filter = 350 - 1000 nm
Zoom = x1,0

DOE (Chapter 4)

Sample = DoE

Piezo parameters
Nb steps = 78
step height = 0,090 µm
Dynamic range = 7,000 µm

Image parameters
X size = 1024 Pixels
Y size = 1024 Pixels
Img size X = 115,826 µm
Img size Y = 116,031 µm
Img size Z = 1 nm

Optical parameters
NA = 0,850 µm
Pixel X = 0,113 µm
Pixel Y = 0,113 µm
Lateral Resol = 0,438 µm
Lambda eff = 720,0 nm
Lambda eff/8 = 90,0 nm
Camera = Basler AVA 1000 Couleur
Objective = x50 Linnik
Filter = 350 - 1000 nm
Zoom = x1,0

Rock (Chapter 4)

Sample = Rock brown

Piezo parameters
Nb steps = 320
step height = 0,072 µm
Dynamic range = 23,000 µm

Image parameters
X size = 1024 Pixels
Y size = 1024 Pixels
Img size X = 115,826 µm
Img size Y = 116,031 µm
Img size Z = 1 nm

Optical parameters
NA = 0,850 µm
Pixel X = 0,113 µm
Pixel Y = 0,113 µm
Lateral Resol = 0,416 µm
Lambda eff = 580,0 nm
Lambda eff/8 = 72,5 nm
Camera = Basler AVA 1000 Couleur
Objective = x50 Linnik
Filter = Choisi
Zoom = x1,0

Cable (Chapter 4)

Leitz Linnik Cronenbourg

[Informations de la mesure]
Nombre d'images = 669,000000
Dynamique (µm) = 60,120000
Pas du piezo (µm) = 0,090000
Largeur de l'image (pixels) = 1392
Hauteur de l'image (pixels) = 1040

Etalon step (Chapter 4)

Leitz Linnik Cronenbourg

[Informations de la mesure]
Nombre d'images = 102
Dynamique (µm) = 9,09
Pas du piezo (µm) = 0,090000
Largeur de l'image (pixels) = 1392
Hauteur de l'image (pixels) = 1040

Etalon step (Chapter 4)

New Fogale Illkirch

[Informations de la mesure]
Nombre d'images = 143
Dynamique (µm) = 10
Pas du piezo (µm) = 0,070000
Largeur de l'image (pixels) = 1392
Hauteur de l'image (pixels) = 1040

Lambda effectif (nm) = 560 Systeme = Fogale Mirau x50 ON 0.55

Etalon step (Chapter 4)
Old Fogale Cronenbourg [Informations de la mesure] Nombre d'images = 114 Dynamique (µm) = 9,12 Pas du piezo (µm) = 0,080000 Largeur de l'image (pixels) = 1392 Hauteur de l'image (pixels) = 1140 Lambda effectif (nm) = 640 Systeme = Fogale Mirau x40 ON 0.60

APPENDIX-2: MULTI-SCALE ROUGHNESS MEASUREMENT OF CEMENTITIOUS MATERIALS USING WINDOW RESIZING ANALYSIS

The work during this PhD also involved a contribution to the development of the "window re-sizing" technique [123],[124],[125] for comparing the results of measurements performed by two different profiling systems (interference microscopy and confocal chromatic microscopy). This work was carried out in the context of collaboration with the GCE team at ICube.

1.1 Development of "window resizing" technique

The usual roughness amplitude parameters are measured, namely H_{mm}, the peak-valley roughness, the difference in height between the highest and lowest measured points, R_a, the arithmetic average of the absolute values of the roughness and R_q, the root mean square (RMS) value of the roughness.

1.2 Sliding window method used

In order to compare data from both techniques, the average value of these roughness parameters (H_{mm}, R_a and R_q) is calculated at different scales from the data in the form of an *XYZ* matrix using sliding windows *XY* of increasing size [126],[127].

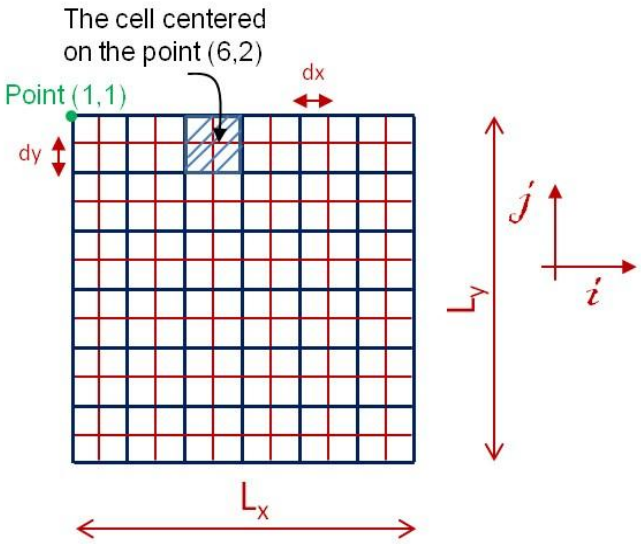

Fig. 114 Coordinate system used showing basic cell for δ = 1 (in this case giving 3x3 = 9 points)

The (*x*,*y*,*z*) coordinates of the measured points are considered on a regular grid as defined in Fig. 114 where the crossings of the grid lines correspond to the positions of

pixels in the image data. The points are positioned every *dx* and *dy* along the *x* and *y* axes respectively (see Fig. 114) and *dx* = *dy*. The height, $z_{i,j}$, measured at a given pixel corresponds to the i^{th} column and j^{th} row.

A sliding window or cell is defined as a set of points forming a square with a size δ, an integer. A cell centred on a point (*i*,*j*), contains all of the points from ($x_{i,j} - \delta dx$) to ($x_{i,j} + \delta dx$) and from ($y_{i,j} - \delta dx$) to ($y_{i,j} + \delta dx$). For example, for δ = 1, the cell contains 9 points; for δ = 2, the cell contains 25 points, etc. The value of δ is increased up to the point where there are less than four cells for averaging the different roughness parameters. Each point is centred on a cell having the length of a side equal to $2\delta dx$ (Fig. 114). The points that are too close to the edges where it is not possible to centre a cell of the correct size are eliminated. The number of columns and rows used are i_{max} and j_{max} respectviely.

The values of ($z_{max} - z_{min}$) are calculated for each cell, and then averaged over all of the cells, where:

$$(z_{max})i,j = Max(z_{n,m}),n \in [i - \delta,i + \delta],m \in [j - \delta,j + \delta]$$

$$(z_{min})i,j = Min(z_{n,m}),n \in [i - \delta,i + \delta],m \in [j - \delta,j + \delta] \quad \textbf{(1.1)}$$

The average value of H_{mm} is then given by:

$$H_{mm}(\delta) = \frac{1}{(i_{max}-2\delta)(j_{max}-2\delta)} \sum_{i=1+\delta}^{i_{max}-\delta} \sum_{j=1+\delta}^{j_{max}-\delta} (z_{max} - z_{min})_{i,j} \quad \textbf{(1.2)}$$

The average value of R_a is given by:

$$R_a(\delta) = \frac{1}{(i_{max}-2\delta)(j_{max}-2\delta)} \sum_{i=1+\delta}^{i_{max}-\delta} \sum_{j=1+\delta}^{j_{max}-\delta} \langle \, | \, z - \overline{z} \, | \, \rangle_{i,j} \quad \textbf{(1.3)}$$

The average value of R_q is given by:

$$R_q(\delta) = H_{rms}(\delta) = \frac{1}{(i_{max}-2\delta)(j_{max}-2\delta)} \sum_{i=1+\delta}^{i_{max}-\delta} \sum_{j=1+\delta}^{j_{max}-\delta} \sqrt{\langle \, (z - \overline{z})^2 \, \rangle_{i,j}} \quad \textbf{(1.4)}$$

Where:

$$\langle \, (z - \overline{z})^2 \, \rangle_{i,j} = \frac{1}{(1+2\delta)^2} \sum_{n=i-\delta} \sum_{m=j-\delta} \left(z_{n,m} - \overline{z}\right)^2 \quad \textbf{(1.5)}$$

With:

$$(\bar{z})_{i,j} = \langle z \rangle_{i,j} = \frac{1}{(1+2\delta)^2} \sum_{n=i-\delta}^{1+\delta} \sum_{m=j-\delta}^{j+\delta} z_{n,m} \quad \textbf{(1.6)}$$

And < . >*i,j* denotes the average of the quantity (.) within the cell centered at the point (*i,j*).

1.3 Results of roughness measurements

The results of the roughness measurements of the unpolished samples using SCM and CSI are shown in Fig. 115. The CSI results show deep roughness up to 20 µm with large grain lateral sizes from µm to tens of µm. The SCM results show that there are larger grains up to several hundreds of µm in width.

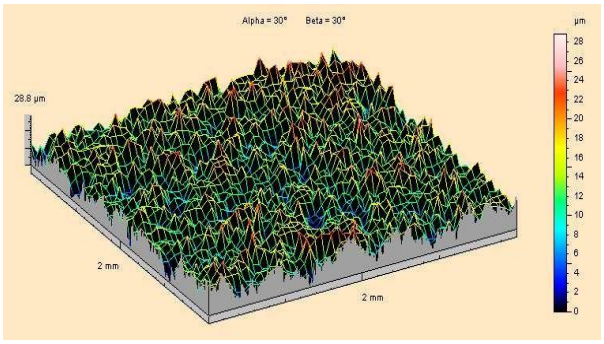

(a) SCM measurement (150 days curing)

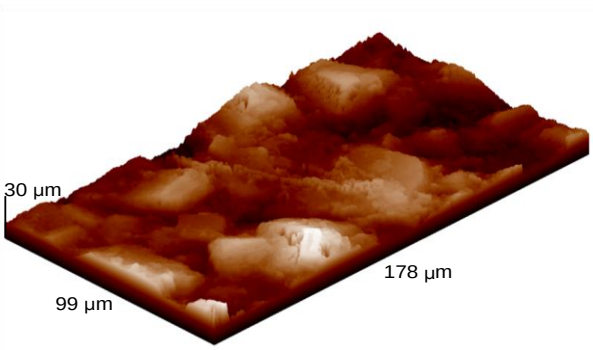

CSI measurement (165 days curing)

Fig. 115 Measurement of surface roughness of unpolished samples using SCM and CSI

The results of the average roughness values H_{mm} and R_q as a function of δdx of the unpolished samples calculated with the Fortran program (developed by Christophe Fond, GCE, ICube) are given in Fig. 116. The plots of the results for the three samples measured with SCM overlap each other, showing very similar results. In the same way, the results for both the samples measured with CSI are very close to each other over the range considered. Comparing both sets of results from the two techniques it can be seen that the curves overlap extremely well in the 4 – 12 µm window size region. The similarity in the results from the two techniques is most likely due to the fact that in the case of the unpolished samples since the surfaces consist mainly of large blocks or grains

with relatively smooth facets, the difference between the lateral resolutions of both techniques does not affect much the results. For the measurement of large smooth grains, the details obtained with both techniques are almost identical. There is a relatively low proportion of high lateral spatial frequency information in the measurements, resulting in the SCM technique being able to resolve most of the details in a similar manner to that of the CSI technique. In addition, the difference (15 days) between the curing times of the samples measured with CSI and SCM has no significant influence on the results.

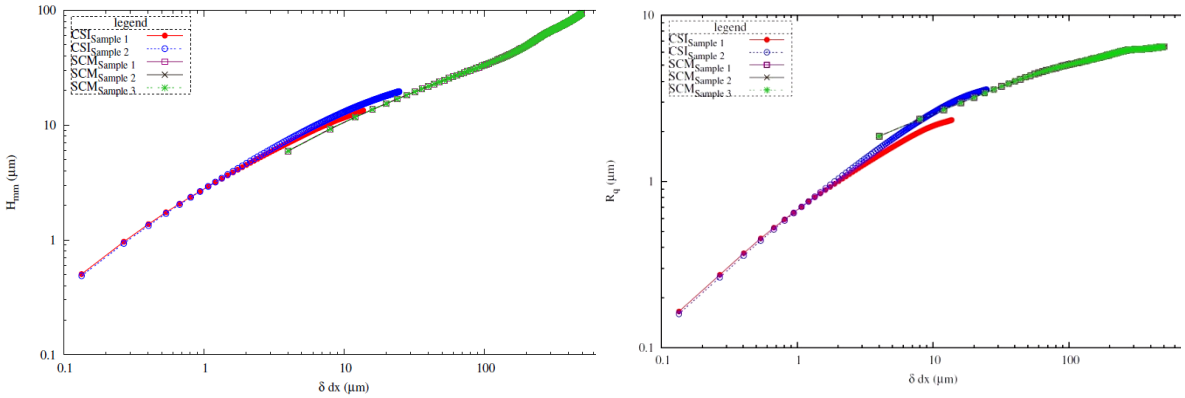

(a) Peak/valley roughness H_{mm} (b) RMS roughness R_q

Fig. 116 Variation of different roughness values as a function of window size δdx for unpolished cement

BIBLIOGRAPHY

[1] J. Schmit, K. Creath, and J. C. Wyant, “Surface Profilers, Multiple Wavelength, and White Light Intereferometry,” *Opt. Shop Test. Third Ed.*, pp. 667–755, 2006.

[2] J. M. Bennett and J. H. Dancy, “Stylus profiling instrument for measuring statistical properties ofsmooth optical surfaces,” *Appl. Opt.*, vol. 20, no. 10, pp. 1785–1802, 1981.

[3] T. Hattori, “Analysis of microscopic areas on wafer surfaces usingg STM/AFM,” *Ultraclean Surf. Process. silicon wafers secrets VLSI Manuf. Springer*, p. 223, 1998.

[4] J. Schmit, J. Reed, E. Novak, and J. K. Gimzewski, “Performance advances in interferometric optical profilers for imaging and testing,” *J. Opt. A Pure Appl. Opt.*, vol. 10, no. 6, pp. 1–7, 2008.

[5] Peter de Groot, “Principles of interference microscopy for the measurement of surface topography,” *Adv. Opt. Phot.*, vol. 7, pp. 1–65, 2015.

[6] P. C. M. and S. L. and A. L.-H. and P. Pfeiffer, “3D nano surface profilometry by combining the photonic nanojet with interferometry,” *J. Phys. Conf. Ser.*, vol. 794, no. 1, p. 12006, 2017.

[7] P. J. Caber, “Interferometric profiler for rough surfaces,” *Appl. Opt.*, vol. 32, no. 19, p. 3438, 1993.

[8] P. de Groot, “Coherence Scanning Interferometry,” *Opt. Meas. Surf. Topogr.*, pp. 187–208, 2011.

[9] C. O’Mahony, M. Hill, M. Brunet, R. Duane, and A. Mathewson, “Characterization of micromechanical structures using white- light interferometry,” *Meas. Sci. Technol.*, vol. 14, no. 10, pp. 1807–1814, 2003.

[10] D. Grigg, E. Felkel, J. Roth, X. C. De Lega, L. Deck, and P. De Groot, “Static and Dynamic Characterization of {MEMS} and {MOEMS} Devices Using Optical Interference Microscope,” *Proc. SPIE*, vol. 55, pp. 429–435, 2004.

[11] A. Bosseboeuf and S. Petitgrand, “Application of microscopic interferometry

techniques in the MEMS field," in *Proc. SPIE*, 2003, vol. 5145, pp. 5116–5145.

[12] P. C. Montgomery, F. Salzenstein, D. Montaner, B. Serio, and P. Pfeiffer, "Implementation of a fringe visibility based algorithm in coherence scanning interferometry for surface roughness measurement," vol. 8788, no. 1, p. 87883G–87883G–11, 2013.

[13] R. T. Blunt, "White Light Interferometry – a production worthy technique for measuring surface roughness on semiconductor wafers," *CS MANTECH Conf.*, vol. 44, no. 0, pp. 59–62, 2006.

[14] A. Dubois, G. Moneron, K. Grieve, and A. C. Boccara, "Three-dimensional cellular-level imaging using full-field optical coherence tomography," *Phys. Med. Biol.*, vol. 49, no. 7, pp. 1227–1234, 2004.

[15] A. Dubois, K. Grieve, G. Moneron, R. Lecaque, L. Vabre, and C. Boccara, "Ultrahigh-resolution full-field optical coherence tomography," *Appl. Opt.*, vol. 43, 2004.

[16] A. Dubois, L. Vabre, A.-C. Boccara, and E. Beaurepaire, "High-resolution full-field optical coherence tomography with a Linnik microscope," *Appl. Opt.*, vol. 41, no. 4, p. 805, 2002.

[17] M. R. Hee, B. Bouma, and G. Tearney, *Handbook of optical coherence tomography*. 2002.

[18] R. Bott, "Optical Coherence Tomography Principles and applications," *Igarss 2014*, no. 1, pp. 1–5, 2014.

[19] D. P. Popescu *et al.*, "Optical coherence tomography: Fundamental principles, instrumental designs and biomedical applications," *Biophys. Rev.*, vol. 3, no. 3, pp. 155–169, 2011.

[20] J. A. Izatt and M. A. Choma, "Theory of Optical Coherence Tomography," pp. 47–72, 2008.

[21] P. Hariharan, *Optical interferometry*. 2003.

[22] Balasubramanian, "Optical system for surface topography measurement," *United*

States Pat., no. 19, 1982.

[23] M. Davidson, K. Kaufman, I. Mazor, and F. Cohen, "An Application Of Interference Microscopy To Integrated Circuit Inspection And Metrology," *Proc. SPIE 0775, Integr. Circuit Metrol. Insp. Process Control*.

[24] B. S. Lee and T. C. Strand, "Profilometry with a coherence scanning microscope," *Appl. Opt.*, vol. 29, no. 26, p. 3784, 1990.

[25] T. Dresel, G. Häusler, and H. Venzke, "Three-dimensional sensing of rough surfaces by coherence radar," *Appl. Opt.*, vol. 31, no. 7, p. 919, 1992.

[26] G. S. Kino and S. S. C. Chim, "Mirau correlation microscope," *Appl. Opt.*, vol. 29, no. 26, p. 3775, 1990.

[27] S. S. C. Chim and G. S. Kino, "Three-dimensional image realization in interference microscopy," *Appl. Opt.*, vol. 31, no. 14, p. 2550, 1992.

[28] P. J. Caber, S. J. Martinek, and R. J. Niemann, "New interferometric profiler for smooth and rough surfaces," 1993, vol. 2088, no., pp. 2088–2089.

[29] P. J. Caber and D. K. Cohen, "Effect of detector noise on the positioning accuracy of an autofocus system.," *Appl. Opt.*, vol. 31, no. 31, pp. 6684–9, 1992.

[30] P. C. Montgomery and J. P. Fillard, "Peak fringe scanning microscopy: submicron 3D measurement of semiconductor components.," *Proc. Int. Conf. Interferom. Tech. Anal. (San Diego, USA. Bellingham Brown G, Kwon OY, Kujawinska M, Reid G.)*, pp. 12–23, 1993.

[31] P. C. Montgomery and J. P. Fillard, "Method and apparatus for interferometrically inspecting a surface of an object.," 1994.

[32] P. Montgomery, F. Anstotz, G. Johnson, and R. Kiefer, "Real time surface morphology analysis of semiconductor materials and devices using 4D interference microscopy," *J. Mater. Sci. Mater. Electron*, vol. 19, pp. 194–198, 2008.

[33] P. Montgomery, F. Anstotz, and J. Montagna, "High-speed, on-line 4D microscopy using continuously scanning white light interferometry with a high-speed camera and real-time FPGA image processing," 2011, vol. 8082, no., pp. 808210–808219.

[34] K. G. Larkin, “Efficient nonlinear algorithm for envelope detection in white light interferometry,” *J. Opt. Soc. Am. A*, vol. 13, no. 4, p. 832, 1996.

[35] F. Salzenstein, P. Montgomery, A. Benatmane, and A. Boudraa, “2d discrete high order energy operators for surface profiling using white light interferometry,” *IEEE-ISSPA*, no. 3, pp. 3–6, 2003.

[36] A. Boudraa and F. Salzenstein, *Time-Frequency Signal Analysis and Processing: TEAGER-KAISER ENERGY OPERATORS IN TIME-FREQUENCY ANALYSIS*. Elsevier Ltd, 2016.

[37] F. Salzenstein, P. C. Montgomery, D. Montaner, and A. O. Boudraa, “Teager-Kaiser energy and higher-order operators in white-light interference microscopy for surface shape measurement,” *EURASIP J. Appl. Signal Processing*, vol. 2005, no. 17, pp. 2804–2815, 2005.

[38] F. Salzenstein, P. Montgomery, and A. O. Boudraa, “Local frequency and envelope estimation by Teager-Kaiser energy operators in white-light scanning interferometry,” vol. 22, no. 15, pp. 18325–18334, 2014.

[39] P. Sandoz, “Wavelet transform as a processing tool in white-light interferometry,” *Opt. Lett.*, vol. 22, no. 14, p. 1065, 1997.

[40] F. Salzenstein, “Two-dimensional continuous higher-order energy operators,” *Opt. Eng.*, vol. 44, no. 11, p. 117001, 2005.

[41] G. Binnig and H. Rohrer, “Scanning Tunneling Microscopy—from Birth to Adolescence (Nobel Lecture),” *Angew. Chemie Int. Ed. English*, vol. 26, no. 7, pp. 606–614, 1987.

[42] P. Markiewicz and M. C. Goh, “Atomic force microscopy probe tip visualization and improvement of images using a simple deconvolution procedure,” *Langmuir*, vol. 10, no. 1, pp. 5–7, Jan. 1994.

[43] S. Y. and H. Y. and Hiroshi Tokumoto, “Nanometer Modifications of Non-Conductive Materials Using Resist-Films by Atomic Force Microscopy,” *Jpn. J. Appl. Phys.*, vol. 34, no. 6S, p. 3396, 1995.

[44] H. Mukhtar, “Development of compensated immersion 3D optical profiler based

on interferometry," 2018.

[45] J. P. Fillard, "Near Field optics and nanoscopy," in *Word Scientific*, 1996, pp. 197–214.

[46] Benatmane Abderrazzaq, "Développement de la microscopie interférométrique pour une meilleure analyse morphologique des couches minces e t épaisses des matériaux semiconducteurs et optiques," 2002.

[47] D Abderrazzaq Benatmane, "Developpement de la microscopie interferometrique pour une meilleure analyse morphologique des couches minces et epaisses des materiaux semiconducteurs et optique," 2002.

[48] A. . Fallis, *Optical Measurement of Surface Topography*, vol. 53, no. 9. 2013.

[49] G. Gianto, P. Montgomery, and F. Salzenstein, "Study of Robustness of 2D Fringe Processing in Coherence Scanning Interferometry for the Characterization of a Transparent Polymer Film," no. 1, pp. 60–65, 2016.

[50] R. Leach, X. J. Leigh Brown, R. Blunt, and D. M. Mike Conroy, "A National Measurement Good Practice Guide," *Natl. Phys. Lab.*, no. 108, p. 56, 2008.

[51] E. HALTER *et al.*, "Characterization of inhomogeneous colloidal layers using adapted coherence probe microscopy," *Appl. Surf. Sci.*, 2010.

[52] P. C. Montgomery, D. Montaner, and F. Salzenstein, "Tomographic analysis of medium thickness transparent layers using white light scanning interferometry and XZ fringe image processing," *Proc. SPIE, 8430*, vol. 2, no. 1, pp. 1–9, 2012.

[53] G. Gianto, F. Salzenstein, and P. Montgomery, "Comparison of envelope detection techniques in coherence scanning interferometry," *Appl. Opt.*, vol. 55, no. 24, pp. 6763–6774, 2016.

[54] F. Kaiser, "On a simple algorithm to calculate the energy of a signal," *Proc. ICASSP*, vol. 2, no. 10, pp. 381–384, 1990.

[55] F. Salzenstein, P. Montgomery, and A. O. Boudraa, "Local frequency and envelope estimation by Teager-Kaiser energy operators in white-light scanning interferometry," *Opt. Express*, vol. 22, no. 15, pp. 18325–18334, 2014.

[56] P. Maragos, T. Quatieri, and J. Kaiser, “Speech nonlinearities, modulations, and energy operators,” *Ieee*, no. 8, pp. 421–424, 1991.

[57] Z. K. Peng and F. L. Chu, “Application of the wavelet transform in machine condition monitoring and fault diagnostics: A review with bibliography,” *Mech. Syst. Signal Process.*, vol. 18, no. 2, pp. 199–221, 2004.

[58] H. Adeli, Z. Zhou, and N. Dadmehr, “Analysis of EEG records in an epileptic patient using wavelet transform,” *J. Neurosci. Methods*, vol. 123, no. 1, pp. 69–87, 2003.

[59] P. D. Swami, R. Sharma, A. Jain, and D. K. Swami, “Speech enhancement by noise driven adaptation of perceptual scales and thresholds of continuous wavelet transform coefficients,” *Speech Commun.*, vol. 70, pp. 1–12, 2015.

[60] C. J. Tay, C. Quan, W. Sun, and X. Y. He, “Demodulation of a single interferogram based on continuous wavelet transform and phase derivative,” *Opt. Commun.*, vol. 280, no. 2, pp. 327–336, Dec. 2007.

[61] H. J. Li, H. J. Chen, J. Zhang, C. Y. Xiong, and J. Fang, “Statistical searching of deformation phases on wavelet transform maps of fringe patterns,” *Opt. Laser Technol.*, vol. 39, no. 2, pp. 275–281, Mar. 2007.

[62] M. Wielgus, “Amplitude demodulation of interferometric signals with a 2D Hilbert transform,” *Challenges Mod. Technol.*, vol. 1, no. 1, 2011.

[63] T. Suzuki, H. Matsui, S. Choi, and O. Sasaki, “Low-coherence interferometry based on continuous wavelet transform,” *Opt. Commun.*, vol. 311, pp. 172–176, 2013.

[64] J. Sokolovsky, Y. Yitzhaky, and I. Abdulhalim, “Analysis of interferograms of multi-layered biological samples obtained from full field optical coherence tomography systems,” *Appl. Opt.*, vol. 51, no. 35, p. 8390, 2012.

[65] K. M. Medicus and M. J. Jansen, “Fourier Transform and Wavelet Algorithms for Calculating Height in White Light Interferometry,” 2010.

[66] A. O. Boudraa, J. C. Cexus, and Z. Saidi, “EMD-based Signal Noise Reduction,” *Int. J. Signal Process*, vol. 1, no. 1, pp. 33–37, 2004.

[67] J. S. Lim, “Two-Dimensional Signal and Image Processing,” *Prentice Hall*, 1990.

[68] A. P. Tomaniac, *Signal processing*, vol. 15, no. 1. 1998.

[69] F. . Jin, P. . Fieguth, L. . Winger, and E. . Jernigan, “ADAPTIVE WIENER FILTERING OF NOISY IMAGES AND IMAGE SEQUENCES,” *Des. Eng.*, no. 1, pp. 3–6, 2003.

[70] H. Azami, K. Mohammadi, and B. Bozorgtabar, “An Improved Signal Segmentation Using Moving Average and Savitzky-Golay Filter,” *J. Signal Inf. Process.*, vol. 3, no. 1, pp. 39–44, 2012.

[71] P. Lehmann, S. Tereschenko, and W. Xie, “Fundamental aspects of resolution and precision in vertical scanning white-light interferometry,” *Surf. Topogr. Metrol. Prop.*, vol. 4, no. 2, 2016.

[72] Y.-S. Ghim and A. Davies, “Complete fringe order determination in scanning white-light interferometry using a Fourier-based technique,” *Appl. Opt.*, vol. 51, no. 12, pp. 1922–1928, 2012.

[73] F. Gao, R. K. Leach, J. Petzing, and J. M. Coupland, “Surface measurement errors using commercial scanning white light interferometers,” *Meas. Sci. Technol.*, vol. 19, no. 1, 2008.

[74] A. Pförtner and J. Schwider, “Dispersion error in white-light Linnik interferometers and its implications for evaluation procedures,” *Appl. Opt.*, vol. 40, no. 34, p. 6223, 2001.

[75] A. Harasaki and J. C. Wyant, “Fringe modulation skewing effect in white-light vertical scanning interferometry.,” *Appl. Opt.*, vol. 39, no. 13, pp. 2101–2106, 2000.

[76] A. Harasaki, J. Schmit, and J. C. Wyant, “Improved vertical-scanning interferometry,” *Appl. Opt.*, vol. 39, no. 13, p. 2107, 2000.

[77] J. M. Coupland and J. Lobera, “Measurement of steep surfaces using white light interferometry,” *Strain*, vol. 46, no. 1, pp. 69–78, 2010.

[78] F. Gao, J. M. Coupland, and J. Petzing, “V-Groove Measurements using White

Light Interferometry," *Phot. 06, Manchester*, 2006.

[79] K. Palodhi, "Absolute surface topography measurement with polarisation sensitive coherence scanning interferometry," 2013.

[80] M. C. Park and S. W. Kim, "Compensation of phase change on reflection in white-light interferometry for step height measurement.," *Opt. Lett.*, vol. 26, no. 7, pp. 420–422, 2001.

[81] A. Harasaki, J. Schmit, and J. C. Wyant, "Offset of coherent envelope position due to phase change on reflection," *Appl. Opt.*, 2001.

[82] E. Pecheva, P. Montgomery, D. Montaner, and L. Pramatarova, "White Light Scanning Interferometry Adapted for Large-Area Optical Analysis of Thick and Rough Hydroxyapatite Layers," *Langmuir*, vol. 23, no. 7, pp. 3912–3918, 2007.

[83] Audrey LEONG-HOI, "Étude des techniques de super-résolution latérale en nanoscopie et développement d'un système interférométrique nano-3D," 2016.

[84] M. Roy, J. Schmit, and P. Hariharan, "White-light interference microscopy: minimization of spurious diffraction effects by geometric phase-shifting.," *Opt. Express*, vol. 17, no. 6, pp. 4495–4499, 2009.

[85] H. Mukhtar, P. Montgomery, G. Gianto, and K. Susanto, "Rock surface roughness measurement using CSI technique and analysis of surface characterization by qualitative and quantitative results," *IOP Conf. Ser. Earth Environ. Sci.*, vol. 29, no. 1, 2016.

[86] M. Flury *et al.*, "Rapid prototyping of diffractive optical elements for high-power lasers using laser ablation lithography fabrication and coherence probe microscopy analysis," *Opt. Eng. 41(10)*, 2002.

[87] A. Benatmane and P. C. Montgomery, "3D analysis of buried interfaces using interference microscopy," *Eur. Phys. J. Appl. Phys.*, vol. 27, no. 1–3, pp. 411–414, Jul. 2004.

[88] A. Leong-hoï *et al.*, "Detection of defects in a transparent polymer with high resolution tomography using white light scanning interferometry and noise reduction," *Proc. SPIE*, vol. 9528, 2015.

[89] A. J. Den Dekker and A. Van Den Bos, “Resolution : a survey,” vol. 14, no. 3, pp. 547–557, 1997.

[90] J. Pichon, “Enregistrement optique haute densité : étude physique et physico-chimique du phénomène de Super-Résolution To cite this version : HAL Id : tel-00363302,” 2009.

[91] X. Colonna De Lega and P. de Groot, “Lateral resolution and instrument transfer function as criteria for selecting surface metrology instruments,” *Imaging Appl. Opt. Tech. Pap.*, p. OTu1D.4, 2012.

[92] R. Heintzmann and G. Ficz, “Breaking the resolution limit in light microscopy,” *Methods Cell Biol.*, vol. 114, no. 4, pp. 525–544, 2013.

[93] P. Maragos, J. F. Kaiser, and T. F. Quatieri, “On amplitude and frequency demodulation using energy operators,” *IEEE Trans. Signal Process*, vol. 41 (4), pp. 1532–1550, 1993.

[94] R.-J. Recknagel and G. Notni, “Measurement and analysis of microtopography using wavelet methods,” in *Proc. SPIE 3098, Optical Inspection and Micromeasurements II*.

[95] L. Huang, Q. Kemao, B. Pan, and A. K. Asundi, “Comparison of Fourier transform, windowed Fourier transform, and wavelet transform methods for phase extraction from a single fringe pattern in fringe projection profilometry,” *Opt. Lasers Eng.*, vol. 48, no. 2, pp. 141–148, 2010.

[96] C. Jiang, S. Jia, J. Dong, Q. Lian, and D. Li, “Multi-frequency fringe projection profilometry based on wavelet transform,” *Opt. Express*, vol. 24, no. 11, p. 11323, 2016.

[97] O. Kocahan, E. Tiryaki, E. Coskun, and S. Ozder, “Determination of phase from the ridge of CWT using generalized Morse wavelet,” *Meas. Sci. Technol.*, vol. 29, no. 3, 2018.

[98] S. Chopra and K. J. Marfurt, “Choice of mother wavelets in CWT spectral decomposition,” *SEG New Orleans Annu. Meet.*, pp. 2957–2961, 2015.

[99] L. Mingzhou, “Development of fringe analysis techniques in white light

interferometry for micro-component measurement," 2008.

[100] F. Yang and X. He, "Two-step phase-shifting fringe projection profilometry :," 2007.

[101] P. Flandrin, P. Goncalves, and G. Rilling, "Detrending and denoising with empirical mode decompositions," *Eur. Signal Process. Conf.*, vol. 06–10–Sept, pp. 1581–1584, 2015.

[102] Standard, "ASME B46.1-1995, ASME B46.1-1985, ISO 4287-1997, ISO 4287/1." 1997.

[103] Standard, "ASME B46.1-1995, ISO 4287." 1997.

[104] F. Salzenstein, A. O. Boudraa, and T. Chonavel, "A new class of multi-dimensional Teager- Kaiser and higher order operators based on directional derivatives," *Multidimens. Sys. Sig. Proc*, 2013.

[105] M. Wielgus and K. Patorski, "Evaluation of amplitude encoded fringe patterns using the bidimensional empirical mode decomposition and the 2D Hilbert transform generalizations," *Appl. Opt.*, vol. 50, no. 28, pp. 5513–5523, 2011.

[106] A. C. Bovik, Ed., *Handbook of image and video processing*, 2nd ed. Austin, Texas: Elsevier Inc., 2005.

[107] D. Hutchison and J. C. Mitchell, *Image Analysis and Recognition*. 1973.

[108] K. G. Larkin, D. J. Bone, and M. A. Oldfield, "Natural demodulation of two-dimensional fringe patterns I General background of the spiral phase quadrature transform," *J. Opt. Soc. Am. A*, vol. 18, no. 8, p. 1862, 2001.

[109] A. Potamianos and P. Maragos, "A comparison of the energy operator and the Hilbert transform approach to signal and speech demodulation," *Signal Processing*, vol. 37, no. 1, pp. 95–120, May 1994.

[110] D. Gabor, "Theory of Communication," *J. IEE*, vol. 93, pp. 429–457, 1946.

[111] T. F. Quatieri, "Energy Separation in Signal Modulations with Application to Speech Analysis," *IEEE Trans. Signal Process.*, vol. 41, no. 10, pp. 3024–3051, 1993.

[112] A. P. P. Maragos, “Higher order differential energy operators,” *IEEE Signal Process*, pp. 152–154, 1995.

[113] A. O. Boudraa *et al.*, “2D Continuous Higher Order Energy Operators ∗,” pp. 1–27, 2005.

[114] F. Salzenstein, A. Boudraa, and J. Cexus, “energy operators,” vol. 24, no. 12, pp. 3717–3727, 2007.

[115] F. S. A. O. B. T. Chonavel, “A new class of multi-dimensional Teager-Kaiser and higher order operators based on directional derivatives,” pp. 543–572, 2013.

[116] F. Salzenstein and A. O. Boudraa, “Multi-dimensional higher order differential operators derived from the Teager – Kaiser energy-tracking function,” *Signal Processing*, vol. 89(4), pp. 623–640, 2009.

[117] B. E. A. Saleh, M. C. Teich, and C. J. Wiley, *Statistical optics 10.1*, vol. 5. 1991.

[118] S. PERRIN, “Development and characterization of an optical coherence tomography micro system,” 2016.

[119] A. Benatmane and P. C. Montgomery, “Buried interface characterization by interference microscopy,” vol. 450, pp. 187–190, 2004.

[120] A. O. Boudraa and F. Salzenstein, “Teager–Kaiser energy methods for signal and image analysis: A review,” *Digit. Signal Process. A Rev. J.*, vol. 78, pp. 338–375, 2018.

[121] P. Maragos and A. C. Bovik, “Image demodulation using,” *Opt. Soc. Am*, vol. 12, no. 9, pp. 1867–1876, 1995.

[122] T. H. Yu, S. K. Mitra, and J. F. Kaiser, “A novel nonlinear filter for image enhancement,” in Image Processing Algorithms and Techniques II,” *Proc. Soc. Photo-Opt. Instrum. Eng*, vol. 1452, pp. 303–309, 1991.

[123] K.L.Apedo *et al.*, “Cement paste surface roughness analysis using coherence scanning interferometry and confocal microscopy,” *Mater. Charact.*, vol. 100, pp. 108–119, 2015.

[124] K.L.Apedo, P.Montgomery, N.Serres, C.Fond, and F.Feugeas, “Geometrical

roughness analysis of cement paste surfaces using coherence scanning interferometry and confocal microscopy," *Mater. Charact.*, vol. 118, pp. 212–224, 2016.

[125] P. C. Montgomery, F. Salzenstein, G. Gianto, K. L. Apedo, N. Serres, and C. F. F. Feugeas;, "Multi-scale roughness measurement of cementitious materials using different optical profilers and window resizing analysis," *Proc. Vol. 9525, Opt. Meas. Syst. Ind. Insp. IX*, 2015.

[126] J. L. and C. F. J.-B. Kopp J. Schmittbuhl O. Noel, "Engineering Fracture Mechanics," vol. 126, pp. 178–189, 2014.

[127] J. B. Kopp, J. Schmittbuhl, O. Noel, J. Lin, and C. Fond, "Fluctuations of the dynamic fracture energy values related to the amount of created fracture surface," *Eng. Fract. Mech.*, vol. 126, pp. 178–189, 2014.